ABSTRACT

MARTIN, ELIJAH HENRY. Electric Field Measurements of the Capacitively Coupled Magnetized RF Sheath Utilizing Passive Optical Emission Spectroscopy. (Under the direction of Steven Shannon.)

A major challenge facing magnetic confinement fusion is the implementation of reliable plasma heating systems. Ion cyclotron resonance heating (ICRH) is a key technique utilized to achieve the ion temperatures necessary for desirable fusion reaction rates. ICRH systems are designed to couple energy into the core plasma ions through a resonant interaction with an electromagnetic wave in the radio frequency range. The interaction of the wave with the scrape off layer plasma establishes an electric field which terminates directly on the plasma facing surfaces and is referred to as the near-field. In order to bridge the gap between the theoretical and actual performance of ICRF antennas, experimental measurement of this electric field is highly desired. However, due to the large amount of power launched by ICRF antennas only non-local measurements have thus far been obtained. The research presented in this dissertation is centered on the development of a non-perturbative diagnostic to locally measure the near-field with high spatial and temporal resolution.

The main objective of the research presented in this dissertation is to develop and validate a spectroscopic diagnostic capable of measuring local time periodic electric fields. The development phase of the diagnostic consisted of atomic physics formulation and was carried out in two steps. The first involved the calculation of the electronic structure of the one and two-electron atom utilizing the hydrogenic wave function. The second involved the calculation of the spectral line profile based on the electric dipole connection operator. The validate phase of the diagnostic consisted of implementation of the atomic physics to measure the electric field topology associated with the capacitively coupled magnetized RF sheath using passive OES. The experimental measurements are then compared to a simple one-dimensional analytical model providing the validation of the developed atomic physics.

Electric Field Measurements of the Capacitively Coupled Magnetized RF Sheath Utilizing Passive Optical Emission Spectroscopy

by
Elijah Henry Martin

A dissertation submitted to the Graduate Faculty of
North Carolina State University
in partial fulfillment of the
requirements for the Degree of
Doctor of Philosophy

Nuclear Engineering

Raleigh, North Carolina

2014

APPROVED BY:

John Caughman	Mohamed Bourham
John Gilligan	Albert Young

Steven Shannon
Chair of Advisory Committee

DEDICATION

This dissertation is dedicated to my parents Steve and Joan Martin who have been a constant source of inspiration and support, I owe them everything! Additionally, the dedication is shared with grandmother Mary Martin ~ until we meet again!

BIOGRAPHY

Elijah Martin was born on April 10th 1984 in Portsmouth Virgina. He grew up in Hendersonville North Carolina, a small mountain town on the far western side of the state. Upon completion of high school he moved to Raleigh North Carolina to begin his undergraduate studies at North Carolina State University (NCSU). In 2007 he graduated summa cum laude with a B.S. in physics and nuclear engineering from NCSU. In 2008 he began his graduate studies at NCSU under the direction of Dr. Steven Shannon. After a 1.5 years of course work he moved to Knoxville Tennessee to conduct his doctoral research in the Fusion and Materials for Nuclear Systems Division at Oak Ridge National Laboratory in collaboration with staff scientist Dr. John Caughman.

ACKNOWLEDGEMENTS

Firstly, I would like to acknowledge my family, especially my parents Steven and Joan Martin, my brother Cameron Martin, and my grandparents Gerald and Mary Martin. They have supported me with their love, encouragement and prayers; without this my accomplishment would not have been successfully realized. Therefore, my honor shall be there honor!

I was blessed to have Dr. Steven Shannon as my advisor, he diligently worked to provide an outstanding environment for me to grow as a person and scientist. I cannot express my gratitude enough for his dedication, mentoring, and friendship. God bless you now and always! It has been my joy and privilege to work with my advisor at Oak Ridge National Laboratory, Dr. John Caughman. His expertise in experimental and RF plasma physics have been my sure guide. Working with these expectational scientist have formed the foundation of my research abilities, I am gratefully indebted to you both.

I have had the honor of studying atomic physics under the direction of Dr. Ralph Isler, without his guidance and tutoring this work would not have been possible. I am continuously amazed at his scientific intuition, knowledge, and ability. God has surely looked favorably upon him! I would also like to acknowledge the staff of the Fusion and Materials for Nuclear Systems Division at Oak Ridge National Laboratory for providing an environment in which the student can easily excel. This research was supported by a contract between Oak Ridge National Laboratory and North Carolina State University.

I acknowledge my closest friends, Brice Terry, David Ferguson, and David Illgen who have traveled this road with me from nearly the vary beginning ~ you are my brothers. The Holy Catholic Church has been my rock, I am forever thankful and indebted to her! I express my most gracious gratitude to the Most Reverend Bishop Richard Stika, the Handmaids of the Precious Blood, and the members of the Knoxville Frassati Fellowship for Young Adults for their prayers and support. In particular, I have been blessed with two very special friends during my time in Knoxville, Brittany Koepke and Jessica Mearns. You both have been a breathe of fresh air and an amazing model of holiness for me.

Finally and most importantly, I am forever indebted to my Lord and my God Jesus Christ for my life and for the ability He has given me to study His most magnificent creation † GLORY TO GOD IN THE HIGHEST † without Him absolutely nothing is possible!

TABLE OF CONTENTS

LIST OF TABLES . . . . . **vii**

LIST OF FIGURES . . . . . **ix**

CHAPTER 1 INTRODUCTION **1**
- **1.1 ICRH in Magnetically Confined Thermonuclear Plasma** 3
- **1.2 Atomic Spectroscopy** 7
- **1.3 Diagnostic Implementation and Validation** 8

CHAPTER 2 THE CAPACITIVELY COUPLED MAGNETIZED RF SHEATH **10**
- **2.1 Introduction** 11
- **2.2 ICRF Antenna Near-Field** 16
- **2.3 Analytical Modeling** 18

CHAPTER 3 PASSIVE OPTICAL EMISSION SPECTROSCOPY **24**
- **3.1 Introduction** 25
- **3.2 Experimental Technique** 29
- **3.3 Atomic Theory** 36
  - **3.3.1 Floquet Method** 38
  - **3.3.2 Calculation of the Spectral Line Profile** 50
  - **3.3.3 Quasi-static Approximation** 61
- **3.4 Spectral Line Profile Fitting** 65
- **3.5 Electronic Transition Selection** 71
  - **3.5.1 Hydrogen** 72
  - **3.5.2 Helium** 74

CHAPTER 4 EXPERIMENTAL APPARATUS **78**
- **4.1 Dynamic Stark Verification Experiment** 79
  - **4.1.1 RF System** 82
  - **4.1.2 Microwave System** 87
  - **4.1.3 Limiter Assembly** 89
- **4.2 Spectroscopic System** 94
  - **4.2.1 Collection Optics** 94
  - **4.2.2 Spectrometer and Detector** 99
- **4.3 Plasma Diagnostics** 102
  - **4.3.1 RF Compensated Langmuir Probe** 102
  - **4.3.2 Capacitive Probe** 111
- **4.4 Control and Data Acquisition** 113

CHAPTER 5 EXPERIMENT AND ANALYSIS **117**
- **5.1 Discharge Characterization** 118
  - **5.1.1 Experimental Scenario** 118
  - **5.1.2 Capacitive Probe Measurement** 120

5.1.3 RF Compensated Langmuir Probe Measurement . . . 124
5.2 Time Averaged Optical Emission Spectroscopy . . . 131
5.2.1 Hydrogen Discharge . . . 132
5.2.2 Helium Discharge . . . 143
5.3 Phase Resolved Optical Emission Spectroscopy . . . 148
5.4 Spectral Line Profile Analysis . . . 153
5.4.1 Calculation of the Fit Error . . . 155
5.4.2 Fitting the Spectral Line Profile . . . 161

CHAPTER 6 SPECTROSCOPIC RESULTS . . . **174**
6.1 Parallel Field Configuration . . . 175
6.1.1 Electric Field . . . 175
6.1.2 Radiator Distribution Function . . . 179
6.2 Perpendicular Field Configuration . . . 180
6.2.1 Electric Field . . . 181
6.2.2 Radiator Distribution Function . . . 183

CHAPTER 7 CONCLUSIONS AND FUTURE WORK . . . **185**

REFERENCES . . . **189**

APPENDICES . . . **198**

APPENDIX A UNPERTURBED ENERGY EIGENVALUES . . . **199**
A.1 Hydrogen . . . 199
A.2 Helium . . . 200

APPENDIX B CALCULATION OF MATRIX ELEMENTS . . . **202**
B.1 Magnetic Field Matrix Elements . . . 205
B.2 Electric Field Field Matrix Elements . . . 206

APPENDIX C SHOT DISCHARGE PARAMETERS . . . **210**
C.1 Parallel Field Configuration . . . 211
C.2 Perpendicular Field Configuration . . . 213

APPENDIX D SPECTRAL LINE PROFILES . . . **215**
D.1 Parallel Field Configuration - H_β . . . 218
D.2 Parallel Field Configuration - $5^3D \rightarrow 2^3P$ He I . . . 220
D.3 Perpendicular Field Configuration - H_β . . . 222
D.4 Perpendicular Field Configuration - $5^3D \rightarrow 2^3P$ He I . . . 224

LIST OF TABLES

Table 3.1 Spectroscopic camera parameters. 34
Table 3.2 Number of states N for the given radial quantum number n. 42
Table 3.3 Radiator and instrument parameters. 59
Table 3.4 Second tier discretization parameters and uncertainty. 67
Table 3.5 Second tier fit results associated with the spectral line profiles presented in Figure 3.24. 69
Table 3.6 Available first tier fit variables. 70

Table 4.1 Vacuum chamber port labels. 80
Table 4.2 Constants associated with the empirical fit to the Laframboise results. 109
Table 4.3 Under compensated I-V characteristic fit results. 111

Table 5.1 Model associated with fitting of the spectral line profiles. 154
Table 5.2 Fit parameters associated with the spectra presented for shot 3. 161
Table 5.3 Fit parameters associated with the spectra presented for shot 19. 161
Table 5.4 Fit parameters associated with the spectra presented for shot 11. 169
Table 5.5 Fit parameters associated with the spectra presented for shot 27. 169

Table A.1 Hydrogen energy levels in cm^{-1} for n=1 through 3. 199
Table A.2 Hydrogen energy levels in cm^{-1} for n=4 through 6. 200
Table A.3 Para-helium energy levels in cm^{-1} for n=1 through 3. 200
Table A.4 Para-helium energy levels in cm^{-1} for n=4 through 6. 200
Table A.5 Ortho-helium energy levels in cm^{-1} for n=1 through 3. 201
Table A.6 Ortho-helium energy levels in cm^{-1} for n=4 through 6. 201

Table B.1 Overlap integral variable definitions. 209

Table C.1 Definitions of set points and the electrical parameters. 210
Table C.2 Definitions of plasma parameter. 211
Table C.3 Power and matching network set points for the hydrogen discharges. 211
Table C.4 Power and matching network set points for the helium discharges. 211
Table C.5 Electrical parameters for the hydrogen discharges. 212
Table C.6 Electrical parameters for the helium discharges. 212
Table C.7 Plasma parameters for the hydrogen discharges. 212
Table C.8 Plasma parameters for the helium discharges. 213
Table C.9 Power and matching network set points for the hydrogen discharges. 213
Table C.10 Power and matching network set points for the helium discharges. 213
Table C.11 Electrical parameters for the hydrogen discharges. 214
Table C.12 Electrical parameters for the helium discharges. 214
Table C.13 Plasma parameters for the hydrogen discharges. 214
Table C.14 Plasma parameters for the helium discharges. 214

Table D.1 Select discharge parameters of the presented shots. 215

Table D.2 Fit parameters associated with the spectra presented for shot 3. 216
Table D.3 Fit parameters associated with the spectra presented for shot 4. 216
Table D.4 Fit parameters associated with the spectra presented for shot 11. 216
Table D.5 Fit parameters associated with the spectra presented for shot 12. 216
Table D.6 Fit parameters associated with the spectra presented for shot 19. 217
Table D.7 Fit parameters associated with the spectra presented for shot 20. 217
Table D.8 Fit parameters associated with the spectra presented for shot 27. 217
Table D.9 Fit parameters associated with the spectra presented for shot 28. 217

LIST OF FIGURES

Figure 1.1 Confined plasma of a tokamak indicating the poloidal and toroidal directions. . . 3
Figure 1.2 Alcator C-Mod ICRH system indicating the various plasma facing components. . 4
Figure 1.3 Cross section of confined tokamak plasma indicating magnetic surfaces and ICRF antenna location. 5
Figure 1.4 Visualization of 3D ICRF wave fields in the equatorial plane of ITER showing the vacuum vessel and ICRF antenna structures, taken from [82]. 6

Figure 2.1 Thermal sheath generated at the interface with a grounded surface. 12
Figure 2.2 (a) Voltage waveform at RF biased electrode for asymmetric discharge and (b) corresponding width of the RF sheath z_o as a function of phase. 14
Figure 2.3 RF sheath corresponding to the points in phase t_1, t_2, and t_3 of the RF voltage waveform given by Figure 2.2a. 15
Figure 2.4 Simulated electric field (kV/cm) at the Faraday screen of a typical two current strap ICRF antenna [36]. The circulating RF currents on the Faraday screen/antenna box are indicated by the arrows. 16
Figure 2.5 Voltage waveform at the electrode used for the RF sheath simulations. 21
Figure 2.6 RF sheath electric field as a function of phase and space for (a) $\tau_R = 4$ ns and (a) $\tau_R = 300$ ns. 21
Figure 2.7 (a) Electric field parameters and associated (b) R^2 fitting parameter as a function of space for $\tau_R = 4$ ns. 22
Figure 2.8 (a) Electric field parameters and associated (b) R^2 fitting parameter as a function of space for $\tau_R = 300$ ns. 22
Figure 2.9 Electric field parameters for (a) $\tau_R = 4$ ns and (b) $\tau_R = 300$ ns as a function of space. 23

Figure 3.1 Theoretical H_β spectral line profile in the presence of an electric field with a 5 kV/cm magnitude and a frequency of 20 GHz. 28
Figure 3.2 Schematic of intensified CCD triggering for phase resolved OES. 31
Figure 3.3 Time dependent emission intensity of H_β in the RF sheath plotted against the RF biased electrode voltage. 32
Figure 3.4 Signal to noise ratio for the (a) PI-MAX III and (b) PyLoN spectroscopic cameras. 35
Figure 3.5 Non-zero matrix elements of $\tilde{\boldsymbol{H}}$ for the $n = 4$ level of hydrogen with $\tilde{s} = 4$ using the field geometry given by Eq. 3.32. 43
Figure 3.6 Eigenvalues in ascending order associated with $\tilde{\boldsymbol{H}}$ for $\omega/2\pi = 200$ GHz using the field geometry given by Eq. 3.32. 46
Figure 3.7 Eigenvalues in ascending order associated with $\tilde{\boldsymbol{H}}$ for $\omega/2\pi = 20$ GHz using the field geometry given by Eq. 3.32. 46
Figure 3.8 Eigenvalues associated with $\tilde{\boldsymbol{H}}$ for $\omega/2\pi \in [20, 97]$ GHz using the field geometry given by Eq. 3.32. 47
Figure 3.9 Eigenvalues of the $s = 0$ set associated with $\tilde{\boldsymbol{H}}$ for $\omega/2\pi \in [20, 97]$ GHz using the field geometry given by Eq. 3.32. 48
Figure 3.10 Select eigenvalues associated with $\tilde{\boldsymbol{H}}$ for $\omega/2\pi \in [30, 31.5]$ GHz using the field geometry given by Eq. 3.32. 49

Figure 3.11 (a) First and (b) second derivatives of the eigenvalues associated with $\tilde{\boldsymbol{H}}$ for $\omega/2\pi \in [30, 31.5]$ GHz using the field geometry given by Eq. 3.32. 50
Figure 3.12 Observation geometry and polarization vector coordinate system. 54
Figure 3.13 Rotation of polarization vector coordinate system. 55
Figure 3.14 Time averaged discrete H_β π profile with a field geometry given by Eq. 3.57 with $\omega = 20$ GHz. 56
Figure 3.15 Time averaged continuous and discrete H_β π profiles with a field geometry given by Eq. 3.57 with $\omega = 20$ GHz. 58
Figure 3.16 Time averaged continuous and discrete H_β π profiles with a field geometry given by Eq. 3.57 with $\omega = 5$ GHz. 58
Figure 3.17 π and σ polarization of the H_β spectrum with a field geometry given by Eq. 3.57 at $\omega = 13.56$ MHz. 59
Figure 3.18 π and σ polarization of the $5^3D \rightarrow 2^3P$ He I spectrum with a field geometry given by Eq. 3.57 with $\omega = 13.56$ MHz. 60
Figure 3.19 Discretization of electric field waveform for the quasi-static approximation of $\tilde{H}(t)$. 61
Figure 3.20 Comparison of the quasi-static solution with that of the Floquet method at various frequencies for the H_β π profile with a field geometry given by Eq. 3.57. 64
Figure 3.21 Schematic of fit algorithm method. 66
Figure 3.22 Experimental H_β (a) π and (b) σ spectral line profiles. 68
Figure 3.23 Continuous and pixelated theoretical H_β (a) π and (b) σ spectral line profiles. . . 68
Figure 3.24 Fitted experimental and theoretical H_β (a) π and (b) σ spectral line profiles. 69
Figure 3.25 Electric field and H_β emission intensity waveforms associated with the fit presented in Figure 3.24. 70
Figure 3.26 H_α spectral line profile associated with an electric field given by (a) $\bar{E}_L(t)$ and (b) $\bar{E}_H(t)$. 73
Figure 3.27 H_β spectral line profile associated with an electric field given by (a) $\bar{E}_L(t)$ and (b) $\bar{E}_H(t)$. 73
Figure 3.28 H_γ spectral line profile associated with an electric field given by (a) $\bar{E}_L(t)$ and (b) $\bar{E}_H(t)$. 73
Figure 3.29 $4^1D \rightarrow 2^1P$ He I profiles for an electric field given by (a) $\bar{E}_L(t)$ and (b) $\bar{E}_H(t)$. 76
Figure 3.30 $5^1D \rightarrow 2^1P$ He I profiles for an electric field given by (a) $\bar{E}_L(t)$ and (b) $\bar{E}_H(t)$. 76
Figure 3.31 $5^3D \rightarrow 2^3P$ He I profiles for an electric field given by (a) $\bar{E}_L(t)$ and (b) $\bar{E}_H(t)$. 76
Figure 3.32 Integrated spectral line profile as a function of pressure. 77

Figure 4.1 Experimental setup for the parallel field configuration. 80
Figure 4.2 Experimental setup for the perpendicular field configuration. 81
Figure 4.3 EIA 3 1/8" I-V probe transmission coefficient (a) magnitude and (b) phase. 83
Figure 4.4 RF directional coupler calibration curves. 84
Figure 4.5 Circuit diagram of the RF system. 85
Figure 4.6 Power efficiency of matching network in tune space of interest. 85
Figure 4.7 Plasma (a) resistance and (b) reactance for tune space of interest. 86
Figure 4.8 Magnetic field intensity for coil current of 180 A. 87
Figure 4.9 Microwave directional coupler calibration curves. 88
Figure 4.10 Theoretical H_β (a) π and (b) σ profiles with and without superposition of unperturbed emission. 90

Figure 4.11 Parallel field configuration limiter assembly (a) viewed along negative z-axis and (b) cross-section viewed along the positive x-axis. 91
Figure 4.12 Perpendicular field configuration limiter assembly (a) viewed along negative z-axis and (b) cross-section viewed along the positive y-axis. 92
Figure 4.13 Experimental Setup for the parallel field configuration. 93
Figure 4.14 Experimental Setup for the perpendicular field configuration. 93
Figure 4.15 Collection optics for beam profile simulation. 94
Figure 4.16 Collection optics beam profile simulation via 2D ray tracing. 95
Figure 4.17 Simulated beam profile of collection optics. 96
Figure 4.18 (a) Measured beam profile of the collection optics and (b) the Full Width at X Maximum (FWXM) of beam profile as a function of the first aperture width. 97
Figure 4.19 Collection optics for alignment simulation. 98
Figure 4.20 (a) Simulated photodiode signal for alignment of collection optics and (b) Footprint of beam profile associated with the aligned collection optics at the various translation stage locations. 98
Figure 4.21 Stray light measured by the collection optics. 99
Figure 4.22 Bi-Gaussian fit to the 4345 Å Ne I line. 100
Figure 4.23 (a) I_{Ii}, (b) λ_{Ii}, and (c) σ_{Ii} instrument function parameters. 101
Figure 4.24 Schematic of phase locked setup. 101
Figure 4.25 I-V characteristic of typical Langmuir probe. 103
Figure 4.26 Effect of the time dependent plasma potential on I-V characteristic of the Langmuir probe. 103
Figure 4.27 Instantaneous I-V characteristic of the Langmuir probe associated with $\tilde{\phi}_p(t_\pm) = \pm 5$ V and $\tilde{\phi}_p(t_o) = 0$ V. 104
Figure 4.28 Schematic of RF compensated Langmuir probe. 105
Figure 4.29 Impedance of RF compensated Langmuir probe. 106
Figure 4.30 RF compensated Langmuir probe sheath (a) resistance and (b) capacitance. 107
Figure 4.31 Schematic of RF compensated Langmuir probe experimental setup. 108
Figure 4.32 Fitted I-V characteristic from under compensated Langmuir probe. 111
Figure 4.33 Schematic of the capacitive probe. 112
Figure 4.34 Capacitive probe transmission coefficient (a) magnitude and (b) phase. 113
Figure 4.35 DStarVE LabVIEW control panel. 114
Figure 4.36 Control software generated signals. 115

Figure 5.1 RF biased electrode voltage and current waveforms for shot (a) 1 and (b) 19. 120
Figure 5.2 Harmonic spectrum of the RF biased electrode voltage and current waveforms for shot (a) 1 and (b) 19. 120
Figure 5.3 Time dependence of plasma potential and RF biased electrode voltage in the parallel field configuration for (a) hydrogen and (b) helium discharges. 121
Figure 5.4 Time dependence of plasma potential and RF biased electrode voltage in the perpendicular field configuration for (a) hydrogen and (b) helium discharges. . . 121
Figure 5.5 Harmonic spectrum of time dependent component of the plasma potential for (a) hydrogen and (b) helium discharges. 122
Figure 5.6 Magnitude of the fundamental of the plasma potential as a function of x-axis position in the parallel field configuration for (a) hydrogen and (b) helium discharges. 123

Figure 5.7 Magnitude of the fundamental of the plasma potential as a function of x-axis position in the perpendicular field configuration for (a) hydrogen and (b) helium discharges. 123
Figure 5.8 I-V characteristic with $P_{RF} = 0$ and 100 W. 124
Figure 5.9 Fitted I-V characteristic with (a) $P_{RF} = 0$ and (b) 100 W. 125
Figure 5.10 Effect of magnetic field on the I-V characteristic fit with (a) A_e as a variable and (b) A_e as a constant. 126
Figure 5.11 Normalized electron collection area as a function of magnetic field intensity. . . . 126
Figure 5.12 (a) n_e, (b) kT_e, and (c) ϕ_{p0} associated with the variable and constant A_e fit scenarios. 127
Figure 5.13 Spatial distribution of (a) n_e, (b) kT_e, and (c) ϕ_{p0} for hydrogen in the parallel field configuration. 127
Figure 5.14 Spatial distribution of (a) n_e, (b) kT_e, and (c) ϕ_{p0} for helium in the parallel field configuration. 128
Figure 5.15 Electron collection area for (a) hydrogen and (b) helium discharge. 128
Figure 5.16 Spatial distribution of (a) n_e, (b) kT_e, and (c) ϕ_{p0} for hydrogen in the perpendicular field configuration. 129
Figure 5.17 Spatial distribution of (a) n_e, (b) kT_e, and (c) ϕ_{p0} for helium in the perpendicular field configuration. 129
Figure 5.18 Electron collection area for (a) hydrogen and (b) helium discharge. 130
Figure 5.19 Time evolution of (a) absorbed RF power, (b) absorbed microwave power, (c) pressure, (d) RF voltage magnitude, (e) DC bias voltage, and (f) ion saturation current. 131
Figure 5.20 H_β spectral line profile as a function of position in the RF sheath for the (a) π and (b) σ components in the parallel field configuration. 132
Figure 5.21 H_β spectral line profile as a function of position in the RF sheath for the (a) π and (b) σ profiles in the perpendicular field configuration 133
Figure 5.22 H_β π profile at a position of (a) z=7.9 and (b) 7.6 mm in the parallel and perpendicular field configuration respectively. 134
Figure 5.23 H_β π spectral line profile at a position of $z = 7.9$ mm in the parallel field configuration showing the (a) superthermal emission fit and (b) removal. 134
Figure 5.24 H_β π spectral line profile at a position of $z = 7.6$ mm in the perpendicular field configuration showing the (a) superthermal emission fit and (b) removal. 135
Figure 5.25 H_β π profile at a position of $z = 7.9$ mm in the parallel field configuration showing the (a) molecular line fit and (b) removal. 136
Figure 5.26 H_β π profiles at a position of (a) $z = 0.8$ and 7.9 mm and (b) $z = 1.0$ and 7.6 mm in the parallel and perpendicular field configurations respectively. 136
Figure 5.27 H_β π and σ profiles at a position of (a) $z = 0.8$ and (b) 1.0 mm in the parallel and perpendicular field configurations respectively. 137
Figure 5.28 H_β π and σ profile integrated area for thermal emission in the (a) parallel and (b) perpendicular field configurations. 138
Figure 5.29 H_β π and σ profile integrated area for superthermal emission in the (a) parallel and (b) perpendicular field configurations. 138
Figure 5.30 Ratio of thermal to superthermal H_β π and σ profile integrated area in the (a) parallel and (b) perpendicular field configurations. 139

Figure 5.31 Phase resolved H_α spectral line profile obtained viewing the RF biased electrode along the z-axis at a phase of 0 ns 140
Figure 5.32 Energy as a function of phase for sputtered and charge exchanged hydrogen atoms. 141
Figure 5.33 Energy as a function of RF biased electrode voltage for (a) sputtered and (b) charge exchanged hydrogen atoms. 142
Figure 5.34 Energy as a function of pressure for sputtered and charge exchanged hydrogen atoms. 142
Figure 5.35 $5^3D \rightarrow 2^3P$ He I spectral line profile as a function of position in the RF sheath for the (a) π and (b) σ components in the parallel field configuration. 143
Figure 5.36 $5^3D \rightarrow 2^3P$ He I spectral line profile as a function of position in the RF sheath for the (a) π and (b) σ components in the perpendicular field configuration. 144
Figure 5.37 $5^3D \rightarrow 2^3P$ He I spectral line profile at a position of $z = 30$ mm. 144
Figure 5.38 $5^3D \rightarrow 2^3P$ He I π profiles at a position of (a) $z = 7.9$ and (b) 7.6 mm in the parallel and perpendicular field configuration respectively. 145
Figure 5.39 $5^3D \rightarrow 2^3P$ He I profile at a position of $z = 7.9$ mm in the parallel field configuration showing the (a) impurity line fit and (b) removal. 146
Figure 5.40 $5^3D \rightarrow 2^3P$ He I π profiles at $z = 0.8$ mm and 7.9 mm and (b) $z = 1.0$ and 7.6 mm in the parallel and perpendicular field configurations respectively. 146
Figure 5.41 $5^3D \rightarrow 2^3P$ He I π and σ profiles at (a) $z = 0.8$ mm and (b) 1.0 mm in the parallel and perpendicular field configurations respectively. 147
Figure 5.42 $5^3D \rightarrow 2^3P$ He I π and σ profile integrated area for total emission in the (a) parallel and (b) perpendicular field configurations. 148
Figure 5.43 H_β and $5^3D \rightarrow 2^3P$ He I π profile integrated area as a function of phase at $z = 1.0mm$ in the parallel field configuration> 149
Figure 5.44 π profile integrated area as a function of phase and space for (a) H_α and (b) H_β in the parallel field configuration. 149
Figure 5.45 H_α π integrated area as a function of phase and space correlated to the RF biased electrode voltage in the parallel field configuration. 150
Figure 5.46 H_α π profile measured at a phase of 0 ns and a position of $z = 2.0$ in the parallel field configuration. 151
Figure 5.47 Thermal and superthermal emission as a function of phase in the parallel field configuration. 151
Figure 5.48 Superthermal emission as a function of phase and space (a) in the parallel and (b) perpendicular field configurations. 152
Figure 5.49 Thermal emission as a function of phase and space (a) in the parallel and (b) perpendicular field configurations. 153
Figure 5.50 H_β π and σ profiles for $E_0 = E_1 = 3.3$ kV/cm and (a) $kT_{R1} = 1.0$ and (b) 2.0 eV with simulated noise. 156
Figure 5.51 E_0 error as a function of electric field parameters E_0 and E_1 for (a) kT_{R1}=1.0 and (b) 2.0 eV. 157
Figure 5.52 E_1 error as a function of electric field parameters E_0 and E_1 for (a) $kT_{R1} = 1.0$ and (b) 2.0 eV. 157
Figure 5.53 kT_{R1} error as a function of electric field parameters E_0 and E_1 for (a) $kT_{R1} = 1.0$ and (b) 2.0 eV. 158

Figure 5.54 (a) Averaged error from π and σ fit scenario and (b) averaged error ratio as a function of radiator temperature for E_0. 158
Figure 5.55 (a) Averaged error from π and σ fit scenario and (b) averaged error ratio as a function of radiator temperature for E_1. 159
Figure 5.56 (a) Averaged error from π and σ fit scenario and (b) averaged error ratio as a function of radiator temperature for kT_{R1}. 159
Figure 5.57 $5^3D \rightarrow 2^3P$ He I π and σ profiles for $E_0 = E_1 = 3.3$ kV/cm with simulated noise. . . 160
Figure 5.58 (a) E_0 and (b) E_1 error as a function of electric field parameters E_0 and E_1. 161
Figure 5.59 Fit to the H_β π profile at a position of $z = 0.8$ and 1.0 mm for (a) shot 3 and (b) 19 respectively. 162
Figure 5.60 Fit to the H_β σ profile at a position of $z = 0.8$ and 1.0 mm for (a) shot 3 and (b) 19 respectively. 163
Figure 5.61 (a) H_β π and σ profiles at a position of $z = 0.8$ mm for shot 3 and (b) simulated molecular hydrogen profile. 164
Figure 5.62 Electric field and transition intensity waveforms associated with the fit to the H_β π and σ profiles at a position of (a) $z = 0.8$ mm for shot 3 and (b) $z = 1.0$ mm for 19. 165
Figure 5.63 H_β π and σ profiles at a position of $z = 7.9$ and 7.6 mm for (a) shot 3 and (b) 19 respectively. 166
Figure 5.64 Fit to the H_β (a) π and (b) σ profiles for shot 3 at a position of $z = 7.9$ mm using the one group model. 167
Figure 5.65 Fit to the H_β (a) π and (b) σ profiles for shot 3 at a position of $z = 7.9$ mm using the two group model. 167
Figure 5.66 Reduced χ fitting parameter associated with the H_β π and σ profiles as a function of position for (a) shot 3 and (b) shot 19. 168
Figure 5.67 Fit to the $5^3D \rightarrow 2^3P$ He I π profile at a position of $z = 0.8$ and 1.0 mm for (a) shot 11 and (b) 27 respectively. 170
Figure 5.68 Fit to the $5^3D \rightarrow 2^3P$ He I σ profile at a position of $z = 0.8$ and 1.0 mm for (a) shot 11 and (b) 27 respectively. 171
Figure 5.69 Fit to the $5^3D \rightarrow 2^3P$ He I (a) π and (b) σ profiles for shot 11 at a position of $z = 7.9$ mm. 172
Figure 5.70 Reduced χ fitting parameter associated with the H_β π and σ profiles as a function of position for (a) shot 3 and (b) shot 19. 172

Figure 6.1 (a) Electric field parameters E_0 and E_1 and (b) minimum electric field waveform intensity as a function of position for shot 3. 175
Figure 6.2 (a) Electric field parameter θ_1 as a function of position and (b) contour plot of electric field as a function of phase and position for shot 3. 176
Figure 6.3 Experimental and modeled minimum electric field waveform intensity as a function of position for shot 3. 177
Figure 6.4 (a) Electric field parameters E_0 and E_1 and (b) minimum electric field waveform intensity as a function of position for shot 11. 178
Figure 6.5 Experimental and modeled minimum electric field waveform intensity as a function of position for shot 11. 178
Figure 6.6 Second thermal group (a) temperature kT_{R2} and (b) intensity I_{R2} as a function position for shot 3. 179

Figure 6.7 Second thermal group (a) temperature kT_{R2} and (b) intensity I_{R2} as a function position for shot 11. 180
Figure 6.8 (a) Electric field parameters E_0 and E_1 and (b) minimum electric field waveform intensity as a function of position for shot 19. 181
Figure 6.9 (a) Electric field parameter θ_1 as a function of position and (b) contour plot of electric field as a function of phase and position for shot 19. 182
Figure 6.10 (a) Electric field parameters E_0 and E_1 and (b) minimum electric field waveform intensity as a function of position for shot 27. 183
Figure 6.11 Second thermal group (a) temperature kT_{R2} and (b) intensity I_{R2} as a function position for shot 19. 183
Figure 6.12 Second thermal group (a) temperature kT_{R2} and (b) intensity I_{R2} as a function position for shot 27. 184

Figure D.1 Fit to the H_β (a) π and (b) σ profiles for shot 3 at a position of $z = 0.8$ mm. 218
Figure D.2 Fit to the H_β (a) π and (b) σ profiles for shot 3 at a position of $z = 3.8$ mm. 218
Figure D.3 Fit to the H_β (a) π and (b) σ profiles for shot 3 at a position of $z = 7.9$ mm. 218
Figure D.4 Fit to the H_β (a) π and (b) σ profiles for shot 4 at a position of $z = 0.8$ mm. 219
Figure D.5 Fit to the H_β (a) π and (b) σ profiles for shot 4 at a position of $z = 3.8$ mm. 219
Figure D.6 Fit to the H_β (a) π and (b) σ profiles for shot 4 at a position of $z = 7.9$ mm. 219
Figure D.7 Fit to the $5^3D \rightarrow 2^3P$ He I (a) π and (b) σ profiles for shot 11 at a position of $z = 0.8$ mm. 220
Figure D.8 Fit to the $5^3D \rightarrow 2^3P$ He I (a) π and (b) σ profiles for shot 11 at a position of $z = 3.8$ mm. 220
Figure D.9 Fit to the $5^3D \rightarrow 2^3P$ He I (a) π and (b) σ profiles for shot 11 at a position of $z = 7.9$ mm. 220
Figure D.10 Fit to the $5^3D \rightarrow 2^3P$ He I (a) π and (b) σ profiles for shot 12 at a position of $z = 0.8$ mm. 221
Figure D.11 Fit to the $5^3D \rightarrow 2^3P$ He I (a) π and (b) σ profiles for shot 12 at a position of $z = 3.8$ mm. 221
Figure D.12 Fit to the $5^3D \rightarrow 2^3P$ He I (a) π and (b) σ profiles for shot 12 at a position of $z = 7.9$ mm. 221
Figure D.13 Fit to the H_β (a) π and (b) σ profiles for shot 19 at a position of $z = 1.0$ mm. 222
Figure D.14 Fit to the H_β (a) π and (b) σ profiles for shot 19 at a position of $z = 4.1$ mm. 222
Figure D.15 Fit to the H_β (a) π and (b) σ profiles for shot 19 at a position of $z = 7.6$ mm. 222
Figure D.16 Fit to the H_β (a) π and (b) σ profiles for shot 20 at a position of $z = 1.0$ mm. 223
Figure D.17 Fit to the H_β (a) π and (b) σ profiles for shot 20 at a position of $z = 4.1$ mm. 223
Figure D.18 Fit to the H_β (a) π and (b) σ profiles for shot 20 at a position of $z = 7.6$ mm. 223
Figure D.19 Fit to the $5^3D \rightarrow 2^3P$ He I (a) π and (b) σ profiles for shot 27 at a position of $z = 1.0$ mm. 224
Figure D.20 Fit to the $5^3D \rightarrow 2^3P$ He I (a) π and (b) σ profiles for shot 27 at a position of $z = 4.1$ mm. 224
Figure D.21 Fit to the $5^3D \rightarrow 2^3P$ He I (a) π and (b) σ profiles for shot 27 at a position of $z = 7.6$ mm. 224
Figure D.22 Fit to the $5^3D \rightarrow 2^3P$ He I (a) π and (b) σ profiles for shot 28 at a position of $z = 1.0$ mm. 225

Figure D.23 Fit to the $5^3D \rightarrow 2^3P$ He I (a) π and (b) σ profiles for shot 28 at a position of $z = 4.1$ mm. 225
Figure D.24 Fit to the $5^3D \rightarrow 2^3P$ He I (a) π and (b) σ profiles for shot 28 at a position of $z = 7.6$ mm. 225

CHAPTER

1

INTRODUCTION

Fossil fuels are the primary source of energy for current society. In 2012 approximately 18 TW of power was consumed by the world population, of which 15.5 TW was the result of fossil fuel combustion [8, 64]. While the remaining recoverable reserves are a matter of debate it is clear that supply will be unable to meet the demands for the entirety of the 21st century. Thus it is imperative to explore long term sources of energy that can fulfill the global requirements. Given the current technology nuclear fission and fusion are the only candidates that meet the criteria. However without a change in the direction of the current nuclear fission program to include breeding and reprocessing the supply of fissile material will eventually be exhausted. The most attractive possibility for long term energy stability is the nuclear fusion of light nuclei. This is due to the fact that the fuel is essentially inexhaustible and has a large energy density. Nuclear fusion has the additionally benefit of having non-radioactive waste products. There are various schemes which nuclear fusion can be realized such as magnetic, inertial, and electrostatic confinement to give a few examples. The international community has deemed magnetic confinement, specifically the tokamak, as the most widely acceptable path to foreseeable near term nuclear fusion by the commitment to ITER [4]. As such this dissertations primary purpose is to aid the advancement of magnetic confinement fusion.

Magnetic confinement fusion faces many challenges such as control of transport, instabilities, and plasma-wall interactions. This dissertation is focused on addressing plasma-wall interactions, specifically those driven by ion cyclotron resonance heating (ICRH). Typically an electric field is the driving mechanism for plasma-wall interactions. In the case of ICRH systems the electric

field near the plasma facing components is responsible and is known as the so called near-field. In order to understand this interaction, experimental measurement of the near-field is highly desired. However, due to the enormous amount of power propagating through this region non-perturbative diagnostics must be utilized and are non-trivial. The work conducted and presented in this dissertation is centered on the development of a non-perturbative diagnostic based on passive optical emission spectroscopy (OES). The diagnostic is capable of determining local time periodic electric fields from a fit to the time averaged spectral line profile of select hydrogenic or helium-like electronic transitions. In order validate and thus have confidence in the spectroscopic diagnostic an experiment was designed and conducted in which the electric field of the capacitively coupled magnetized radio frequency (RF) sheath was determined. This particular RF sheath was selected because the electric field dynamic and topology is similar to that of the near-field of ion cyclotron resonant frequency (ICRF) antenna. In summary the primary objective of this dissertation is the development and validation of a diagnostic which can be utilized to aid the design of ICRH systems such that the required and optimal performance can be realized.

This dissertation is organized as follows: Chapter 1 provides an introduction to the dissertation. A description of ICRH in the thermonuclear reactor and the associated performance limiting factors is discussed. To mitigate the parasitic effects of the near-field a non-perturbative spectroscopic diagnostic was developed and validated; a brief discussion is provided. Chapter 2, introduces the capacitively coupled magnetized RF sheath and discusses its relevance to the near-field of ICRF antenna. Additionally a simple analytical model is presented to compare with the experimentally determined electric field measurements. In Chapter 3, the spectroscopic technique and the associated atomic physics constituting the theoretical framework of the diagnostic is formulated and developed. The specific electronic transitions utilized in the implementation of the diagnostic to measure the capacitively coupled magnetized RF sheath electric field is presented. In Chapter 4, the experimental apparatus, DStarVE, utilized to generate the capacitively coupled magnetized RF sheath is discussed. In addition the supporting non-spectroscopic diagnostics used to determine the DStraVE plasma parameters are formulated and presented. In Chapter 5, the characterization of the investigated DStarVE discharges and the systematic spectroscopic analysis of the time averaged line profiles are presented. The spectral analysis results in the time dependent electric field topology of the capacitively coupled magnetized RF sheath and is utilized to validate the diagnostic. In Chapter 6, the capacitively coupled magnetized RF sheath electric field topology and radiator distribution function associated with the investigated DStarVE discharges is presented. These parameters were determined by fitting the time averaged spectral line profile. In Chapter 7, the passive spectroscopic technique and corresponding results obtained through its validation utilizing the capacitively coupled magnetized RF sheath is summarized. The capability of the theoretical spectral line profile modeling is explored and the implementation of an active spectroscopic technique for measurement of the ICRF antenna near-field is discussed.

This chapter provides an introduction to the primary objective of the work conducted and presented in this dissertation. The approach taken to achieve the desired objective, through development and validation of a non-perturbative spectroscopic diagnostic, will be discussed. The chapter is structured as follows: Section 1.1 introduces the concept of ICRH in magnetically confined thermonuclear plasmas and the associated performance limiting factors. Section 1.2 introduces the spectroscopic technique and the atomic physics formulating the basis of the diagnostic. Section 1.3 introduces the experiment and methodology utilized to validate the spectroscopic diagnostic.

1.1 ICRH in Magnetically Confined Thermonuclear Plasma

In this section an overview of ICRH in magnetically confined thermonuclear plasma associated with the tokamak will be discussed. Comprehension of ICRH physics begins with a brief overview of the magnetically confined thermonuclear reactor. The tokamak geometry will be considered here.

The tokamak is a device in which a plasma is confined in the shape of a torus by a magnetic field and heated to thermonuclear conditions. For the plasma equilibrium to be stable the magnetic field must be helical. This is achieved by the superposition of poloidal and toroidal magnetic field, B_p and B_t respectively. To generate the poloidal magnetic field a plasma current I_p is driven utilizing both inductive and non-inductive methods. The toroidal magnetic field is generated by external coils placed symmetrically around the torus. Figure 1.1 gives a diagram of the confined plasma of a tokamak indicating the poloidal and toroidal directions. Figure 1.1 is taken from [3].

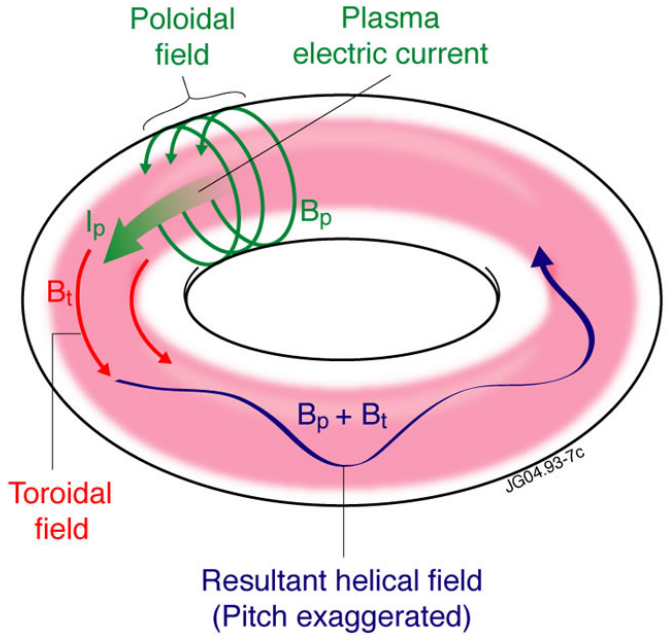

Figure 1.1: Confined plasma of a tokamak indicating the poloidal and toroidal directions.

In addition to confinement the plasma must be heated to thermonuclear conditions such that the cross section for fusion is favorable, 10 to 20 keV. This is achieved by various methods such as Ohmic heating, neutral-beam injection, and electromagnetic wave absorption [149]. In this dissertation the later will be considered in the form of ICRH. A major challenge facing magnetic confinement fusion and the success of ITER is the implementation of reliable plasma heating systems. ICRH systems are designed to couple energy into the core plasma ions through a resonant interaction with electromagnetic radiation in the RF range, 10 to 100 MHz for reactor-like plasma parameters [140, 149]. The RF electromagnetic radiation is launched from ICRF antennas which are properly shielded with a Faraday screen. Figure 1.2 gives an in-vessel view of the Alcator C-Mod ICRH system showing the current strap, Faraday screen, and antenna box. Figure 1.2 is derived from [2, 108].

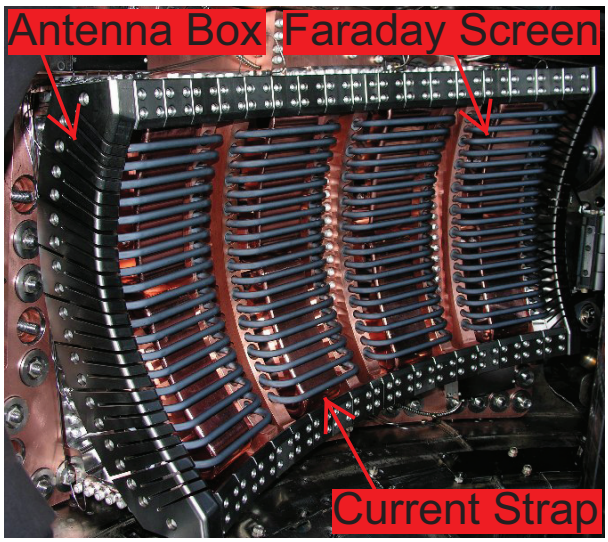

Figure 1.2: Alcator C-Mod ICRH system indicating the various plasma facing components.

The current strap is powered by an RF generator and thus radiates the electromagnetic wave. The Faraday screen is designed to eliminate electrostatic or capacitively coupling between the current strap and the plasma. The antenna box is designed to limit plasma from entering the region between the current strap and Faraday screen. The plasma facing material armoring the antenna box is in direct contact with the scrape off layer (SOL) plasma. Therefore the material must be able to withstand high a heat load and particle flux to prevent melting and erosion respectively. High-Z refractory metals such as molybdenum and tungsten are typically used because they have high melting temperatures and low physical sputtering yields. However, low-Z carbon based materials have been traditionally used to maintain a low Z effective in the core plasma.

ICRH is seen to be a key technique in which the required ion temperatures for favorable fusion

reactions can be reached. The ITER experiment [4] has been deemed by the international community to be the next step towards an economically viable power producing thermonuclear reactor. ITER utilizes a magnetic confinement technique, the tokamak, and will require 20 MW of ICRH power to achieve is scientific mission [1]. Therefore a detail understanding of the performance limiting factors and how to provide mitigation is crucial. Previous operation of ICRH systems at major installations around the world such as the National Spherical Torus Experiment (NSTX) [154], the Joint European Experiment (JET) [79], and Tore Supra [40] have shown that a universal and consistent performance limiting factor is the so called near-field associated with ICRF antenna. The near-field refers to the electric field in the vicinity of the ICRH system hardware facing the plasma. The interaction of the near-field with a material surface manifests as an RF sheath having an electric field that terminates directly on the Faraday screen and antenna box structures. When the RF sheath electric field has a direction parallel to the normal of the material surface a large heat and particle flux is driven, thus resulting in local power deposition in the SOL plasma and the interacting material surface. This has been shown to cause melting, sputtering, and arcing and severely limits the performance of the ICRH system [37, 53]. Figure 1.3 gives a cross section of a confined tokamak plasma indicating the magnetic surfaces and ICRF antenna location.

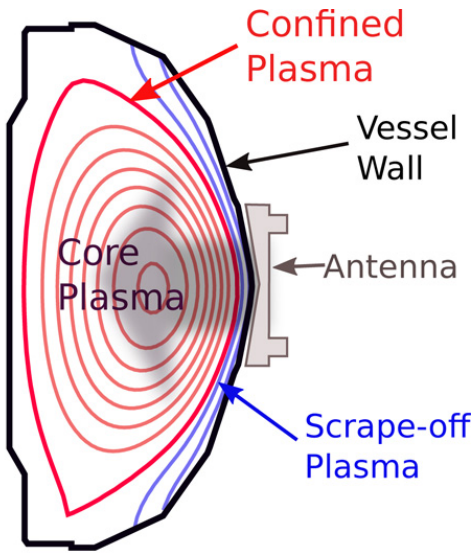

Figure 1.3: Cross section of confined tokamak plasma indicating magnetic surfaces and ICRF antenna location.

It is necessary that the ICRF antenna launch tens of megawatts of power across the SOL plasma into the core for reactor-like scenarios. Once the electromagnetic radiation is past the SOL the physics associated with the dissipation of the wave energy is fairly well understood [140, 40]. A simulation of

the ICRF wave propagating and absorbing in the core of an ITER plasma and is shown in Figure 1.4 [82]. The simulation was conducted with the state of the art AORSA globalwave solver [81, 80]. However, in the SOL coupling of wave energy into the near-field is not well understood. Therefore to continuously launch the required megawatts of power across the SOL, mitigation of the ICRF antenna near-field must be achieved and thus requires an understanding of the underlying physics. The diagnostic developed here will be capable, for the first time, of experimentally determining the needed data for our theoretical understanding of near-field physics.

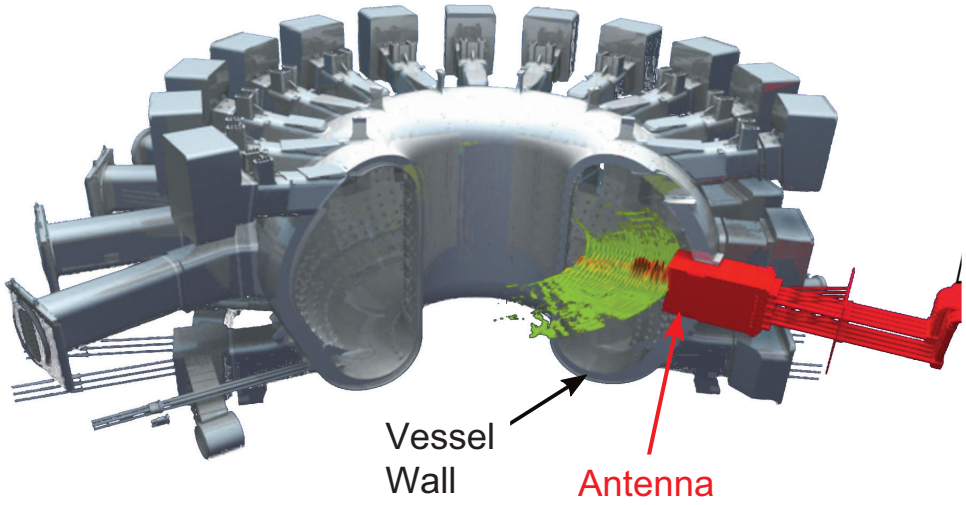

Figure 1.4: Visualization of 3D ICRF wave fields in the equatorial plane of ITER showing the vacuum vessel and ICRF antenna structures, taken from [82].

The physics associated with ICRF wave propagation, absorption, and mode conversion is quite complicated and is covered in detail elsewhere [140, 25, 58], a basic overview is provided here. ICRF antenna are capable of exciting both the fast and slow wave, where the nomenclature fast/slow references the behavior of the wave normal surface [140]. The antenna is ideally designed to launch only the fast wave. The slow wave is excited if the antenna's current strap is not aligned such that the wave electric field is perpendicular to the magnetic field. This misalignment induces an electric field in the parallel direction which excites the slow wave. In addition the fast wave can mode convert into the slow wave upon interaction with a material surface [104]. Chapter 2 will discuss the near field of ICRF antenna and the applicability of modeling using the capacitively coupled magnetized RF sheath.

1.2 Atomic Spectroscopy

To mitigate the parasitic effects of the ICRF antenna near-field the fundamental physics governing its behavior must be understood. To bridge the gap between the theoretical and actual performance of reactor-like ICRF antenna, experimental measurements of the near-field are desired. Due to the large energy flux in front of the antenna, local measurements with physical probes are not possible. Therefore this research is centered on the development of a non-perturbative diagnostic based on OES to locally measure the near-field. In this section, the atomic physics associated with this diagnostic is presented.

Optical measurement of electric field properties is based on quantifying the transition frequency of the photon emitted during de-excitation of an electron. The foundation of this diagnostic is the calculation of the theoretical spectral line profile. This requires a mathematical description of the electronic structure of the atom. In this dissertation the influence of arbitrary static magnetic and time periodic electric field vectors with be considered. To simplify the problem the magnetic field vector is defined to lie along the z-axis. Due to its static nature, the coordinate system can be rotated to achieve the definition and results in no loss of generality. The electric fields of interest, namely those of the capacitively coupled RF sheath and the near-field of ICRF antenna, are typically non-monochromatic [125, 95, 103]. Therefore the electric field vector is represented as a Fourier cosine series with N_H components. In this dissertation, the one and two-electron atom will be considered, however the wave functions of the two-electron atom are approximated as those of the one-electron atom. For the purposes considered here this is a good approximation and will discussed further in Section 3.3.

The calculation of the theoretical spectral line profile can be carried out in a three step process. ***First*** the solution to the appropriate Schrödinger equation is found. This results in a set of energies and wave functions associated with the perturbed quantum states of the atom. ***Second*** a new Schrödinger equation is formulated from the original by the addition of a connection operator. Utilizing the set of perturbed wave functions as the new basis the transition probabilities are calculated. ***Third*** the continuous theoretical spectral line profile is calculated from the energies and transition probabilities given the instrument and radiator distribution functions.

Due to the time periodic nature of the Schrödinger equation Floquet's theorem [18] is implemented and an eigenvalue/eigenvector problem is formulated. The eigenvalue and eigenvector pairs represent the energies and wave functions of the perturbed quantum states of the atom. For the electron in the upper level to decay to the lower level and emit a photon the atom must be perturbed electromagnetically. In this research spontaneous emission is the dominate de-excitation mechanism and therefore the electric dipole connection operator is utilized. The transition probabilities are calculated by solving a new Schrödinger equation given by the old with the addition of the connection operator. The solution is found by a expansion in the perturbed wave functions. The

discrete theoretical spectrum consists of a series of delta functions with an intensity given by the transition probability. The continuous theoretical spectrum is calculated by convolving the discrete spectrum with the instrument and radiator distribution functions.

To solve the Schrödinger equation a basis must be chosen to work within. A logical choice is the coupled basis due to the fact they are eigenfunctions of the unperturbed Hamiltonian. In choosing the coupled basis, the assumption is made that the L-S coupling scheme is appropriate, which is a good assumption for low Z atoms [76].

To extract the electric field from the measured spectral line profile a fit must be performed utilizing the theoretical calculations. The fitting algorithm implements a brute force method in which the entire space associated with the fit variables is discretized evenly within each dimension. The algorithm methodology is as follows: the χ associated with each point in the discretized space is calculated, the point in which the minima occurs is selected. The boundaries associated with the space are then reduced to those points adjacent to the selected point. The new space is then discretized and the χ at each point is calculated in which the minimum value is again taken. This process is iterated until the desired precision in the fit variables is achieved.

1.3 Diagnostic Implementation and Validation

The development of a diagnostic on a tokamak is highly undesirable due to the large operational costs and limited availability of run time. Therefore a small scale laboratory experiment was designed to serve as a test stand in which the edge environment of the tokamak could be simulated. In this section the OES technique and experimental apparatus, presented in detail in Chapters 3 and 4 respectively, are described.

The primary focus of implementing this diagnostic is to validate the atomic physics associated with the theoretical modeling of the spectral line profile and to demonstrate proof of principal on a simple 'bench top' experiment. Passive time averaged OES was selected for implementation because the experimental setup is simplistic and the equipment was available. The technique is passive in the sense that the observed emission arises from natural processes occurring within the plasma, namely collisional excitation and spontaneous decay [59]. The spectral resolution of passive techniques is low but is acceptable when considering the purpose of the work and the expected electric field intensities, 1 to 10 kV/cm. Successful implementation will intrinsically lead way into more elaborate active laser based techniques having superior spatial and spectral resolution [10, 16].

The spectral line profile is measured by observing the grating diffracted emission with a spectroscopic camera. As described in Section 3.5 the H_β $(n = 4 \rightarrow 2)$ transition of hydrogen and the $5^3D \rightarrow 2^3P$ transition of neutral helium were selected for study by optimizing the electric field sensitivity and emission intensity. Additionally the π and σ polarized components were measured independently. As discussed in Section 5.4 when both polarizations are fit together as an object the

accuracy of the extracted electric field parameters is increased.

The diagnostic was implemented to measure the electric field topology of the capacitively coupled magnetized RF sheath for two reasons. The first is due to the fact that the RF sheath has been well studied both experimentally and theoretically and second, upon interaction with a material surface the ICRF antenna near-field manifests as an RF sheath. The experimental apparatus was given the name DStarVE, an acronym standing for Dynamic Stark Verification Experiment. The basis of DStarVE consists of an electrode biased at 13.56 MHz immersed in a magnetized plasma generated by excitation of an electron cyclotron wave (ECW) at 2.45 GHz. Capacitively coupled plasma sources typically operate in low density regimes due to power going into electron and ion heating rather then ionization [97, 62, 110]. Thus to simulate the edge environment of the tokamak where the plasma density is on the order of 10^{18} m^{-3} [153, 93] an additional plasma source is necessary. To access this density regime an electron cyclotron resonance (ECR) based source is utilized. Typically the ordinary circular polarized wave is excited, which cannot propagate above the cutoff density, $n_c = 7.2 \cdot 10^{16}$ m^{-3} at 2.45 GHz. The whistler wave does not experience a cutoff and therefore is excited to achieve the desired density.

Two experimental configurations are investigated: electric and magnetic field vectors parallel and perpendicular. The study of these two field configurations is of particular importance. The parallel field configuration has been well studied both experimentally [17] and theoretically [95, 125, 103, 146] and thus will be the focus for diagnostic validation. The perpendicular field configuration is desired due to the fact that it is representative of that associated with the ICRF antenna near-field.

A total of 28 discharges, with varying experimental conditions, were investigate and characterized in terms of electrical parameters, plasma parameters, and RF sheath electric field. The electrical parameters were measured by use of the DC and I-V probes as described in Section 4.1. The plasma parameters were measured by the use of the capacitive and RF compensated Langmuir probes as described in Section 4.3. The RF sheath electric field was determined through a fit to time averaged π and σ spectral line profiles obtained by the spectroscopic system described in Section 4.2.

CHAPTER

2

THE CAPACITIVELY COUPLED MAGNETIZED RF SHEATH

In Chapter 1 the scope of this dissertation was outlined. The basic operation of ICRF antenna in the tokamak was introduced and the underlying problem of the near-field was addressed. Chapter 1 concluded that experimental measurements of the near-field are necessary for progressive of ICRH operations. The non-perturbative passive OES diagnostics which will be utilized for these measurements was outlined. An experiment was presented which will serve to validated the diagnostic by measurement of the capacitively coupled magnetized RF sheath electric field topology.

In this chapter the capacitively coupled magnetized RF sheath is introduced. The selection of the RF sheath for validation and implementation of the spectroscopic diagnostic and its relevance to the thermonuclear reactor is discussed. A simple analytical model of the RF sheath is presented which will be utilized to validate the experimental spectroscopic measurements. The chapter is structured as follows: Section 2.1 introduces the capacitively coupled magnetized RF sheath and provides a discussion on why it is of interest. Section 2.2 presents an analytical model of the capacitively coupled magnetized RF sheath in the parallel field configuration. Section 2.3 provides a discussion on the relevance of the RF sheath to ion cyclotron resonance heating.

The capacitively coupled magnetized RF sheath is studied having two experimental configurations: electric and magnetic field vectors parallel and perpendicular. The governing physics associated with the parallel field configuration is equivalent to the unmagnetized case and has been

well studied both experimentally [17, 43, 57] and theoretically [95, 125, 103, 146]. Due to the fact theoretical models of the electric field topology exist in this configuration the diagnostic can be validated. The perpendicular field configuration is of interest due to the fact that it is representative of that associated with the ICRF antenna near-field.

2.1 Introduction

In this section an introduction to the RF sheath will be given. To most easily comprehend RF sheath physics it is appropriate to begin with the static case, the direct current (DC) sheath. The DC sheath is intrinsically generated by a plasma due to its interaction with a material surface and is referred to as a thermal sheath if the material surface is unbiased. In most plasmas the mobility of the charged species is vastly different. In this dissertation we will consider the electropositive plasma in which the ionic species are positive and have mobilities two to three orders of magnitude lower then the electrons. The difference in mobility is driven by two factors: mass and thermal velocity of the species. Compared to the electron the ionic species is more massive by at least three orders of magnitude and therefore experiences a higher impedance to motion by its inertia. Additionally, the ionic species typically has a temperature two orders of magnitude lower the that of the electrons. The mass and energetics of these species leads to large differences in the thermal velocity which can be correlated to the mobility. The thermal sheath is therefore established to retard or confine the more mobile species, the electrons.

Considering the case where the electron mobility is dominate, a potential is established in the plasma on the order of a few kT_e to confine the electrons and is refereed to as the plasma potential ϕ_p. In the bulk of the plasma quasi-neutrality, $n_e \approx n_i$, must be maintained due to the inability of the charged species to sustain charge separation. Therefore the plasma potential is dropped in the thermal sheath over a few Debye lengths λ_D, the characteristic scale length in which charge is shielded. The resulting electric field has an intensity on the order of kT_e/λ_D and points toward the material surface. A basic diagram of a thermal sheath generated from the interface of a plasma with a grounded material surface is given in Figure 2.1. There are two distinct regions in a thermal sheath: the presheath and sheath. The presheath is a nearly quasi-neutral region defined by a weak electric field directed towards the sheath. In the presheath the ions are accelerated to the Bohm velocity

$$u_b = \left[\frac{kT_e}{m_i}\right]^{1/2}, \tag{2.1}$$

which is required to maintain conservation of flux in the sheath and is known as the Bohm criterion [98]. However, self consistent kinetic descriptions of the presheath indicate that this criterion is over simplified [12]. Once the Bohm velocity is reached, substantial charge separation occurs and the division between the presheath and sheath is defined. The presheath can extend 100's of Debye

lengths. The sheath is a region of positive charge density, $n_i \gg n_e$, and provides the majority of the electric field required to retard the electrons. The presheath is a fundamental component to all sheaths but is neglected here because the corresponding electric field is weak and is not measurable with passive OES. The presheath will only be considered in the fact that it decreases the plasma density at the presheath/sheath interface when compared with the bulk plasma. The density at the presheath/sheath interface can be estimated for a collisionless plasma as

$$n_s = n_b e^{-\frac{e\phi_p}{kT_e}} \tag{2.2}$$

from the Boltzmann relation.

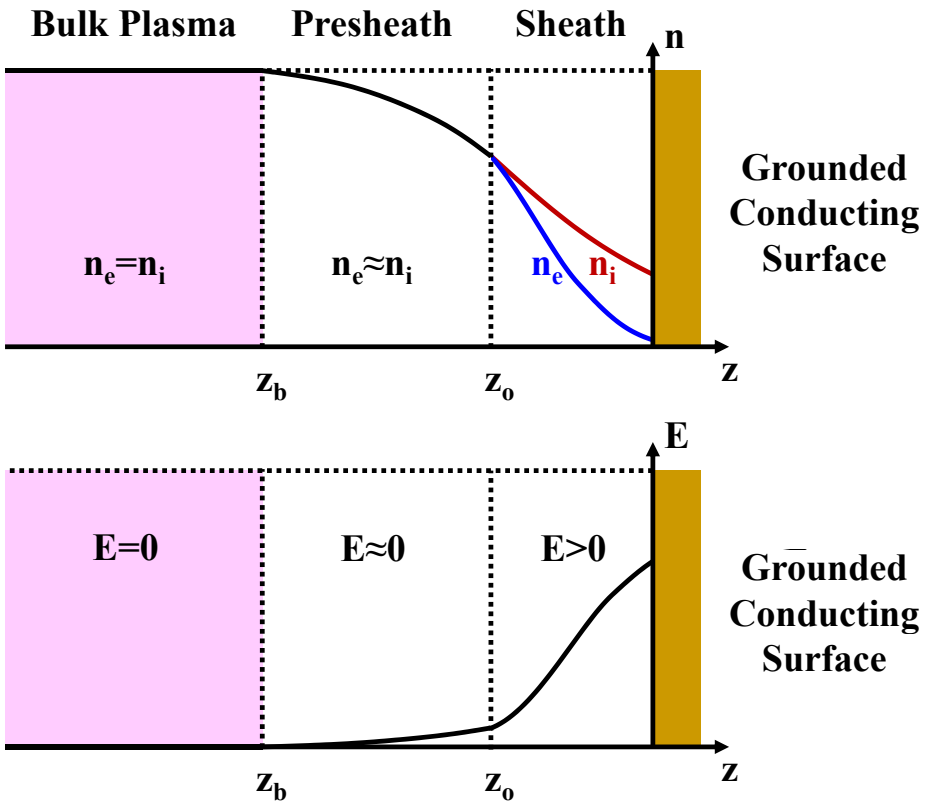

Figure 2.1: Thermal sheath generated at the interface with a grounded surface.

Biasing the surface at low voltages, <100 V, below the plasma potential leads to an extension of the scale length of the sheath. In this case there is essentially no alteration of the fundamental physics because power absorption in the sheath is negligible. However biasing beyond this range can lead to significant alterations due to power absorption and secondary electron production. This

results in similar sheath characteristics to that associated with the DC discharge [98].

The RF sheath is generated by biasing the material surface, the electrode, with a potential whose magnitude varies periodically. In this dissertation only sinusoidal potentials in the RF range of frequencies will be considered. In the 10's of MHz range and below both the electrons and ions can respond to the RF sheath electric field. However the ions response is more limited due to its inertia. The RF sheath can be generated by either electromagnetic or electrostatic coupling to the electrode. Electromagnetic coupling is inductive and results in an electric field having a direction perpendicular to the normal of the electrode surface. In this scenario the RF sheath can operate in a regime that is nearly detached from the electrode surface. This is because the corresponding electric field drives particle motion perpendicular to the normal of electrode surface resulting in minimal power deposition at the electrode surface. For this reason the electromagnetic RF sheath is the desired mechanism in which power is coupled into the bulk plasma and its existence on ICRF antenna plasma facing surfaces is not a significant concern.

Electrostatic coupling is capacitive and therefore results in a sheath electric field having a direction parallel to the normal of the electrode surface. The electrostatic RF sheath resembles a capacitor in the sense that a large fraction of power is transmitted through a displacement current. Therefore this type of RF sheath is referred to as being capacitively coupled and will be the focus in this dissertation. The direction of the RF sheath electric field vector is such that the coupled material surface experiences a substantially increased heat and particle flux. These parasitic effects can severely restrict operational limits as will be discussed in Section 2.2. Thus the capacitively coupled RF sheath is not desired on the ICRF antenna plasma facing surface.

Most RF discharges are asymmetric in the sense that more electrode surface area is grounded then powered. Additionally, the power delivery system is typically capacitively coupled to the electrode. In this situation conservation of current is maintained by the natural development of a negative DC bias voltage on the powered electrode. For the extreme asymmetric discharge the DC bias voltage is approximately equivalent to the magnitude of the applied RF voltage. This is the case of the experiment presented in Chapter 4. A typical voltage waveform for a largely asymmetric discharge over one RF period is given by Figure 2.2. Additionally, the corresponding width of the RF sheath z_o as a function of phase is presented. The voltage waveform at the RF electrode is such that the electric field in the sheath is essentially always directed towards the wall. As was found for the thermal sheath this is established to retain the more mobile electrons. The unipolar RF sheath electric field continuously accelerates the ions towards the electrode surface. Therefore because the RF sheath electric field is time dependent the ion and electron density is as well.

Figure 2.3 presents the RF sheath associated with three points in the phase: t_1, t_2, and t_3 of the RF voltage waveform given by Figure 2.2. At the first point in phase t_1 the applied RF voltage at the electrode is zero. The RF sheath at this instance has a minimum in its width z_o and is approximated as a thermal sheath. As the voltage is increased on the electrode surface the RF sheath expands. At

the phase associated with t_3 the sheath has reached its maximum width. During this first half of the waveform $t_1 \leq t \leq t_3$ the RF sheath is in an expansion phase. Consequently an electron beam is directed towards the bulk plasma due to electrons reflecting in the strong potential of the RF sheath. This is easily realized by the fact that $e|V_{RF}|$ quickly increases well beyond kT_e by orders of magnitude. The energetic gain acquired is referred to as collisionless heating [97]. Through kinetic simulations it was found that the beam-like formation of electrons causes intense ionization [146].

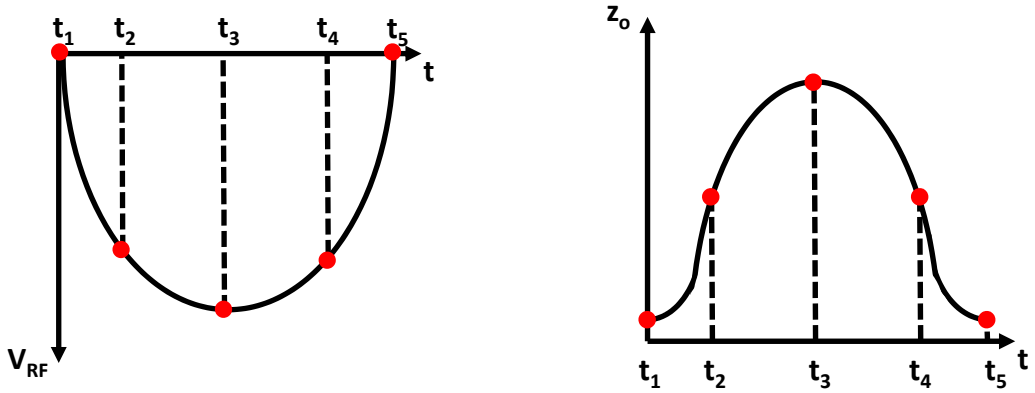

Figure 2.2: (a) Voltage waveform at RF biased electrode for asymmetric discharge and (b) corresponding width of the RF sheath z_o as a function of phase.

During the second half of the waveform $t_3 \leq t \leq t_5$ the RF sheath is contracting and the electrons experience a cooling effect because of similar interactions as those described above. Both the heating and cooling effects experienced by the electrons during an RF waveform are due to the exponentially decaying density in the RF sheath. The electron energy distribution function in the sheath is non-Maxwellian due to the electron interaction with the moving sheath boundary [155]. Although the electron density decays exponentially once past the sheath boundary z_o its time dependent nature of the ensures optical emission in the entire sheath region. Typically intense emission is seen during the expansion phase due to electron heating and can be highly time dependent depending on the electronic transition [63].

In the tokamak a substantial magnetic field is always present to provide confinement of the plasma. The RF sheath can be significantly altered depending on the magnetic field orientation with respect to the electric field of the RF sheath. In this dissertation two magnetic field configurations will be considered. The first is magnetic and electric field parallel and the second is magnetic and electric field perpendicular. In the first case the magnetic field does not alter the RF sheath electric field. This is due to the fact that the electric field accelerates the particles parallel to the magnetic

field, $\bar{E} \times \bar{B} = 0$. The particles only orbit the magnetic field based on their velocity distribution function perpendicular to the magnetic field. The RF sheath in the parallel field configuration has been well studied experimentally [17, 43, 100, 57] and theoretically [95, 124, 125, 65].

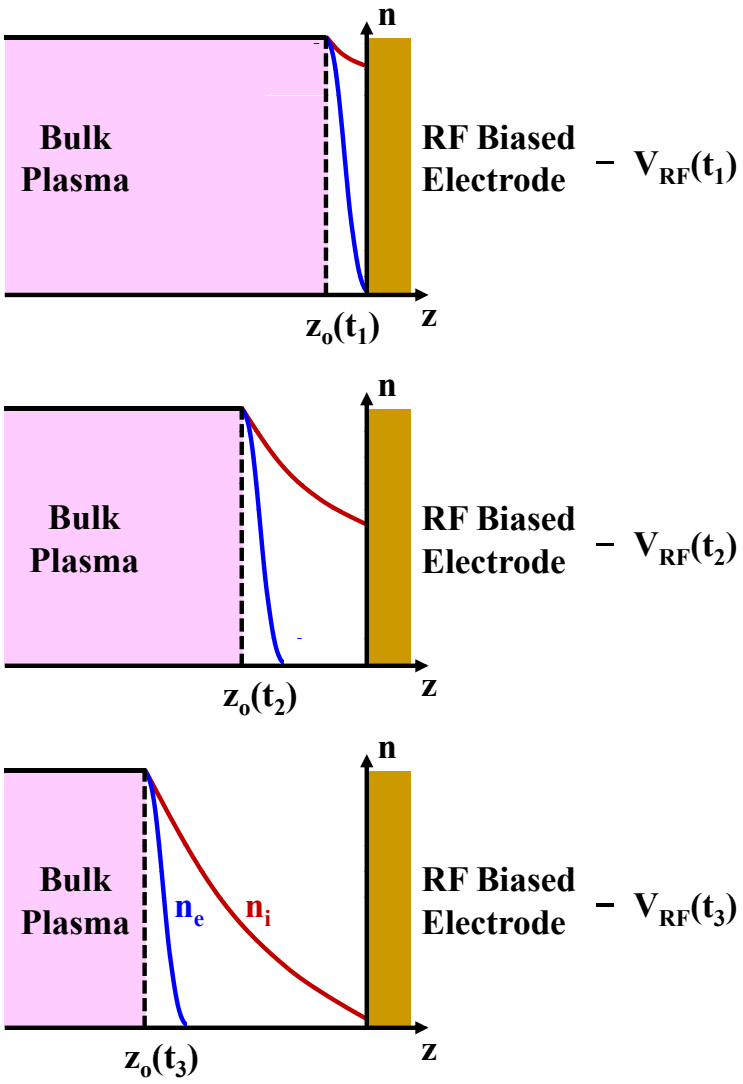

Figure 2.3: RF sheath corresponding to the points in phase t_1, t_2, and t_3 of the RF voltage waveform given by Figure 2.2a.

In the perpendicular field configuration the particles experience the full $\bar{E} \times \bar{B}$ force, resulting in a significantly altered RF sheath [32, 123, 15]. The ion dynamics play a much more essential role then in the parallel field configuration because the electron mobility is substantially decreased by the magnetic field. In this configuration the sheath width is dominated by the Larmor radius of the

ions [32, 31, 138]. Additionally it was found that the electron density decreases more rapidly moving towards the bulk plasma [137]. This is due to the fact the Larmor radius of the electrons is much smaller then the sheath width and thus acts to restrict their motion. The thermal sheath width has been shown to increase as a function of magnetic field strength [9]. However, the behavior for an RF sheath is uncertain but expected to depend on the magnetic field intensity.

2.2 ICRF Antenna Near-Field

In this section the interaction of the ICRF antenna near-field with a material surface and its relevance to the capacitively coupled magnetized RF sheath is discussed. The ICRF antenna near-field is generated by circulating RF currents on the Faraday screen/antenna box and excitation of the slow wave. Circulating RF currents on the Faraday screen/antenna box capacitively couple to the SOL plasma in a manner resembling that associated with the capacitively coupled discharge [33]. This resulting in similar RF sheath characteristics. The interaction of the slow wave with a material surface also leads to capacitive coupling and the formation of an RF sheath. However, the sheath characteristics are expected to be somewhat altered due to the wave nature of the interaction. A contour plot of the simulated electric field (kV/cm) at the Faraday screen of a typical two current strap ICRF antenna is given in Figure 2.4 [36]. The magnitude and direction of the circulating RF currents on the Faraday screen/antenna box are indicated by the size and direction, respectively, of the arrows.

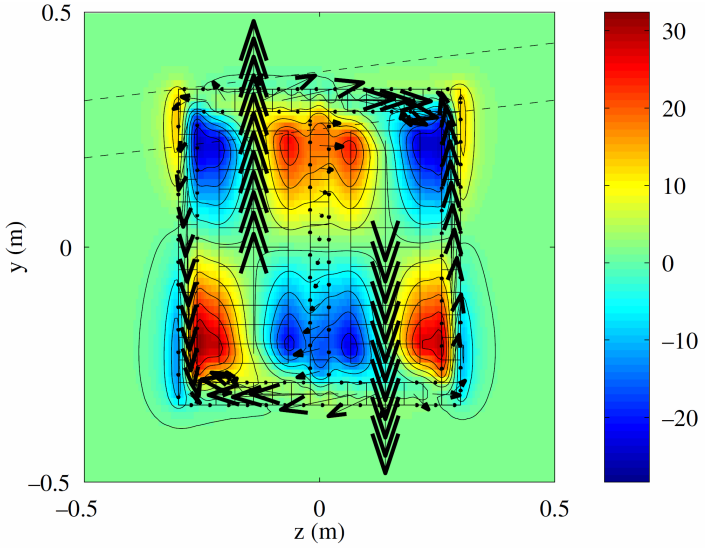

Figure 2.4: Simulated electric field (kV/cm) at the Faraday screen of a typical two current strap ICRF antenna [36]. The circulating RF currents on the Faraday screen/antenna box are indicated by the arrows.

The ICRF antenna can launch two types of waves: the so called fast and slow wave. The fast wave is the desired mode for power coupling. The slow wave is excited by either mode conversion or misalignment of the antenna geometry with the magnetic field. The fast wave is used to heat the core plasma ions and has an electric field perpendicular to the static magnetic field. However, upon interaction with a material surface mode conversion can take place [104, 48, 47]. In the misalignment case an electric field is induced in the parallel direction which excites the slow wave. The slow wave can only propagate in the low density region of the plasma, below the density associated with the lower hybrid resonance n_{LH}. Above this density the slow wave is strongly evanescent. Additionally, below the cut-off density given by $\omega_{pe} = \omega$ the slow wave becomes evanescent. Therefore the slow wave can only propagate in the following density regime

$$n_{pe} < n_e < n_{LH} \, . \tag{2.3}$$

The slow wave propagates in the form of resonance cones [105] until a material surface is reached. At which point the parallel electric field drives an RF sheath at the material surface. This interaction is modeled as having a static DC potential proportional to the parallel electric field and the sheath thickness estimated by the Child-Langmuir Law [106, 105, 89]. These models do not include the time dependent properties of the RF sheath and therefore neglect an important part of the physics governing the interaction. Other models have been developed to calculate and predict the near-field sheath [50, 49, 51, 56, 36] but do not capture the RF sheath physics fully.

Due to the large energy flux radiated by the ICRF antenna measurement of the near-field cannot be conducted locally by physical probes. However, non-local measurements of the plasma potential can be made and correlated to the near-field. The correlation is valid if the magnetic field connects the measurement point to the ICRF antenna near field. Many experiments have been conducted on Alcator C-Mod that show an increased plasma potential of >100 V on magnetic field lines connected to the ICRF antenna. This was found to be a factor of ten greater than ohomically heated discharges [108]. Additionally, many other experiments have shown that an increased plasma potential is measured when the ICRH operates and SOL plasma alteration [27, 109, 38]. An increased plasma potential has been shown to lead to enhanced impurity production [157, 99, 83]. In Tore Supra hot spots have been observed on the ICRF antenna which are attributed to the RF sheath and can lead to limited operation [35, 53]. In JET magnetic connection of the ICRF antenna to the LH system has shown to negatively impact current drive [87]. Simulations have shown that these parasitic effects of the near-field will led to a parallel heat flux of approximately 16 MW/m^2 for the ITER ICRF antenna at full power, an unacceptably high value [39].

2.3 Analytical Modeling

Analytic models that are available to calculated the electric properties associated with the RF sheath in the parallel field configuration include: the Lieberman model [98, 95], the Metze, Ernie, and Oskam (denoted MEO) model [96], and the Riley model [125]. The Lieberman model was developed in the limit that the ions were completely inertial, that is they only respond to time averaged electric field. The MEO model takes the opposite limit of Lieberman's model and assumes the ions are inertialess and thus respond instantaneously to the electric field. The Riley model was developed to provide a bridge between these extreme limits. The Riley model assumes that the ions respond to a dampened electric field and is considered a generalization of the MEO model. The Riley model will be presented here because the inertial response of the ions is expected to be an important factor in the sheath dynamics.

In this derivation the plasma is considered to be one-dimensional with time independent bulk plasma quantities. The electrons are taken to be in a Boltzmann distribution and respond instantaneously to the electric field. The ions are assumed to be cold and respond instantaneously to a damped potential. The electric field $E(z,t)$ is determined from the negative gradient in the potential $V(z,t)$ as given by

$$E(z,t) = -\frac{\partial}{\partial z} V(z,t)\,. \tag{2.4}$$

The electric field is defined by the differential form of Gauss's law

$$\frac{\partial}{\partial z} E(z,t) = \frac{e}{\epsilon_o}\left[n_i(z,t) - n_e(z,t)\right]\,, \tag{2.5}$$

where $n_i(z,t)$ and $n_e(z,t)$ represent the ion and electron density in the sheath. The Boltzmann distribution of electrons at a temperature of kT_e is given by

$$n_e(z,t) = n_e(z_o) e^{\frac{e}{kT_e}(V(z,t) - V(z_o))}\,, \tag{2.6}$$

where $n_e(z_o)$ is the time independent electron density at the boundary of the bulk plasma and the sheath. The quantity z_o is the spatial location at which this boundary occurs. All parameters are time independent at z_o and therefore the variable t is suppressed. The ions are assumed to respond to a dampened potential $\tilde{V}(z,t)$ defined by

$$\frac{\partial}{\partial t} \tilde{V}(z,t) = \frac{V(z,t) - \tilde{V}(z,t)}{\tau_R}\,. \tag{2.7}$$

The dampened potential is a relaxed form of the actual and is controlled by the time constant

τ_R. An estimate of τ_R can be obtained by calculating the approximate time the ion requires to transverse the RF sheath [125]. In this research τ_R is set to a fit parameter when the comparison to the experimental data is made. The solution to Eq. 2.7 is found through integration and is given by

$$\tilde{V}(z,t) = \tilde{V}(z,0)e^{-\frac{t}{\tau_R}} + \frac{1}{\tau_R}e^{-\frac{t}{\tau_R}}\int_0^t V(z,t')e^{\frac{t'}{\tau_R}}\,dt'\,. \tag{2.8}$$

The solution to the dampened potential requires an initial condition and thus must be solved iteratively. For the first iteration the initial condition $\tilde{V}(z,0)$ is set to zero, for successive iterations $\tilde{V}(z,0) = \tilde{V}(z,\tau)$ is utilized because the waveform is periodic with a period τ. The ion density is determined from the conservation of flux

$$n_i(z,t)u_i(z,t) = n_i(z_o)u_i(z_o) \tag{2.9}$$

and energy

$$\frac{1}{2}M_i u_i^2(z,t) + e\,\tilde{V}(z,t) = \frac{1}{2}m_i u_i^2(z_o) + e\,\tilde{V}(z_o)\,, \tag{2.10}$$

where m_i and u_i are the mass and velocity of the ion respectively. The potential at the interface of the bulk plasma and the sheath is assumed to have a small time dependent component and is neglected, therefore the damped potential is also time independent at z_o. The unknown parameters of equations Eq. 2.9 and Eq. 2.10 are $n_i(z,t)$ and $u_i(z,t)$, therefore they can be solved simultaneously to yield an expression for $n_i(z,t)$

$$n_i(z,t) = n_i(z_o)\left[1 - \frac{2e}{M\,k\,T_e}\left(\tilde{V}(z,t) - \tilde{V}(z_o,t)\right)\right]^{-1/2}, \tag{2.11}$$

$$M = \frac{u_i(z_o)}{u_b}\,.$$

Where M is the Mach number and u_b is the Bohm velocity. The electron and ion density given by Eq. 2.6 and Eq. 2.11 are substituted into Eq. 2.5 to yield

$$\frac{\partial}{\partial z}E(z,t) = \frac{e\,n_e(z_o)}{\epsilon_o}\left[\left[1 - \frac{2e}{M^2 k\,T_e}\left(\tilde{V}(z,t) - \tilde{V}(z_o)\right)\right]^{-1/2} - e^{\frac{e}{kT_e}(V(z,t)-V(z_o))}\right]. \tag{2.12}$$

Eq. 2.4, Eq. 2.8, and Eq. 2.12 form a set of coupled partial differential equations to be solved for the sheath potential $V(z,t)$, damped sheath potential $\tilde{V}(z,t)$, and sheath electric field $E(z,t)$. In order to solve this system of equations the assumption is made that both $V(z,t)$ and $\tilde{V}(x,t)$ can be separated in space and time. Utilizing this assumption the spatial dependence of these variables is equivalent given the functional form of $\tilde{V}(z,t)$ expressed in Eq. 2.8. Thus the following can be

written

$$\tilde{V}(z,t) = R(t)V(z,t)\,, \tag{2.13}$$

$$R(t) = \frac{\tilde{V}(0,t)}{V(0,t)}\,.$$

The potential at the RF electrode $V(0,t)$ is a boundary condition and is measured experimentally thus $\tilde{V}(0,t)$ is known, as well as $R(t)$. Substituting Eq. 2.13 into Eq. 2.12 yields

$$\frac{\partial}{\partial z}E(z,t) = \frac{e\,n_e(z_o)}{\epsilon_o}\left[\left[1-\frac{2e}{M^2 k T_e}\left[R(t)V(z,t)-\tilde{V}(z_o)\right]\right]^{-1/2} - e^{\frac{e}{kT_e}[V(z,t)-V(z_o)]}\right]. \tag{2.14}$$

Eq. 2.4 and Eq. 2.14 form a set of coupled partial differential equations to be solved for the sheath potential and electric field $V(z,t)$ and $E(z,t)$ respectively. To solve this set the boundary condition $E(0,t)$ must be calculated. This is done by integrating Eq. 2.14 from $z = z_o$ to $z = 0$

$$E(0,t) = \left[E(z_o)^2 + \frac{n_e(z_o)kT_e}{\epsilon_o}\left[\frac{M^2}{R(t)}\left[\left[1-\frac{2e}{M^2 k T_e}\left[R(t)V(0,t)-\tilde{V}(z_o)\right]\right]^{-1/2} - 1\right] + e^{\frac{e}{kT_e}[V(0,t)-V(z_o)]} - 1\right]\right]^{1/2}. \tag{2.15}$$

The electric field at the interface of the bulk plasma and sheath $E(z_0,t)$ is assumed to be negligible and is thus set to zero. Given the nonzero boundary conditions $E(0,t)$, $V(0,t)$, and $V(z_o)$ Eq. 2.4 and Eq. 2.14 are solved for the spatial and temporally dependent sheath potential and electric field $V(z,t)$ and $E(z,t)$ respectively.

The effect of the ion dynamics in this model can be determined through the dampening time constant τ_R. The simulation results for two cases will be presented: $\tau_R \ll \tau$ and $\tau_R \gg \tau$, where τ is the period of the voltage waveform of the electrode. The first case simulates ions that respond instantaneously to the electric field. The second case simulates ions that only respond to the time average of the electric field. At the bulk plasma and sheath interface the electron density was taken as $n_e(z_o) = 10^{17}$ m^{-3} with an temperature of $kT_e = 4$ eV. The voltage at this interface was taken as $V(z_o) = 20$ V and has a negligible impact on the solution. The voltage waveform applied to the electrode $V(0,t)$ is sinusodial with a DC component and is given by Figure 2.5. The frequency of the voltage waveform was taken to be 13.56 MHz giving a period of $\tau = 73.7$ ns. The simulated electric field topology and dynamic for $\tau_R = 4$ and 300 ns is given in Figure 2.6a and Figure 2.6b respectively.

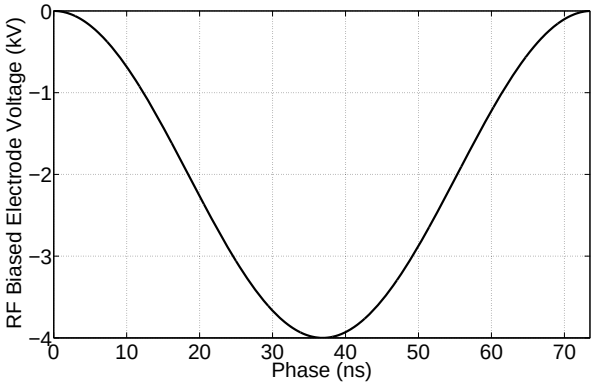

Figure 2.5: Voltage waveform at the electrode used for the RF sheath simulations.

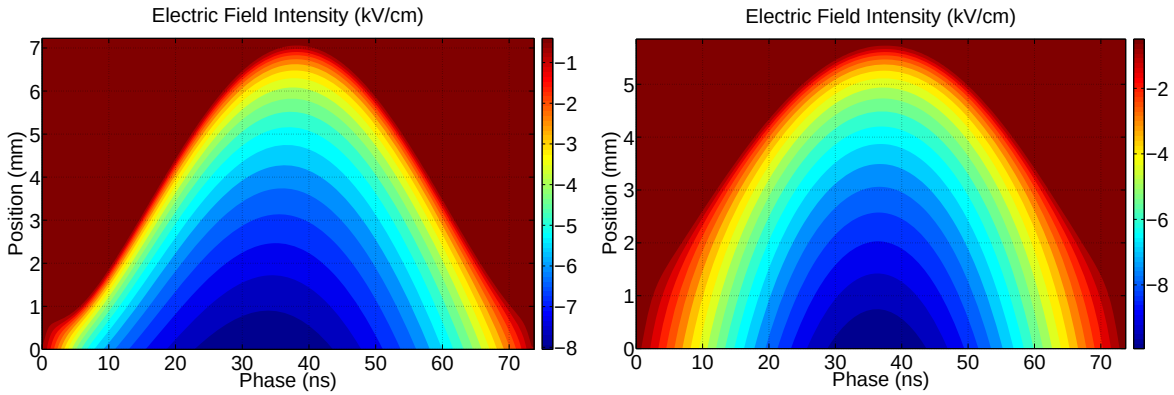

(a) (b)

Figure 2.6: RF sheath electric field as a function of phase and space for (a) $\tau_R = 4$ ns and (a) $\tau_R = 300$ ns.

A comparison of Figure 2.6a with Figure 2.6b shows that the most significant effect of the ion dynamics is to extend the sheath and consequently reduce the electric field magnitude. It was found that the RF sheath was extended over 1 mm by completely removing the inertia of the ions such that they would respond instantaneously to the electric field. Due to the fact the voltage waveform applied to the electrode is equivalent for both cases, the extension of the RF sheath leads to an decrease in the electric field intensity. To quantify the temporal and spatial response of the electric field a fit was performed to the simulated data utilizing a Fourier expansion given by

$$E(z,t) = E_0(z) + \sum_{n=1}^{N_H} E_n(z) cos(n\omega t + \theta_n)\,. \tag{2.16}$$

For reasons discussed in Section 5.4 the electric field is constrained to have only negative values. To

achieve this the waveform is clamped at zero (see Figure 3.25).

Figure 2.7 and Figure 2.8 provide the fit associated with a Fourier expansion having only one harmonic, $N_H = 1$, for the electric field presented in Figure 2.6a and Figure 2.6b respectively. A Fourier expansion having only one harmonic was consider to determine how non-sinusodial the electric field waveform is as a function of space. It was found that for the non-inertial case the waveform did not fit well close to the electrode. However, for the completely inertial case the waveform fit well within the entire sheath. This difference leads to the conclusion that ion motion in the sheath leads to harmonic generation in the electric field waveform.

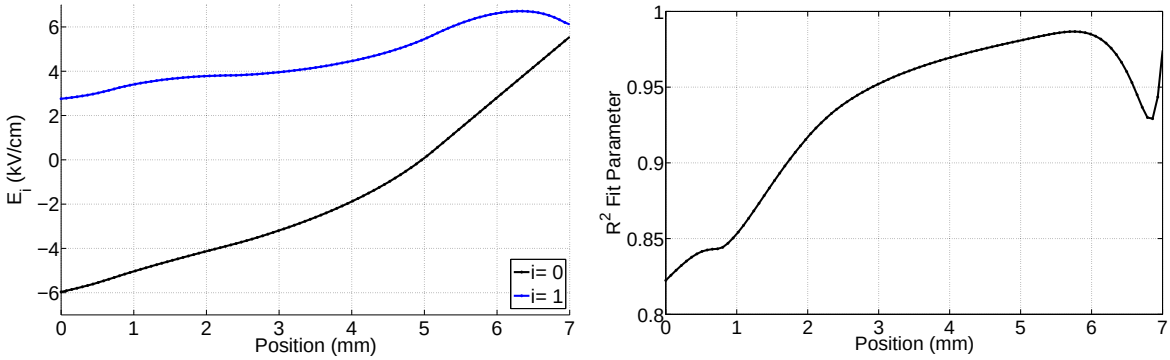

(a) (b)

Figure 2.7: (a) Electric field parameters and associated (b) R^2 fitting parameter as a function of space for $\tau_R = 4$ ns.

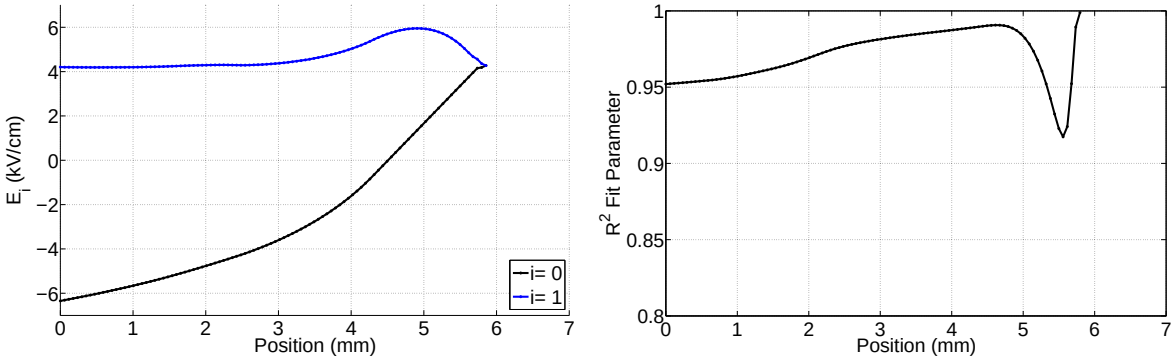

(a) (b)

Figure 2.8: (a) Electric field parameters and associated (b) R^2 fitting parameter as a function of space for $\tau_R = 300$ ns.

Figure 2.8a and Figure 2.8b provide the fit associated with a Fourier expansion having three harmonics, $N_H = 3$, for the electric field presented in Figure 2.6a and Figure 2.6b respectively.

A harmonic spectrum with four components, including the DC component, was found to very accurately represent both cases. It was found that for the both cases the DC component of the fitted electric field spectrum is relatively robust regardless of the fidelity of the fit, however the same was not found for the fundamental. In conclusion the major difference in the temporal behavior is the non-sinusodial behavior introduced by the ion dynamics.

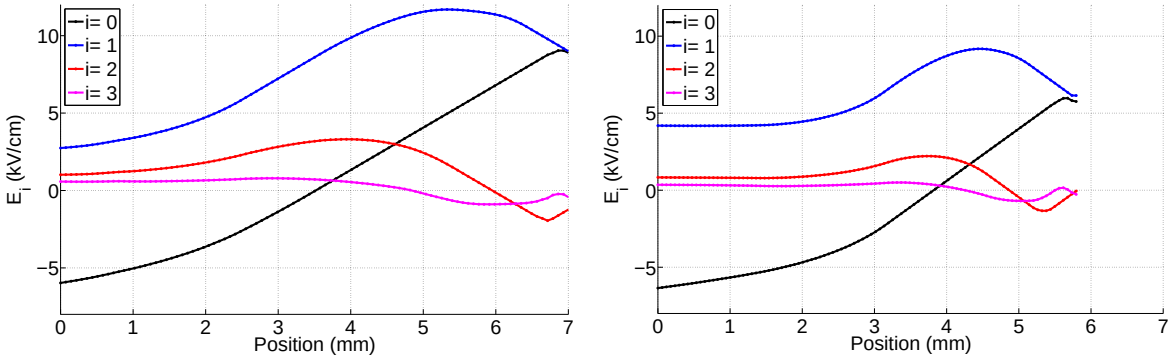

Figure 2.9: Electric field parameters for (a) $\tau_R = 4$ ns and (b) $\tau_R = 300$ ns as a function of space.

CHAPTER

3

PASSIVE OPTICAL EMISSION SPECTROSCOPY

In Chapter 2 it was determined that the capacitively coupled magnetized RF sheath was the most appropriate candidate to validate the passive OES diagnostic. Chapter 2 provides an introduced and a basic description of the associated RF sheath physics. In addition, the relevance of the RF sheath to the near-field of ICRF antenna was discussed. The chapter was concluded with a simple analytical model of the capacitively coupled RF sheath.

In this chapter the spectroscopic technique and the associated atomic physics constituting the theoretical framework of the diagnostic are formulated and developed. The chapter is structured as follows: Section 3.1 introduces the effect of the electric field on the quantum states of a one-electron atom and provides a discussion on the previously conducted work. Section 3.2 presents and discusses the available passive Optical Emission Spectroscopy (OES) techniques. Section 3.3 presents the atomic physics associated with the calculation of the theoretical spectral line profile. Section 3.4 presents the methodology and algorithm implemented to fit the experimental spectral line profile. Section 3.5 provides a discussion on the selection of the hydrogen and helium electronic transitions utilized for the validation of the diagnostic.

Passive OES is defined as the study of radiated energy naturally omitted from matter. Specifically for this dissertation, the radiation intensity as a function of wavelength for select electronic transitions. This is referred to as the spectral line profile. The OES technique utilized in this research

is based on measuring the spectral line profile by observing the grating diffracted emission with a spectroscopic camera.

The technique is passive in the sense that the observed emission arises from natural processes occurring within the plasma, namely collisional excitation and spontaneous decay [59]. Due to reasons that will be described in Section 3.5 the H_β $(n = 4 \rightarrow 2)$ transition of hydrogen and the $5^3D \rightarrow 2^3P$ transition of neutral helium were selected for the development of the diagnostic.

The shape of the spectral line profile contains information regarding the local environment in which the radiating atom is present such as the electric and magnetic field vectors and the plasma kinetics [67, 59]. The purpose of the research described in this dissertation is to develop and present a diagnostic in which a time periodic electric field vector can be determined from an analysis of the shape of the spectral line profile. The primary focus in developing the diagnostic is to validate the atomic physics associated with the theoretical modeling of the spectral line profile and to demonstrate proof of principal on a simple 'bench top' experiment. Therefore, the atomic physics and fitting software were developed such that extension beyond the selected electronic transitions and the implementation of high resolution techniques would be natural.

Passive OES was selected for the development because of the relatively inexpensive equipment cost and simplistic experimental set-up. The spectral resolution of passive OES techniques is low but is acceptable when considering the purpose of the work and the expected electric field intensities, 1 to 10 kV/cm, reinforcing its attractiveness for atomic physics validation and proof of principal demonstration. Successful implementation will intrinsically lead way into more elaborate active laser based techniques having superior spatial and spectral resolution [10, 16].

3.1 Introduction

Optical measurement of electric field properties is based on quantifying the transition frequency of the photon emitted during de-excitation of an electron. In this section the effect of the electric field on the one-electron atom with degenerate magnetic substates is introduced. The simplified electronic structure enables analytic calculation of the spectra allowing concepts to be conveyed easily. The phenomena behind the diagnostic is the dynamic Stark effect and describes the perturbation of electronic structure of the atom due to a time dependent electric field. To convey underlying concepts a detailed analytical treatment is provided in this section.

The effect of a static electric field on the one electron atom was first measured experimentally by Stark [139]. In this work the shift in the transition frequency was found to be orders of magnitude greater than that predicted. Theoretical advancements in the treatment were initially made using the Bohr-Sommerfeld theory [54]. Later, following the development of the mathematical basis of modern quantum mechanics, [132] the Schrödinger equation was implemented by Epstein [55] and Pauli [114] yielding excellent agreement with the experimental observations. The Stark effect has

since been well studied theoretically and experimentally. A summary of this work is presented in a monograph by Ryde [128].

The Schrödinger equation of the one electron atom with degenerate magnetic substates in the presence of a static electric field with intensity E_{DC} along the z-axis is given by

$$i\hbar\frac{\partial\Phi}{\partial t} = H^o\Phi + e\,z\,E_{DC}\Phi\,. \tag{3.1}$$

Where Φ is the wave function and H^o is the unperturbed Hamiltonian. Ignoring the electron spin, relativity, and quantum electrodynamics, H^o is given by

$$H^o = -\frac{\hbar^2}{2m_e}\nabla^2 - \frac{e^2}{4\pi\epsilon}\frac{1}{r}\,.$$

Epstein showed that a solution to Eq. 3.1 could be found with first order perturbation theory in the parabolic basis $|n\,n_1\,n_2\,m>$. Utilizing the electric dipole connection operator $\bar{\epsilon}\cdot\bar{r}$ and the solution to Eq. 3.1 the first order correct spontaneous emission spectrum can be determined and is given by

$$I_{nn^*}(\tilde{\omega}) = \sum_{n_1 n_2}\sum_{n_1^* n_2^*} I^{n\,n_1\,n_2}_{n^*\,n_1^*\,n_2^*}\,\delta(\omega_{nn^*} + \alpha_{DC}X - \tilde{\omega})\,, \tag{3.2}$$

$$I^{n\,n_1\,n_2}_{n^*\,n_1^*\,n_2^*} = <\phi_{n\,n_1\,n_2\,m}|\bar{\epsilon}\cdot\bar{r}|\phi_{n^*\,n_1^*\,n_2^*\,m^*}>^2$$

$$m = n - n_1 - n_2 - 1$$

$$\alpha_{DC} = \frac{6\pi\epsilon_o\hbar E_{DC}}{Z\,e\,m_e}$$

$$X = n(n_1 - n_2) - n^*(n_1^* - n_2^*)\,.$$

Where ϵ is the polarization vector of the emitted photon and ω_{nn^*} is the angular frequency of the unperturbed $n^* \rightarrow n$. Specifically, the quantity I_{nn^*} is the discrete spectral line profile associated with the $n^* \rightarrow n$ transitions. The transition intensity is given by $I^{n\,n_1\,n_2}_{n^*\,n_1^*\,n_2^*}$ and is a function of the quantum numbers of both the upper and lower levels. Ryde has calculated and presented tabulated values of the $I^{n\,n_1\,n_2}_{n^*\,n_1^*\,n_2^*}$ in the literature for $n \leq 3$ and $n^* \leq 5$ [128, 127]. The spontaneous emission spectrum, under the action of the static Stark effect, has two properties of particular interest. First the frequency associated with the transitions are shifted with a linear dependence on the electric field magnitude through the parameter α_{DC}. Second the intensity associated with the transitions are independent of the electric field. As indicated by $I^{n\,n_1\,n_2}_{n^*\,n_1^*\,n_2^*}$ the transition intensity is only dependent on the electronic structure of the atom and the polarization vector ϵ of the observed photon.

In contrast, the dynamic Stark effect is defined as the atom under the action of a time dependent

electric field. In particular for this work we will only consider time periodic electric fields. The first to study the dynamic Stark effect was Blochinzew [21] in which the one-electron atom with degenerate magnetic substates under the action of a monochromatic electric field was investigated. Defining the electric field to lie along the z-axis with intensity E_{RF} and angular frequency ω the Schrödinger equation is given by

$$i\hbar\frac{\partial\Phi}{\partial t} = H^o\Phi + e\,z\,E_{RF}\cos(\omega t)\Phi\,. \tag{3.3}$$

In the parabolic basis Blochinzew arrived at a solution to Eq. 3.3 within the framework of first order perturbation theory utilizing separation of variables and an expansion of the time dependent component. Using the electric dipole connection operator and the solution to Eq. 3.3 the first order correct time averaged spontaneous emission spectrum can be determined and is given by

$$I_{nn^*}(\tilde{\omega}) = \sum_{n_1 n_2}\sum_{n_1^* n_2^*} I^{n n_1 n_2}_{n^* n_1^* n_2^*}\sum_{s=-\infty}^{\infty} J_s^2(\alpha_{RF}X)\delta(\omega_{nn^*} + s\omega - \tilde{\omega})\,, \tag{3.4}$$

$$\alpha_{RF} = \frac{6\pi\epsilon_o\hbar E_{RF}}{Z e\, m_e\omega}\,.$$

Where J_s is the s^{th} Bessel function of the first kind. The most outstanding feature of the spontaneous emission spectrum is that it consists of an infinite number of transitions whose frequency is now dependent on the electric field angular frequency ω instead of its magnitude. As given by the argument of the delta function of Eq. 3.4 the transitions are centered about the unperturbed transition frequency spaced at integer multiples of ω given by the index s. Thus Blochinzew mathematically discovered that the dynamic Stark effect was due to a multi-photon process where photons associated with the electric field are emitted/absorbed with the photon associated with the electronic transition [145, 11, 111].

Here the transition intensity is given by the product of $I^{n n_1 n_2}_{n^* n_1^* n_2^*}$ and the square of the J_s Bessel function. Thus the transition intensity is nonlinearly dependent on the electric field magnitude through the parameter α_{RF} associated with the argument of the Bessel function. As the summation of Eq. 3.4 is carried out towards infinity, the value of $J_s^2(\alpha_{RF}\chi)$ tends to decrease. While these values do not decrease monotonically there exists a predictable value of s in which the infinite sum can be truncated. Effectively, the spontaneous emission spectrum consists of a finite number of transitions separated by the s^{th} multiple of the frequency in which the electric field is oscillating. Due to this structure the $s \neq 0$ components are referred to as satellites in the literature.

In comparing the static and dynamic Stark effects, Eq. 3.2 and Eq. 3.4 respectively, it is seen that the behavior is nearly opposite. For the static electric field it was found that the transition frequency was linearly dependent on the electric field magnitude. Conversely, for the dynamic electric field the

transition frequency is now independent of the magnitude and linearly dependent on the frequency. Therefore under the static Stark effect the position, in frequency space, of the transition correlates with the electric field magnitude. Similarly for the dynamic Stark effect a correlation exists but now with the electric field frequency instead of the magnitude. For the static electric field the transition intensity was found to be independent of the electric field parameters. Conversely, for the dynamic electric field the transition intensity is now nonlinearly dependent on the electric field magnitude.

To demonstrate the dynamic Stark effect, Figure 3.1 presents both the discrete and continuous theoretical time averaged spectral line profiles associated with the H_β transition with degenerate magnetic substates. The electric field is modeled with a magnitude of 5 kV/cm and a frequency of 20 GHz. The discrete spectral line profile is given in the absence of broadening mechanisms such as instrument and Doppler. The discrete profile is completely theoretical due to the fact broadening mechanisms will always be present even if only by the uncertainty principal. The discrete spectral line profile is typical show to indicate the wavelength and intensity associated with the transitions. The continuous spectral line profile is measured experimentally and is calculated by convolving the discrete with the broadening mechanisms.

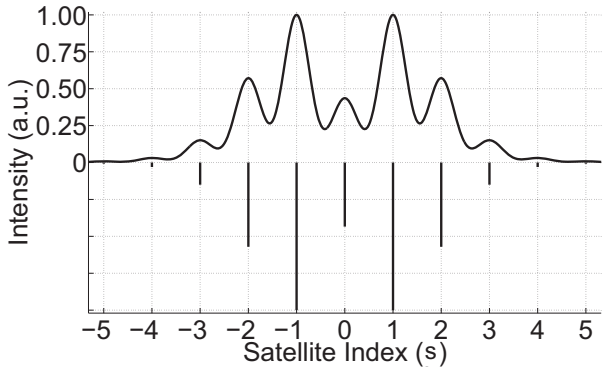

Figure 3.1: Theoretical H_β spectral line profile in the presence of an electric field with a 5 kV/cm magnitude and a frequency of 20 GHz.

Figure 3.1 depicts that the spacing between the discrete transitions is exactly 20 GHz illustrating the multi-photon nature of the dynamic Stark effect. The index s of Eq. 3.4 is truncated at a value of five due to negligible intensity of higher order satellites.

The dynamic Stark effect has been extensively studied theoretically utilizing various analytic and numerical methods. The analytic methods are based on partial fraction expansion [11] and perturbation theory [13]. Additionally a monograph recently written by Oks [111] investigates a vast range of electric field scenarios in terms of intensity, frequency, and topology analytically utilizing perturbation based methods. The numeric method is based on the Floquet theorem and a Fourier

series expansion [70].

Extensive experimental observation of the satellite structure of the hydrogen Lyman and Balmer series spectral lines and select neutral helium transitions have been carried out [112, 85, 72, 71, 73] where Ad hoc methods were used to determine the electric field parameters of interest. Due to the relatively complex theory and the computation resources required to simulate the spectral line profile there exists a limited number of experimental investigations where the electric field parameters were determined systematically from a fit [70, 22, 75, 74]. The majority of the experimental endeavors have been carried out for high frequency electric fields in the GHz range due to the fact individual satellites can be observed with passive OES techniques. It has been shown that excellent agreement exists between the theory and experiment in the GHz range of frequencies with the numerical theoretical treatment being the most accurate [70]. The frequency of the electric field in which this research is focused, the RF range of 10 to 50 MHz, is a relatively unexplored regime of the dynamic Stark effect both theoretically and experimentally. This dissertation presents the systematic theoretical investigation of the dynamic Stark effect in the RF range of frequencies. The numerical method of Hicks *et al.* [70] is implemented because it is the most accurate and easily generalizable to non-monochromatic electric fields.

3.2 Experimental Technique

In this section the available experimental passive techniques, phase resolved and time averaged OES, are discussed. The time averaged technique was selected for this research based on the capabilities of the available spectroscopic equipment. The logic associated with this choice will be presented.

The electric fields of interest, namely those of the capacitively coupled RF sheath and the near field of an ICRF antenna, are typically non-monochromatic [125, 95, 103]. Taking advantage of the time periodic nature, an electric field of arbitrary spatial dependence can be compactly parametrized by representing it as a Fourier cosine series as given by

$$\bar{E}(t) = \bar{E}_0 + \sum_{n=1}^{N_H} \bar{E}_n \, cos(n\omega t + \theta_n) \, . \tag{3.5}$$

The diagnostic was developed such that the electric field vectors, $\bar{E}_n$, and phase angles, θ_n, associated with the spectrum consisting of N_H harmonics could be determined by analysis of the spectral line profile. The spatial dependence of the parameters has been suppressed for compactness.

As indicated by the modeling presented in Section 2.3 the RF sheath electric field can be accurately represented with a spectrum containing three harmonics. The numerical modeling of the theoretical spectral line profile is conducted in such a way to allow for a general time periodic electric field and thus is not limiting. On the other hand, depending on the OES technique, the

routines utilized to fit the experimental data can be highly limiting in the number of harmonics that can be accurately determined. For the phase resolved technique this limitation is negligible but for the time averaged technique it is substantial.

The fitting routine limitation is essentially due to the broadening mechanisms of the spectral line profile with a slight dependence on the computational time. Assuming no spatial variation of the electric field along the line of sight, the spectral resolution of the OES technique and the Doppler effect are the primary broadening mechanisms determining the truncation value of N_H.

The experiment described in this dissertation was designed such that the electric field did not vary significantly along the line of sight in which emission was collected. This was done such that the truncation value of N_H would be solely dictated by the instrument and Doppler broadening. In the tokamak a significant challenge will be associated with the collection of emission such that the electric field does not vary significantly along the line of sight. This challenge is primarily due to the small physical dimensions of the RF sheath, on the order of 1 mm due to the high density in the tokamak, and complex geometry. In addition limitations of viable experimental real estate on the machine are problematic. Due to the above, implementation of a passive OES based diagnostic in a tokamak is seen to be formidable and thus requiring a more elaborate scheme to measure the spectral line profile such as a laser based technique [10, 16]. The premise of the research presented in this dissertation is twofold: first provide a test for the theoretical modeling of the spectral line profile and second to investigate basic capacitively coupled magnetized RF sheath physics. The theoretical modeling of the spectral line profile and the fitting routines utilized to extract the electric field parameters are essentially universal with regard to the spectroscopic technique.

Two techniques are available to obtain the spectral line profile: phase resolved and time averaged OES. The applicability is determined by the emission intensity of the transition of interest. Both methods involve fitting theoretical to experimental spectral line profiles by minimizing the reduced χ fitting parameter and will be discussed in Section 3.4.

The first technique is based on measuring the spectral line profile as a function of time within the period of the electric field waveform. The phase resolved spectral line profile is obtained by integrating optical emission over a window that is small compared to the period, typically $\tau/10$ to $\tau/20$ gives adequate temporal resolution. In order to perform phase resolved spectroscopy one must have the capability of producing a TTL waveform which is phase locked to that of the electric field. This TTL waveform is responsible for triggering the spectroscopic camera. Due to the fact the electric field waveform is unknown another source must be utilized. The RF voltage and current waveforms driving the discharge are inherently phase locked to the electric field waveform and thus are acceptable sources. In addition, if these waveforms are not available those of the reflected or forward power may be used. A schematic depicting the triggering of the spectroscopic camera is given by Figure 3.2. The details of the experimental setup will be presented in Section 4.2.

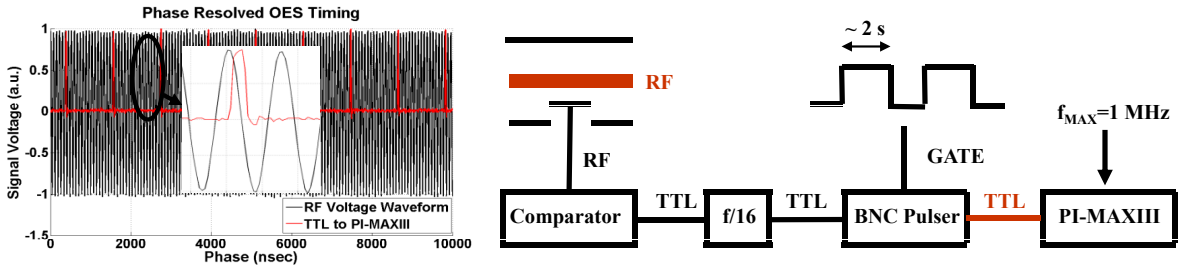

Figure 3.2: Schematic of intensified CCD triggering for phase resolved OES.

An acceptable signal to noise ratio typically requires the accumulation of millions of acquisitions, which reveals the importance of triggering the spectroscopic camera consistently at the desired phase for each acquisition. To obtain the spectral line profile at various phases within the RF period a variable phase delay is inserted after the camera is triggered and is programmable in the software.

Given the experimental phase resolved spectral line profiles, $I_E(t_i,\lambda)$, the electric field waveform is determined by a fit to the theoretical phase resolved spectral line profiles, $I(t_i,\lambda)$. The fit is different depending on the ordering of the RF period and the lifetime of the excited state. If the RF period is much less then the lifetime of the excited state the electric field is determined from a simultaneous fit to the phase resolved spectra as given by

$$\chi\left(\{I(t_i,\lambda),I_E(t_i,\lambda)\ ;\ t_i\in[0,\tau]\}_{i=1..N}\right)\quad\xrightarrow{FIT}\quad E(t)\quad for\quad \tau\ll\tau^*\,. \tag{3.6}$$

If the RF period is much greater then the lifetime of the excited state the phase resolved spectra may be fitted individually as given by

$$\left\{\chi\left(I(t_i,\lambda),I_E(t_i,\lambda)\right)\quad\xrightarrow{FIT}\quad E(t_i)\ ;\ t_i\in[0,\tau]\right\}_{i=1..N}\quad for\quad \tau\gg\tau^*\,. \tag{3.7}$$

In this case the instantaneous electric field waveform is determined from the compilation of the instantaneous electric field values.

Phase resolved OES is ideal due to the fact that the fitting routines pose no limitations. This is due to the fact that the time dependence of the electric field is contained within the collection of phase resolved spectra associated with the various investigated phases. Thus the limiting factor concerning the number of harmonics that can be extracted is not determined by the broadening mechanisms but by the integration time. The major drawback to the phase resolved technique is that the intensity of the observed emission must be very high in order to obtain an adequate signal to noise ratio.

The second technique is based on measuring the time averaged spectral line profile. Here the integration time is set to be much larger than the RF period such that the collected emission can be

approximated as the time average over one period. The electric field is determined by fitting the time averaged theoretical and experimental spectra as described by

$$\chi\left(I(\lambda), I_E(\lambda)\right) \quad \xrightarrow{FIT} \quad E(t)\,. \tag{3.8}$$

The calculation of a time dependent quantity from a time integrated measurement is defined as a inverse integral problem. Due to the problem nature and broadening mechanisms the fitting routines are highly limited in the number of harmonics that can be accurately determined. In order to perform the fit the theoretical time averaged spectral line profile, $I(\lambda)$, must be calculated which is carried out differently depending on the ordering of the RF period and the lifetime of the excited state. If the RF period is much less then the lifetime of the excited state then the emission intensity is constant. The time averaged spectral line profile is calculated by integrating the theoretical phase resolved spectral line profile over an RF period as given by

$$I(\lambda) = \int_0^{\tau} I(t,\lambda)dt \quad for \quad \tau \ll \tau^*\,. \tag{3.9}$$

If the RF period is much greater then the lifetime of the excited state then the emission intensity is potentially a function of time. The characteristic lifetime for spontaneous emission of the upper level associated with the H_β and the $5^3D \rightarrow 2^3P$ He I transitions is 33 and 105 ns respectively [152]. Comparing these characteristic lifetimes with the 74 ns RF period it is expected that the emission intensity of the H_β transition will be time dependent while that of the $5^3D \rightarrow 2^3P$ He I will not. The experimental investigation of the time dependence of the emission intensity of both transitions will be discussed in detail in Section 5.3 to aid comprehension the experimental measurement of the emission intensity of the H_β transition is presented in Figure 3.3 with the RF biased electrode voltage.

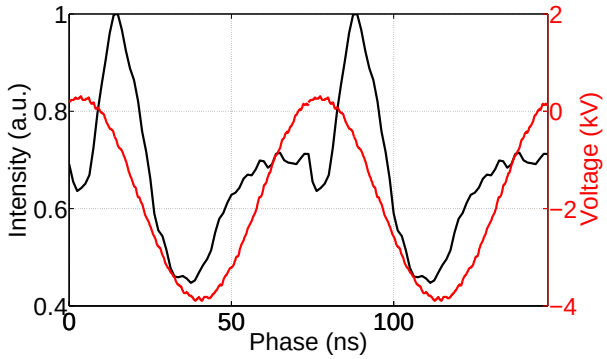

Figure 3.3: Time dependent emission intensity of H_β in the RF sheath plotted against the RF biased electrode voltage.

Two observations can be drawn from Figure 3.3: first the intensity of the H_β transition is a strong function of time within the RF sheath. Second the intensity is intrinsically phase locked to the RF voltage waveform and thus that of the electric field. To calculate the theoretical time averaged spectral line profile it is made evident from Figure 3.3 that the phase resolved spectral line profile must be averaged over an RF period utilizing the appropriate weight function as given by

$$I(\lambda) = \int_0^\tau A(t) I(t,\lambda) dt \quad for \quad \tau \gg \tau^* . \tag{3.10}$$

Where the weight function is given by the time dependent emission intensity, A(t).

A comparison of Eq. 3.6 and Eq. 3.7 with Eq. 3.10 reveals that the phase resolved technique is superior to that of the time averaged. Utilizing the phase resolved technique the electric waveform can be determined from either a simultaneous fit to a set of N spectra, Eq. 3.6, or directly from the instantaneous electric field values obtained by fitting the N spectra independently, Eq. 3.7. The time averaged technique requires that the electric field waveform be determined from a fit to a single spectrum. Utilizing equation Eq. 3.6 or Eq. 3.10 the electric field waveform is determined from a simultaneous fit to the spectra. If the electric field waveform is represented in the time domain the number of required fit variables is equivalent to the number of temporal points, typically 20 to 30. However this can be reduced to $2H+1$, typically 11 to 13, by representing the electric field waveform in the frequency domain. This reduction greatly reduces the computational time associated with the fit. Thus the electric field is represented as a Fourier cosine series in the fitting routines.

In the limit that Eq. 3.7 is appropriate the electric field waveform is determined point by point in time by individually fitting the spectra. This requires only a single fit variable, the instantaneous electric field intensity. Assuming an acceptable signal to noise ratio the electric field waveform is determined most efficiently from Eq. 3.7. This is due to the large decease in the number of fit variables.

The accuracy of Eq. 3.6 and Eq. 3.7 in the determination of the electric field waveform is approximately equivalent and is primarily set by the integration time and the number of acquired spectra. For Eq. 3.10 this accuracy is set by the broadening mechanisms associated with the spectral line profile, namely that of instrument and Doppler. Due to the expected degree of broadening the value of N_H that can be accurately determined from Eq. 3.10 will be highly limited. Therefore it is preferred to use a phase resolved technique in which the electric field waveform can be determined from Eq. 3.7. To determine if a phased resolved technique can be utilized the signal to noise ratio must be investigated.

To achieve an equivalent spectrum intensity utilizing the phase resolved technique in comparison with that of the time averaged, a minimum total integration time of $\frac{\tau}{\tau_{PR}}\tau_{TA}$ is required. Where τ_{PR} and τ_{TA} are the phase resolved and time averaged integration times respectively. In addition

this assumes that the spectroscopic camera can be triggered at a frequency equal to that of the electric field waveform, which is typically not the case. The phase resolved capable spectroscopic camera available has a maximum trigger rate of 1 MHz, thus at a minimum the total integration time must be multiplied by 13.56. For a typical phase resolved integration time of $\tau_{PR} = \tau/10$ a total acquisition time of approximately $136\tau_{TA}$ is required for equivalent spectrum intensity. According to Knoll [88] the signal to noise ratio for a typically CCD can be approximated by

$$SNR = \frac{\phi P \tau_I E G}{\left(\phi P \tau_I E G^2 + e_{DC} P \tau_I + e_{AD}^2\right)^{1/2}} . \tag{3.11}$$

Where ϕ is the photon flux at the detector, P is the number of binned pixels, τ_I is the integration time, E is the quantum efficiency, G is the detector gain, e_{DC} is the dark charge accumulation per pixel per unit time, and e_{AD} is the standard deviation associated with digitization.

The numerator and denominator of Eq. 3.11 represent the total number of counts obtained after digitization and the associated standard deviation respectively. The denominator terms from left to right represent the standard deviation associated with Poisson statics, dark charge accumulation, and digitization respectively. A comparison of the signal to noise ratio for the two available spectroscopic cameras is made. The first camera is the Princeton Instruments PI-MAX III with an intensified CCD, this camera is capable of both phase resolved and time averaged measurements. The second camera is the Princeton Instruments PyLoN liquid nitrogen cooled CCD, this camera is only capable of time averaged measurements. A detailed description of the spectroscopic cameras is given in Section 4.2. For the spectral line profile measurements presented in this dissertation the photon flux at the detector is typically 1 s^{-1} $pixel^{-1}$. 100 vertical pixels are binned yielding an incident photon rate of 100 s^{-1}. Table 3.1 gives the parameters associated with the PI-MAX III and PyLoN cameras.

Table 3.1: Spectroscopic camera parameters.

Parameter	**PI-MAX III**	**PyLoN**
E	0.15	0.9
G	30	1
e_{DC} (e^-/pixel/sec)	1.7	0.004
e_{AD} (e^-)	8	4

As shown by Table 3.1 the cameras have significantly different noise characteristics. The dark charge accumulation associated with the PI-MAX III camera is 425 times larger then that of the PyLoN. The signal to noise ratio is presented in Figure 3.4 for the PI-MAX III and PyLoN cameras utilizing an incident photon rate of 100 s^{-1} and the parameters presented in Table 3.1. The signal to

noise ratio converges asymptotically to a value on the order of 2 for the PI-MAX III camera and 100 for the PyLoN camera. The maximum signal to noise ratio determines whether the phase resolved technique can be effectively utilized to determine the electric field waveform. The required signal to noise ratio for the fitting routines is typically 20 thus indicating that the phase resolved technique implemented by the PI-MAX III camera will not be possible. To meet the desired signal to noise ratio the time averaged technique will be implemented utilizing the PyLoN camera.

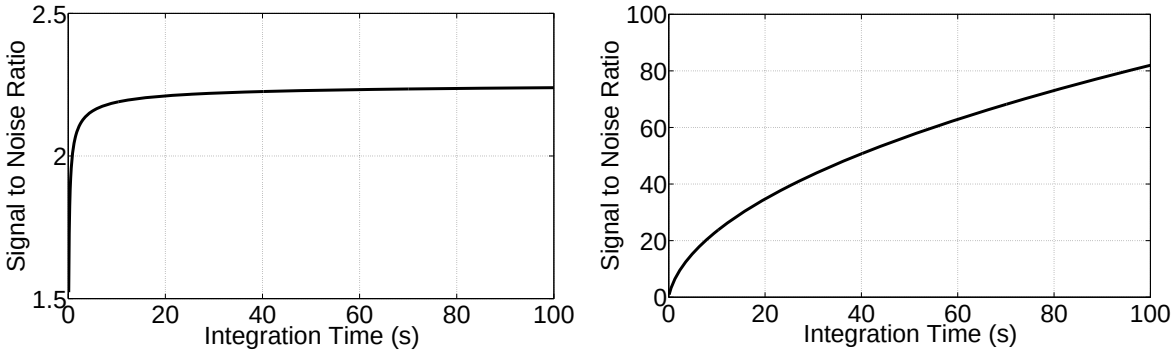

(a) (b)

Figure 3.4: Signal to noise ratio for the (a) PI-MAX III and (b) PyLoN spectroscopic cameras.

Due to the fact that the time averaged technique must be implemented it is desired to increase the certainty in the fit. This is done by increasing the number of unique spectra that can be fit simultaneously. To achieve this two methods are investigated: obtain multiple spectral line profiles associated with different electronic transitions and/or measure the polarized spectral line profile for the two linearly independent polarizations. These polarized spectra are referred to as the π and σ components, in which the polarization vector of the photon is parallel and perpendicular to the field respectively.

Due to the spectral resolution required to extract an electric field with intensity on the order of 1 kV/cm only a 100 Å window is observable in the spectrum. In addition, the transitions of interest are isolated within the range of 100 Å. To measure the spectral line profile of multiple transitions the grating angle must be changed. The experimental operational time associated with the measurement of a spectral line profile is expected to be on the order of ten minutes. Thus due to time constraints no more than two spectral line profiles can be measured having similar experimental conditions. The simplest solution given this restraint is to observe the π and σ components independently. Implementation of this only requires a rotation of an element contained within the collection optics. In addition the radiator distribution function associated with the π and σ components is typically equivalent while this is not the case for different transitions.

3.3 Atomic Theory

This section presents the Schrödinger equation for the one-electron atom in the presence of arbitrary static magnetic and time periodic electric field vectors. The solution will be derived and discussed. The atomic theory utilized to calculate the discrete spectral line profile will be developed. Additionally, a method to approximate the continuous spectral line profile is presented.

The operator connecting the upper and lower levels via emission of a photon is assumed to have a negligible effect on the quantum states. Thus the calculation of the theoretical spectral line profile can be carried out in a three step process, simplifying the problem. ***First*** the solution to the appropriate Schrödinger equation is found, resulting in a set of energies and wave functions associated with the perturbed quantum states of the atom. ***Second*** a new Schrödinger equation is formulated from the original by the addition of a connection operator. Utilizing the set of perturbed wave functions as the new basis the transition probabilities are calculated. ***Third*** the continuous theoretical spectral line profile is calculated from the energies and transition probabilities given the instrument and radiator distribution functions.

The Schrödinger equation for the one-electron atom in the presence of arbitrary static magnetic and time periodic electric field vectors is given by

$$i\hbar\frac{\partial\tilde{\Psi}}{\partial t} = \tilde{H}(t)\tilde{\Psi}\,. \tag{3.12}$$

The time periodic Hamiltonian $\tilde{H}(t)$ is given by

$$\tilde{H}(t) = H + H^B + \frac{1}{2}\sum_{n=0}^{N_H} H^{E_n}\left[\mathrm{e}^{i(n\omega t+\theta_n)} + \mathrm{e}^{-i(n\omega t+\theta_n)}\right],$$

$$H = H^o + H^{'}$$

$$H^B = \frac{\mu_\beta}{\hbar}B_z(J_z + S_z)$$

$$H^{E_n} = e\,\bar{E}_n\cdot\bar{r}\,.$$

Where H is the complete unperturbed Hamiltonian encompassing the electron spin, relativity, and quantum electrodynamics. When considering the helium atom additional terms are added to H^o which are associated with second electron and its interaction with the first. As will be discussed at the end of this section the functional form of H is irrelevant because of the vector space the problem is solved in. H^B is the Hamiltonian associated with a static magnetic field defined along the z-axis. The Hamiltonian associated with the time periodic electric field vector is the remaining

term in $\tilde{H}(t)$. In order to simplify the solution to Eq. 3.12 the magnetic field vector was defined to lie along the z-axis. Due to the static nature of the magnetic field vector the coordinate system can be rotated to achieve the definition, thus resulting in no loss of generality. The time periodic nature of the Hamiltonian $\tilde{H}(t)$ allows for Floquet's theory [18] to be implemented and consequently the reduction of Eq. 3.12 to an eigenvalue/eigenvector problem. The eigenvalue and eigenvector pairs represent the energies and wave functions of the perturbed quantum states of the atom.

In order for de-excitation to occur the upper level must be perturbed electromagnetically. For passive OES techniques this perturbation is carried out by the vacuum fields predicted by quantum electrodynamics and is called spontaneous emission. For typical laboratory plasmas it can be assumed that the spontaneous emission connection operator can be replaced with the dipole approximation [67]. The transition probabilities are calculated from a new Schrödinger equation obtained from Eq. 3.12 with the addition of the dipole connection operator as given by

$$i\hbar\frac{\partial\Theta}{\partial t} = \left[\tilde{H}(t) + \hat{H}\right]\Theta \,. \tag{3.13}$$

The Hamiltonian associated with the dipole connection operator is given by $\hat{H}$. Only the relative intensity of the spectral line profile is desired thus all constants associated with this operator are dropped giving

$$\hat{H} \propto \bar{\epsilon}\cdot\bar{r} \,.$$

The solution to Eq. 3.13 is found by expanding the Θ wave functions in terms of linear combinations of the Ψ wave functions. The energies and transition probabilities determined from the solution to Eq. 3.12 and Eq. 3.13 respectively represent the discrete theoretical spectrum, which consists of a series of delta functions. The continuous theoretical spectrum is calculated by convolving the discrete spectrum with the instrument and radiator distribution functions.

To solve Eq. 3.12 a basis must be chosen within which to work. A logical choice would be the coupled basis due to the fact they are eigenfunctions of the complete unperturbed Hamiltonian H. In choosing the coupled basis the assumption is made that the L-S coupling scheme is appropriate, this is a good assumption for low Z atoms [76]. The wave function associated with the coupled basis represented in the so called bar and ket notation is given by

$$\Phi = |n, l, s, j, m_j> \,, \tag{3.14}$$

$$j \in |l-s|, |l-s|+1 \;..\; |l+s|$$

$$m_j \in -j, -j+1 \,..\, j \,.$$

Where n is the principal quantum number and can take on any positive non-zero value. The orbital and spin angular momentum quantum numbers are given by l and s respectively. For atoms containing multiple electrons the orbital and spin angular momentum quantum numbers are calculated by summing the projected values of all electrons and taking the absolute value. j is the total angular momentum quantum number and m_j is its projection.

The wave function Φ can be expressed analytically for the one electron atom and is obtained from the unperturbed Schrödinger [19]. The Schrödinger equation associated with the two electron atom is substantially more difficult to solve, currently the wave function is not expressible analytically. In order to calculate the theoretical spectral line profile for the $5^3D \rightarrow 2^3P$ He I transition an approximation to the wave function must be made. Typically one electron is always present in the ground state of the neutral helium atom. When both electrons are in excited states the probability of ionization by the Auger effect is much greater than a radiative transition to a bound state in neutral helium. This can be realized because any state in helium in which both electrons are excited has an energy greater then the ground state of singly ionized helium and the free electron pair. Due to the above and the large energy difference in the ground and first excited states hydrogenic wave functions will be utilized as the approximation [19, 46, 70].

The energies associated with the unperturbed quantum states of many atoms have been experimentally measured with a high degree of accuracy and tabulated by the United States National Institute of Standards and Technology (NIST) [5]. Utilizing the coupled basis set

$$H\Phi_i = E_i\Phi_i \tag{3.15}$$

can be written and the eigenvalues $E_i^{'}$ associated with the unperturbed Hamiltonian can be taken from NIST tables. Where i represents the complete set of quantum numbers. The unperturbed energy eigenvalues for the $n \leq 6$ magnetic substates of hydrogen and helium are given in Appendix A.

3.3.1 Floquet Method

The time periodic nature of the Hamiltonian $\tilde{H}(t)$ allows Eq. 3.12 to be solved utilizing Floquet's theorem [18] and a Fourier series expansion of time periodic coefficients. The solution to be found will be perturbative in the sense that only states within a given n-level are allowed to mix. This is an excellent approximation for the expected electric field intensities of <15 kV/cm [128]. Floquet's theorem asserts that a differential equation with time periodic coefficients will have a solution of the form given by

$$\tilde{\Psi}(t) = T(t)e^{-i\tilde{\lambda}t} \ . \tag{3.16}$$

Where the spatial dependence of the variables is suppressed for compactness while the temporal dependence in retained for effect. The spatially dependent time periodic coefficients $T(t)$ are expanded in the coupled basis set giving

$$T(t)=\sum_{j=1}^{N}\tau_j(t)\Phi_j\ . \tag{3.17}$$

Substitution into Eq. 3.16 yields

$$\tilde{\Psi}_k(t)=\sum_{j=1}^{N}\tau_{kj}(t)\Phi_j e^{-i\tilde{\lambda}_k t} \tag{3.18}$$

for $k=1..N$, where k refers to the k^{th} function in the new N-dimensional basis set. The spatially independent time periodic coefficients $\tau(t)$ are expanded in a Fourier series giving

$$\tau_{kj}(t)=\sum_{s=-\infty}^{\infty}c_{kj}^{s}e^{-is\omega t}\ . \tag{3.19}$$

Substitution into Eq. 3.18 and defining $\tilde{\lambda}_k=\frac{\tilde{E}_k}{\hbar}$ yields

$$\tilde{\Psi}_k(t)=\sum_{s=-\infty}^{\infty}\sum_{j=1}^{N}c_{kj}^{s}\Phi_j e^{-\frac{i}{\hbar}(\tilde{E}_k+s\hbar\omega)t}\ . \tag{3.20}$$

The set of wave functions given by Eq. 3.20 represents the new basis set and are expressed as a linear combination of the coupled basis set. The solution to Eq. 3.12 will require the expansion coefficients, c_{kj}^{s}, and the eigenvalues, E_k, to be found. Eq. 3.20 is substituted into Eq. 3.12 to yield

$$\begin{aligned}\sum_{s=-\infty}^{\infty}(\tilde{E}_k+s\hbar\omega)e^{-is\omega t}\sum_{j=1}^{N}c_{kj}^{s}\Phi_j=\sum_{s=-\infty}^{\infty}\Bigg[&e^{-is\omega t}\sum_{j=1}^{N}c_{kj}^{s}H\Phi_j+e^{-is\omega t}\sum_{j=1}^{N}c_{kj}^{s}H^{B}\Phi_j\\&+\frac{1}{2}\sum_{n=0}^{N_H}e^{-i(s-n)\omega t}e^{i\theta_n}\sum_{j=1}^{N}c_{kj}^{s}H^{E_n}\Phi_j+\frac{1}{2}\sum_{n=0}^{N_H}e^{-i(s+n)\omega t}e^{-i\theta_n}\sum_{j=1}^{N}c_{kj}^{s}H^{E_n}\Phi_j\Bigg]\ .\end{aligned} \tag{3.21}$$

Allowing the Hamiltonians H, H^B, and H^{E_n} to operate on the coupled basis set wave function Φ_j yields

$$H\Phi_j=E_j\Phi_j\ , \tag{3.22}$$

$$H^{B}\Phi_j=\sum_{m=1}^{N}E_{jm}^{B}\Phi_m\ , \tag{3.23}$$

and

$$H^{E_n}\Phi_j = \sum_{m=1}^{N} E_{jm}^{E_n}\Phi_m \tag{3.24}$$

respectively. E_j is the energy of the quantum state associated with the j^{th} wave function of the unperturbed atom. E_{jm}^{B} is the energy coupled between the quantum states associated with the j^{th} and m^{th} wave functions due to the magnetic field, B_z. $E_{jm}^{E_n}$ is the energy coupled between the quantum states associated with the j^{th} and m^{th} wave functions due to the n^{th} harmonic of the electric field vector, $\bar{E}_n$. The calculation of the quantities E_{jm}^{B} and $E_{jm}^{E_n}$ is non-trivial and thus is presented in Appendix B. Upon substitution of Eq. 3.22 through Eq. 3.24 yields

$$\sum_{s=-\infty}^{\infty}(\tilde{E}_k + s\hbar\omega)e^{-is\omega t}\sum_{j=1}^{N}c_{kj}^{s}\Phi_j = \sum_{s=-\infty}^{\infty}\Bigg[e^{-is\omega t}\sum_{j=1}^{N}c_{kj}^{s}E_j\Phi_j + e^{-is\omega t}\sum_{j=1}^{N}c_{kj}^{s}\sum_{m=1}^{N}E_j^{B}\Phi_m + \frac{1}{2}\sum_{n=0}^{N_H}e^{-i(s-n)\omega t}e^{i\theta_n}\sum_{j=1}^{N}c_{kj}^{s}\sum_{m=1}^{N}E_{jm}^{E_n}\Phi_m + \frac{1}{2}\sum_{n=0}^{N_H}e^{-i(s+n)\omega t}e^{-i\theta_n}\sum_{j=1}^{N}c_{kj}^{s}\sum_{m=1}^{N}E_{jm}^{E_n}\Phi_m\Bigg]. \tag{3.25}$$

Utilizing the orthogonality of the coupled basis set Eq. 3.25 can multiplied by Φ_l and integrated over all space to yield a set of N algebraic equations given by

$$\sum_{s=-\infty}^{\infty}(\tilde{E}_k + s\hbar\omega)e^{-is\omega t}c_{kl}^{s}\Phi_l = \sum_{s=-\infty}^{\infty}\Bigg[e^{-is\omega t}c_{kl}^{s}E_l\Phi_l + e^{-is\omega t}\sum_{j=1}^{N}c_{kj}^{s}E_{jl}^{B}\Phi_l + \frac{1}{2}\sum_{n=0}^{N_H}e^{-i(s-n)\omega t}e^{i\theta_n}\sum_{j=1}^{N}c_{kj}^{s}E_{jl}^{E_n}\Phi_l + \frac{1}{2}\sum_{n=0}^{N_H}e^{-i(s+n)\omega t}e^{-i\theta_n}\sum_{j=1}^{N}c_{kj}^{s}E_{jl}^{E_n}\Phi_l\Bigg] \tag{3.26}$$

for $l = 1..N$. In order for Eq. 3.26 to be satisfied at all time t the coefficients of equal powers of the exponential $e^{is\omega t}$ must equate. Equating the coefficients results in the following set of equations

$$(\tilde{E}_k + s\hbar\omega)c_{kl}^{s}\Phi_l = c_{kl}^{s}E_l\Phi_l + \sum_{j=1}^{N}c_{kj}^{s}E_{jl}^{B}\Phi_l + \frac{1}{2}\sum_{n=0}^{N_H}\Bigg[e^{i\theta_n}\sum_{j=1}^{N}c_{kj}^{s+n}E_{jl}^{E_n}\Phi_l + e^{-i\theta_n}\sum_{j=1}^{N}c_{kj}^{s-n}E_{jl}^{E_n}\Phi_l\Bigg] \tag{3.27}$$

for $s = -\infty..\infty$. This infinite set of algebraic equations must be truncated in order to obtain a solution. To truncate we assume that the expansion coefficients are zero for $|s| > \tilde{s}$ as given by

$$c_{kj}^{s} = 0 \quad \text{for} \quad |s| \geq \tilde{s}\,,\, k = 1..N\,,\, l = 1..N\,. \tag{3.28}$$

The appropriate value of $\tilde{s}$ will be discussed below. The set given by Eq. 3.27 is rearranged and

truncated to yield a set of $2\tilde{s}+1$ equations given by

$$\tilde{E}_k c_{kl}^s \Phi_l = (-s\hbar\omega + E_l) c_{kl}^s \Phi_l + \sum_{j=1}^{N} c_{kj}^s E_{jl}^B \Phi_l + \frac{1}{2}\sum_{n=0}^{N_H}\Bigg[e^{i\theta_n} \sum_{j=1}^{N} c_{kj}^{s+n} E_{jl}^{E_n} \Phi_l + e^{-i\theta_n} \sum_{j=1}^{N} c_{kj}^{s-n} E_{jl}^{E_n} \Phi_l \Bigg] . \quad (3.29)$$

Eq. 3.29 can be compactly written utilizing matrix notation, absorbing the j and l indices yields

$$\tilde{E}_k \tilde{\boldsymbol{\Psi}}_k^s = (-s\hbar\omega \boldsymbol{I} + \boldsymbol{E} + \boldsymbol{E}^B) \cdot \tilde{\boldsymbol{\Psi}}_k^s + \frac{1}{2}\sum_{n=0}^{N_H} \boldsymbol{E}^{E_n} \cdot [e^{i\theta_n} \tilde{\boldsymbol{\Psi}}_k^{s+n} + e^{-i\theta_n} \tilde{\boldsymbol{\Psi}}_k^{s-n}] . \quad (3.30)$$

The vector $\tilde{\boldsymbol{\Psi}}_k^s$ is given by

$$\tilde{\boldsymbol{\Psi}}_k^s = \begin{bmatrix} c_{k1}^s \Phi_1 \\ \vdots \\ c_{kN}^s \Phi_N \end{bmatrix}$$

and the matrices $\boldsymbol{E}$, $\boldsymbol{E}^B$, and $\boldsymbol{E}^{E_n}$ are given by

$$\boldsymbol{E} = \begin{bmatrix} E_1' & \cdots & 0 \\ \vdots & \ddots & \vdots \\ 0 & \cdots & E_N' \end{bmatrix}, \qquad \boldsymbol{E}^B = \begin{bmatrix} E_{11}^B & \cdots & E_{N1}^B \\ \vdots & \ddots & \vdots \\ E_{1N}^B & \cdots & E_{NN}^B \end{bmatrix}, \text{ and } \qquad \boldsymbol{E}^{E_n} = \begin{bmatrix} E_{11}^{E_n} & \cdots & E_{N1}^{E_n} \\ \vdots & \ddots & \vdots \\ E_{1N}^{E_n} & \cdots & E_{NN}^{E_n} \end{bmatrix}$$

respectively. Absorbing the s index Eq. 3.30 is expressed in its final form:

$$\tilde{\boldsymbol{H}} \tilde{\boldsymbol{\Psi}}_k = \tilde{E}_k \tilde{\boldsymbol{\Psi}}_k . \quad (3.31)$$

The eigenvector $\tilde{\boldsymbol{\Psi}}_k$ is given by

$$\tilde{\boldsymbol{\Psi}}_k = \begin{bmatrix} \tilde{\boldsymbol{\Psi}}_k^{-\tilde{s}} \\ \vdots \\ \tilde{\boldsymbol{\Psi}}_k^{\tilde{s}} \end{bmatrix}$$

and the Hamiltonian matrix $\tilde{\boldsymbol{H}}$ is given by

$$\tilde{\boldsymbol{H}} = \begin{bmatrix} \tilde{s}\hbar\omega\boldsymbol{I} + \boldsymbol{E}^D & \cdots & \frac{1}{2}e^{i\theta_H}\boldsymbol{E}^{E_H} & \cdots & \cdots & 0 \\ \frac{1}{2}e^{-i\theta_1}\boldsymbol{E}^{E_1} & (\tilde{s}-1)\hbar\omega\boldsymbol{I} + \boldsymbol{E}^D & \cdots & \frac{1}{2}e^{i\theta_H}\boldsymbol{E}^{E_H} & \cdots & 0 \\ \vdots & \ddots & \ddots & \ddots & \ddots & \vdots \\ \vdots & \ddots & \ddots & \ddots & \ddots & \vdots \\ 0 & \cdots & \frac{1}{2}e^{-i\theta_H}\boldsymbol{E}^{E_H} & \cdots & (-\tilde{s}+1)\hbar\omega\boldsymbol{I} + \boldsymbol{E}^D & \frac{1}{2}e^{i\theta_1}\boldsymbol{E}^{E_1} \\ 0 & \cdots & \cdots & \frac{1}{2}e^{-i\theta_H}\boldsymbol{E}^{E_H} & \cdots & -\tilde{s}\hbar\omega\boldsymbol{I} + \boldsymbol{E}^D \end{bmatrix},$$

where the matrix $\boldsymbol{E}^D$ is given by

$$\boldsymbol{E}^D = \boldsymbol{E} + \boldsymbol{E}^B + \frac{1}{2}\boldsymbol{E}^{E_0}\left(e^{i\theta_0} + e^{-i\theta_0}\right).$$

When considering transitions in which the emission intensity is time dependent θ_0 will be utilized to correlate the electric field and emission intensity waveforms. Otherwise, θ_0 has no effect on the solution and is thus typically taken to be zero. Eq. 3.31 is an eigenvalue problem, the Hamiltonian matrix $\tilde{\boldsymbol{H}}$ has N distinct eigenvalue and eigenvector pairs given by $\tilde{E}_k$ and $\tilde{\boldsymbol{\Psi}}_k$ respectively. The size of the $\tilde{\boldsymbol{H}}$ matrix is given by $(2\tilde{s}+1)N \times (2\tilde{s}+1)N$ and is dependent on two parameters $\tilde{s}$ and N, the index at which the Fourier series is truncated and the number of magnetic substates within the n level interest respectively. Possible values of N are given in Table 3.2 for hydrogen and neutral helium for $n \leq 6$.

The concepts associated with Eq. 3.31 and its solutions are most easily conveyed graphically. Therefore the field geometry given by

$$\bar{B}_z = 1000 \text{ Gauss} \qquad E_z(t) = 2 + \cos(\omega t) + \cos(2\omega t + \pi/3) \text{ kV/cm} \tag{3.32}$$

will be considered and applicable to the figures contained within the remainder of the this section. The angular frequency of the electric field is varied depending on the presented figure.

Table 3.2: Number of states N for the given radial quantum number n.

n	**Para-helium (s=0)**	**Hydrogen (s=1/2)**	**Ortho-helium (s=1)**
1	1	2	3
2	4	8	12
3	9	18	27
4	16	32	48
5	25	50	75
6	36	72	108

The location of the non-zero elements associated with the $\tilde{\boldsymbol{H}}$ matrix of Eq. 3.31 for $n = 4$ in hydrogen with $H = 2$ and $\tilde{s} = 4$ is given by Figure 3.5. Positive and negative matrix elements are indicated with red and black markers respectively. In terms of the global s block structure Figure 3.5 shows that the Hamiltonian matrix has a banded $2H + 1$-diagonal structure.

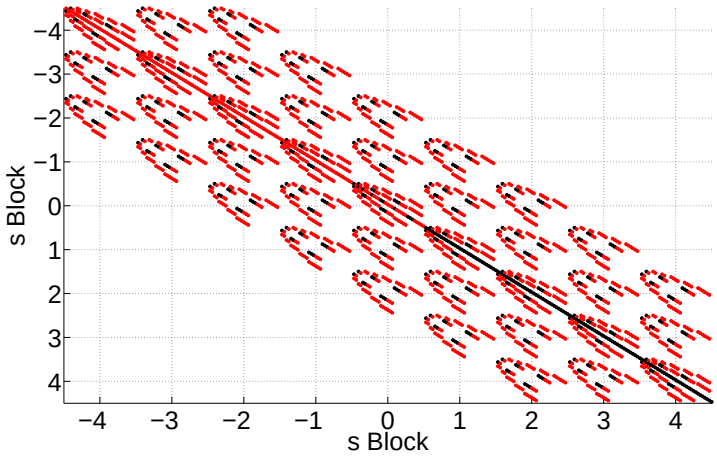

Figure 3.5: Non-zero matrix elements of $\tilde{\boldsymbol{H}}$ for the $n = 4$ level of hydrogen with $\tilde{s} = 4$ using the field geometry given by Eq. 3.32.

Where the s blocks themselves are $N \times N$ matrices. By a comparison to Eq. 3.31 it is visually shown that the band along the diagonal consists of matrix elements associated with the magnetic and static electric field and the off-diagonal bands consists of matrix elements associated with the dynamic electric field only. The s blocks that have been truncated are easily identifiable due to the banded structure of the matrix. Ignoring truncation each band should have the same number of s blocks.

The number of magnetic substates within a given n level is constant. Thus the new quantum mechanical system associated with the magnetic and electric field perturbation will consist of N new basis functions given by linear combinations of the old, the coupled basis. Due to the fact that the coefficients $\tau(t)_{jk}$ were expanded in a Fourier series the solution to Eq. 3.31 consists of $(2\tilde{s} + 1)N$ eigenvalue/eigenvector pairs and is thus over defined. Therefore only N of these eigenvalue/eigenvector pairs are distinct which results in $2\tilde{s} + 1$ equivalent sets, ignoring truncation error. The relationship between the $2\tilde{s} + 1$ sets of equivalent eigenvalues and eigenvectors is

$$\tilde{E}_{k'} = \tilde{E}_k + m\hbar\omega \tag{3.33}$$

and

$$\tilde{\boldsymbol{\Psi}}^{s}_{k'} = \tilde{\boldsymbol{\Psi}}^{s+m}_{k} \tag{3.34}$$

respectively, where $m = [-\tilde{s} - s..\tilde{s} - s]$. These expressions are derived in the absence of truncation error, as s tends towards its extreme values they become invalid.

The atom in a oscillating electric field consists of a combination of real and virtual states. The real states are those that exist by virtue of the atom alone. Virtual states are those that exist to mediate potential interactions with an external perturbation, specifically here the oscillating electric field, that would otherwise be forbidden. At sufficiently high frequencies the real states are those having $s = 0$ and the virtual states are those having $s \neq 0$. In this case the real states have no interaction with the oscillating electric field. The virtual states however interact such that s photons associated with the oscillating electric field are absorbed or emitted during a transition involving the state. As the frequency is decreased the real and virtual states can potentially interact resulting in $s \neq 0$ real states and mixing.

In order to correctly describe the quantum mechanical system a single set of N eigenvalue and eigenvector pairs must be selected out of the possible $(2\tilde{s}+1)N$. Typically it was found that the truncation error can be minimized by selecting the set corresponding to $s = 0$. As described below this would seemingly be a trivial task given the relationships of Eq. 3.33 and Eq. 3.34. Ignoring truncation error the $(2\tilde{s}+1)N$ eigenvalue and eigenvector pairs can be easily sorted into the $2\tilde{s}+1$ sets utilizing the following method. Identical eigenvalues are sorted into N groups each with $2\tilde{s}+1$ members by Eq. 3.33 and ordered numerically. The $2\tilde{s}+1$ sets are then formed by selecting the eigenvalue and corresponding eigenvector out of all N groups having identical locations in the ordering. The set corresponding to $s = 0$ are composed of those members located at the center location in the ordered N groups.

Unfortunately due to truncation error both Eq. 3.33 and Eq. 3.34 do not hold for the extreme values of s to such a degree that the method discussed above cannot be used even with the addition of Eq. 3.34. A significant research effort was carried out to ensure this. A method in which a set of N distinct eigenvalue and eigenvector pairs can be selected is non-trivial and has not been adequately addressed in the literature [70, 129, 117]. This is due to the large values of ω investigated, which resulted in trivial mixing of states and natural grouping. In order to select a consistent set one of two approaches must be followed based on the quantity $\triangle\tilde{E}$ given by

$$\triangle\tilde{E} = \left\{\tilde{E}_k \,;\, k \in [1,N]\right\}\Big|_{max} - \left\{\tilde{E}_k \,;\, k \in [1,N]\right\}\Big|_{min} \quad \text{for} \quad m = 0\,. \tag{3.35}$$

In order to calculate the quantity $\triangle\tilde{E}$ a prior knowledge of the $s = 0$ set of eigenvalues is required, thus a conservative approximation must be made. The quantity $\triangle\tilde{E}$ is approximated utilizing a set of eigenvalues obtained from the Schrödinger equation given by

$$i\hbar\frac{\partial\Phi^*}{\partial t} = H^*\Phi^*\,, \tag{3.36}$$

$$H^* = H + H^B + H^E$$

$$H^E = \sum_{n=0}^{n=H}\left[e\left|E_{x,n}\right|x + e\left|E_{y,n}\right|y + e\left|E_{z,n}\right|z\right].$$

Utilizing similar techniques as presented above an eigenvalue problem is formulated and given by

$$\boldsymbol{H}^*\boldsymbol{\Phi}_k^* = E_k^*\boldsymbol{\Phi}_k^*\,. \tag{3.37}$$

The Hamiltonian matrix $\boldsymbol{H}^*$ is given by

$$\boldsymbol{H}^* = \begin{bmatrix} E_1 + E_{11}^B + E_{11}^E & \cdots & E_{N1}^B + E_{N1}^E \\ \vdots & \ddots & \vdots \\ E_{1N}^B + E_{1N}^E & \cdots & E_N + E_{NN}^B + E_{NN}^E \end{bmatrix}$$

where the terms E_{jm}^E are given by

$$H^E\Phi_j = \sum_{m=1}^{N} E_{jm}^E\Phi_m \tag{3.38}$$

and are calculated utilizing the procedure given in Appendix B. The set of N eigenvalues E_k^* are utilized to approximate those of $\tilde{E}_k$ in Eq. 3.35 such that $\triangle\tilde{E}$ can be calculated. This approximation is typically a significant over estimate of the true value of $\triangle\tilde{E}$ and therefore is conservative.

The accuracy of the Floquet method is completely determined by $\tilde{s}$, the value in which the series of Eq. 3.19 is truncated. The Floquet method is valid regardless of the parameters associated with the magnetic and electric field vectors including the angular frequency ω. As will be derived in Section 3.3.2 the validity of the spectral line profile calculation will be dependent on the ordering of ω and the lifetime of the excited state. The appropriate value of $\tilde{s}$ for an accurate solution of Eq. 3.12 is highly dependent on the magnetic and electric field vectors and the transition of interest. Typically $\tilde{s}$ is estimated by the expression $2\triangle\tilde{E}/\hbar\omega$ during tracking, with a minimum value set to four. For spectral line profile calculations expressions for $\tilde{s}$ have been presented in the literature [129].

If $\triangle\tilde{E} < \hbar\omega$ then the eigenvalues are naturally separated into $2\tilde{s}+1$ sets. The eigenvalues of $\tilde{\boldsymbol{H}}$ are calculated for $\omega/2\pi = 200$ GHz and presented in ascending numerical order in Figure 3.6. When naturally separation occurs the $s = 0$ set is taken as the center N eigenvalues when order numerically, these eigenvalues are represented by the colored markers. All eigenvalues presented in

the remainder of this section are offset by a constant value such that the $s = 0$ set is center about zero. Figure 3.6 conveys Eq. 3.33 nicely, that is the $2\tilde{s}+1$ sets of eigenvalues are offset by integer multiples of $\hbar\omega$.

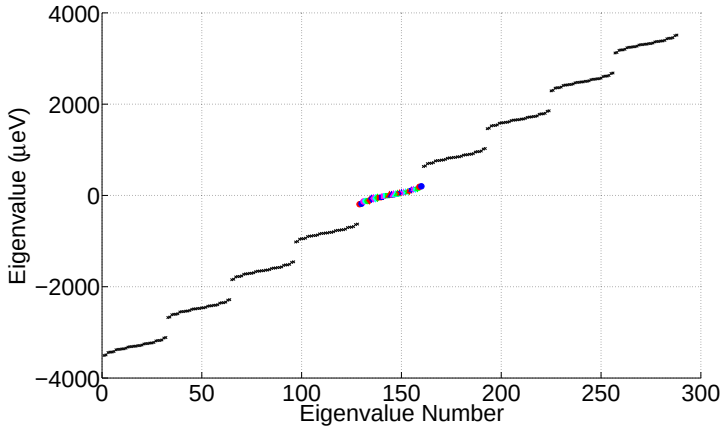

Figure 3.6: Eigenvalues in ascending order associated with $\tilde{\boldsymbol{H}}$ for $\omega/2\pi = 200$ GHz using the field geometry given by Eq. 3.32.

If $\triangle\tilde{E} \leq \hbar\omega$ then a more complicated approach must be taken due to the fact the eigenvalues are no longer naturally separated. The eigenvalues of $\tilde{\boldsymbol{H}}$ are calculated for $\omega/2\pi = 20$ GHz and presented in ascending numerical order in Figure 3.7, with the $s = 0$ set given by the colored markers.

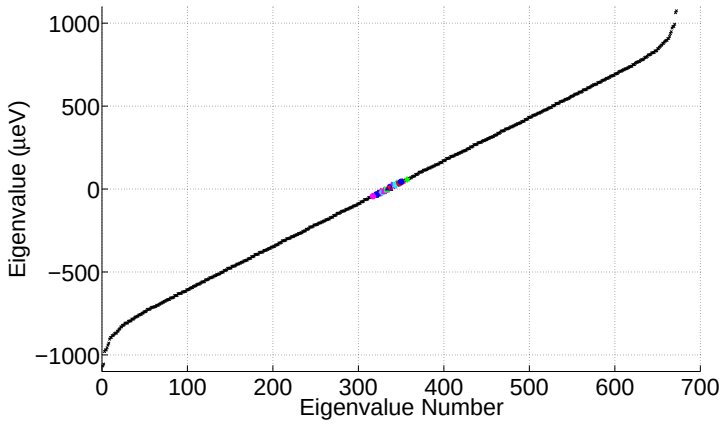

Figure 3.7: Eigenvalues in ascending order associated with $\tilde{\boldsymbol{H}}$ for $\omega/2\pi = 20$ GHz using the field geometry given by Eq. 3.32.

Comparing Figure 3.6 with Figure 3.7, where the frequency differs by an order of magnitude, it is evident that the eigenvalue sets are no longer naturally separated. As discussed above and

represented by Eq. 3.33 the eigenvalue sets are separated by $\hbar\omega$ and thus as the frequency deceases the spacing decreases proportionally, inevitably causing mixing as depicted by Figure 3.7. In addition, the effect of truncation can be seen in the eigenvalues at the extremes in Figure 3.7. The method utilized to select the $s=0$ set when $\triangle\tilde{E} \leq \hbar\omega$ is based on tracking the eigenvalues from a frequency in which naturally grouping of the sets occurs. Tracking is initiated by increasing the angular frequency such that $\triangle\tilde{E} < \hbar\omega_G$, ω_G is calculated by

$$\omega_G = A\frac{\triangle\tilde{E}}{\hbar}\,. \tag{3.39}$$

Where A is a constant typically set to 1.2. At the frequency ω_G the eigenvalues are naturally separated into $2\tilde{s}+1$ sets, as depicted by Figure 3.6. The $s=0$ set is then selected and tracked as the frequency is incrementally decreased to ω. Each tracking step requires the calculation of the $\tilde{\boldsymbol{H}}$ matrix eigenvalues due to the fact ω is changed. Relatively fast routines exist to carry out this computation when the eigenvectors do not need to be calculated, therefore making this method feasible on standard machines. For the field configuration under consideration Eq. 3.39 gives a value of 97 GHz for $\omega_G/2\pi$, the tracking process to a frequency of 20 GHz is depicted by Figure 3.8. The colored lines are associated with the $s=0$ set with the black markers indicated $s\neq 0$ eigenvalues.

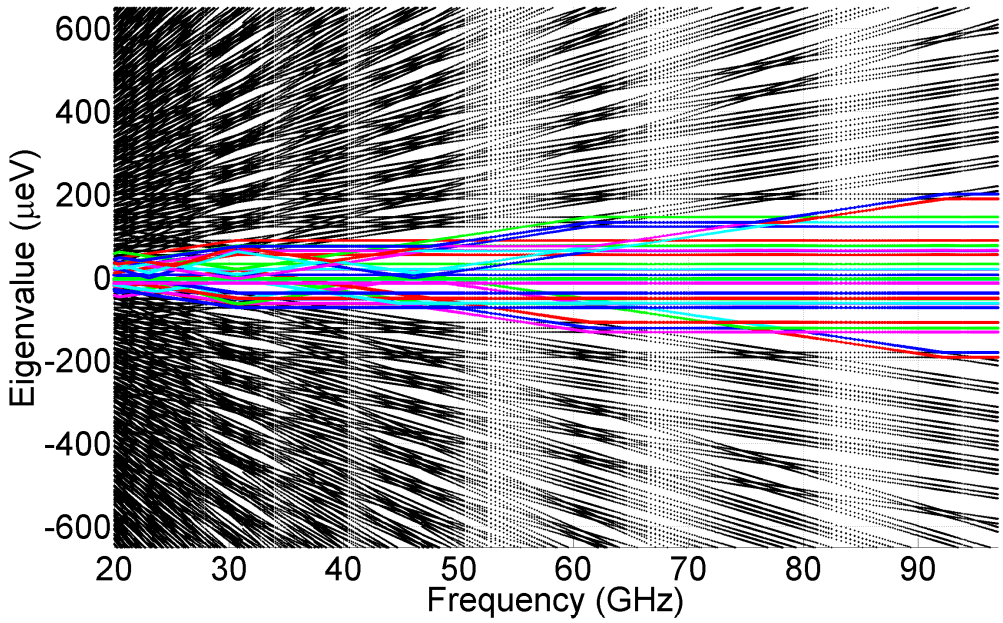

Figure 3.8: Eigenvalues associated with $\tilde{\boldsymbol{H}}$ for $\omega/2\pi \in [20,97]$ GHz using the field geometry given by Eq. 3.32.

Figure 3.8 indicates the necessity for tracking as shown by the interaction of the real and vir-

tual states. This results in complex coupling and thus far unpredictable patterns in the mixing of eigenvalue sets. As will be discussed below the tracking algorithm varies the step size and the value of $\tilde{s}$ as a function of frequency. In addition it was found that during tracking the value of $\tilde{s}$ could be substantially less, typically by a factor of two, then that needed for accurate spectral line profile calculations. At a frequency of 97 GHz the value of $\tilde{s}$ was three as the eigenvalues were tracked to 20 GHz this value was incrementally increased to ten, illustrating the relationship between ω and $\tilde{s}$. To better portray the coupling of the real and virtual states Figure 3.9 presents only the $s=0$ set of eigenvalues associated with Figure 3.8.

At frequencies well above ω_G the $s=0$ and $s\neq 0$ states are purely real and virtual respectively, here the eigenvectors $\tilde{\boldsymbol{\Psi}}_k$ only contain characteristics of the corresponding states. This is illustrated by the fact that initially the $s=0$ eigenvalues are constant with respect to the frequency with those of the $s\neq 0$ sets being linearly dependent as depicted in Figure 3.8 and Figure 3.9. As the frequency is decreased to ω_G and below the states can potentially interact resulting in a coupling between the real and the virtual states. That is the eigenvectors $\tilde{\boldsymbol{\Psi}}_k$ associated with the interacting states now contain both real and virtual characteristics. The simplest example is given in Figure 3.9 at 92 GHz where the maximum eigenvalue of the $s=0$ set interacts with the minimum eigenvalue of the $s=1$ set.

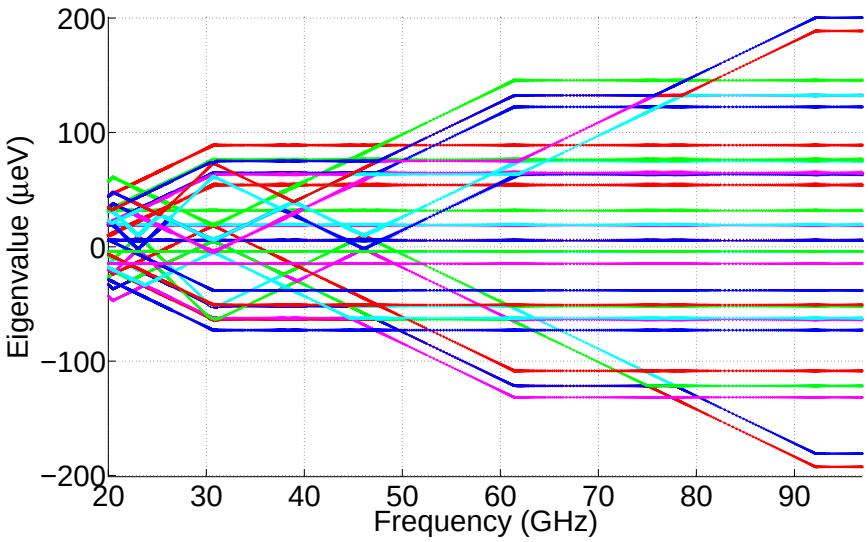

Figure 3.9: Eigenvalues of the $s=0$ set associated with $\tilde{\boldsymbol{H}}$ for $\omega/2\pi\in[20,97]$ GHz using the field geometry given by Eq. 3.32.

Initially these states are purely real and virtual respectively, however after the interaction it is found that the states completely change characteristics resulting in a purely virtual $s=0$ state as indicated

by the linear dependence on frequency. As the frequency is decreased further multiply states can interact collectively resulting in complex coupling as presented by Figure 3.10 where states within the $s = 0$, 1, and 2 sets mix. Here the eigenvalues associated with Figure 3.8 are plotted over a select energy and frequency range.

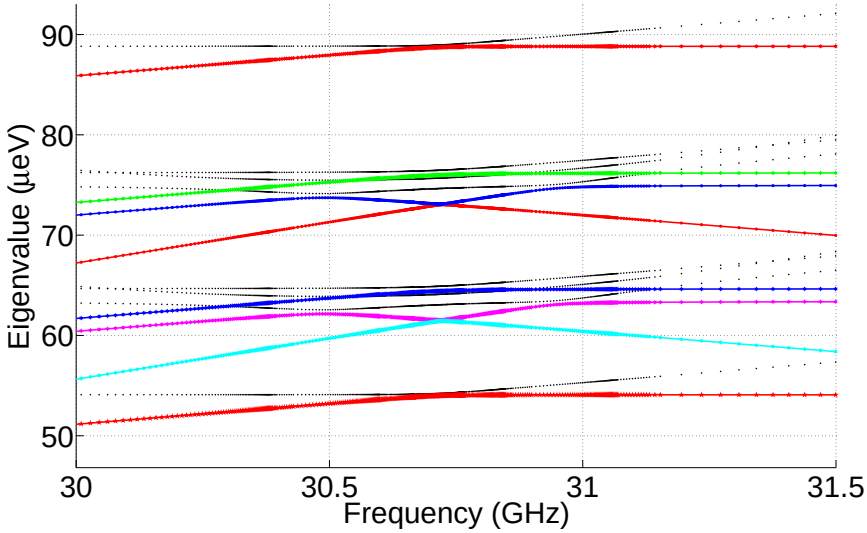

Figure 3.10: Select eigenvalues associated with $\tilde{\boldsymbol{H}}$ for $\omega/2\pi \in [30, 31.5]$ GHz using the field geometry given by Eq. 3.32.

Due to the fact the eigenvalues are typically strong functions of frequency tracking is implemented by predicting its value and derivatives, with respect to frequency, by linear extrapolation. The eigenvalue is selected by minimizing difference between the linearly extrapolated and actual values. The tracking algorithm determines how many derivatives to track per frequency step based on there magnitudes. For slowly varying eigenvalues the addition of derivative predicting is unnecessary, however during interactions it has proven to be invaluable. The frequency step size is calculated per step and is changed to maintain a desired error level associated with the linearly extrapolated values. As can be seen by Figure 3.10 when states strongly interact the step size must be significantly reduced to maintain the track.

The interaction of states can be easily identified by the eigenvalue derivatives with respect to frequency. The second derivative represents the rate of change in the slope and is thus the strongest indicator. The first and second derivatives of the eigenvalues of $\tilde{\boldsymbol{H}}$ in the [30,31.5] GHz frequency range are presented in Figure 3.11. If the interaction is only between two states the second derivatives are equal and opposite in sign, as depicted by Figure 3.11b. In addition the sum of all first and second derivatives within the same s order is constant and zero respectively.

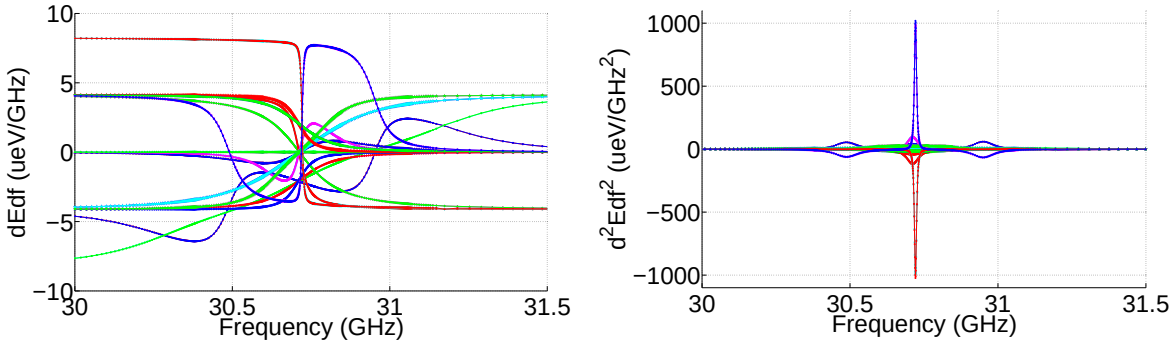

(a) (b)

Figure 3.11: (a) First and (b) second derivatives of the eigenvalues associated with $\tilde{\boldsymbol{H}}$ for $\omega/2\pi \in [30, 31.5]$ GHz using the field geometry given by Eq. 3.32.

As depicted by the presented figures, the tracking process requires small frequency steps and is thus computationally intensive especially for $\triangle\tilde{E} \gg \hbar\omega$. The presented computation required approximately one thousand steps to track the eigenvalues to 20 GHz, resulting in a compute time on the order of minutes. In order to carry the computation down into the MHz range of frequencies requires hundreds of thousands of steps increasing the compute time to formidable levels. In addition for more complex field geometries such as non-parallel magnetic and electric field vectors the state interactions become much stronger further increasing the computational time. Thus to fit the experimental data a fast and efficient method must be developed due to the fact thousands of spectral line profiles are calculated per fit.

In summary time dependent Schrödinger equation given by Eq. 3.12 is reduced to an eigenvalue problem utilizing Floquets theorem and a Fourier series expansion of time periodic coefficients. The corresponding solution is perturbative in the sense that mixing of the magnetic substates only within the n level is allowed. For a non-perturbative solution all discrete and continuous states must be considered. Due to the formidable computation time required to arrive at this solution an approximate method is developed and presented in Section 3.3.3.

3.3.2 Calculation of the Spectral Line Profile

This section presents the calculation of the spectral line profile given the energies and wave functions associated with the upper and lower levels. The spectral line profile is calculated in two steps: first the discrete spectra is found by solving the Schrödinger equation given by Eq. 3.13, second the continuous spectra is generated from the discrete given the broadening mechanisms. The connection operator $\hat{H}$ is the electric dipole approximation of the exact spontaneous emission operator given by

$$\hat{H} \propto \nabla \cdot \bar{\epsilon}\, e^{i\bar{k}\cdot\bar{r}} = \nabla \cdot \bar{\epsilon}\left[1 + i\bar{k}\cdot\bar{r} + ...\right] . \tag{3.40}$$

Where ϵ is the polarization vector of the emitted photon. The electric dipole operator is derived by expanding the exponential of Eq. 3.40 in a Taylor series. Only the first term in the Taylor series expansion is kept and the ∇ operator is replaced with $\bar{r}$, by use of the relationship $-i\hbar\nabla = i\omega m_e \bar{r}$. Only the relative intensity of the spectral line profile is desired thus all constants can be dropped. Although the angular frequency of the emitted photon ω is different for the transitions composing the spectral line profile the variation with respect to the magnitude is insignificant and is thus treated as a constant. Following substitution and truncating after the first term yields

$$\hat{H} \approx \nabla \cdot \bar{\epsilon} \propto \bar{r} \cdot \bar{\epsilon} . \tag{3.41}$$

The electric dipole approximation of the spontaneous emission connection operator is valid for most laboratory plasmas with substantial collisionality [67].

The derivation of the time dependent and time averaged discrete spectral line profiles is presented below. The wave functions $\tilde{\Psi}$ of Eq. 3.12 form a complete set, thus the expansion given by

$$\Theta(t) = \sum_{l=1}^{N} \Gamma_l(t)\tilde{\Psi}_l(t) \tag{3.42}$$

can be made. Where Θ is the wave function associated with the Schrödinger equation, given by Eq. 3.13, describing the perturbed atom undergoing an electronic transition. Substituting Eq. 3.42 into this Schrödinger equation yields

$$i\hbar \sum_{l=1}^{N} \frac{d\Gamma_l}{dt}\tilde{\Psi}_l = \sum_{l=1}^{N} \Gamma_l \hat{H}\tilde{\Psi}_l . \tag{3.43}$$

Eq. 3.43 is multiplied by $\tilde{\Psi}_k^*$ and integrated over all space to arrive at

$$i\hbar \frac{d\Gamma_k}{dt} = \sum_{l=1}^{N} \left\langle \tilde{\Psi}_k \left| \hat{H} \right| \tilde{\Psi}_l \right\rangle \Gamma_l , \tag{3.44}$$

governing the time dependence of the expansion coefficients Γ_k.

The assumption is made that the system is initially in state $\Theta = \tilde{\Psi}_i$. The probability that the system in state i at time τ will by time t transition to state k by emitting a photon is $|\Gamma_k(t)|^2$. The time interval $t - \tau$ is taken to be small compared to the lifetime of the state i such that the solution of Eq. 3.44 can be solved utilizing first order time dependent perturbation theory. The expansion coefficients Γ_k are then written as

$$\Gamma_k(t) = \Gamma_k^0 + \Gamma_k^1(t) + \ldots \quad \text{where} \quad \Gamma_k^0 = \delta_{ki} \,. \tag{3.45}$$

Upon substitution of Γ_k into Eq. 3.44 and equating the first order terms yields

$$\Gamma_k^1(t) = -\frac{i}{\hbar}\int_\tau^t \left\langle \tilde{\Psi}_k \left| \hat{H} \right| \tilde{\Psi}_i \right\rangle dt' \,. \tag{3.46}$$

The wave functions $\tilde{\Psi}_i$ and $\tilde{\Psi}_k$ are given by

$$\tilde{\Psi}_i(t') = \sum_{s=-\tilde{s}}^{\tilde{s}} \sum_{j=1}^{N} c_{ij}^s \Phi_j e^{-i(\tilde{\omega}_i + s\omega)t'} \qquad \text{and} \qquad \tilde{\Psi}_k(t') = \sum_{s=-\tilde{s}}^{\tilde{s}} \sum_{m=1}^{N} c_{km}^s \Phi_m e^{-i(\tilde{\omega}_k + s\omega + \hat{\omega})t'}$$

as defined by Eq. 3.20, where $\hat{\omega}$ is the angular frequency of the emitted photon and $\tilde{\omega}_i = \tilde{E}_i/\hbar$. Performing the integration yields

$$\Gamma_k^1(t) = -\frac{2i}{\hbar}\sum_{j=1}^{N}\sum_{m=1}^{N} \left\langle \Phi_m \left| \hat{H} \right| \Phi_j \right\rangle \sum_{s_1=-\tilde{s}}^{\tilde{s}} \sum_{s_2=-\tilde{s}}^{\tilde{s}} {c_{km}^{s_2}}^* c_{ij}^{s_1} e^{-\frac{i}{2}(\tilde{\omega}_{ik} + (s_1-s_2)\omega - \hat{\omega})(t+\tau)} \cdot \frac{\sin\left(\frac{1}{2}(\tilde{\omega}_{ik} + (s_1-s_2)\omega - \hat{\omega})(t-\tau)\right)}{\tilde{\omega}_{ik} + (s_1-s_2)\omega - \hat{\omega}} \,, \tag{3.47}$$

where $\tilde{\omega}_{ik} = \tilde{\omega}_i - \tilde{\omega}_k$. Taking the magnitude squared of the first order correct expansion coefficient Γ_k^1 yields the transition probability as given by

$$\begin{aligned} \left|\Gamma_k^1(t)\right|^2 = \frac{4}{\hbar^2} &\sum_{j=1}^{N}\sum_{m=1}^{N}\sum_{j'=1}^{N}\sum_{m'=1}^{N} \left\langle \Phi_m \left| \hat{H} \right| \Phi_j \right\rangle \left\langle \Phi_{j'} \left| \hat{H} \right| \Phi_{m'} \right\rangle \\ &\cdot \sum_{s_1=-\tilde{s}}^{\tilde{s}} \sum_{s_2=-\tilde{s}}^{\tilde{s}} \sum_{s_1'=-\tilde{s}}^{\tilde{s}} \sum_{s_2'=-\tilde{s}}^{\tilde{s}} {c_{km}^{s_2}}^* c_{ij}^{s_1} c_{km'}^{s_2'} {c_{ij'}^{s_1'}}^* e^{-\frac{i}{2}(s_1 - s_2 - s_1' + s_2')\omega(t+\tau)} \\ &\cdot \frac{\sin\left(\frac{1}{2}(\tilde{\omega}_{ik} + (s_1-s_2)\omega - \hat{\omega})(t-\tau)\right)}{\tilde{\omega}_{ik} + (s_1-s_2)\omega - \hat{\omega}} \frac{\sin\left(\frac{1}{2}(\tilde{\omega}_{ik} + (s_1'-s_2')\omega - \hat{\omega})(t-\tau)\right)}{\tilde{\omega}_{ik} + (s_1'-s_2')\omega - \hat{\omega}} \,. \end{aligned} \tag{3.48}$$

The transition probability as a function of the emitted photon frequency consists of a series of peaks centered about $\tilde{\omega}_{ik} + (s_1 - s_2)\omega$ having widths of approximately $1/(t-\tau)$. It is assumed that the time $t-\tau$ is much larger then the fundamental period of the electric field such that the peaks are narrow relative to the interpeak spacing ω. In this limit the transition probability can be approximated by

$$\left|\Gamma_k^1(t)\right|^2 \approx \int \sum_{s_1=-\tilde{s}}^{\tilde{s}} \sum_{s_2=-\tilde{s}}^{\tilde{s}} \delta(\tilde{\omega}_{ik} + (s_1-s_2)\omega - \hat{\omega}) S_{ki}^{s_{1,2}}(t) d\hat{\omega} \,. \tag{3.49}$$

Where $S_{ki}^{s_{1,2}}$ is the number of photons emitted by transitions from state $i \rightarrow k$ into the solid angle $d\Omega$ with angular frequency $\hat{\omega} \approx \tilde{\omega}_{ik} + (s_1 - s_2)\omega$ during the time interval $[\tau, t]$ and is given by

$$S_{ki}^{s_{1,2}}(t) = \frac{1}{\hbar^2} \sum_{j=1}^{N} \sum_{m=1}^{N} \sum_{j'=1}^{N} \sum_{m'=1}^{N} \left\langle \Phi_m \left| \hat{H} \right| \Phi_j \right\rangle \left\langle \Phi_{j'} \left| \hat{H} \right| \Phi_{m'} \right\rangle \cdot \sum_{s_1'=-\tilde{s}}^{\tilde{s}} \sum_{s_2'=-\tilde{s}}^{\tilde{s}} c_{km}^{s_2\,*} c_{ij}^{s_1} c_{km'}^{s_2'} c_{ij'}^{s_1'\,*} \frac{e^{-i(s_1 - s_2 - s_1' + s_2')\omega\tau} - e^{-i(s_1 - s_2 - s_1' + s_2')\omega t}}{i(s_1 - s_2 - s_1' + s_2')\omega} \rho(\hat{\omega}) d\Omega \,. \tag{3.50}$$

Where $\rho(\hat{\omega})$ is the density of photon states per steradian. As discussed above when deriving $\hat{H}$ the relative spectral line profile is of interest therefore all constants are dropped including $\rho(\hat{\omega})$. It has been assumed that the time $t - \tau$ is much smaller then the lifetime of the excited state and much larger then fundamental period of the electric field. This implies that the Eq. 3.49 is valid in the limit that the period of the electric field is much smaller then the lifetime of the excited state. The emission intensity per unit solid angle per unit time is given by differentiating the integrand of the transition probability as given by

$$I_{ki}(\hat{\omega}, t) \equiv \frac{d}{d\Omega} \frac{d}{dt} \left[\sum_{s_1=-\tilde{s}}^{\tilde{s}} \sum_{s_2=-\tilde{s}}^{\tilde{s}} \delta(\tilde{\omega}_{ik} + (s_1 - s_2)\omega - \hat{\omega}) S_{ki}^{s_{1,2}}(t) \right].$$

Carrying out the differentiation the time dependent emission intensity for the $i \rightarrow k$ transition is found and is given by

$$I_{ki}(\hat{\omega}, t) \approx \sum_{j=1}^{N} \sum_{m=1}^{N} \sum_{j'=1}^{N} \sum_{m'=1}^{N} \left\langle \Phi_m \left| \hat{H} \right| \Phi_j \right\rangle \left\langle \Phi_{j'} \left| \hat{H} \right| \Phi_{m'} \right\rangle \sum_{s_1=-\tilde{s}}^{\tilde{s}} \sum_{s_2=-\tilde{s}}^{\tilde{s}} \delta(\tilde{\omega}_{ik} + (s_1 - s_2)\omega - \hat{\omega}) \cdot \sum_{s_1'=-\tilde{s}}^{\tilde{s}} \sum_{s_2'=-\tilde{s}}^{\tilde{s}} c_{km}^{s_2\,*} c_{ij}^{s_1} c_{km'}^{s_2'} c_{ij'}^{s_1'\,*} e^{-i(s_1 - s_2 - s_1' + s_2')\omega t} \,. \tag{3.51}$$

The time averaged intensity is obtained by averaging Eq. 3.51 over the electric field period and is given by

$$I_{ki}(\hat{\omega}) \approx \sum_{j=1}^{N} \sum_{m=1}^{N} \sum_{j'=1}^{N} \sum_{m'=1}^{N} \left\langle \Phi_m \left| \hat{H} \right| \Phi_j \right\rangle \left\langle \Phi_{j'} \left| \hat{H} \right| \Phi_{m'} \right\rangle \sum_{s_1=-\tilde{s}}^{\tilde{s}} \sum_{s_2=-\tilde{s}}^{\tilde{s}} \delta(\tilde{\omega}_{ik} + (s_1 - s_2)\omega - \hat{\omega}) \cdot \sum_{s_1'=-\tilde{s}}^{\tilde{s}} \sum_{s_2'=-\tilde{s}}^{\tilde{s}} \delta(s_1 - s_2 - s_1' + s_2') c_{km}^{s_2\,*} c_{ij}^{s_1} c_{km'}^{s_2'} c_{ij'}^{s_1'\,*} \,. \tag{3.52}$$

The time dependent and time averaged discrete spectral line profiles are obtained by summing over all the magnetic substates as given by

$$I_D(\hat{\lambda},t)=\sum_{i=1}^{N}\sum_{k=1}^{N}I_{ki}(\hat{\lambda},t) \tag{3.53}$$

and

$$I_D(\hat{\lambda})=\sum_{i=1}^{N}\sum_{k=1}^{N}I_{ki}(\hat{\lambda}) \tag{3.54}$$

respectively. The units of angular frequency have been converted to wavelength by $\hat{\omega}=2\pi c/\hat{\lambda}$. The matrix elements associated with the electric dipole operator $\langle\Phi_m|\hat{H}|\Phi_j\rangle$ are calculated as outlined in Appendix B with the quantity $e\bar{E}_n$ replaced by the polarization vector $\bar{\epsilon}$.

The polarization vector is calculated based on the observation geometry as given by Figure 3.12, where the radiating atom is located at the origin of the coordinate system.

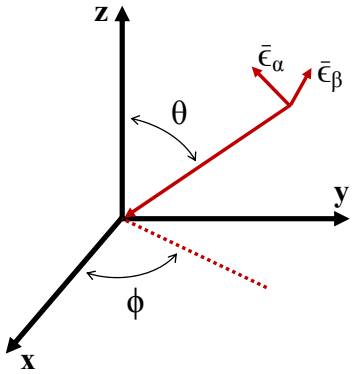

Figure 3.12: Observation geometry and polarization vector coordinate system.

The total emission originating from the atom is unpolarized and isotropic if the magnetic substates are statistically populated. If an observer is viewing the atom along a cord defined by the polar angle θ and the azimuthal angle ϕ the collected emission will be polarized. The polarization vector of the photons propagating along the observation cord is projected into the directions $\bar{\epsilon}_\alpha$ and $\bar{\epsilon}_\beta$ which in addition to the observation cord form an orthogonal set. Due to the orthogonality the product of the two matrix elements must be summed over both vectors as given by

$$\begin{aligned}\langle\Phi_m|\hat{H}|\Phi_j\rangle\langle\Phi_{j'}|\hat{H}|\Phi_{m'}\rangle &= \langle\Phi_m|\bar{\epsilon}_\alpha\cdot\bar{r}|\Phi_j\rangle\langle\Phi_{j'}|\bar{\epsilon}_\alpha\cdot\bar{r}|\Phi_{m'}\rangle \\ &\quad+\langle\Phi_m|\bar{\epsilon}_\beta\cdot\bar{r}|\Phi_j\rangle\langle\Phi_{j'}|\bar{\epsilon}_\beta\cdot\bar{r}|\Phi_{m'}\rangle\ .\end{aligned} \tag{3.55}$$

The vectors $\bar{\epsilon}_\alpha$ and $\bar{\epsilon}_\beta$ are given in terms of the angles associated with the observation cord as given by

$$\bar{\epsilon}_\alpha = -\cos\phi\cos\theta\,\hat{x} - \sin\phi\cos\theta\,\hat{y} + \sin\theta\,\hat{z}$$

$$\bar{\epsilon}_\beta = -\sin\phi\,\hat{x} + \cos\phi\,\hat{y}\ .$$

Typically the angles θ and ϕ are fixed. Thus to take advantage of the spectral line profile dependence on the polarization vector a polarizer is utilized. The polarizing optical element is defined as transmitting along the $\bar{\epsilon}'_\alpha$ and $\bar{\epsilon}'_\beta$ orthogonal directions with transmission coefficients T_1 and T_2 respectively. These new vectors lie in the plane defined by the original, $\bar{\epsilon}_\alpha$ and $\bar{\epsilon}_\alpha$, and are rotated by the angle χ as given in Figure 3.10.

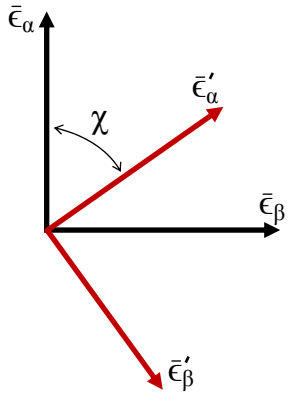

Figure 3.13: Rotation of polarization vector coordinate system.

The product of the two matrix elements must be summed over the rotated vectors:

$$\left\langle \Phi_{j_2}\middle|\hat{H}\middle|\Phi_{j_1}\right\rangle\left\langle \Phi_{j'_1}\middle|\hat{H}\middle|\Phi_{j'_2}\right\rangle = \left\langle \Phi_{j_2}\middle|\bar{\epsilon}'_\alpha\cdot\bar{r}\middle|\Phi_{j_1}\right\rangle\left\langle \Phi_{j'_1}\middle|\bar{\epsilon}'_\alpha\cdot\bar{r}\middle|\Phi_{j'_2}\right\rangle + \left\langle \Phi_{j_2}\middle|\bar{\epsilon}'_\beta\cdot\bar{r}\middle|\Phi_{j_1}\right\rangle\left\langle \Phi_{j'_1}\middle|\bar{\epsilon}'_\beta\cdot\bar{r}\middle|\Phi_{j'_2}\right\rangle\ . \tag{3.56}$$

The new vectors $\bar{\epsilon}'_\alpha$ and $\bar{\epsilon}'_\beta$ are given in terms of the polarizer angle χ and the original vectors:

$$\bar{\epsilon}'_\alpha = T_1\left(\bar{\epsilon}_\alpha\cos(\chi) + \bar{\epsilon}_\beta\sin(\chi)\right)$$

$$\bar{\epsilon}'_\beta = T_2\left(-\bar{\epsilon}_\alpha\sin(\chi) + \bar{\epsilon}_\beta\cos(\chi)\right)\ .$$

For the purposes of this dissertation we define the π components of the spectral line profile such that the polarizer is parallel to the electric field and the σ components of the spectral line such

the polarizer is perpendicular to the electric field, regardless of the orientation of the magnetic field. This is due to the fact that the spectral line profile is not significantly effected by a 1000 Gauss magnetic field given the associated broadening mechanisms.

Due to reasons discussed in Section 3.2 the time averaged spectral line profile is of interest for the experimental measurements and thus only the corresponding theoretical calculations will be presented. Unless otherwise stated the spectral line profile is taken to be time averaged for the remainder of this dissertation. For the purpose of concept development the field geometry given by

$$\bar{B} = 1000\,\hat{z}\ \text{Gauss} \qquad \bar{E}(t) = 5\cos(\omega t)\,\hat{z}\ \text{kV/cm} \tag{3.57}$$

will be considered and applicable to the figures contained within the remainder of the this section. The angular frequency of the electric field is varied depending on the presented figure.

Figure 3.14 gives the discrete spectral line profile at 20 GHz for the π components of the H_β transition as calculated by Eq. 3.54. The frequency was chosen such that the satellite structure could be identified. For the given field geometry seven satellites are present to the left and right of the line center. Each satellite is composed of many transitions at various wavelengths and is due to the fine structure effects and magnetic field.

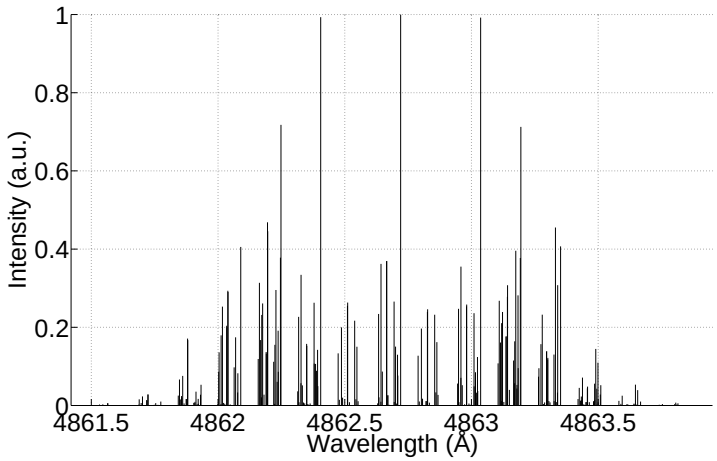

Figure 3.14: Time averaged discrete H_β π profile with a field geometry given by Eq. 3.57 with $\omega = 20$ GHz.

The continuous spectral line profile is obtained by convolving the discrete with both the instrument function of the spectroscopic system and the radiator distribution function. The radiator distribution function is taken to be Gaussian with an arbitrary number of groups as given by

$$I_R(\lambda) = \sum_{i=1}^{N_R} I_{Ri} e^{-\left(\frac{\lambda-\lambda_{Ri}}{\sqrt{2}\sigma_{Ri}}\right)^2} . \tag{3.58}$$

The instrument function is experimentally measured and as will be shown in Section 4.2.2 is accurately represented with a bi-Gaussian function. For the sake of generality the instrument function is represented as a summation of Gaussian functions as given by

$$I_I(\lambda) = \sum_{i=1}^{N_I} I_{Ii} e^{-\left(\frac{\lambda-\lambda_{Ii}}{\sqrt{2}\sigma_{Ii}}\right)^2} . \tag{3.59}$$

The continuous spectral line profile is found by the convolution of $I_D(\hat{\lambda})$ with $I_R(\lambda)$ and $I_I(\lambda)$ as given by

$$I(\lambda) = \int_{-\infty}^{\infty} \int_{-\infty}^{\infty} \left[I_D(\hat{\lambda}) I_R(\Lambda - \hat{\lambda}) d\hat{\lambda} \right] I_I(\lambda - \Lambda) d\Lambda . \tag{3.60}$$

An analytical expression can be obtained for Eq. 3.60 due to the fact the discrete spectrum consists of Dirac delta functions and the radiator distribution and instrument functions are decomposed into a summation of Gaussian functions. Performing the integration yields

$$I(\lambda) = \sum_{i=1}^{N} \sum_{k=1}^{N} \sum_{m=1}^{N_R} \sum_{n=1}^{N_I} I_{ki}(\hat{\lambda}) I_{Rm} I_{In} e^{-\left(\frac{\lambda-\lambda_{Rm}-\lambda_{In}-\hat{\lambda}}{\sqrt{2}\sigma_{mn}}\right)^2} . \tag{3.61}$$

Where the broadening parameter σ_{mn} is given by

$$\sigma_{mn} = \left(\frac{k T_{Rm}}{M_R c^2} \hat{\lambda}^2 + {\sigma_{In}}^2 \right)^{1/2} ,$$

where M_R is the mass of the radiating atom or ion. The radiator distribution function broadening parameter σ_{Ri} is given in terms of the radiator temperature kT_{Ri} associated with the i^{th} group [67].

The continuous and discrete spectral line profiles associated with the π components of the H_β transition are presented in Figure 3.15 and Figure 3.16 for an electric field frequency of 20 and 5 GHz respectively. The discrete spectral line profile is plotted with negative intensities such that the effect of the broadening mechanisms can be seen. The radiator distribution function is taken to be at zero temperature and the instrument function is Gaussian with $\sigma_{I1} = 0.005$ Å. The broadening parameters were chosen such that the satellites would be visual if they were naturally separated.

As was seen in Figure 3.14, which presented only the discrete spectral line profile of Figure 3.15, seven satellites to the left and right of the line center are visible in the continuous spectral line profile. In addition each satellite has a unique structure which becomes more prominent as the broadening parameter is decreased. At 5 GHz the satellites are not separated in either the continuous or discrete

spectral line profile, as shown by Figure 3.16. Here the spread in energy associated with the fine structure effects and magnetic field is greater then the overall satellite spacing $\hbar\omega$, thus resulting in overlap and a non-distinguishable satellite structure.

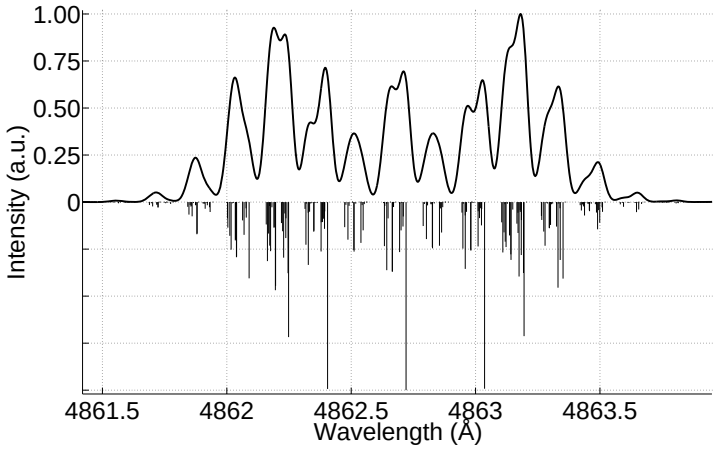

Figure 3.15: Time averaged continuous and discrete H_β π profiles with a field geometry given by Eq. 3.57 with $\omega = 20$ GHz.

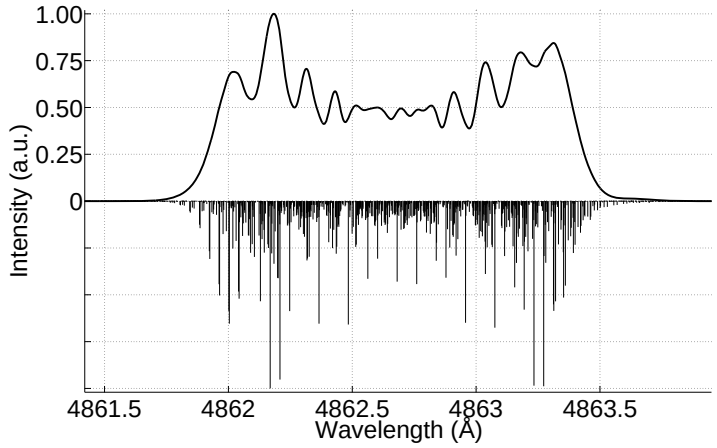

Figure 3.16: Time averaged continuous and discrete H_β π profiles with a field geometry given by Eq. 3.57 with $\omega = 5$ GHz.

As discussed above the separate measurement of the π and σ components of the spectral line profile is expected to increase the certainty in the extracted fit variables. This is due to the fact that the π and σ components are effected differently by the magnetic and electric fields. The H_β and the $5^3D \rightarrow 2^3P$ He I π and σ components of the spectral line profile will be presented for an

electric field frequency of 13.56 MHz. Only a discussion on the differences associated with the π and σ components will be provided here, the overall line shape is discussed in Section 3.5. The expected radiator distribution and instrument function parameters associated with the experimental measurements will be utilized to calculate the continuous spectral line profile and are given in Table 3.3.

Table 3.3: Radiator and instrument parameters.

Parameter	$\mathbf{H_\beta}$	$\mathbf{5^3D \rightarrow 2^3P}$ **He I**
N_R	1	1
I_{R1} (a.u.)	1	1
λ_{R1} (Å)	0	0
kT_{R1} (eV)	1	0

Parameter	$\mathbf{H_\beta}$	$\mathbf{5^3D \rightarrow 2^3P}$ **He I**
N_I	1	1
I_{I1} (a.u.)	1	1
λ_{I1} (Å)	0	0
σ_{I1} (Å)	0.11	0.11

The radiator distribution function is a single temperature for both the H_β and the $5^3D \rightarrow 2^3P$ He I transitions with temperatures of 1 and 0 eV respectively. The instrument function is Gaussian and equivalent for both transitions. Figure 3.17 presents the spectral line profile for the π and σ components of the H_β transition.

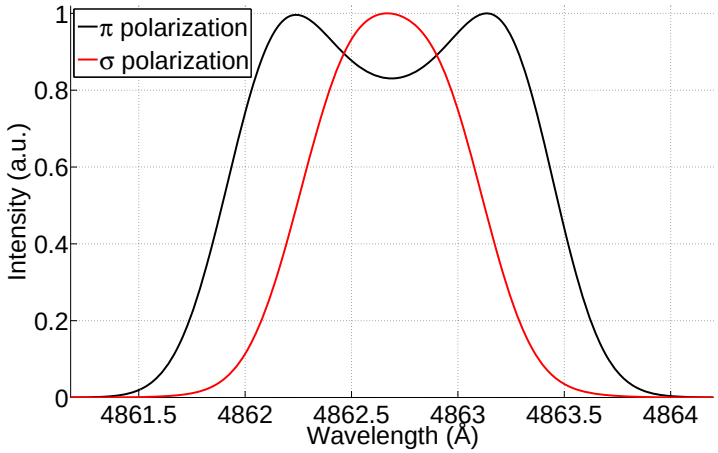

Figure 3.17: π and σ polarization of the H_β spectrum with a field geometry given by Eq. 3.57 at $\omega = 13.56$ MHz.

The magnetic substates associated with the transitions giving rise to the π polarized photons have energies that scale more strongly with the electric field then those of the σ, a factor of 2 for the $n = 4$ level. In fact for all hydrogen-like transitions the π profile is always significantly more effected by the electric field then the σ profile. In terms of the magnetic field the opposite is the case,

those associated with the σ components are more strongly effected. As depicted by Figure 3.17 the difference between the profiles is significant and is thus expected to be a great benefit when fitting the data.

Figure 3.18 presents the spectral line profile for the π and σ components of the $5^3D \rightarrow 2^3P$ He I transition. As was found above, the magnetic substates associated with the π components have energies that scale more strongly with the electric field then those of the σ. The difference in the scaling is much less significant when compared to hydrogen resulting in π and σ profiles with very similar characteristics. As the electric field intensity increases the differences in the profiles become more pronounced. This is due to the fact that the scaling is proportional to the electric field intensity squared where that of hydrogen is linear. Thus for helium-like transitions greater electric field intensities are required for substantial differences in the profiles.

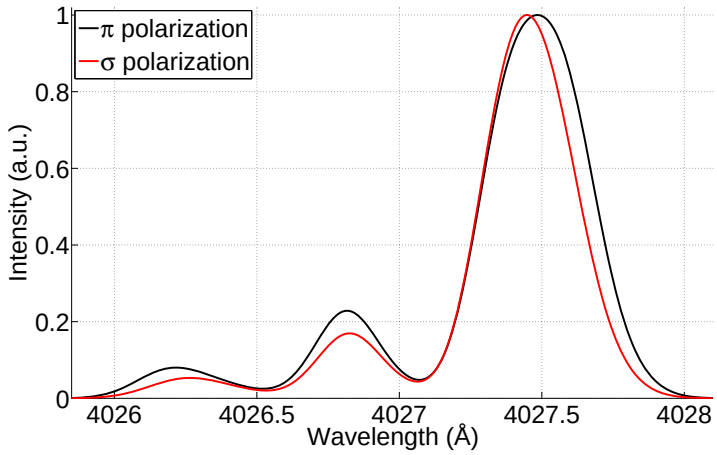

Figure 3.18: π and σ polarization of the $5^3D \rightarrow 2^3P$ He I spectrum with a field geometry given by Eq. 3.57 with $\omega = 13.56$ MHz.

In summary the spectral line profile as calculated by Eq. 3.54 is valid for the lifetime of the excited state τ^* much greater then the period of the electric field waveform τ. The lifetime of the H_β and $5^3D \rightarrow 2^3P$ He I excited states is 33 and 105 ns respectively, both are on the order of the electric field waveform period 74 ns. Thus the validity of this approximation must be addressed. In addition the computational difficulties associated with tracking the eigenvalues of Eq. 3.31 to the MHz range of frequencies is formidable. The validity of our approximation and the extensive computational time required to implement the Floquet method is addressed in the quasistatic approximation of Eq. 3.12 and is presented in the following section.

3.3.3 Quasi-static Approximation

This section presents and explores the validity of the quasi-static solution to the Schrödinger equation given by Eq. 3.12. The quasi-static solution is approximate and valid in the limit that the lifetime of the excited state is much less then the period of the electric field waveform: $\tau^* \ll \tau$. As discussed above the Floquet method is exact, ignoring truncation error, and is thus valid regardless of this ordering. It is in the approximation of the transition probability given by Eq. 3.49 which is invalidated in this limit. Additionally, regardless of the above this approximation is valid in the limit that the dominate spectral broadening parameter is much greater then the satellite spacing.

Solving the Schrödinger equation given by Eq. 3.12 in the MHz range of frequencies utilizing the Floquet method is unrealistic due to the immense computationally time required to calculate and track the eigenvalues. Therefore, to explore solutions significantly less computational intensive the quasi-static approximation is investigated. This approximation is made by a time discretization of the Hamiltonian $\tilde{H}(t)$ resulting in the set of non-coupled time independent Schrödinger equations

$$i\hbar\frac{\partial\tilde{\Psi}}{\partial t} = \tilde{H}(t_d)\tilde{\Psi} \qquad t_d \in [0,\tau] \quad \text{for} \quad d = [1, N_D]\,. \tag{3.62}$$

The time periodic Hamiltonian $\tilde{H}(t)$ is discretized evenly over N_D cells within a period of the electric field waveform. The only time dependent quantity associated with $\tilde{H}(t)$ is the electric field. Therefore the discretization is completely carried out by discretizing the electric field waveform as presented in Figure 3.19. The solid line is the exact waveform while the markers indicate the discretized values.

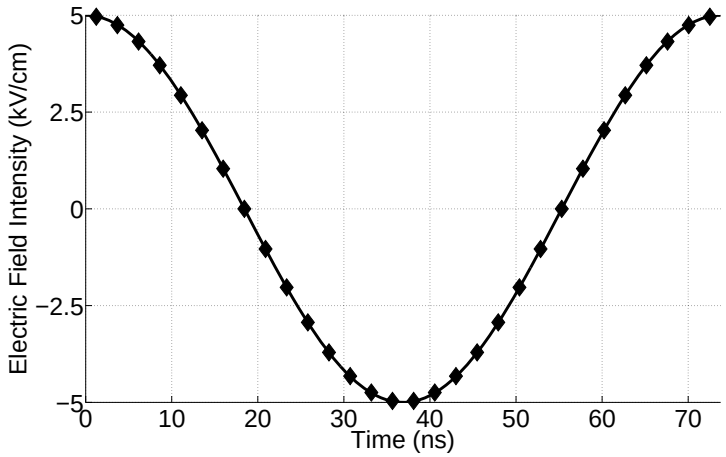

Figure 3.19: Discretization of electric field waveform for the quasi-static approximation of $\tilde{H}(t)$.

The quasi-static approximation is interpreted as the limit in which the quantum states respond instantaneously to the time dependent perturbations. As such, these states at any point in time are

approximated by the solution of the time independent Schrödinger equation associated with the instantaneous values of the time dependent quantities. The discretized Schrödinger equation of Eq. 3.62 is therefore representative of the system at time t_i under the influence of a static electric field given by $\bar{E}(t_i)$. However, it should be noted that this approximation of the quantum states at time t_i is not representative of the exact obtained utilizing the Floquet method, in fact the differences can be quite extreme. The quasi-static solution is not meant to approximate the energy and wave function of the quantum states but only the dominant transition probabilities. Thus it is only in the calculation of the continuous spectral line profile that the quasi-static solution is accurate.

The set of N_D time independent Schrödinger equations are solved in a similar manner to that presented in Section 3.3.1 resulting in a reduction to a set of eigenvalue problems as given by

$$\tilde{\boldsymbol{H}}^d \tilde{\boldsymbol{\Psi}}_k^d = \tilde{E}_k^d \tilde{\boldsymbol{\Psi}}_k^d \,. \tag{3.63}$$

Where the instantaneous Hamiltonian $\tilde{\boldsymbol{H}}^i$ at time t_i is given by

$$\tilde{\boldsymbol{H}}^d = \begin{bmatrix} E_1 + E_{11}^B + E_{11}^{E^d} & \cdots & E_{N1}^B + E_{N1}^{E^d} \\ \vdots & \ddots & \vdots \\ E_{1N}^B + E_{1N}^{E^d} & \cdots & E_N + E_{NN}^B + E_{NN}^{E^d} \end{bmatrix}$$

having eigenvectors $\boldsymbol{\Psi}_k^i$ given by

$$\boldsymbol{\Psi}_k^d = \begin{bmatrix} c_{k1}^d \Phi_1 \\ \vdots \\ c_{kN}^d \Phi_N \end{bmatrix} .$$

The matrix elements $E_{jm}^{E^d}$ associated with the instantaneous electric field $\bar{E}_d$ are given by

$$E_{jm}^{E^d} = \langle \Phi_m | H^{E^d} | \Phi_j \rangle \,. \tag{3.64}$$

The matrix elements are calculated utilizing the procedure given in Appendix B, substituting for the approximate Hamiltonian H^{E^i} as given by

$$H^{E^d} = e\,\bar{E}(t_d) \cdot \bar{r} \,.$$

Following the calculation of the matrix elements of $\tilde{\boldsymbol{H}}^d$ the N eigenvalue and eigenvector pairs, $\tilde{E}_k^d$ and $\tilde{\boldsymbol{\Psi}}_k^d$ respectively, associated with each of the N_D Schrödinger equations can be found. Utilizing the method presented in Section 3.3.2 with the appropriate eigenvalue and eigenvector pairs the emission intensity of the $i \rightarrow k$ transition at time t_d can be calculated and is given by

$$I_{ki}^{d}(\hat{\omega}) \approx \delta(\tilde{\omega}_{lk}^{d} - \hat{\omega}) \sum_{j=1}^{N} \sum_{m=1}^{N} \sum_{j'=1}^{N} \sum_{m'=1}^{N} \left\langle \Phi_m \left| \hat{H} \right| \Phi_j \right\rangle \left\langle \Phi_{j'} \left| \hat{H} \right| \Phi_{m'} \right\rangle \; c_{km}^{d\,*} c_{ij}^{d} c_{km'}^{d} c_{ij'}^{d\,*} \,. \tag{3.65}$$

The time dependent discrete spectral line profile is obtained by summing over all magnetic substates as given by

$$I_D(\hat{\lambda}, t_d) \approx \sum_{i=1}^{N} \sum_{k=1}^{N} I_{ki}^{d}(\hat{\lambda}) \,. \tag{3.66}$$

That of the time averaged is obtained by performing the same summation in addition to summing over the set of N_D time discretized solutions. The time averaged discrete spectral line profile as given by

$$I_D(\hat{\lambda}) \approx \sum_{i=1}^{N} \sum_{k=1}^{N} \sum_{d=1}^{N_D} I_{ki}^{d}(\hat{\lambda}) \,. \tag{3.67}$$

Where the units of angular frequency have been converted to wavelength by $\hat{\omega} = 2\pi c / \hat{\lambda}$.

The discrete spectral line profiles given by Eq. 3.66 and Eq. 3.67 have no physical significance due to the fact that the energy and wave function of the quantum states are inaccurate. Additionally, when $\tau^* \leq \tau$ the transition probability becomes continuous and can no longer be approximated as a series of delta functions as given by Eq. 3.49. Therefore in this limit the discrete spectral line profile becomes continuous autonomously. Thus, only when the discrete is convolved with the radiator distribution and instrument functions is a physically significant profile gained. In the limit that $\tau^* \ll \tau$ the continuous spectral line profile obtained utilizing the quasi-static approximation is found to be accurate where that associated with the Floquet method is not.

To explore the possibility of the quasi-static solution yielding accurate estimates of the continuous spectral line profile regardless of the ordering of τ^* and τ the quasi-static solution was compared to that obtained utilizing the Floquet method. Figure 3.20 presents the quasi-static solution plotted with that obtained utilizing the Floquet method at various frequencies with a field geometry given by Eq. 3.57. The discrete spectral line profile was calculated utilizing Eq. 3.54 and Eq. 3.67 for the Floquet method and the quasi-static approximation respectively, with the continuous calculated by Eq. 3.60. The expected radiator distribution and instrument function parameters associated with the experimental measurements were utilized as given by Table 3.3. The quasi-static solution is independent of frequency and only depends on the magnitudes and phase angles associated with the harmonic spectrum of the electric field waveform. In contrast the solution obtained utilizing the Floquet method is in addition to the mentioned parameters dependent on the frequency.

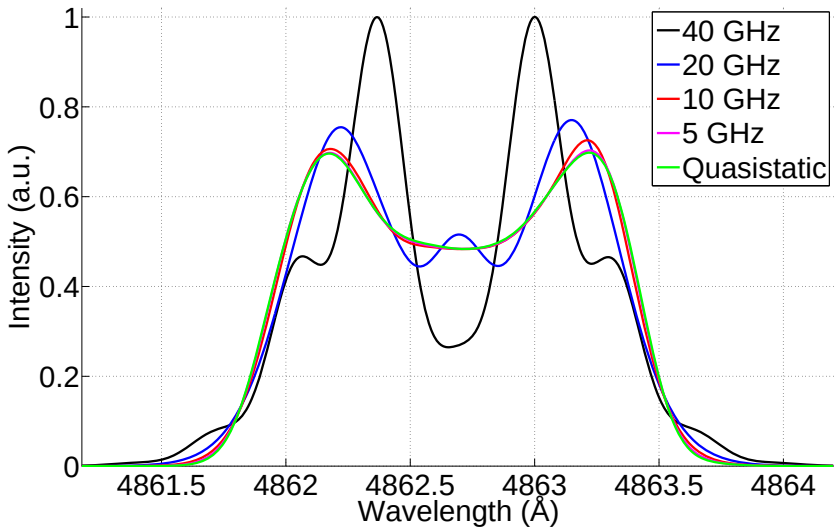

Figure 3.20: Comparison of the quasi-static solution with that of the Floquet method at various frequencies for the H_β π profile with a field geometry given by Eq. 3.57.

As depicted by Figure 3.20 the continuous spectral line profile obtained utilizing the Floquet method converges to that of the quasi-static approximation as the frequency is decreased. For the case under consideration the convergence is nearly complete at 5 GHz, thus regardless of the ordering of τ^* and τ both methods will result in the same solution for frequencies below 5 GHz. The convergence of these methods is purely based on the broadening parameter magnitudes of the radiator distribution and instrument functions. The profile associated with the Floquet method always has a satellite-like structure where the visibility of this structure depends on the ordering of the dominant broadening parameter σ and the spacing of the satellites. In the limit that σ is much greater then the satellite spacing

$$\sigma \gg \left| \hat{\lambda} - \frac{2\pi c}{\hat{\omega} \pm \omega} \right| \tag{3.68}$$

the structure is completely removed by the broadening mechanisms and the profile converges to that of quasi-static approximation.

The convergence of the profiles is completely contingent of the broadening mechanisms removing the satellite structure due to the fact that the quasi-static solution is incapable of producing such a structure. The value of ω at which this convergence takes place is dominated by the broadening mechanisms but is also dependent on both the magnetic and electric field vectors and the quantum states associated with electronic transition. For the frequency in which this work is concerned, 13.56 MHz, the spectral line profiles of interest have converged given the spectroscopic instrument function regardless of the radiator distribution function. Thus the quasi-static approximation is

utilized exclusively when fitting the experimental data.

In summary the quasi-static solution to the Schrödinger equation given by Eq. 3.12 is only appropriate for the calculation of the continuous spectral line profile in either of the following two limits. The first states that the lifetime of the exited state must be much less then the period of the electric field waveform: $\tau^* \ll \tau$. The Floquet method always yields exact solutions to the Schrödinger equation, ignoring truncation error, but in this limit the associated spectral line profile as calculated in Section 3.3.2 is inaccurate. The second states that the broadening parameters must be much greater then the satellite spacing as given by Eq. 3.68. In this limit both the quasi-static approximation and the Floquet method yield the same continuous spectral line profile. Typically the quasi-static calculation requires significantly less computational time, by orders of magnitudes, and is thus preferred if applicable.

3.4 Spectral Line Profile Fitting

This section presents the methodology utilized to fit the theoretical to the experimental spectral line profile. In order to conduct the fit an algorithm was devised and a program was written, this section contains the details associate with that work. The fitting algorithm is based on minimizing the reduced χ statistical parameter given by

$$\chi = \left[\frac{1}{N_P - 1} \sum_{i}^{N_P} \left[W_{Ei} \frac{I_i - I_{Ei}}{\sigma_{Ei}} \right]^2 \right]^{1/2} . \tag{3.69}$$

Where N_P is the number of experimental data points, I_i is the intensity of the i^{th} theoretical data point, and W_{Ei}, I_{Ei} and σ_{Ei} are the weight, intensity and standard deviation associated with the i^{th} experimental data point. The reduced χ was formulated to allow for weighting of individual data points through the parameter W_{Ei}. This allows for emphasis to be placed on various parts of the spectral line profile. The weights are normalized such that

$$\sum_{i}^{N_P} \frac{N_P}{W_{Ei}} = 1 .$$

This is done to ensure the absolute value of χ maintains its significance. The ideal value of χ is unity indicating a perfect fit, values much greater and less then unity indicate an underdetermined and overdetermined model respectively.

The fitting algorithm implements a brute force method in which the entire space associated with the fit variables is discretized evenly within each dimension. The algorithm methodology is as follows: the χ associated with each point in the discretized space is calculated, the point in which the minima occurs is selected. The boundaries associated with the space are then reduced to those

points adjacent to the selected point. The new space is then discretized and the χ at each point is calculated in which the minimum value is again taken. This process is iterated until the desired precision in the fit variables is achieved. Figure 3.21 gives a schematic of the fit process implemented by the algorithm for a one dimensional space consisting of the fit variable E_0, three iterations are carried out.

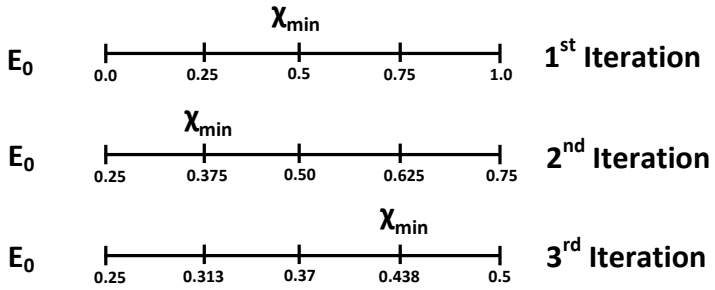

Figure 3.21: Schematic of fit algorithm method.

The precision of the algorithm associated with the i^{th} fit variable is taken as the cell width associated with the corresponding dimension in the discretized space and is given by

$$\sigma_i = \frac{B_{2i} - B_{1i}}{N_{Di}} \left(\frac{2}{N_{Di}} \right)^{N_{IT}-1} . \tag{3.70}$$

Where B_{1i} and B_{2i} are the boundaries of the i^{th} fit variable, N_{Di} is the degree of discretization for the i^{th} fit variable, and N_{IT} is the number of iterations. The number of iterations is typically selected such that the uncertainty in the fitted variable is dominated by the spectral noise and not Eq. 3.70. Typically for problems having a space with high dimensionality gradient based methods utilizing global search algorithms are implemented [119]. Therefore, along with the presented brute force algorithm these methods were pursued but dismissed because the computational time was not significantly decreased. In addition these elaborate methods do not search the entire space and can potentially be trapped in a local minima. The brute force algorithm searches the entire space and is therefore guaranteed to located the global minimum given adequate discretization. It was found that this problem has a large number of local minima and thus revealing the logic behind the algorithm selection.

The fitting of the spectral line profiles must be conducted in a two tier process due to the presence of spectral noise and because the measured data is pixelated. The minimization algorithm discussed above is implemented in both tiers. In the first tier the algorithm is implemented on the fit variables associated with the physical quantities, such as the electric field parameters E_i and θ_i. Thus a theoretical spectral line profile must be calculated for each point in this discretized space. In

order to calculate the associated χ implementation of the minimization algorithm at a second tier level is required. In this tier the experimental and theoretical spectral line profiles are fit by shifting and scaling the experimental data. Once the minimization algorithm is complete in the second tier the χ is assigned to the specific point in the discretized space associated with the physical quantities in the first tier. Therefore the sole purpose of the second tier is to determine the most appropriate χ given the theoretical spectral line profile.

There are two fit variables in the second tier S_H and S_V corresponding to shifting of the wavelength, the horizontal axis, and scaling of the intensity, the vertical axis, respectively. The discretization parameters and the number of iterations associated with the second tier minimization is constant for all fitting presented in this dissertation and are given in Table 3.4.

Table 3.4: Second tier discretization parameters and uncertainty.

Parameter	$\mathbf{S_V}$	$\mathbf{S_H}$
N_D	10	10
B_1	93.0 %	-0.1 Å
B_2	107.0 %	0.1 Å
σ	0.011 %	0.016 Å

The second tier implementation of the minimization algorithm is required due to the spectral noise and pixelation. The presence of spectral noise inhibits accurate normalization of the experimental data and as such requires determination through the scaling fitting parameter S_V. Accurate wavelength calibration becomes formidable on the order of and less then the pixel width. Thus pixelation necessitates that the absolute wavelength calibration of the experimental data be carried out through the shifting fitting parameter S_H.

The experimental spectral line profile is measured at discrete points according to the pixels associated with the CCD. If the CCD has a pixel width of $\Delta\lambda_P$ then the intensity associated with i^{th} pixel is given by the integral

$$I_{Ei} = \int_{\lambda_{Pi}-\Delta\lambda_P}^{\lambda_{Pi}+\Delta\lambda_P} I_E(\lambda) d\lambda \,. \tag{3.71}$$

Where λ_{Pi} is the wavelength associated with the i^{th} pixel. In order to develop the data fitting concepts a typical experimentally determined spectra line profile is presented. The data selected was obtained in the RF sheath immediately adjacent to the RF biased electrode where the electric field is expected to be at a maximum. The fit was conducted and the electric field and radiator distribution function parameters were determined. Figure 3.22 presents the H_β π and σ spectral

line profiles giving the error associated with each pixelated intensity.

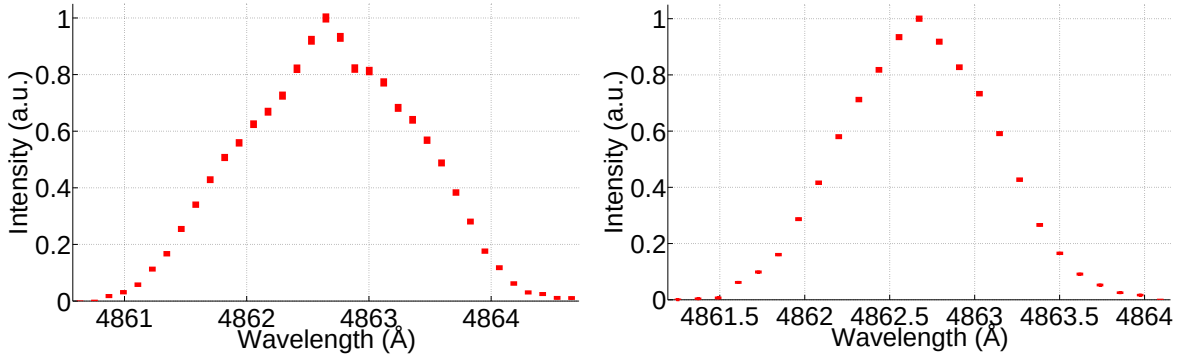

(a) (b)

Figure 3.22: Experimental H_β (a) π and (b) σ spectral line profiles.

To calculate χ the theoretical profile must first be pixelated by application of Eq. 3.71. The continuous and pixelated theoretical H_β π and σ spectral line profiles are presented in Figure 3.23. The electric field and radiator distribution function parameters determined from the fit to the experimental profiles presented in Figure 3.22 were used in this calculation.

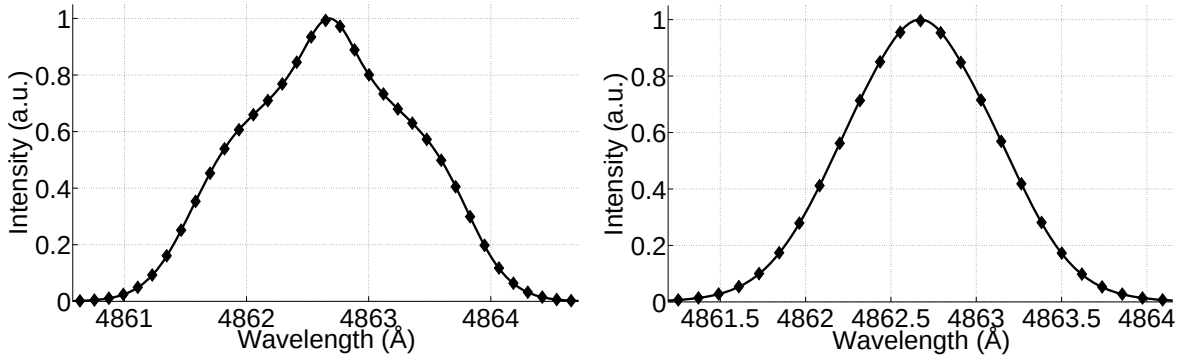

(a) (b)

Figure 3.23: Continuous and pixelated theoretical H_β (a) π and (b) σ spectral line profiles.

Typically the pixelated values are very similar to the continuous, as seen by Figure 3.23. Only when the spectral features are on the order of a pixel width do noticeable differences occur. Given the appropriate values of the electric field fit variables the discrete theoretical spectral line profile is calculated by Eq. 3.66 and Eq. 3.10 if the emission intensity is time dependent and by Eq. 3.67 if it is not. The continuous profile is calculated by Eq. 3.60 utilizing the radiator distribution function fit variables values. The fit variable values used to calculate the discrete and continuous profiles are

determined by the first tier minimization algorithm.

The second tier minimization algorithm requires pixelation of the theoretical spectral line profile for each value of the shift fit variable. This is due to the fact that the grid over which the pixelation occurs is being altered. Applying the second tier minimization algorithm to the experimental and theoretical spectral line profiles given in Figure 3.22 and Figure 3.23 respectively results in scaling and shifting fit variables with values given by Table 3.5. The fitted profiles are presented in Figure 3.24. As discussed above the π and σ profiles are fit together as an object. This is carried out by minimizing the summation of the χ's associated with the two spectral line profiles. The specific model utilized to fit the H_β and $5^3D \rightarrow 2^3P$ He I spectral line profiles will be discussed in detail in Section 5.4. Table 3.6 provides a list of the possible fit variables associated with the physical quantities of the first tier minimization.

Table 3.5: Second tier fit results associated with the spectral line profiles presented in Figure 3.24.

	π **profile**	σ **profile**
S_H	-0.024 Å	-0.022 Å
S_V	103.6 %	100.9 %
χ	1.41	1.17

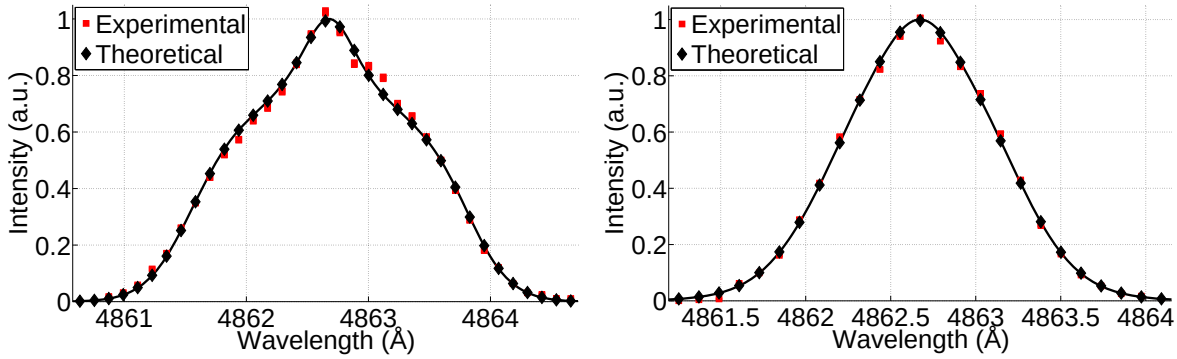

(a) (b)

Figure 3.24: Fitted experimental and theoretical H_β (a) π and (b) σ spectral line profiles.

As given by Eq. 3.5 the electric field is modeled as a Fourier cosine series having N_H harmonics. The number of harmonics that can be accurately determined by the spectral line fitting program will be discussed in Section 5.4. The radiator distribution function is modeled as a two temperature Maxwellian. The electric field is perpendicular to the line of sight thus the Doppler shift is assumed

to be negligible and therefore is not included as a fit variable. Only the intensity associated with the second radiator distribution function group is a fit variable because the data is normalized.

Table 3.6: Available first tier fit variables.

Fit Variable
E_0 to E_H
θ_1 to θ_H
kT_{R1} to kT_{R2}
I_{R2}

The electric field parameter θ_1 does not have a unique value unless the emission intensity is a function of time. This is due to the fact that the electric field waveform is determined from a time averaged quantity. If the emission intensity is a function of time then its measurement must be made in order to calculate the time averaged spectral line profile as given by Eq. 3.10. The measured emission intensity waveform is intrinsically correlated to that of the electric field through the unknown parameter θ_1. Therefore it is only when the emission intensity is time dependent that a unique value of θ_1 can be determined.

As discussed above the quasi-static method is utilized to calculated the spectral line profile. The electric field and emission intensity waveforms associated with the fit presented in Figure 3.24 are given in Figure 3.25. The markers and dashed lines indicate the locations at which the waveforms were discretized, the value of N_D was 30.

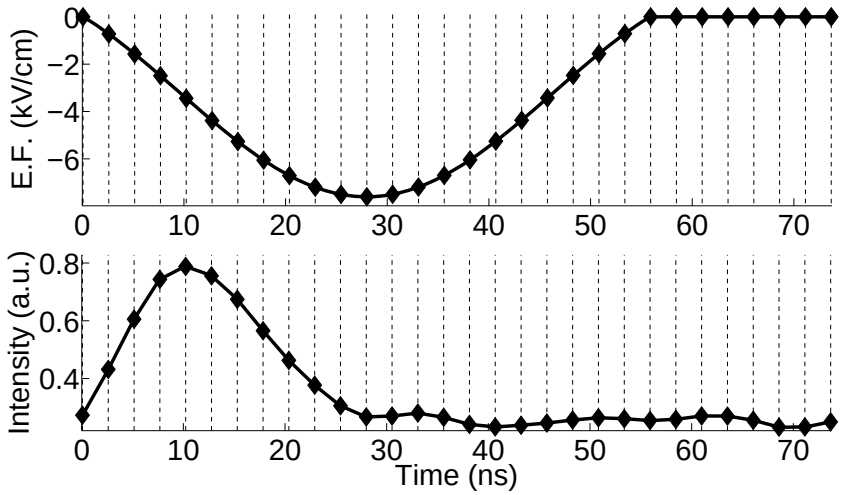

Figure 3.25: Electric field and H_β emission intensity waveforms associated with the fit presented in Figure 3.24.

The modern CPU contains multiple cores and thus makes hardware implementation of parallel processing trivial. The spectral line fitting program was written in light of this to take advantage of the CPU's parallel computing capabilities. The most time consuming fit variables to search through are those of the electric field parameters. As such the space associated with these variables is distributed evenly to the available parallel processing nodes, typically eight for the fitted data presented in this dissertation. The space associate with the remaining fit variables is distributed to all nodes and is searched through in serial.

The electric field fit variables are the most time consuming to search through because at each discretized point in the space a new discrete spectral line profile must be calculated. Therefore to further decrease the computation time a library was formulated containing the discrete π and σ spectral line profiles of the H_β and $5^3D \rightarrow 2^3P$ He I transitions. The library contains profiles associated with static electric field intensities of 0 to 20 kV/cm in 5.0 V/cm steps. The fitting algorithm calls the profile associated with the static electric field having a value closest to that of the discretized electric field waveform. A call to the library greatly reduces the computation time due to the fact a discrete spectral line profile requires a couple seconds to compute.

In summary the fitting program implements a brute force algorithm in a two tier scheme to fit the theoretical spectral line profile to that of the experimental. The minimization algorithm is deemed a brute force method due to the fact the entire space associated with the fit variables in searched. This was found to be required due to the large number of local minima associated with the quantity χ being minimized. Additionally a two tier process was required due to spectral noise and pixelation of the experimental data.

3.5 Electronic Transition Selection

This section presents the sensitivity of a selected group of hydrogen and helium electronic transitions on the simplified electric field associated with an RF sheath. The group of transitions were selected based on those available for observation utilizing passive OES in the visible range of the spectrum. The logic behind the selection of the H_β and $5^3D \rightarrow 2^3P$ He I transitions for the focus of this research will be discussed.

The accuracy of the extracted electric field fit variables is increased with the number of spectral line profiles able to be fit simultaneously as an object. As discussed in Section 3.2 this is to be achieved by the measurement of the π and σ polarized emission independently, therefore both profiles will be presented below for each investigated transition. Due to the anticipated long integration times required to achieve an adequate signal to noise ratio, selection of an optimal transition is critical for the successful application of this diagnostic. The transition was selected based on two criteria: the sensitivity to the electric field and the magnitude of the emission intensity. The sensitivity of the transition on the electric field increases with both the n of the upper and lower levels. To first

order the scaling is linear and quadratic with the electric field magnitude for hydrogen and helium respectively in the absence of a magnetic field. The emission intensity of the transition decreases exponential with the quantum state energy and therefore increasing n [67]. Thus a transition will be chosen by maximizing the n of both the upper and lower levels such that an adequate signal to noise ratio can be achieved within the desired integration time on the order of minutes. The transition sensitivity to the electric field is explored theoretically utilizing the developed atomic theory presented in Section 3.3. The emission intensity of the transitions of interest are explored experimentally.

The electric field waveform utilized for the modeling presented in this section is taken to have a harmonic spectrum with $N_H = 1$ and a frequency of $\omega/2\pi = 13.56$ MHz. The magnitude of the DC component E_0 and the first harmonic E_1 are equivalent which to first order approximates the electric field of the capacitively coupled RF sheath [98]. The transitions are modeled for two electric field waveforms:

$$\bar{E}_L(t) = 0.5 + 0.5\cos(\omega t)\,\hat{z} \text{ kV/cm} \qquad \text{and} \qquad \bar{E}_H(t) = 5 + 5\cos(\omega t)\,\hat{z} \text{ kV/cm}$$

having low and high intensities respectively. The magnetic field is taken to have only a z component with a magnitude of 1000 Gauss.

The magnitude associated with the components of the electric field waveform $\bar{E}_L(t)$ was selected to represent the desired minimum obtainable from a fit to the spectral profiles. A systematic error analysis was conducted and presented in Section 5.4.1, the results of which determined this value. The radiator distribution and instrument functions are taken to be representative of those associated with the experimental measurements. The radiator distribution function is modeled as a one temperature Maxwellian and the instrument function is taken to be Gaussian, the parameters are given in Table 3.3.

3.5.1 Hydrogen

Hydrogenic transitions are an obvious candidate for implementation of this diagnostic for multiple reasons. First, hydrogen is readily available and its isotopes are the fuel gas for typical thermonuclear reactors. Second, the electric field perturbs the electronic structure of hydrogen more strongly then any other atom. Third, the effect is relatively easy to quantify with high precision due to the fact the wave functions are the only known analytically. The first three Balmer series transitions are of interest H_α ($n = 3 \rightarrow 2$), H_β ($n = 4 \rightarrow 2$), and H_γ ($n = 5 \rightarrow 2$). These transition were selected due to the fact they occur in the visible range of the spectrum and have the largest upper level value of n with measurable intensities. The π and σ spectral line profiles associated with an electric field given by $\bar{E}_L(t)$ and $\bar{E}_H(t)$ are given by Figure 3.26, Figure 3.27, and Figure 3.28 respectively.

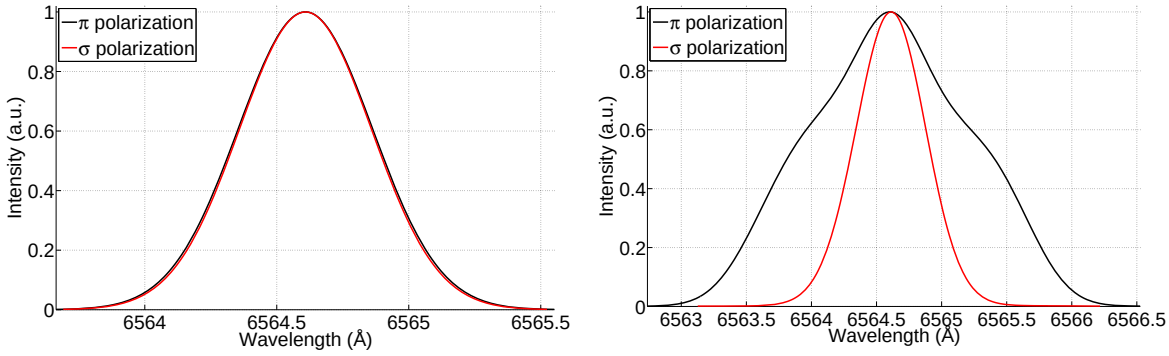

(a) (b)

Figure 3.26: H_α spectral line profile associated with an electric field given by (a) $\bar{E}_L(t)$ and (b) $\bar{E}_H(t)$.

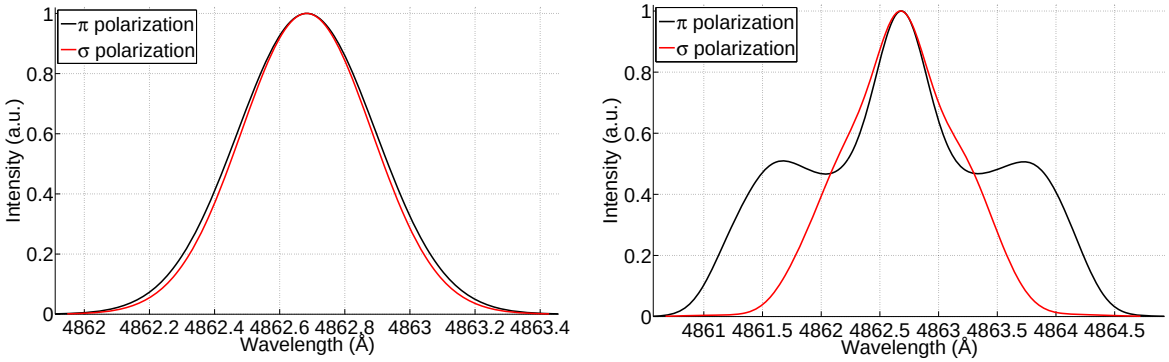

(a) (b)

Figure 3.27: H_β spectral line profile associated with an electric field given by (a) $\bar{E}_L(t)$ and (b) $\bar{E}_H(t)$.

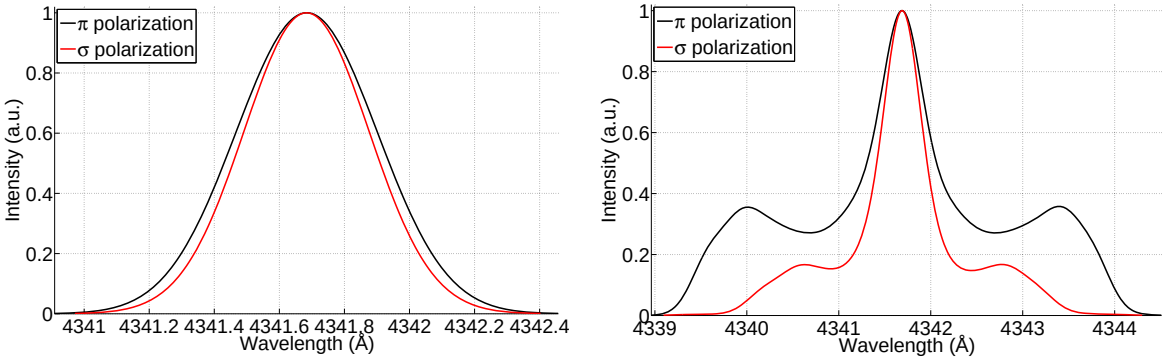

(a) (b)

Figure 3.28: H_γ spectral line profile associated with an electric field given by (a) $\bar{E}_L(t)$ and (b) $\bar{E}_H(t)$.

In the presence of a static electric field the profile associated with the Balmer series transitions undergoes a relatively symmetric splitting. This is due to the fact that the magnetic substates within a given n level are nearly degenerate. As the broadening parameters are decreased the symmetry becomes completely broken. For both the π and σ profiles of the H_β transition a doubly peaked profile is formed if the electric field magnitude is intense enough. The same result is also found for the π profile of the H_α and H_γ transitions. However an additional feature is present in the σ profile of these transitions. Here an intense component unaffected by the electric field is present resulting in a triply peaked profile about the line center. For the H_α transition this component dominates the spectrum leaving the σ profile essentially unaffected by the electric field.

The quasi-static approximation is utilized for the calculation and thus the profiles are arrived at by averaging over those obtained in the presence of a static electric field. The values of which are determined by a discretization of the waveform. Therefore following the description of the static electric field effect the waveform $\bar{E}_H(t)$ would produce a triply peaked profile about the line center. Where the peak at the line center is either completely or partly due to the fact that the electric field waveform spends an appreciable amount of time near zero. As seen by Figure 3.26 through Figure 3.28 only the π profile of H_β and the π and σ profile of H_γ portray this structure, the remaining profiles require a much stronger electric field. The symmetric splitting of the Balmer series transitions can be easily masked by thermal broadening, especially at low electric field intensities such as $\bar{E}_L(t)$. However, measurement of the polarizations independently can be a substantial deterrent. This is due to the fact that the π profiles are significantly more effected by the electric field then those of the σ, as discussed in Section 3.3.2. Therefore this measurement is an excellent indication of the presence of an electric field in addition to increasing the certainty in the fit variables.

Comparing Figure 3.26 through Figure 3.28 it is seen that the H_α profiles have the weakest dependence on the electric field. As discussed above this is due to the fact the upper level n value is the smallest. Therefore either the H_β or H_γ transition will be utilized depending on there emission intensity. It was found experimentally that the H_γ spectral line profile has an unacceptable signal to noise ratio given the allocated integration time. Thus the H_β transition was selected for the development of this diagnostic in hydrogen discharges.

3.5.2 Helium

Due to the fact that the electric field perturbs the profile of hydrogenic transitions almost symmetrically an additional transition was investigated. That of a neutral helium was chosen for the reasons stated below. First, while only found in thermonuclear reactors as a by product of fusion helium gas injectors have been developed and implemented for various diagnostics. Second, the electric field perturbs the spectral line profile highly asymmetrically. Third, for the electronic transitions of interest the wave functions can be accurately represented by those of hydrogen as discussed in

beginning of Section 3.3. The following three neutral helium transitions are of interest $4^1D \rightarrow 2^1P$, $5^1D \rightarrow 2^1P$, and $5^3D \rightarrow 2^3P$. These transition were selected due to the fact they occur in the visible range of the spectrum and have the largest upper level value of n with measurable intensities. The π and σ spectral line profiles associated with an electric field given by $\bar{E}_L(t)$ and $\bar{E}_H(t)$ are given by Figure 3.29, Figure 3.30, and Figure 3.31 respectively.

The electron-electron interaction in the helium atom removes the near degeneracy seen within hydrogen for a given n level. Therefore, the neutral helium spectral line profiles of interest do not experience a splitting but instead forbidden transitions are allowed and the wavelength of the line center is shifted. The result is a multi-peaked profile which is highly asymmetric.

Due to the fact the quasi-static approximation is utilized to calculate the line profiles a description of the effect of the static electric field on the spectral line profile will aid in understanding the effect of a dynamic electric field. In the presence of a static electric field the line center of all investigated He I transitions is shifted to the red. Additionally forbidden transitions are allowed and appear on blue side of the line center. Specifically, for the $4^1D \rightarrow 2^1P$ He I transition two peaks appear, for the $5^1D \rightarrow 2^1P$ He I transition three peaks appear, and for the $5^3D \rightarrow 2^3P$ He I transition two peaks appear. These peaks associated with the forbidden transitions always have intensities less then that of the line center for electric field intensities of interest ≤ 15 kV/cm. In addition the intensities are all functions of the electric field intensity while the same is true for the wavelengths some of the transitions have only a weak dependence. The far blue peak of the $4^1D \rightarrow 2^1P$ He I transition has a very low intensity for this field strength and is not of interest. The remaining peak is stationary in terms of wavelength. For the $5^1D \rightarrow 2^1P$ He I transition only the middle peak has a wavelength that is dependent on the electric field magnitude, the other two peaks are approximately stationary in terms of wavelength. For the $5^3D \rightarrow 2^3P$ He I transition the far blue peak the wavelength is dependent on the electric field intensity while the remaining is not.

The previous description of the static electric field effect allows for that of the waveform $\bar{E}_H(t)$ to be realized. The electric field waveform $\bar{E}_H(t)$ spends a significant amount of time near zero intensity thus the profiles will display a large peak at the unperturbed line center. In addition an equivalent amount of time is spent at the waveform maximum which results in a peak to the red of the line center. This peak is due to the shifting of the line center and not a forbidden transition. The forbidden transition peaks that have wavelengths dependent on the electric field are smeared out. This is seen in middle peak of Figure 3.30 and the far blue peak of Figure 3.31. The remaining peaks have approximately stationary wavelengths and retain its shape even in the presence of a time dependent field.

As discussed in Section 3.3.2 the difference in the π and σ profiles are not as significant as that for Balmer series transitions, although, as the electric field is increased the differences become significantly more prominent. As indicated by Figure 3.30 the $5^1D \rightarrow 2^1P$ He I profiles have the strongest differences. In general, it was found that the singlet lines ($S = 1$) had π and σ profiles

exhibiting more signification differences then those of the triplet ($S = 3$).

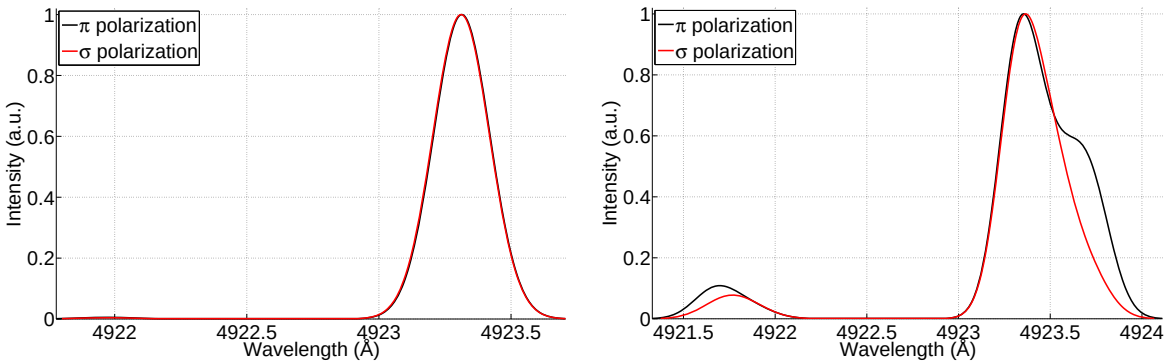

(a) (b)

Figure 3.29: $4^1D \rightarrow 2^1P$ He I profiles for an electric field given by (a) $\bar{E}_L(t)$ and (b) $\bar{E}_H(t)$.

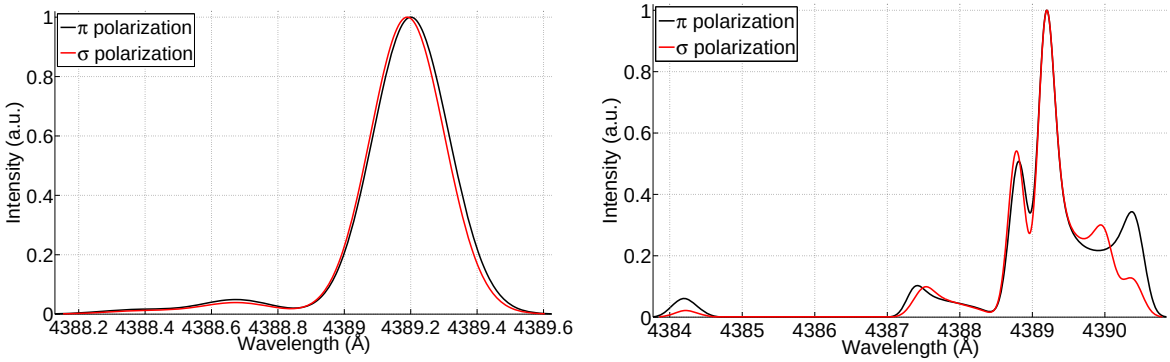

(a) (b)

Figure 3.30: $5^1D \rightarrow 2^1P$ He I profiles for an electric field given by (a) $\bar{E}_L(t)$ and (b) $\bar{E}_H(t)$.

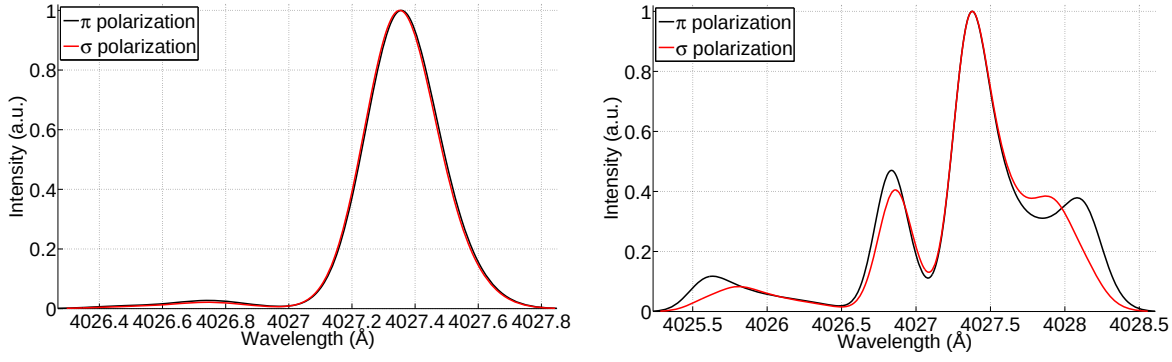

(a) (b)

Figure 3.31: $5^3D \rightarrow 2^3P$ He I profiles for an electric field given by (a) $\bar{E}_L(t)$ and (b) $\bar{E}_H(t)$.

Comparing Figure 3.29 through Figure 3.31 it is seen that the $4^1D \rightarrow 2^1P$ He I profiles have the weakest dependence on the electric field. As discussed above this is due to the fact the upper level n value is the smallest. Therefore either the $5^1D \rightarrow 2^1P$ He I or $5^3D \rightarrow 2^3P$ He I transitions will be utilized depending on there emission intensity. However, it is desired that the $5^1D \rightarrow 2^1P$ He I transition be utilized because the electric field effects the profile strongest. The emission intensity was measured experimentally as a function of pressure for these two transitions and is presented in Figure 3.32. Due to the fact that the $5^3D \rightarrow 2^3P$ He I transition has the greater emission intensity by a factor of nearly 2.5 it was chosen for the development of this diagnostic for the helium discharges.

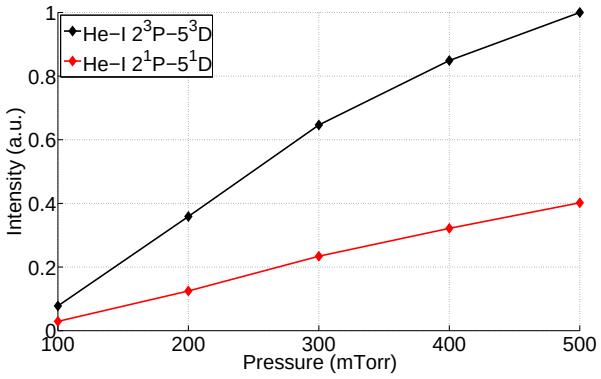

Figure 3.32: Integrated spectral line profile as a function of pressure.

CHAPTER

4

EXPERIMENTAL APPARATUS

In Chapter 3 it was shown that, from a signal to noise standpoint, that a time averaged passive OES technique must be implemented to measure the spectral line profile. The majority of the chapter was dedicated to the derivation of the corresponding atomic physics required to calculate the theoretical spectral line profile. In addition, Chapter 3 presented the methodology and algorithm implemented to fit the experimental data and a discussion on the selection of the H_β and $5^3D \rightarrow 2^3P$ He I electronic transitions.

This chapter presents the experimental apparatus utilized to develop and implement time averaged passive OES to measure the electric field of the capacitively coupled magnetized RF sheath. The chapter is structured as follows: Section 4.1 presents and describes the experimental apparatus utilized to generate the capacitively coupled magnetized RF sheath. Section 4.2 describes the system utilized to obtain the spectroscopic data necessary to determine the RF sheath electric field. Section 4.3 describes the diagnostics utilized to characterize the discharge in terms of plasma parameters. Section 4.4 describes the National Instruments hardware and software utilized to control and automate the experiment.

The development of a diagnostic on a tokamak is highly undesirable due to the large operational costs and limited availability of run time. Therefore a small scale laboratory experiment was designed to serve as a test stand in which the edge environment of the tokamak could be simulated. The basis of the experiment consists of an electrode biased at 13.56 MHz immersed in a magnetized plasma generated by excitation of electron cyclotron waves. The RF biased electrode was designed

to capacitively couple to the magnetized plasma thus forming the focus of the experimental research efforts, the capacitively coupled magnetized RF sheath. The experiment was designed to generate relatively strong electric fields, ≤ 15 kV/cm in magnitude, extending approximately 1 cm from the RF biased electrode surface. Direct access to optical emission originating in the RF sheath region is critical for the development of the diagnostic. This is due to the fact that unperturbed emission can severely alter and mask the effects of the electric field on the spectral line profile. Typically unperturbed emission is obtained from integration along the line of sight. In order to circumvent this issue a limiter assembly was designed to mate directly to the RF biased electrode. This provides an 8 mm in width and 2 mm in height plasma free channel surrounding the RF sheath along the line of sight. It is along the width of this channel that the line of sight is scanned and the spatially resolved spectral line profiles are obtained.

Two experimental configurations are investigated: electric and magnetic field vectors parallel and perpendicular. The study of these two field configurations is of particular importance. The parallel field configuration has been well studied both experimentally [17] and theoretically [95, 125, 103, 146] and thus will be the focus for diagnostic validation. The perpendicular field configuration has received significantly less attention and will therefore be the focus for diagnostic implementation. In addition this focus is desired due to the fact that it is representative of that associated with the ICRF antenna near-field.

4.1 Dynamic Stark Verification Experiment

This section presents and describes the experimental apparatus utilized to generate the capacitively coupled magnetized RF sheath. The experimental apparatus was given the name DStarVE, an acronym standing for Dynamic Stark Verification Experiment. The basis of DStarVE consists of an electrode biased at 13.56 MHz immersed in a magnetized plasma generated by excitation of the electron cyclotron wave (ECW) at 2.45 GHz. Capacitively coupled plasma sources typically operate in low density regimes due to power going into ion heating rather then electron heating [97, 62, 110]. Thus to simulate the edge environment of the tokamak where the plasma density is on the order of 10^{18} m^{-3} an additional plasma source is necessary [153, 93]. ECW driven discharges can operate above the density cutoff, $n_c = 7.2 \cdot 10^{16}$ m^{-3} at 2.45 GHz, and thus are desirable.

The experimental apparatus was designed utilizing the Pro/ENGINEER software due to the need for machining and fabrication of components. The vacuum chamber is a standard 6" cube, the port labels are given in Table 4.1. Two field configurations are investigated: magnetic and electric field vectors parallel and perpendicular. Figure 4.1 and Figure 4.2 give the cross section for the experimental setup associated with the parallel and perpendicular field configurations respectively. The port labels are equivalent for both field configurations while the coordinate system is changed. This was done such that the axes in which the experimental measurements are being conducted

is equivalent. The plasma parameters and spectroscopic data are scanned along the x and z-axes respectively. The origin of the coordinate system is located at the center of the RF biased electrode surface for both field configurations.

Table 4.1: Vacuum chamber port labels.

Label	**Location**
1	Left
2	Top
3	Right
4	Bottom
5	Back
6	Front

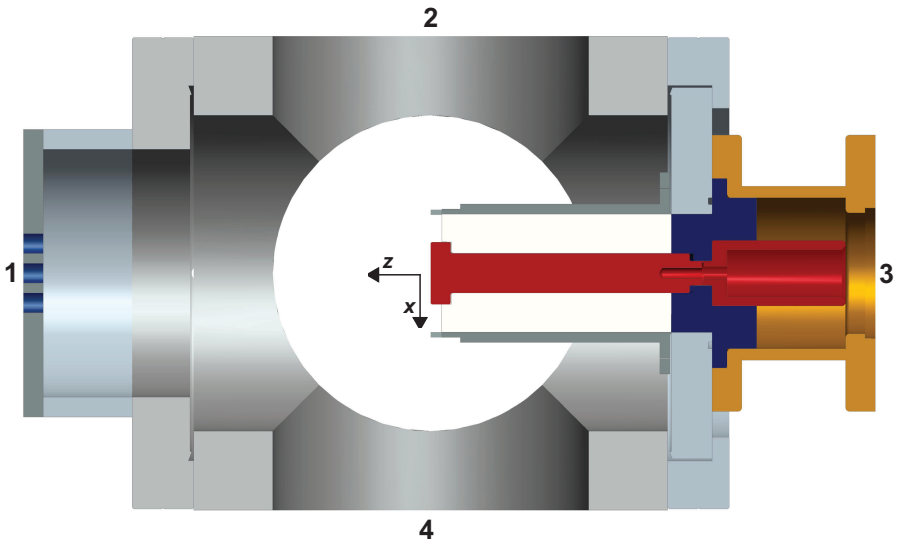

Figure 4.1: Experimental setup for the parallel field configuration.

The magnetic field is generated by two water cooled toroidal coils placed collinearly about ports 1 and 3. The magnetic field coils are power by 1 kW Electrical Measurements Inc. power supplies. The power supplies are driven by a ramped square waveform constructed in the DStarVE control software and generated by a National Instruments PXI-6251 data acquisition board. The waveform ramp up, steady state, and ramp down times are programmable. In order to achieve steady state the ramp up time was set to 2 s to account for coil response. The steady state time was typically set to 10

s but varied depending on the discharge operating parameters. The ramp down time was set to 0.5 s. The amplitude of the waveform is programmable and was set to achieve a coil current of 180 A. This results in a magnetic field intensity of 975 G at the RF biased electrode surface.

The magnetic field vector is along the negative z-axis for the coordinate system given in Figure 4.1. The spacing between the toroidal coils is slightly larger then that required for a Helmholtz geometry. This allows for a favorable magnetic field topology to excite the ECW [101]. Microwaves are launched from microwave window at port 1 which is located at the center of the magnetic field coil. Research grade hydrogen or helium gas flows into the vacuum chamber from port 5, the flow rate is controlled manually be use of a needle valve. The vacuum chamber is pumped from port 4 by either a turbo molecular or rotary vain pump depending on the working pressure. Optical access through the vacuum chamber is granted by use of a quartz window located at port 6. The utilization of the ports described above is universal with regard to the field configuration.

The simplest way to change the field configuration was to move the RF biased electrode. For the parallel and perpendicular field configuration the RF biased electrode is located at port 3 and 2 respectively as depicted in Figure 4.1 and Figure 4.2.

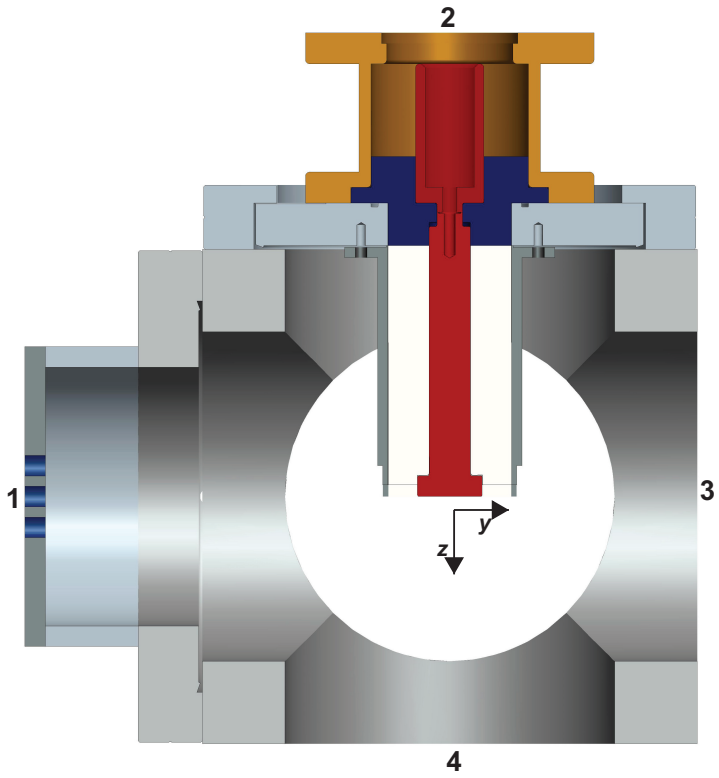

Figure 4.2: Experimental setup for the perpendicular field configuration.

The electron density and temperature and plasma potential waveform are measured by use of RF compensated Langmuir and capacitive probes. The probes interface with the vacuum chamber by use of a Wilson seal located at ports 2 and 6 for the parallel and perpendicular field configurations respectively. These ports where chosen such that spatial scans could be conducted perpendicular to the magnetic field vector. The location of the Wilson seal on ports 2 and 6 is equivalent such that the measurement is made in the same spatial location relative to the RF biased electrode.

4.1.1 RF System

The RF electrode assembly and feedthrough are coaxial in geometry with an impedance of approximately 50 Ω. The coaxial RF electrode assembly consists of a copper inner conductor, boron nitride dielectric, and aluminum outer conductor. At the plasma facing surface the inner conductor, referred to as the RF biased electrode, has a diameter of 2 cm. The RF biased electrode was designed to have a small diameter to allow for a large RF current density. This in turn drives large RF sheath voltages [98] producing the desired electric field intensity of $\leq$ 15 kV/cm. The outer conductor has an inner and outer diameter of 3.8 and 4.4 cm respectively. At the plasma facing surface the outer electrode is keyed to mate with the limiter assembly while maintaining accurate alignment. Accurate alignment is necessary because the collection optics are aligned with respect to the RF biased electrode surface utilizing a detector mounted on the limiter assembly. The outer conductor bolts directly to the port flange. The inner diameter of the outer conductors mating surface is raised to provide a superior RF contact. Electrical mating of this type is typically required due to the fact the RF current flows only in the first few skin depths, 100 μm for aluminum at 13.56 MHz.

The RF electrode feedthrough also has a copper inner conductor and a aluminum outer conductor, however the dielectric is different and consists of two sections. The first section is Teflon, colored blue in Figure 4.1 and Figure 4.2, and provides both electrical isolation and the vacuum seal. The second section is air such that the impedance is maintained at 50 Ω for the majority of the feedthrough. The inner conductor on the atmospheric side bolts directly to the RF biased electrode providing the electric connection and the compression required for the vacuum seal. The outer diameter of the inner conductors mating surface is raised to provide a superior RF contact. The vacuum seal is provided at two locations. First the Teflon component is vacuum sealed to the port flange by O-ring compression provided by the outer conductor. Second the RF biased electrode is vacuum sealed to the Teflon component by O-ring compression provided by bolting to the inner conductor. The atmospheric side of the RF electrode feedthrough was designed to mate with an EIA 3 1/8" RF connector.

The RF electrode was biased at 13.56 MHz by use of an RF Plasma Products (RFPP) 500 W RF generator. The power level of the generator was set manually utilizing a potentiometer. While the output was determined by a logic pulse generated by a National Instruments PXI-6251 data

acquisition board. The logic pulse is formed in the DStarVE control software with a programmable delay time and pulse width. Typically the delay time was set to 2 s and the pulse width was set to 10 s. These characteristic times were determined by the ramp up and steady state times, respectively, associated with the magnetic field.

A standard EIA 3 1/8" I-V probe is used to measure the RF voltage and current waveforms utilizing capacitive and inductive pickups respectively. The I-V probe directly mounts to the RF electrode feedthrough such that the waveforms are measured as close as possible to the RF biased electrode surface. The I-V probe waveforms are digitized with a TDS 2024 oscilloscope terminated to 50 Ω. The oscilloscope connects with the National Instruments platform by use of a GPIB interface. The DStarVE control software reads the oscilloscope and preprocesses the data. Calibration and analysis are conducted post-experiment in a computer program written in MATLAB.

The I-V probe was calibrated with a network analyzer with an 2 port S-parameter test set utilizing the following procedure. Port 1 of the network analyzer was connected to one side of the probe body via a 3 1/8" EIA to N-type adapter while the remaining side of the probe body was terminated to a 50 Ω load. The transmission coefficient, S_{12}, was measured by connecting port 2 of the S-parameter test set to either the capacitative or inductive probe. The frequency was swept from 5 MHz to 250 MHz. The magnitude and phase of the transmission coefficients are give below in Figure 4.3.

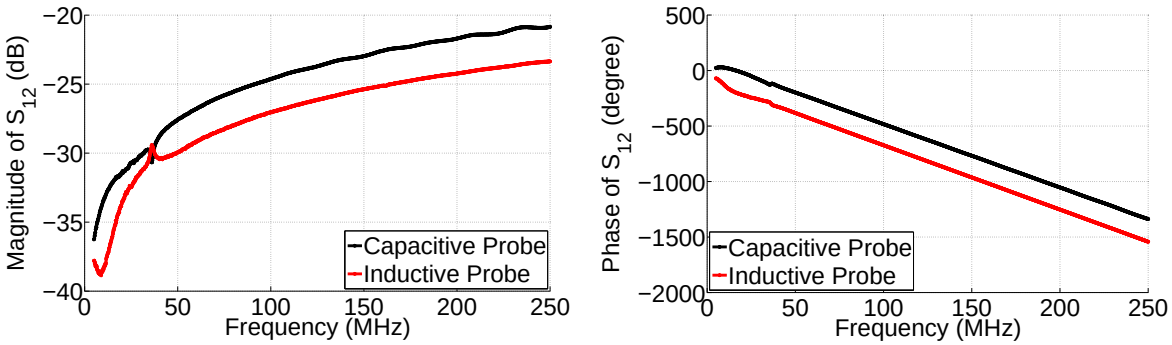

(a) (b)

Figure 4.3: EIA 3 1/8" I-V probe transmission coefficient (a) magnitude and (b) phase.

The capacitative and inductive probe signals are calibrated by first taking the Fourier transform. The expansion coefficients are corrected utilizing the data given in Figure 4.3 and the inverse Fourier transform is taken to arrive at the RF voltage and current waveforms. The I-V probe is located approximately 15 cm from the RF biased electrode surface. It is expected that the fundamental will be in the dominate component therefore due to the large wavelength, 22 m, the transformation of the waveforms to the electrode surface is negligible.

In order to match the load to the 50 Ω impedance of the RF generator and thus minimize the reflected power an L-type RFPP matching network was utilized. The matching network is located immediately after the EIA 3 1/8" I-V probe. The matching network was optimized for capacitively dominated loads and consists of three components: a shunted variable load capacitor, series inductor, and a series variable tune capacitor. The load capacitor C_L can have a possible capacitance of 800 to 1800 pF. The series inductor has a value of 5.6 μH. The tune capacitor C_T and can have a possible capacitance of 10 to 500 pF. The capacitance of C_L and C_T is controlled by use of an RFPP controller. The controller outputs two voltage signals ranging from 0 to 5 V corresponding to the capacitor positions. These signals are digitized by a National Instruments PXI-6251 data acquisition board.

The DC voltage induced on the RF biased electrode is measured by use of an RF choked 1:404 voltage divider located in the matchbox after the tune capacitor. This signal is digitized by a National Instruments PXI-6251 data acquisition board. The acquired data is preprocessed and calibrated by the DStarVE control software.

The forward and reflected power were measured by two Bird Thruline -50 dB directional couplers mounted in 50 Ω EIA 3 1/8" line located between the RF generator and matchbox. The directional coupler waveforms are digitized with a TDS 2024 oscilloscope terminated to 50 Ω. The oscilloscope connects with the National Instruments platform by use of a GPIB interface. The DStarVE control software reads the oscilloscope and preprocesses the data. Calibration and analysis are conducted post-experiment in a computer program written in MATLAB.

The directional couplers were calibrated utilizing the RF generator power meter as follows. The EIA 3 1/8" line housing the directional couplers were feed with the RF generator and terminated with a 50 Ω load. The directional coupler signal was measured with a digital oscilloscope and the peak to peak value was recorded as a function of input power. The calibration curves are given in Figure 4.4 for the forward and reflected directional couplers

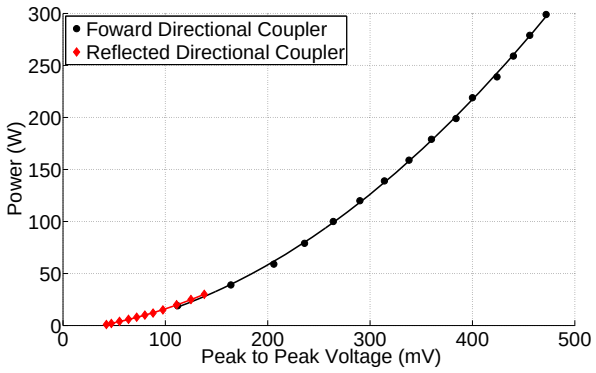

Figure 4.4: RF directional coupler calibration curves.

A circuit diagram of the RF system is given in Figure 4.5 showing the location of the various measurement points and the elements of the matching network.

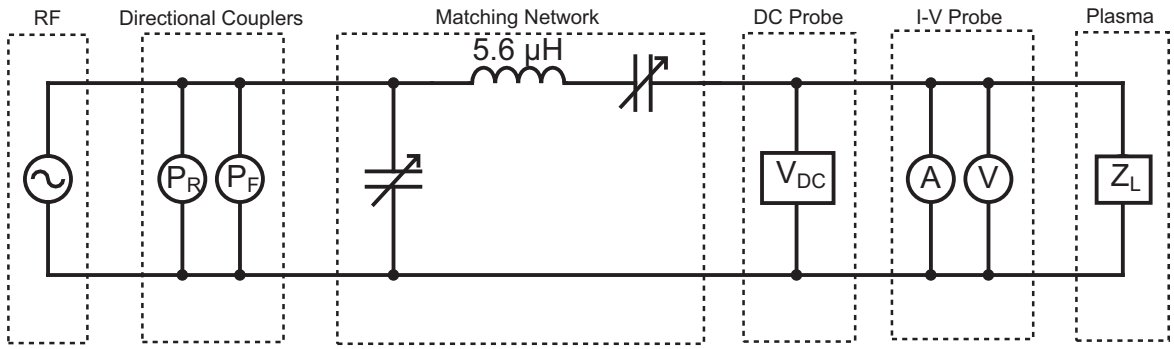

Figure 4.5: Circuit diagram of the RF system.

Ideally a matching network has a purely imaginary impedance. In reality the inductive elements give rise to a finite resistance causing unwanted power absorption. To determine the power absorbed by the plasma the efficiency of the matching network must be determined. Given the transmission S_{21} and reflection S_{11} coefficients in Decibels the matching network power efficiency is determined by

$$P_E = \frac{2 \cdot 10^{S_{21}/10} + 10^{S_{11}/10} - 1}{10^{S_{21}/10}} \,. \tag{4.1}$$

S_{21} and S_{11} were measured by connecting the output and input of the matching network to ports 1 and 2, respectively, of a network analyzer with an S-parameter test set. The S-parameters were measured at 13.56 MHz for values of C_L and C_T corresponding to the tune space of interest. The calculated power efficiency of the matching network is given in Figure 4.6.

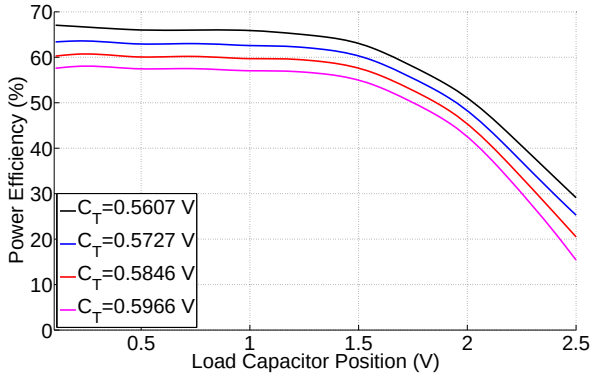

Figure 4.6: Power efficiency of matching network in tune space of interest.

The Q-factor of the RF system is very high and thus C_T is only swept over a very narrow range as indicated by Figure 4.6. The match efficiency was found to be severely reduced for $C_L \geq 1.5$ such that over 50 % of the power is deposited in the matching network.

If the RF system is in a matched state the load impedance can be determined from the reflection coefficient S_{11} of the matching network. The impedance of the load z_L is given by

$$z_L = \left[\frac{1+S_{11}}{1-S_{11}}\right]^* z_o \ , \tag{4.2}$$

where $z_o = 50\ \Omega$ is the termination input impedance. The plasma impedance z_P can then be calculated form that of the load and the matching network efficiency as given by

$$z_P = R_P + iX_P \ , \tag{4.3}$$

$$R_P = Re\{z_L\} - 2Re\{z_L\}(1-P_E)$$

$$X_P = Im\{z_L\} \ ,$$

where R_P and X_P are the plasma resistance and reactance respectively. The second term of R_P is due to the finite resistance associated with the matching network otherwise the plasma and load resistance would be equivalent. Utilizing the S_{21} and S_{11} coefficients measured to calculate the match efficiency the plasma impedance is calculated and presented in Figure 4.7. For the investigated discharges the matching network efficiency and plasma impedance are calculated by interpolating or extrapolating the data contained in Figure 4.6 and Figure 4.7 given the load and tune capacitor positions.

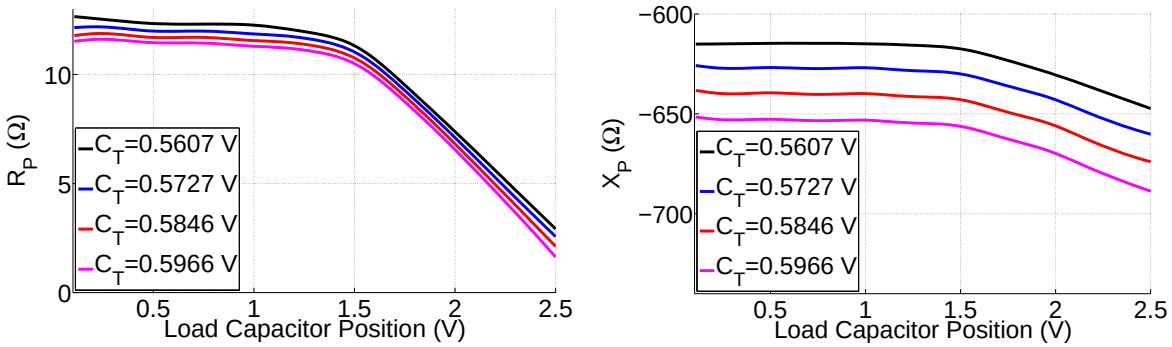

(a) (b)

Figure 4.7: Plasma (a) resistance and (b) reactance for tune space of interest.

4.1.2 Microwave System

The edge environment of a tokamak seen by ICRF antenna and the Faraday screen typically has an electron density and temperature on the order of 10^{18} m^{-3} and 10 eV respectively [153, 93]. The capacitively coupled plasma generated by the RF electrode assembly described above is incapable of producing plasma with these parameters. Thus to simulate this environment an additional plasma source is required.

To access these plasma parameters a source based on the absorption of the whistler wave in the electron cyclotron range of frequency, an electron cyclotron wave (ECW), is utilized. The whistler wave is applicable because its propagation is not limited by the cutoff density $n_c = 7.2 \cdot 10^{16}$ m^{-3} associated with absorption of the ordinary circularly polarized wave at 2.45 GHz. It has been shown that launching microwaves into a region in which a negative gradient in the magnetic field exists leads to absorption of the whistler wave [101, 68]. This requires launching the microwaves from a point in which the magnetic field magnitude is greater than that required for resonance, 875 Gauss at 2.45 GHz [120, 23].

To achieve a negative gradient in the magnetic field topology the spacing of the coils is increased. In the Helmholtz geometry the ratio of the coil radius to spacing is unity, here it is decreased to 0.8. The magnetic field coils are operated at 180 A, the associated magnetic field intensity is given in Figure 4.8 utilizing the coordinate system of the parallel field configuration. The coil current was determined experimentally from that in which the maximum density was achieved at a given microwave power level. The magnetic field coils are centered about the positions (0,0,±12) cm.

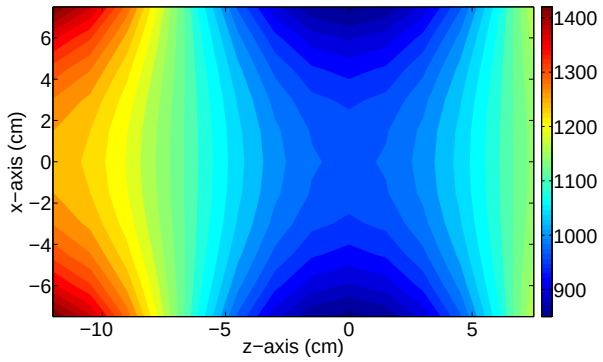

Figure 4.8: Magnetic field intensity for coil current of 180 A.

The microwave window is located in the throat of the magnetic field coil centered about a position of (0,0,-12) cm. In order to achieve this port 1 was extended by 4.4 cm utilizing a custom fabricated adapter as depicted in Figure 4.1. The microwave window seals to the adapter by O-ring compression and mates the waveguide to port 1. The center of the RF biased electrode surface

is located at a position of (0,0,0) cm for both parallel and perpendicular field configurations. The magnetic field intensity decreases from 1225 Gauss at the microwave window to 975 Gauss at the center of the RF biased electrode surface.

A Micro-Now Instrument Company 2.45 GHz 500 W generator is utilized to supply the microwaves. The generator was modified to operator in a pulsed mode. The power output by the generator was set manually by a potentiometer on the front panel. While the output was determined by a logic pulse generated by a National Instruments PXI-6251 data acquisition board. The logic pulse is formed in the DStarVE control software with a programmable delay time and pulse width. Typically the delay time was set to 1.5 s and the pulse width was set to 10.5 s. These characteristic times are determined such that steady state conditions would be achieved by the time the RF power supply was activated.

WR340 waveguide is used for the microwave components which are comprised of an isolator, dummy load, directional coupler, three stub tuner, and vacuum compatible microwave window. The output of the generator is an N-type termination. Thus a low loss N-type coaxial cable is utilized to mate the microwave components. By use of the N-type coaxial cable the generator feeds the input of a Raytheon isolator. The reflected port of the isolator is terminated to a dummy load with an attenuation factor of -27 dB. The forward port of the isolator is connected to a waveguide containing two -60 dB directional couplers, sampling the forward and reflected waves. The directional couplers are terminated with 432A HP crystal detectors which are utilized to measure the forward and reflected power, Figure 4.9 gives the calibration curves. The waveguide containing the directional couplers is connected to a three stub tuner. The three stub tuner mates the microwave window to the adapter mounted to port 1 utilizing O-ring compression and thus providing the vacuum seal.

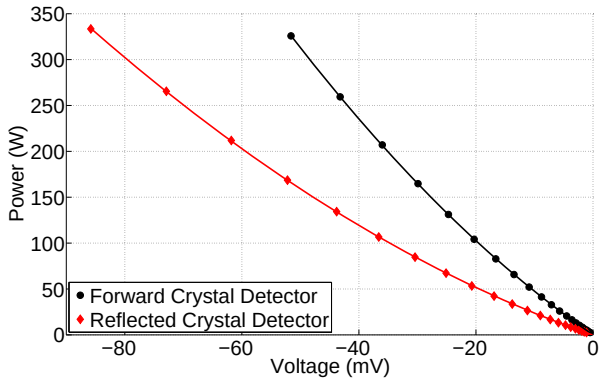

Figure 4.9: Microwave directional coupler calibration curves.

To calibrate the 432A HP crystal detectors the generator and dummy load were connected directly to the waveguide containing the directional couplers. The order of the connection determined which

crystal detector was being calibrated. The output signal of the crystal detector was measured with an oscilloscope and recorded as a function of power determined from the meter on the generator. Thus the power meter on the generator is assumed to be accurate. The 432A HP crystal detector signals were digitized by a National Instruments PXI-6251 data acquisition board. The acquired data is preprocessed and calibrated by the DStarVE control software.

4.1.3 Limiter Assembly

The spectral line profile obtained utilizing passive OES is an integration of the emission along the optical line of sight. Typically the spatial dimension associated with the region in which the electric field exist is small compared to the overall length of the line of sight. Therefore the resulting spectral line profile is dominated by emission originating in the bulk plasma where the electric field is negligible. This emission is referred to as unperturbed because the electric field magnitude is essentially zero when compared to that of the RF sheath.

The intensity associated with the unperturbed emission is unknown and difficult to estimate. Therefore without an accurate estimate of this dominating intensity, determination of the electric field from the spectral line profile is severely compromised. In order to demonstrate the effect of unperturbed emission on the spectral line profile the H_β transition is modeled for three cases: zero, equal, and ten times the intensity of unperturbed emission. The magnetic and electric field vectors are modeled as

$$\bar{B} = 1000\,\hat{z}\ \text{Gauss} \qquad \bar{E}(t) = 5 + 5\cos(\omega t)\,\hat{z}\ \text{kV/cm}\,,$$

where $\omega/2\pi = 13.56$ MHz. The radiator distribution and instrument functions are taken to be representative of those associated with the experimental measurements. The radiator distribution function is modeled as a one temperature Maxwellian and the instrument function is taken to be Gaussian, the parameters are given in Table 3.3. The spectral line profiles are given in Figure 4.10.

Figure 4.10 shows that the unperturbed emission severely alters the spectral line profile and begins to mask the electric field effect especially for the σ profile. The modeled electric field magnitude corresponds to the 10-15 kV/cm maximum intensity expected in the experimental work, at this value its effect can still be seen. However for lower electric field intensities the effects will be completely masked by the unperturbed emission rendering the spectral line profile unusable. The intensity of the unperturbed emission associated with DStarVE is predicted be one to ten times, given the dimensions of the RF biased electrode. Therefore removal along the line of sight is necessary in this work.

In order to collect emission originating solely from the RF sheath region a limiter was designed to provide a plasma free channel adjacent to the RF sheath along the line of sight of the collection optics. The dimensions of the channel are 9 mm in width and 2 mm in height. The channel walls are

blacked out to reduce collection of reflected emission. Additionally, to minimize reflections at the channel boundary only the first 8 mm of RF sheath is investigated. This is expected to be adequate based on the estimated 10 mm RF sheath width [98].

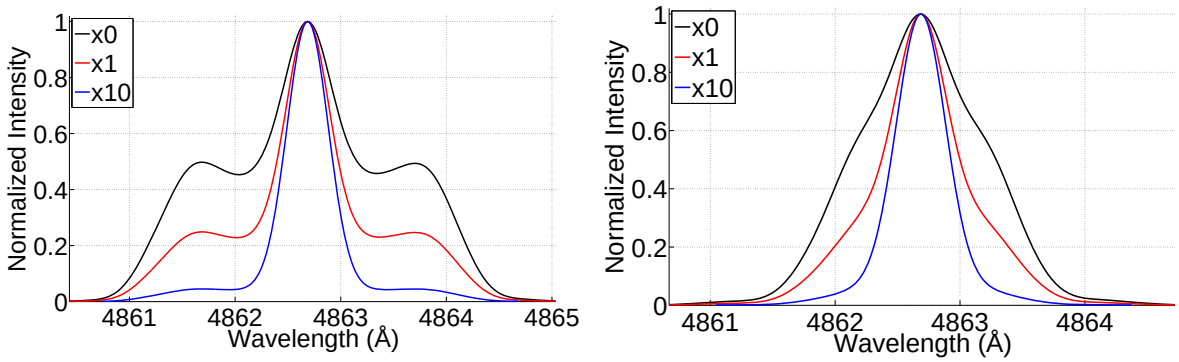

(a) (b)

Figure 4.10: Theoretical H_β (a) π and (b) σ profiles with and without superposition of unperturbed emission.

The limiter assembly consists of a support structure, limiter, and a detector. The support structure is aluminum and mates concentrically to the outer conductor of the RF electrode assembly. This mating scheme provides a flush surface to mount the limiter and detector. The support structure is keyed to ensure alignment of the limiter assembly with respect to the RF biased electrode surface. This is required because the collection optics are aligned with respect to the RF biased electrode surface utilizing the detector mounted on the support structure. The limiter consists of two sections, the first is composed of aluminum and extends from the quartz window of port 6 to the outer conductor of the RF electrode assembly. The second is composed of machinable glass ceramic and extends from the aluminum limiter components to the RF biased electrode surface. The limiter component interfacing with the RF sheath was chosen to be a ceramic such that a grounded surface would not be immediately adjacent to the RF biased electrode. The channel provided by the limiter components is extended past the RF biased electrode surface in the same two component scheme. The detector immediately follows the far limiter components along line of sight.

The ceramic limiter components were designed such that the magnetic field lines intersecting with the RF sheath would remain perpendicular to the normal of their surface. This criteria ensures that plasma tied to the magnetic field lines intersecting the RF sheath is not limited. In order to meet this criteria the ceramic limiter components must be designed differently for the parallel and perpendicular field configurations. The limiter assemblies associated the parallel and perpendicular field configurations are given by Figure 4.11 and Figure 4.12 respectively. The support structure

is the dark gray, the aluminum limiter components are orange and yellow respectively, and the detector is light gray. The limit channel is seen in the cross-section view given by Figure 4.11b and Figure 4.12b for parallel and perpendicular field configurations respectively.

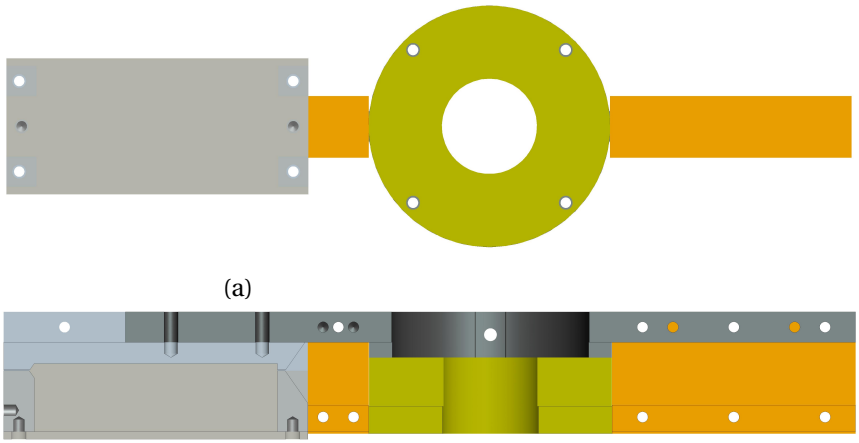

(a)

(b)

Figure 4.11: Parallel field configuration limiter assembly (a) viewed along negative z-axis and (b) cross-section viewed along the positive x-axis.

In the parallel field configuration the ceramic limiter is symmetric about the z-axis and limits the plasma concentrically about the RF biased electrode surface. In the perpendicular field geometry the ceramic limiters are not symmetric and only limit plasma directly adjacent to the aluminum limiter components. In these experimental setups a highly peaked density profile would be expected in the RF sheath due to the small diameter of the RF biased electrode and surrounding ceramic limiter. However the magnetic field is assumed to relax the density profile significantly. This assumption will be investigated experimentally by use of the RF compensated Langmuir probe described in Section 4.3.1, the results will be presented in Section 5.1.

The detector located on the far side of the limiter assembly was designed to allow alignment of the collection optics such that the corresponding line of sight is perpendicular to the normal of the RF biased electrode surface to within 0.2 degree. The detector consists of a photodiode mounted to the far end of two 200 μm in width linear apertures. The linear apertures are separated by 6 cm and are located 2.8 mm from the RF biased electrode surface on the z-axis. The detector is based on the principal of line of sight. Therefore linear apertures were implemented in the design to limit the photodiodes field of view such that it is nearly perpendicular to the normal of the RF biased electrode surface. The linear aperture width and separation dictate the uncertainty in the alignment and were determined from ray trace simulations described in Section 4.2.1. The cross

section of the detector can be seen in Figure 4.11a and Figure 4.11b for parallel and perpendicular field configurations respectively, the photodiode is not shown.

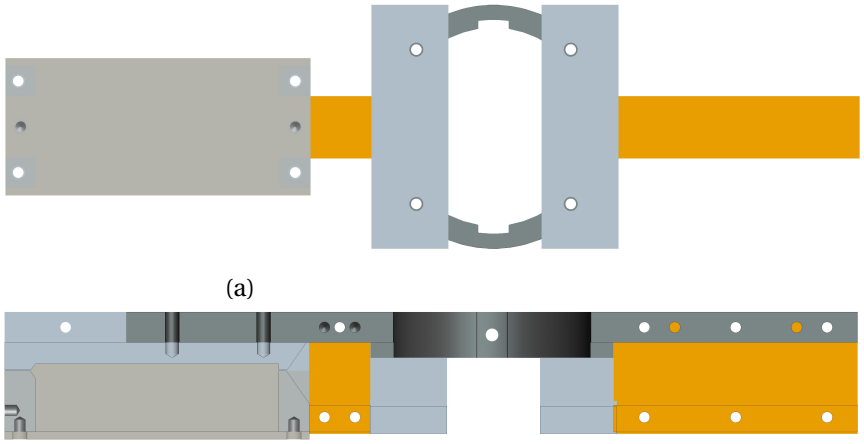

Figure 4.12: Perpendicular field configuration limiter assembly (a) viewed along negative z-axis and (b) cross-section viewed along the positive y-axis.

The collections optics are mounted on a translation and rotational stage, alignment is achieved by utilizing these two degrees of freedom to maximize the signal associated with the photodiode during back illumination. During alignment the photodiode signal is very weak due to diffraction and collimation caused by the linear apertures. Therefore a two stage operational amplifier was built with a gain of approximately 10^6 to measure the signal. The output of the operational amplifier is digitized by a National Instruments PXI-6251 data acquisition board. A LabVIEW code was written to average the signal over many samples and display the result such that the alignment of the collection optics can be conducted in real time. The alignment of the collection optics will be further discussed in Section 4.2.1.

The cross section of the limiter assembly mated to the RF electrode assembly is depicted in Figure 4.13 viewed from port 3 and Figure 4.14 viewed from port 4 for the parallel and perpendicular field configurations respectively. A typical line of sight as viewed by the collection optics is given by the black dashed line. The 2 cm emission region associated with the RF sheath is shaded rose. The line of sight is translated along the z-axis, with $\triangle z$ indicating the possible observation locations.

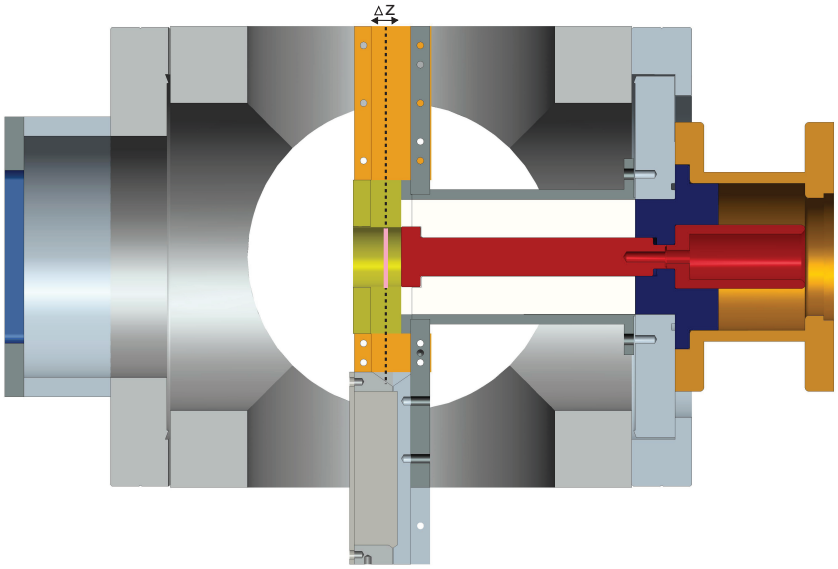

Figure 4.13: Experimental Setup for the parallel field configuration.

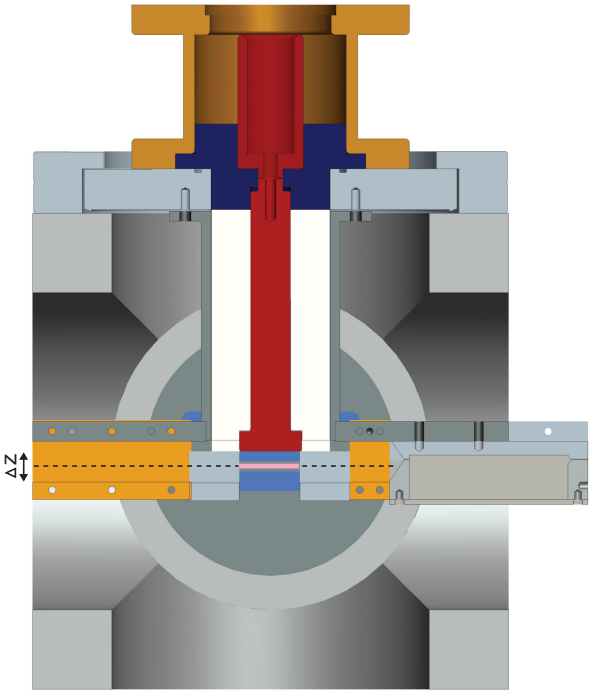

Figure 4.14: Experimental Setup for the perpendicular field configuration.

4.2 Spectroscopic System

This section describes the spectroscopic system which consists of the collection optics, spectrometer, and CCD detector. The collection optics were designed to observe optical emission with high spatial resolution, ≤500 μm at the full width half maximum (FWHM) of the beam. The collection optics mate to the spectrometer via fiber optic cable. The spectrometer is a Czerny-Turner type with a focal length of 0.5 m. Depending on the nature of the experiment the detector is either a liquid nitrogen cooled back illuminated or intensified CCD and directly mounts to the spectrometer.

4.2.1 Collection Optics

The collection optics were designed to observe a beam of emission with high spatial resolution, ≤ 500 μm FWHM, by use of a collimating lens and two linear apertures. A nearly collimated beam is collected by use of $f = 70$ mm achromatic lens focused on a 200 μm in diameter fiber optic. The desired spatial resolution is achieved by limiting the collected emission by the two linear apertures appropriately sized and spaced [148]. The linear apertures are mechanical having possible widths ranging from 25 μm to 2500 μm. The layout of the collection optics including the limiter assembly channel and RF biased electrode is given in Figure 4.15.

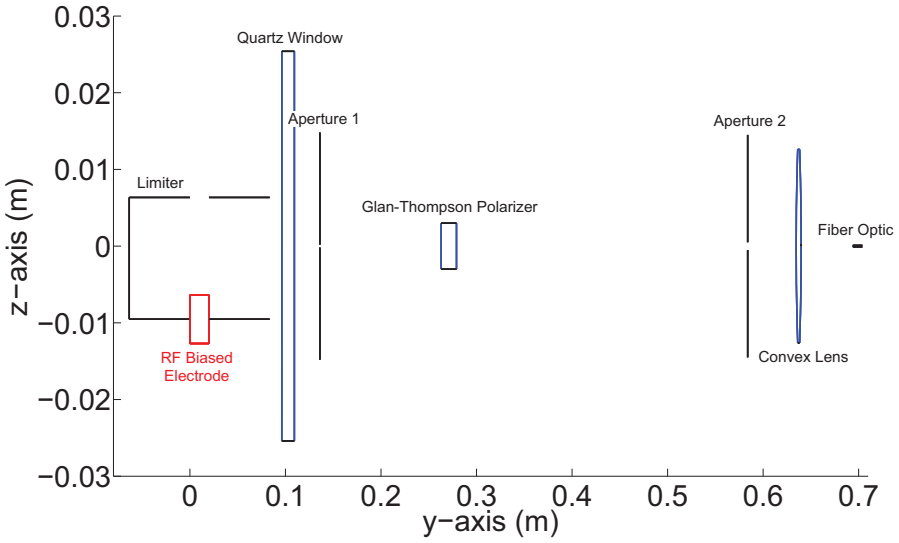

Figure 4.15: Collection optics for beam profile simulation.

As depicted by Figure 4.15 the ordering of the collection optics elements is as follows: first aperture, Glan-Thompson polarizer, second aperture, collimating lens, and fiber optic. The first aperture has a width of 375 μm and dominates the resolution of the observed beam. A Glan-Thompson

polarizer is located after the first aperture and is utilized to measure the π and σ polarizations independently. The location of the polarizer in the optical train is unimportant as long as it occurs before the fiber optic. The second aperture has a width of 1000 μm and has a small effect on the resolution. The main purpose of the second aperture is to attenuate stray light due to reflections. The spacing between the first and second apertures is 45 cm. The collimating lens focuses the light that is not attenuated by the second aperture to the fiber optic cable. The fiber optic cable mates the collection optics to the spectrometer and is attached to the collection optics via an SMA connector. The collection optics are completely contained within Thorlabs lens tubes thus eliminating the collection of stray emission. The Glan-Thompson polarizer is mounted inside of a rotatable lens tube thus allowing for the π and σ polarizations to be measured independently by a rotation of the lens tube of 90 degrees. The collection optics are mounted on a rotational and translation stage allowing for alignment and scanning.

A 2D ray tracing code was written in MATLAB to aid the design process. The spacing and widths of the linear apertures associated with both the collection optics and limiter assembly detector were determined from simulation. However due to diffraction, appropriate widths for the collection optics linear apertures were determined from experimental measurements. The effect of the misalignment of the collection optics elements at its most severe level was included in the simulations. Figure 4.16 gives the modeled collection optics with the launched rays in its final configuration, absorbed and collected rays are given in black and magenta respectively. The z-axis has been shifted such that it is centered about the limiter assembly channel. The y-axis is shifted to far edge of the RF biased electrode.

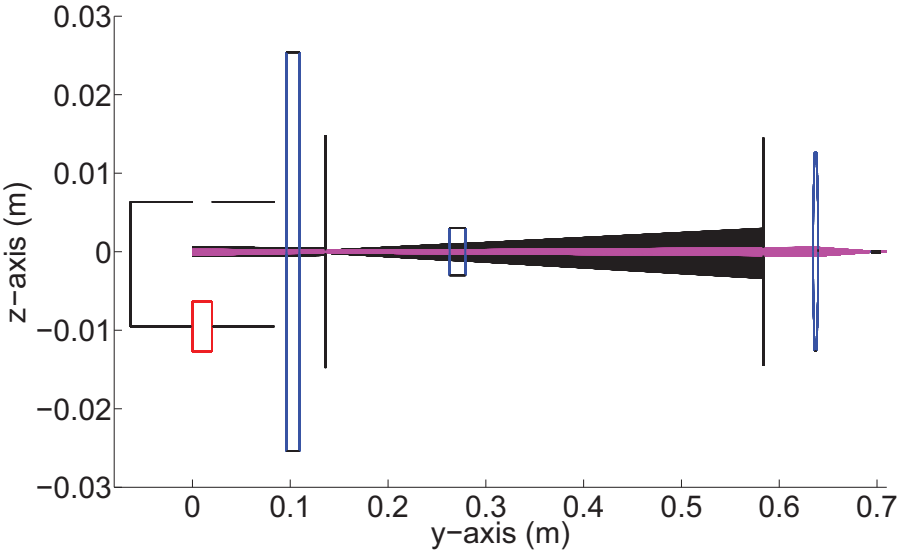

Figure 4.16: Collection optics beam profile simulation via 2D ray tracing.

The optimum spacing of the apertures was found to be approximately 45 cm from maximizing resolution and intensity given a reasonable physical size constraint.

The beam profile is simulated by launching rays from the emission region, the rays that enter the fiber optic are counted and there position of origin is stored. The beam profile is integrated along the y-axis, the divergence of the beam along this axis will be discussed below. The simulated beam profile is given in Figure 4.17.

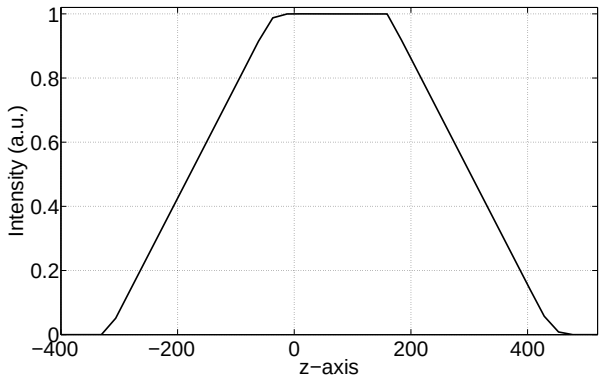

Figure 4.17: Simulated beam profile of collection optics.

Due to misalignment the simulated beam profile is not symmetrical and not centered about the z-axis, the FWHM is approximately 500 μm. In order to determine the most appropriate values for the widths of the linear apertures the beam profile was measured as a function of the aperture width. The collected beam profile is approximated by that obtained by back illuminating the collection optics with a white light source. A CCD array positioned 12 cm from the first aperture, a distance equivalent to the center of the RF sheath, was utilized to measure the beam profile. Figure 4.18 gives the measured beam profile for the final configuration of the collection optics and the beam profile broadening parameters as a function of the first aperture width with the second having a value of 1000 μm.

The second aperture width does not effect the beam resolution significantly and thus only the final configuration is presented. Figure 4.18a shows that the measured beam profile is highly peaked in comparison to the simulated, this results in a 225 μm FWHM. In addition the measured beam profile has very broad wings extending $\pm$ 1500 μm from the center. The above characteristics indicate that diffraction effects are significant. Figure 4.18b shows that there is a minimum in the curves occurring at an aperture width of 375 μm. This minimum is due to the diffraction limit at small aperture widths and represents the maximum obtainable spatial resolution. The beam profile was observed at the ends of the emission region, positions of 11 and 13 cm from the first aperture, such that the divergence could be measured. It was found that the divergence of the beam profile

for the final configuration was approximately 50 μm.

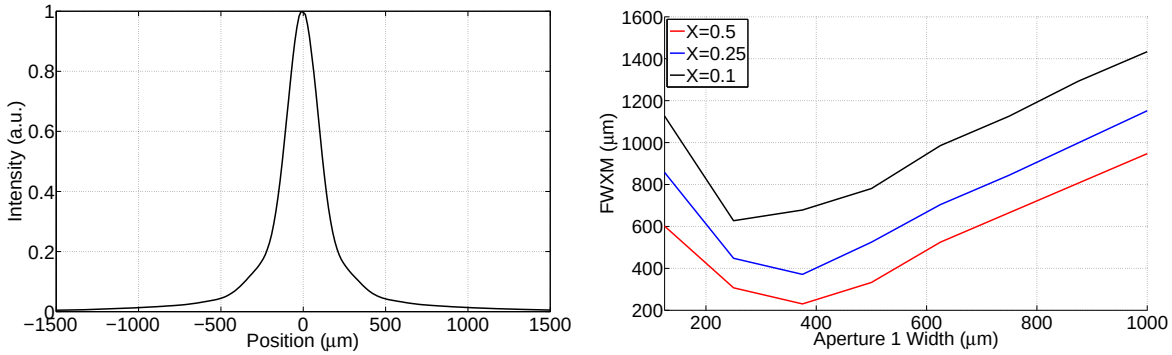

(a) (b)

Figure 4.18: (a) Measured beam profile of the collection optics and (b) the Full Width at X Maximum (FWXM) of beam profile as a function of the first aperture width.

The collection optics are mounted onto a translational and rotational stage which is in turn mounted to the bench top. The translation stage allows emission to be collected as a function of z-axis position. The rotational stage allows for the collection optics to be aligned perpendicular to the z-axis. The alignment of the collection optics is carried out utilizing the limiter assembly detector. With the collection optics aligned, the translation stage is calibrated with respect to the RF biased electrode surface and is at a position of $z = 2.8$ mm. As discussed in Section 4.1.3 the collection optics are aligned by back illuminating with a bright white light source. The photodiode signal is maximized as a function of stage angle and translation position. At a given translation position the collection optics are rotated until the maximum signal generated by the photodiode has been reached. This process is continued for various z-axis positions which are accessed by the translation stage. The collection optics are aligned when the photodiode signal has reached its maximum point. The ray tracing code was utilized to simulate the alignment of the collection optics, again including misalignments at the most severe level. The aligned collection optics showing the launched rays is given in Figure 4.19, absorbed and collected rays are given in black and magenta respectively. The z-axis has been shifted such that it is centered about the limiter assembly detector. The y-axis is shifted to the location in which the rays are launched.

In the simulation the rays were launched from the fiber optic. The limiter assembly detector is the last component on the right side of Figure 4.19, the exiting rays are counted and assumed to be proportional to the photodiode signal. Figure 4.20 presents the photodiode signal from the simulated alignment and the footprint in the emission region corresponding to the aligned collection optics at the various translational stage positions.

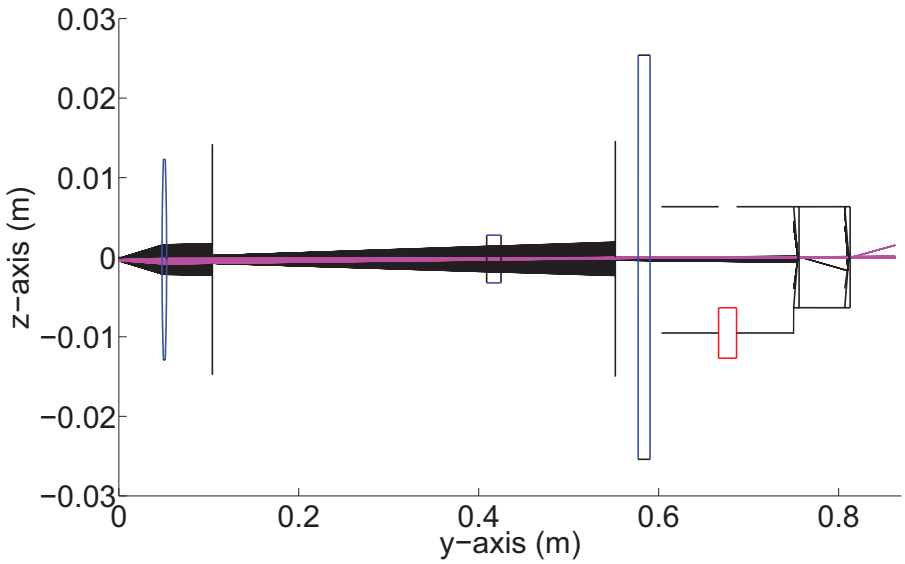

Figure 4.19: Collection optics for alignment simulation.

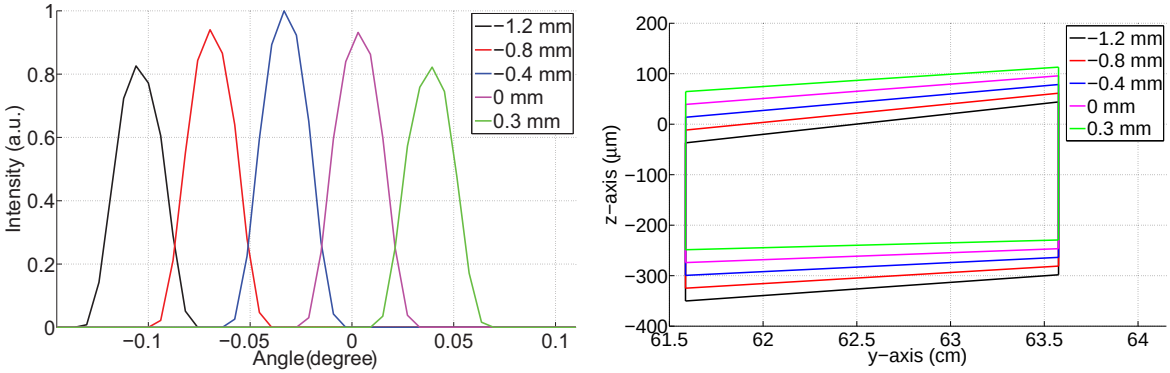

(a) (b)

Figure 4.20: (a) Simulated photodiode signal for alignment of collection optics and (b) Footprint of beam profile associated with the aligned collection optics at the various translation stage locations.

The legend of Figure 4.20 gives the position of the translation stage on the z-axis. The collection optics can be locally aligned at the various positions of the translational stage, given by the maximum of the peaks of Figure 4.20a. The corresponding beam footprint in the RF sheath emission region is given in Figure 4.20b. Due to the simulated misalignment of the collection optics elements the position of the rotational and translational stages are non-zero, in addition the beam footprint is skewed. Diffraction effects and the relatively weak signal of the photodiode limit the alignment to within ± 0.1 degree and was confirmed experimentally. Thus at the most extreme misalignment

the beam footprint is skewed by ≤ 100 μm with an offset on the z-axis of ≤ 250 μm. Therefore the divergence in the beam profile in the emission region is estimated at 150 μm and the accuracy in the z-axis position is estimated at approximately 250 μm. The relative accuracy in the z-axis position is 25 μm and determined by the increments on the translation stage.

The reflected emission was measured to make sure that the blacked out limiter assembly channel surfaces where absorbing stray emission. The reflected emission was simulated by illuminating the RF biased electrode along the z-axis with an intense white light source, this required removed of the flange at port 1. The reflected emission intensity was found to be approximately two orders of magnitude lower then the intensity associated with the spectral line profile. Figure 4.21 gives the normalized intensity of the collected reflected emission.

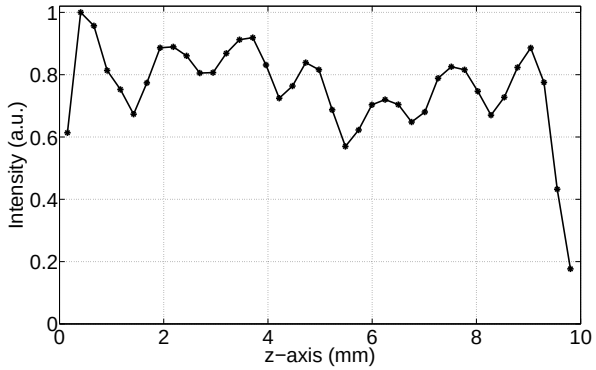

Figure 4.21: Stray light measured by the collection optics.

4.2.2 Spectrometer and Detector

The system consists of a diffraction grating spectrometer and a spectroscopic CCD camera. The camera is mounted directly to the spectrometer. The collection optics are connected to the spectrometer by use of a 200 μm in diameter fiber optic and is mounted flush with the side entrance slit of the spectrometer.

A Princeton Instruments Acton series SP2500i Czerny-Turner spectrometer is utilized to disperse the emission. The spectrometer has a focal length of 500 mm with an aperture ratio of f/6.5. The spectrometer has a motorized triple grating turret with the following gratings: a 100 lines/mm blazed at 400 nm, a 1200 lines/mm blazed at 500 nm, and a 2400 lines/mm blazed at 400 nm. The entrance slit to the spectrometer is mechanical and kept at 25 μm when the shape of the spectral line profile is of interest and 100 μm when the integrated area of the spectral line profile is of interest. Diffraction based spectroscopy is extensively described in the literature [6].

The measurement of the time averaged spectral line profile required a low noise CCD due to the

long integration times, typically 50 to 300 s as discussed in Section 3.2. A Princeton Instruments PyLoN 100BR eXcelon liquid nitrogen cooled spectroscopic CCD was utilized for these measurements. The associated dark current at -120°C is ≤ 1 e^-/pixel/hour which allowed for a signal to noise ratio required for the accurate fitting. To access the desired spectral resolution the width of the entrance slit to the spectrometer was set to 25 μm and the 2400 lines/mm grating was used.

The instrument function associated with this spectroscopic setup for the H_β transition at 4863 Å and the $5^3D \rightarrow 2^3P$ He I transition at 4027 Å was determined utilizing an Ar/Ne lamp. The lamp was mounted to the front entrance slit of the spectrometer which was set to have a width of 25 μm. The line broadening associated with the Ar and Ne transitions are negligible compared with the broadening associated with the spectroscopic system therefore the instrument function can be determined from these lines.

The CCD is focused such that the highest spectral resolution is obtained. Typically this causes the instrument function to be slightly asymmetric due to optical aberrations. It was found that the instrument function is well represented by a summation of two Gaussian functions. Due to the fact the instrument function is dependent on the wavelength the following procedure is utilized to determine the instrument function. A bi-Gaussian function was fit to the three Ne I lines: 4044 Å, 4345 Å, and 5331 Å. The resulting parameters where then fit to a second order polynomial. At the wavelengths of interest 4027 Å and 4863 Å the parameters were then interpolated. The bi-Gaussian fit to the Ne I 4345 Å line is given in Figure 4.22.

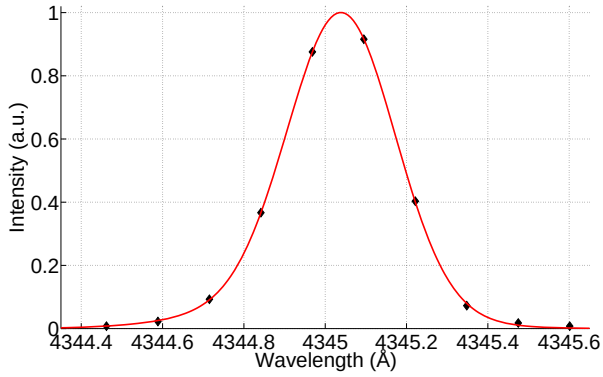

Figure 4.22: Bi-Gaussian fit to the 4345 Å Ne I line.

As given by Eq. 3.59 the parameters associated with the instrument function are I_{Ii}, λ_{Ii}, and σ_{Ii} where $i = 1$ and 2 for a bi-Gaussian. Figure 4.23 presents the instruments function parameters. The markers indicate the values determined from the fit to the Ne I lines with the solid line representing the second order polynomial fit.

The measurements of the time dependent spectral line profile required an intensified CCD due

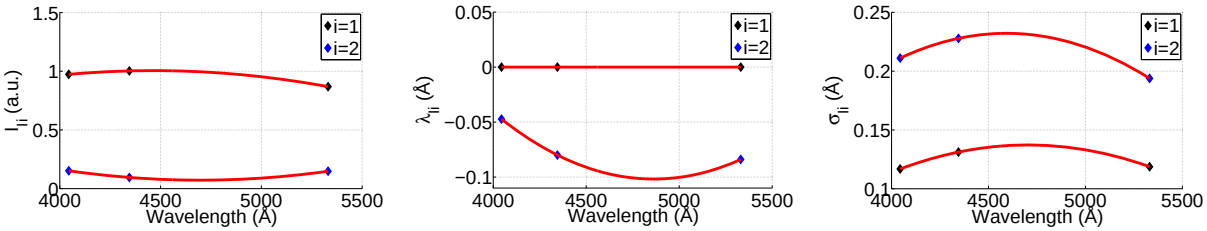

Figure 4.23: (a) I_{Ii}, (b) λ_{Ii}, and (c) σ_{Ii} instrument function parameters.

to the short integration times, on the order of a ns. A Princeton Instruments PI-MAX III spectroscopic CCD was utilized for these measurements. The particular PI-MAX III camera used in this work has a minimum integration time of 3.6 ns and a maximum repetition rate of 1 MHz. The integrated area of the line profile is desired here and thus the spectral resolution of these measurements can be relaxed. The width of the entrance slit to the spectrometer was set to 100 μm and the 1200 lines/mm grating was used.

In order to obtain the time resolved data typically 10^6 phase locked acquisitions were obtained on the CCD before the data was read out and digitized. In order to acquire emission at the same phase within the RF period the PI-MAX III camera is triggered indirectly from the RF voltage waveform. A signal approximately proportional to this waveform is obtained from the capacitive pickup associated with the I-V probe, described in section 4.1.1, is utilized. The PI-MAX III requires a TTL signal at a frequency $\leq$ 1 MHz thus this RF waveform is turned into a TTL signal by a comparator. The TTL signal is then frequency divided by a factor of 16. The resulting signal is fed into a BNC model 575 pulse generator which is utilized as a gate. This is done such that the PI-MAX III camera is only triggered when the plasma has reached steady state. A logic pulse generated by a National Instruments PXI-6251 data acquisition board determines the gate. The logic pulse is formed in the DStarVE control software with a programmable delay time and pulse width. Figure 4.24 gives the schematic of the triggering. The spectroscopic system for both configurations: time averaged and time resolved was controlled by the Princeton Instruments Lightfield software.

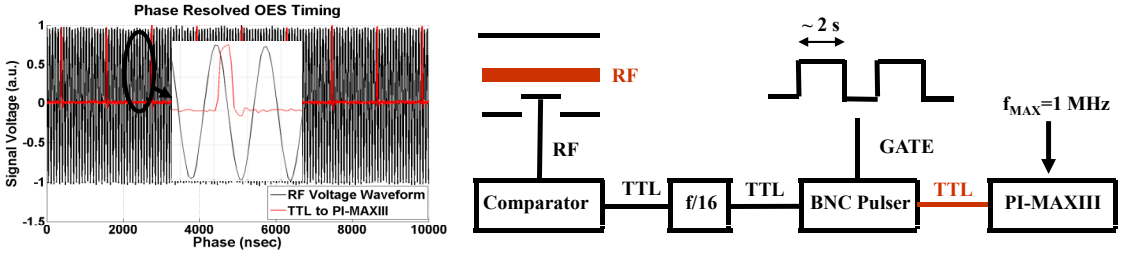

Figure 4.24: Schematic of phase locked setup.

4.3 Plasma Diagnostics

This section describes the diagnostics utilized to characterize the plasma in terms of electron density, electron temperature, and plasma potential. These plasma parameters are of interest because they supply the boundary conditions associated with the analytical modeling of the RF sheath described in Section 2.2. In addition they allow correlations to be made to the measured RF sheath electric field.

In the RF range of frequencies and below the plasma parameters stated above can have a substantial time dependence. However for the purposes of the work presented in this dissertation it is assumed that the plasma potential is the only time dependent quantity. Due to its periodic nature the plasma potential can be expanded in a Fourier cosine series

$$\phi_p(t) = \phi_{p0} + \tilde{\phi}_p(t)\,. \tag{4.4}$$

Where ϕ_{p0} and $\tilde{\phi}_p(t)$ are the time independent and dependent components respectively. The time dependent component is given by

$$\tilde{\phi}_p(t) = \sum_{n=1}^{\infty} \phi_{pn} cos(\omega t + \theta_n)$$

and has a time average of zero. Therefore the time averaged plasma potential is given by ϕ_{p0}. The electron density n_e, electron temperature kT_e, and time averaged plasma potential ϕ_{p0} are determined from a fit to the I-V characteristic obtained with an RF compensated Langmuir probe. The time dependent component of the plasma potential $\tilde{\phi}_p(t)$ is measured by a capacitive probe.

4.3.1 RF Compensated Langmuir Probe

In discharges driven in the RF range of frequencies the plasma parameters can have a substantial time dependence, especially the plasma potential. In this frequency range a typical Langmuir probe, regardless of the compensation, cannot be used to accurately determine these time dependent parameters [20]. This is due to the fact that displacement currents are induced that cannot be discriminated from the real current driven by the time dependent electron density and temperature. Therefore in this frequency range a typical Langmuir probe should only be implemented to measure the time averaged properties when the time dependence of these parameters is weak. The magnitude of the time dependence of the plasma potential is not a limiting factor for the RF compensated Langmuir probe. Here we assume that the electron density and temperature are time independent and therefore the use of a Langmuir probe is justified.

The I-V characteristic of a typical Langmuir probe in a time independent plasma with an electron density and temperature of 10^{18} m^{-3} and 5 eV respectively is given by Figure 4.25.

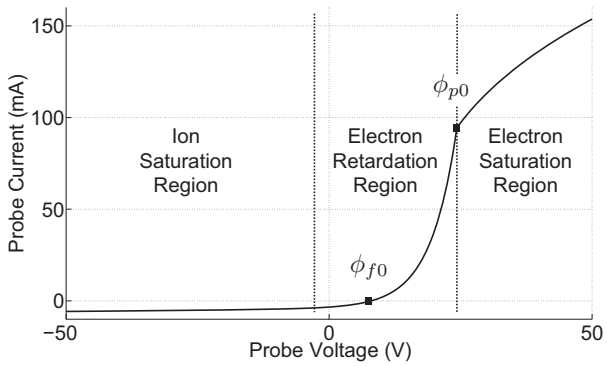

Figure 4.25: I-V characteristic of typical Langmuir probe.

The I-V characteristic is categorized into three regions: ion saturation, electron retardation, and electron saturation [143]. The ion and electron saturation regions correspond to collection of only ion and electron species respectively. The electron retardation region is a transition region in which both ion and electron species are collected. Typically the ions are cold and thus a discrete transition from electron retardation to saturation occurs at the plasma potential ϕ_p. An important point on the I-V characteristic is the floating potential ϕ_f which occurs at $I(\phi_f) = 0$. The floating potential corresponds to a balance in ion and electron current to the probe.

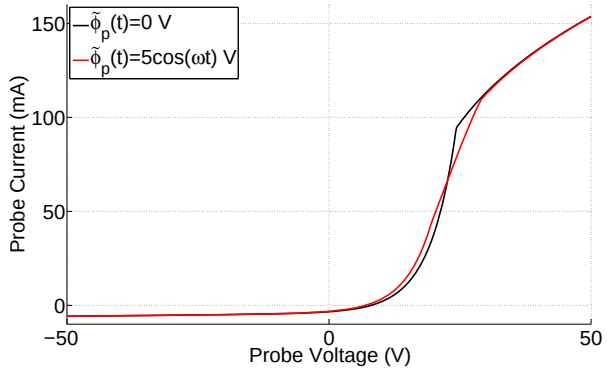

Figure 4.26: Effect of the time dependent plasma potential on I-V characteristic of the Langmuir probe.

In order to accurate measure the electron density and temperature in a discharge having a substantial time dependent plasma potential the Langmuir probe must be compensated. This is achieved by biasing the Langmuir probe tip actively or passively at a potential equivalent to that of the plasmas time dependent component. Thus when the compensation is complete no current is drawn due to the time dependent component of the plasma potential because the Langmuir probe is

oscillating in unison. Compensation is required because the I-V characteristic of an uncompensated Langmuir probe will have an altered shape and a negatively shifted floating potential [143, 91]. Figure 4.26 depicts these effects on the I-V characteristic obtained in a plasma with an electron density and temperature of 10^{18} m^{-3} and 5 eV respectively.

The alteration of the I-V characteristic can be summarized by the following three traits: negative shift in the floating potential, decrease in the slope of the electron retarding region, and positive shift in the plasma potential. These effects are easily realized by plotting the instantaneous I-V characteristic at the extreme values of the plasma potential as given by Figure 4.27. The red and black curves are associated with the instantaneous values of the time dependent component of the plasma potential given by $\tilde{\phi}_p(t_\pm) = \pm 5$ V and $\tilde{\phi}_p(t_o) = 0$ V respectively.

Figure 4.27 shows that the shape of the instantaneous I-V characteristics are equivalent and equal to that associated with $\tilde{\phi}_p(t) = 0$ V plotted on Figure 4.26. Additionally the I-V characteristics are shifted on the voltage axis by the corresponding instantaneous value of the plasma potentials time dependent component. The I-V characteristic measured by the uncompensated Langmuir probe is obtained by averaging over time. This is carried out discretely by averaging the instantaneous I-V characteristics. The traits described above can be easily conceptualized by averaging the three curves presented by Figure 4.27.

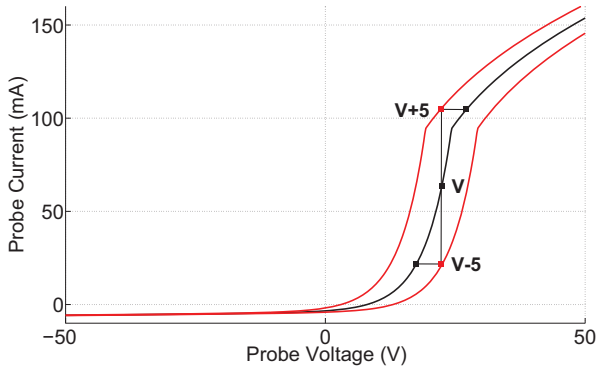

Figure 4.27: Instantaneous I-V characteristic of the Langmuir probe associated with $\tilde{\phi}_p(t_\pm) = \pm 5$ V and $\tilde{\phi}_p(t_o) = 0$ V.

In order eliminate these parasitic effects from the I-V characteristic the Langmuir probe must be actively or passively compensated. Active compensation requires biasing the Langmuir probe tip with a externally generated voltage waveform equivalent to that of the time dependent component of the plasma potential. This is nontrivial to implement due to the required accurate measurement and reconstruction of the time dependent component plasma potential which typically has significant harmonic content [102]. Passive compensation is based on the same principal and can be imple-

mented by high impedance circuit elements in combination with an internally generated voltage waveform. Typically this is carried out by LC chokes resonant at the plasma potential frequency and a self compensating electrode respectively [141, 28].

It has been shown that due to the sheath impedance compensation by LC chokes is insufficient for low electron density plasmas or when the magnitude of the time dependent component of the plasma potential is large [141]. This is due to the fact that the LC choke and sheath impedance are in series and thus act as a voltage divider. Therefore as the sheath impedance is increased compensation by LC chokes becomes ineffective because its impedance is limited to the MΩ range due to stray capacitance [141]. In this situation compensation must be carried out by the use of a self compensating electrode.

The Langmuir probe utilized for these experiments is only compensated with LC chokes due to the small dimensions of the discharge. Effects from incomplete compensation on the plasma parameters determined from the I-V characteristic will be investigated below. The schematic of the RF compensated Langmuir probe utilized for this work is given in Figure 4.28.

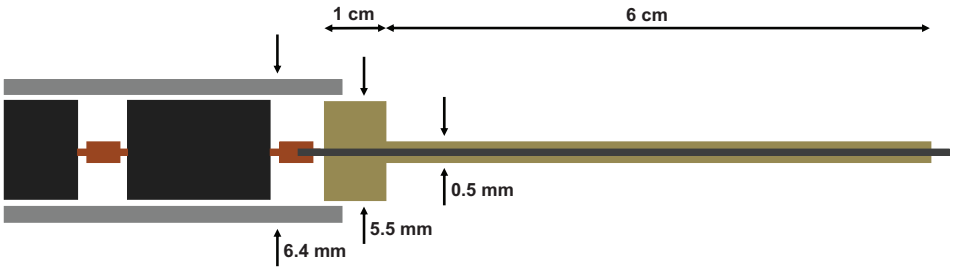

Figure 4.28: Schematic of RF compensated Langmuir probe.

The RF compensated Langmuir probe consists of two sections. This was done to minimize shadowing of the ECW generated plasma from the RF biased electrode and perturbations. The first section interfaces with the plasma and was designed to have the smallest diameter possible. This section consists of a 0.125 mm in diameter tungsten wire sleeved in an alumina shroud having an inner diameter of 0.3 mm and an outer diameter of 0.5 mm. The total length of this section is 6 cm. At the end of the first section 1 mm of tungsten wire is exposed which consists of the current collecting probe tip. For the perpendicular field configuration the probe tip was bent 90° such that probe tip was aligned perpendicular to the magnetic field lines. The tip length was chosen to be approximately eight times the diameter in order to minimized finite length effects on the I-V characteristic [77]. The second section is 25 cm in length and consists of a stainless steel tube with an outer diameter of 6.4 mm. This section houses the LC chokes and interfaces with the vacuum chamber by use of a Wilson seal.

The Langmuir probe was compensated with six LC chokes connected in series: three resonant at 13.56 MHz and three resonant at 27.12 MHz. The transmission coefficient S_{12} of the RF compensated Langmuir probe was measured using a network analyzer with an S-parameter test set. The impedance was calculated from Eq. 4.2 using S_{11}=1-S_{12} and is presented in Figure 4.29.

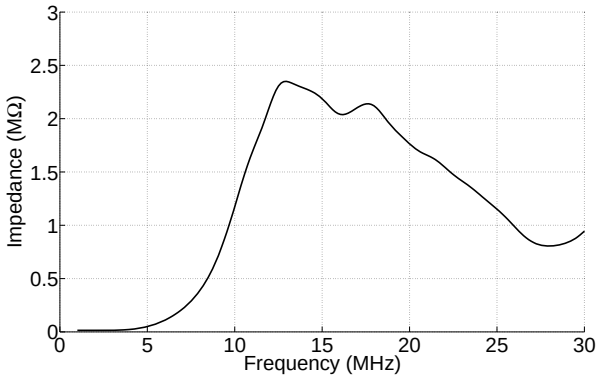

Figure 4.29: Impedance of RF compensated Langmuir probe.

The impedance at 13.56 MHz is 2.3 MΩ and at 27.12 MHz is 850 kΩ. In order for the probe tip to follow the time dependent component of the plasma potential the LC choke impedance must be much greater then that of the sheath according to

$$|Z_c| \gg |Z_s| \left[\frac{e\phi_p}{kT_e} - 1 \right] \tag{4.5}$$

[141]. Where the sheath impedance is given by

$$|Z_s| = R_s \left[1 + (\omega C_s R_s)^2 \right]^{-1/2} \tag{4.6}$$

The sheath resistance R_s and capacitance C_s are approximated by

$$R_s = \frac{2\lambda_D^2}{\epsilon_o A} \left[\frac{M_i}{kT_e} \right]^{1/2} \tag{4.7}$$

and

$$C_s = \frac{\epsilon_o A}{2^{7/4}\lambda_D} \left[\frac{e}{kT_e} \left(\phi_p - V \right) \right]^{-3/4} \tag{4.8}$$

respectively. Where the plasma potential ϕ_p and the probe potential V in the above are taken at a time that results in the maximum and minimum values respectively. This is done such that the minimum sheath capacitance is calculated which results in the largest sheath impedance. The

sheath resistance and capacitance is calculated for the applicable range of electron density and temperature and is presented in Figure 4.30. The Langmuir probe tip dimensions were taken as those presented above.

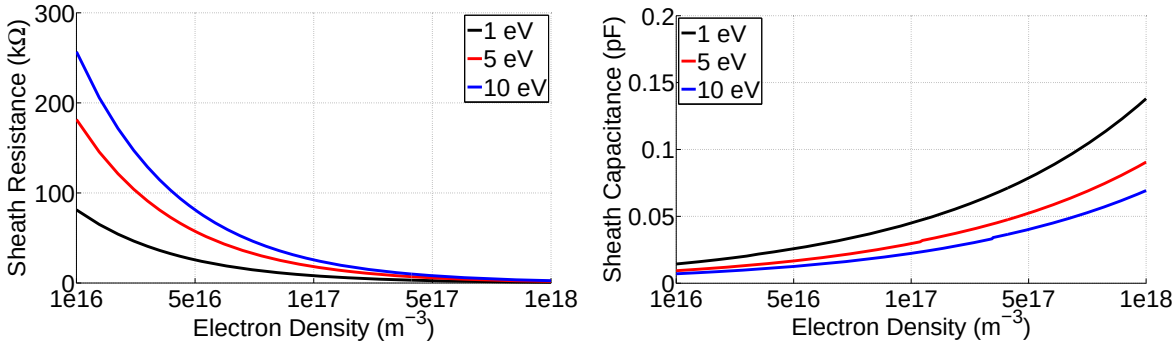

(a) (b)

Figure 4.30: RF compensated Langmuir probe sheath (a) resistance and (b) capacitance.

The sheath capacitance is small enough that $|Z_s| \approx R_s$ is a very good approximation. Assuming that $\phi_p = 30$ V and that $kT_e = 5$ eV requires that the choke impedance be much greater then five times the sheath impedance according to Eq. 4.5. The sheath resistance given in Figure 4.30a indicates that the plasma density must be greater then $5 \cdot 10^{16}$ m^{-3} for the LC chokes to effective compensate the Langmuir probe.

The RF compensated Langmuir probe is powered by a Kepco bipolar power supply with a gain of -9.9. The Kepco power supply is driven by either a modified triangle or square waveform depending on the mode of operation. The two waveforms where used to measure the I-V characteristics and ion saturation current respectively. The waveform is constructed by the DStarVE control software and generated by a National Instruments PXI-6251 data acquisition board.

The modified triangle waveform consists of the standard having flattened maximums and minimums, referred to as the dead time because the corresponding data is discarded. The sweep and dead time are programmable and set to 70 and 10 ms respectively. These values give an acceptably low displacement generated from the lead coaxial cable capacitance. The maximum and minimum amplitude of the waveform is programmable and typically set such that the RF compensated Langmuir probe would swing from -50 to 20 V. The square waveform has a programmable amplitude and is typically set to -50 V. The delay and length of each waveform is programmable and set to collect data during steady state operation.

The probe current is measured across a variable resistor, the voltage drop across this resistor is fed into an Analog Electronic isolation amplifier with a gain of 33.3. The output of the isolation

amplifier is sampled and digitized by a National Instruments PXI-6251 data acquisition board. The acquired data is preprocessed by the DStarVE control software and analyzed post-experiment utilizing a computer program written in MATLAB. The schematic of the Langmuir probe circuit is given in Figure 4.31.

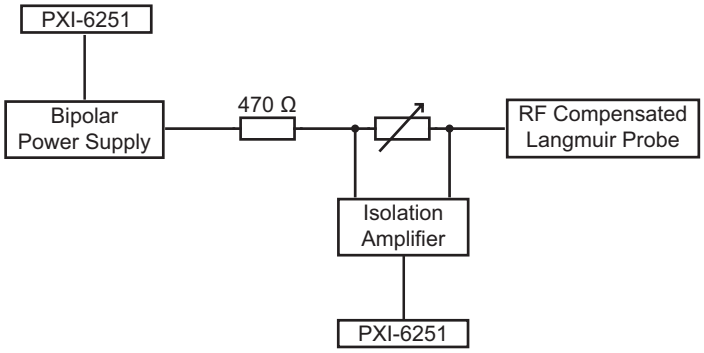

Figure 4.31: Schematic of RF compensated Langmuir probe experimental setup.

The electron density, electron temperature, and time averaged plasma potential where determined from the I-V characteristic by fitting the experimental data to the theory. The Langmuir probe theory utilized to fit the data is that derived from Laframboise for non magnetized plasma [92]. Laframboise conducted simulations of the ion and electron current to the ideal cylindrical and spherical Langmuir probes. The electrons and ions were taken to have Maxwellian distribution functions, for our purposes we will utilize the cold ion approximation $kT_i \approx 0$. The simulation results obtained by Laframboise have been semi-empirically fit and will presented below [86, 115]. Assuming that the RF compensation is complete, that is $\phi_p(t) = \phi_{p0}$, the probe current is given by

$$\begin{aligned} I &= i_- - i_+ \qquad \text{for} \qquad V < \phi_p \\ I &= i_- \qquad\quad\ \ \text{for} \qquad V \geq \phi_p \,. \end{aligned} \tag{4.9}$$

Where i_- and i_+ are the electron and ion current respectively. The electron and ion current are dependent on the ratio of the probe tip radius to the Debye length, $X = r_p/\lambda_D$. The electron current is given by

$$i_- = e\, n_e A \left(\frac{kT_e}{2\pi m_e}\right)^{1/2} \left[1 + \chi_e \frac{e\left(V-\phi_p\right)}{kT_e}\right]^{\eta_e} \,. \tag{4.10}$$

Where χ_e and η_e are empirical functions of X given by

$$\chi_e = e^{C_1 + C_2 X + e^{C_3 + C_4 X + C_5 X^2}}$$

and

$$\eta_e = C_6 + e^{C_7 + C_8 X + C_9 X^2}$$

respectively. For $X \leq 2.5$ the ion current is given by

$$i_+ = e\, n_e A \left[\frac{2 Z_i}{\pi^2 M_i} e\left(\phi_p - V\right) \right]^{1/2} \tag{4.11}$$

and is independent of X. For $X \geq 3.5$ the ion current is given by

$$i_+ = e\, n_e A_p \left[\frac{Z_i k T_e}{2\pi M_i} \right]^{1/2} \chi_i \left[\frac{e\left(\phi_p - V\right)}{k T_e} \right]^{\eta_i} . \tag{4.12}$$

Where χ_i and η_i are empirical functions of X and are given by

$$\chi_i = 1 + C_{10} X^{C_{11}}$$

and

$$\eta_i = C_{12} \left(X + C_{13}\right)^{C_{14}}$$

respectively. The ion current cannot be expressed in simple empirical expressions for $2.5 \leq X \leq 3.5$. The constants associated with the empirical functions are given in Table 4.2.

Table 4.2: Constants associated with the empirical fit to the Laframboise results.

Electron Current Constants	**Value**
C_1	-0.09165
C_2	-0.5008
C_3	-0.853076
C_4	-0.275077
C_5	-0.58100
C_6	0.22905
C_7	-1.328512
C_8	-0.068044
C_9	-0.006374

Ion Current Constants	**Value**
C_{10}	0.636996
C_{11}	-0.655816
C_{12}	1.5590047
C_{13}	3.772423
C_{14}	-0.6791809

A magnetic field can significant alter the I-V characteristic of a Langmuir probe due to altered orbital motion of the electrons and ions and strongly anisotropic transport coefficients [34]. The extent to which the I-V characteristic is altered depends on the ratio of the electron and ion Larmor radii to that of the Langmuir probe. There are three regimes: the weak, intermediate, and strong magnetic field. In the weak magnetic field regime both the electrons and ions have Larmor radii much greater then the Lagnmuir probe radius and the unmagnetized theory can be applied. In the intermediate field regime only the electrons have a small Larmor radius in comparison to the Langmuir probe radius and thus the unmagnetized theory can be applied to the ion current. In the strong magnetic field regime both the electron and ion Larmor radii are small compared to the Langmuir probe radius and the magnetized theory must be applied.

To determine the applicable theory utilized in fitting the I-V characteristic the Larmor radii of a hydrogen ion, helium ion, and electron are calculated. The maximum magnetic field seen by the Langmuir probe is 1020 Gauss and will be used for a conservative approach. The Larmor radius is calculated for the hydrogen ions assuming they have a temperature of 1 eV. This non-zero value is due to Frank-Condon dissociation of the molecule [14]. The Larmor radius is calculated for the helium ions assuming that they are at room temperature due to the fact the ionization comes from electron impact and the momentum transfer is negligible. The Larmor radius for the electrons is calculated assuming a temperature of 3 eV. The Larmor radii are thus: 1.6, 0.5, and 0.065 mm for hydrogen, helium, and the electron respectively. The probe radius is 0.125 mm thus giving ratios of 12.8, 4, and 0.52. Thus it is determined that we are in the intermediate magnetic field regime where the ion orbits are not effected by the magnetic field but the electron orbits are. In addition caution must be taken when the Langmuir probe is biased above the floating potential. This is due to the fact that the electron Larmor radius is less then that of the Langmuir probe which can potentially cause plasma perturbations [30].

The electron current to the probe in the intermediate magnetic field regime is assumed to be proportional to the expression given by Eq. 4.9. This approximation is made due to the fact the electron saturation current was found to scale proportionally with the square root of the electron transport coefficient [29, 142]. The proportionality constant multiplied by the electron collection current is absorbed by the probe area for simplicity and is referred to as the electron collection area A_e. The electron transport coefficient is strongly dependent on the magnetic field intensity and the electron temperature. Therefore the electron collection area is allowed to be a fit variable such that the entire I-V characteristic can be utilized.

In order to fit the I-V characteristic of the Langmuir probe a computer program was written in MATLAB. The fitting routine utilizes the theory presented above and the same algorithm as described in Section 3.4. The fit variables are the electron density, electron temperature, and the collection area for the electrons.

In order to estimate the error associated with an under compensated Langmuir probe the I-V

characteristic of Figure 4.26 having $\tilde{\phi}_p(t) = 5\cos(\omega t)$ V is fit. The fit is presented in Figure 4.32.

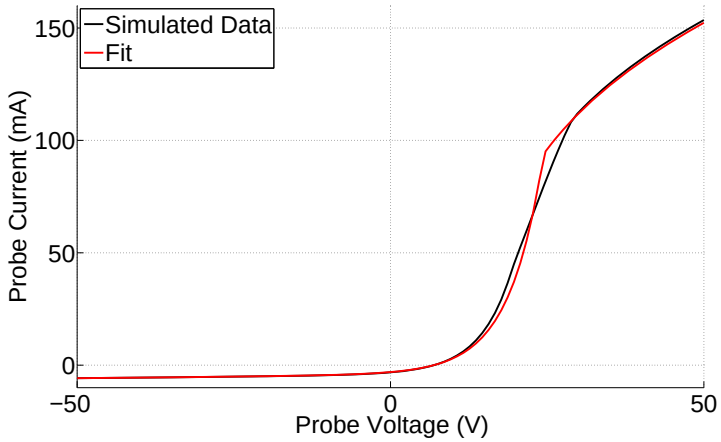

Figure 4.32: Fitted I-V characteristic from under compensated Langmuir probe.

The modeled and fit plasma parameters are presented in Table 4.3.

Table 4.3: Under compensated I-V characteristic fit results.

Plasma Parameter	**Modeled**	**Fit**	**Error**
$n_e\ (10^{18}\ m^{-3})$	1.0	0.96	4 %
$kT_e\ (eV)$	5.0	5.4	8 %
$\phi_f\ (V)$	8.0	6.9	14 %
$\phi_p\ (V)$	24.2	24.4	1 %

The fitted results indicate that the electron temperature and floating potential are most severely altered. It is expected that the error associated with electron density will be ≤ 10 % and the error associated with the electron temperature to be ≤ 25 %. These conservative estimates are taken by combining the error induced by incomplete RF compensation with that associated with having A_e as a fit variable. The latter error will be discussed in Section 5.1.3.

4.3.2 Capacitive Probe

The plasma potential can directly measured by use of an emissive probe, however the response in the RF range of frequencies is undesirable. A capacitive probe has an excellent response in this range and is easily calibrated as a function of frequency [131, 27]. Assuming that the capacitance between the plasma and probe tip is small the capacitive probe measures the time dependent

component of the floating potential [130]. Furthermore if the electron density and temperature are time independent, the floating and plasma potentials have equivalent time dependent components [69]. Therefore the capacitive probe was selected for an indirect measurement of the time dependent component of the plasma potential based on its frequency response.

The capacitive probe consists of an RG405/U semi-rigid coaxial cable having inner and outer conductor diameters of 0.5 and 2.2 mm respectively. The coaxial cable is sleeved with an alumina shroud with an inner diameter of 2.5 mm and an outer diameter of 3.9 mm. At the tip of the probe the coaxial cable extends 3.5 mm past the alumina shroud, the dielectric and outer conductor were removed and the inner conductor was sleeved with an alumina shroud having an inner diameter of 1 mm and an outer diameter of 1.6 mm. The tip was vacuum sealed with high temperature epoxy. The atmospheric end of the probe was vacuum sealed with standard epoxy and mounted in a stainless steel tube with an outer diameter of 6.4 mm. The stainless steel tube interfaced with the vacuum chamber by use of a Wilson seal. The overall length of the probe was 20 cm. The atmospheric end of the probe was terminated with a male BNC connector. This was done such that the 50 Ω impedance would be maintained throughout the entire probe. Figure 4.33 gives the schematic of the capacitive probe.

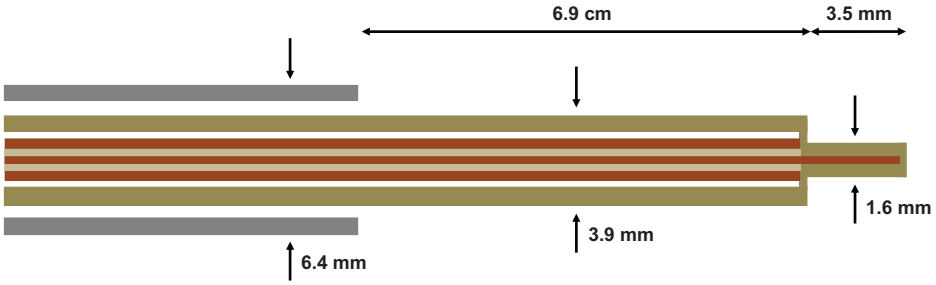

Figure 4.33: Schematic of the capacitive probe.

The capacitive probe was calibrated similarly to the method implemented by Caughman [27] using a network analyzer with an S-parameter test set. To calibrate, port 1 of the S-parameter test set was connected to a coaxial cable terminating on the probe via a female to female adapter. This coaxial cable is utilized to connect the probe to the oscilloscope during the measurements. It is important to include the exact coaxial cable length in the calibration because of the anticipated high harmonic content. The probe tip was inserted into a female N-type connector which in turn was connected to port 2 of the S parameter test set. The transmission coefficient was measured as a function of frequency ranging from 1 to 250 MHz. The calibration curves consist of the magnitude and phase of the transmission coefficient and are given in Figure 4.34.

As seen by Figure 4.34 the sensitivity of the capacitive probe increases by over three orders of magnitude for the frequency range investigated. This indicates the importance of calibrating as a function of frequency. The waveform measured by the capacitive probe is calibrated by first taking the Fourier transform. The expansion coefficients are corrected utilizing the data given in Figure 4.34 and the inverse Fourier transform is taken to arrive at the calibrated waveform.

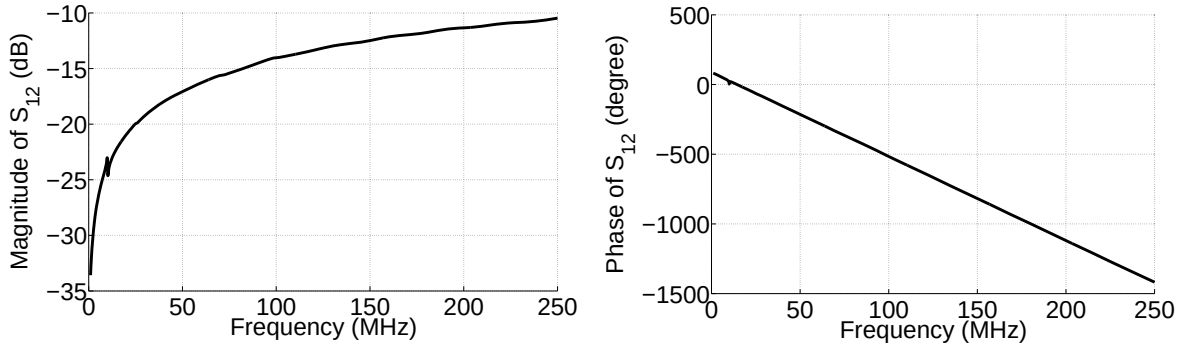

(a) (b)

Figure 4.34: Capacitive probe transmission coefficient (a) magnitude and (b) phase.

The capacitive probe waveform is sampled and digitized utilizing a TDS 2024 oscilloscope terminated to 50 Ω. The oscilloscope connects with the National Instruments platform by use of a GPIB interface. The DStarVE control software reads the oscilloscope and preprocesses the data. Calibration and analysis of the data is conducted utilizing a computer program written in MATLAB post-experiment.

4.4 Control and Data Acquisition

This section describes the hardware and software used to control the instrumentation and acquire the desired signals. The system is governed by a National Instruments PXI-8105 controller based on the PCI eXtensions for Instruments (PXI) platform. The utilized PXI hardware is as follows. A PXI-6251 data acquisition board is used to sample and digitize the analog signals of interest and to generate the waveforms driving the various experimental equipment and diagnostics. A PXI-GPIB controller is utilized to control and read a TDS 2024 oscilloscope. A PXI-8252 IEEE 1394 host adapter controls a camera used to monitor the discharge. To control the hardware and write the acquired data to files a program was written in the National Instruments LabVIEW software. A graphical user interface (GUI) was designed to access the set points.

The only components of the experiment that are actively cooled are the magnetic field coils. To maintain steady state conditions over long run times the system must be pulsed with a low duty

cycle, typically 25 % depending on the RF and microwave power levels. The shot time is dictated by that required to obtain an adequate spectral line profile signal to noise ratio, typically 50 to 300 seconds. A shot is defined as the conglomeration of all the discharge pulses, referred to as trigger events, utilized to determine the RF sheath electric field. The discharge pulse length was set to the maximum value in which steady state conditions could be maintained over the pulse, typically 10 seconds. Thus between 5 and 30 trigger events are need per spectral line profile acquisition. As will be discussed in Chapter 5 thirty spectral line profiles are utilized to determine the RF sheath electric field. Therefore a shot typically consists of 150 to 900 trigger events. Depending on the RF power level, microwave power level, and working pressure of the discharge being investigated a shot requires four to eight hours of operational time. Thus the need for a pulsed automated system is realized. A subsection of the GUI is presented in Figure 4.35, showing the system indicators and all of the possible set points.

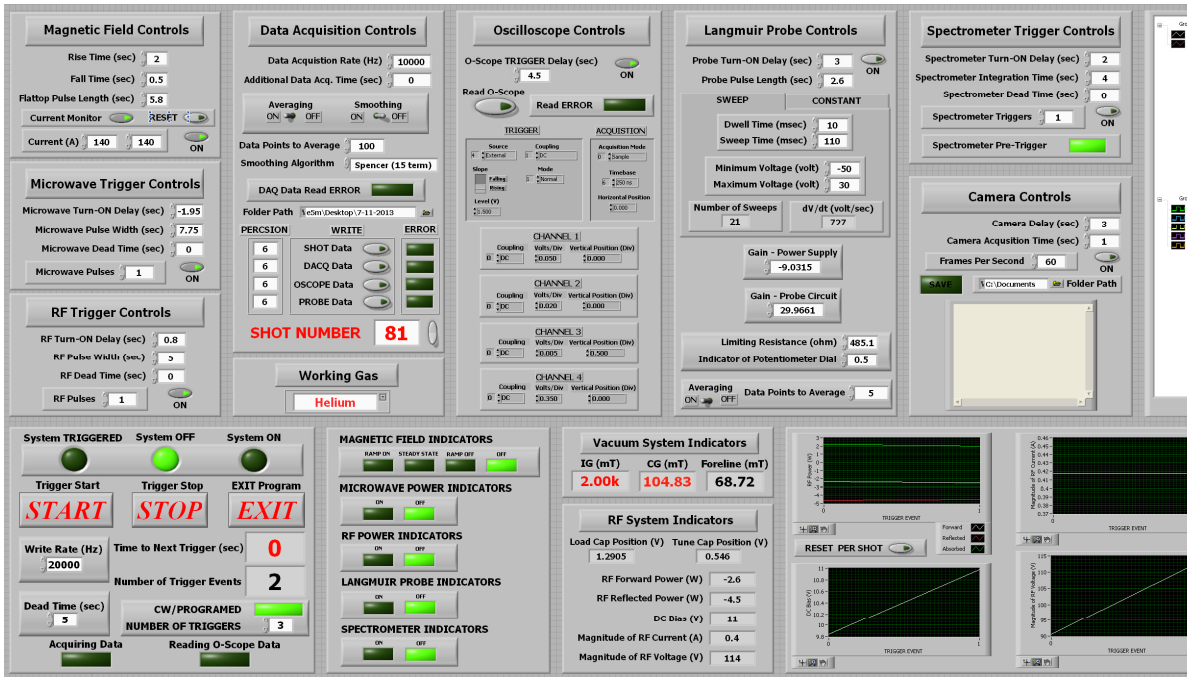

Figure 4.35: DStarVE LabVIEW control panel.

In addition the GUI provides monitoring of the discharge per trigger event by plotting the acquired signals. The steady state condition is monitored over the entire shot by plotting the signal average as a function of trigger event. Vacuum system pressure is monitored during the dead time.

Two analog waveforms were constructed within the DStarVE control software. The first driving the magnetic field coil power supplies and the second driving that of the Langmuir probe. The

magnetic field coil power supplies were controlled by a ramped square waveform described in Section 4.1. The Langmuir probe power supply is driven by either a modified triangle or square waveform described in section 4.3.1. Five logic waveforms were constructed with the software controlling the microwave and RF power supplies output state, oscilloscope and spectroscopic system triggering, and camera acquisition state. The delay and pulse width are programmable for all of the logic waveforms with the exception of that of the oscilloscope whose pulse width is set to 1 ms. The number of trigger events per spectral line profile acquisition and corresponding dead time are programmable. The analog and logic waveforms constructed by the control software are presented in Figure 4.36 corresponding to a single trigger event.

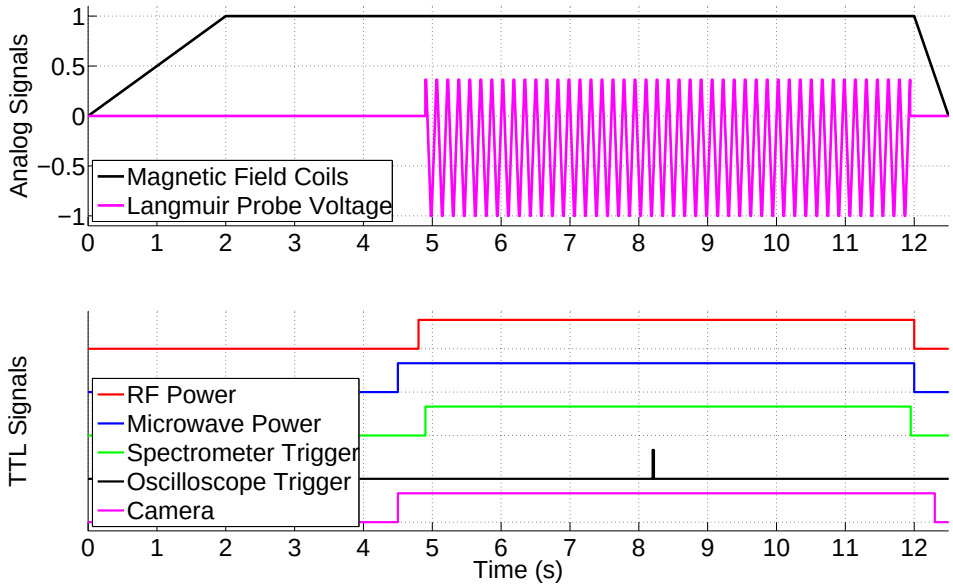

Figure 4.36: Control software generated signals.

Figure 4.36 gives the typical ordering of the waveforms. The magnetic field is given a couple of seconds to reach steady state. Microwave power is turned on prior to the RF power to allow plasma equilibrium to be reached. The spectroscopic system is triggered and Langmuir probe is powered within the RF power pulse.

Sixteen analog signals are sampled and digitized. Twelve of which have a characteristic frequency that can be captured within the sampling limits of the PXI-6251 while the remaining four must be acquired with an oscilloscope. The analog signals obtained with the PXI-6251 were the chamber pressure measured by ion and convectron gages, foreline pressure, current of magnetic field coils, Langmuir probe current and voltage, reflected and forward microwave power, tune and load capacitor positions, and the DC voltage of the RF biased electrode. These signals were sampled at 10 kHz.

In order to filter the noise every 100 data points were averaged yielding an acquisition rate of 100 Hz. The analog signals obtained with the oscilloscope were the RF voltage and current waveforms and reflected and forward RF power. The oscilloscope parameters were set within the GUI, typically a timebase of 250 ns was utilized. The capacitive probe voltage was only measured for a limited number of experiments. For this measurement the reflected RF power channel was replaced with the capacitive probe. The oscilloscope data is read by the control software. The resulting sixteen signals are acquired per trigger event and preprocessed in terms of calibrating, filtering, and organizing. At the conclusion of the programed number of trigger events the stored preprocessed data is written to text files. An additional text file is generated containing all of the experimental set points.

CHAPTER

5

EXPERIMENT AND ANALYSIS

In Chapter 4 the experimental apparatus, DStarVE, utilized to generate the capacitively coupled magnetized RF sheath was discussed. Following, the spectroscopic equipment utilized to implement time averaged passive OES to measure the RF sheath electric field was presented and characterized. In addition, Chapter 4 included the presentation and discussion of the diagnostics utilized to characterize the discharge in terms of various electrical and plasma parameters. The conclusion contained a description of the National Instruments hardware and software utilized to control and automate the experiment.

This chapter presents the analysis and select results associated with the experiments conducted on DStarVE. The primary purpose of these experiments is to measure the time dependent electric field topology of the capacitively coupled magnetized RF sheath utilizing the time averaged spectral line profile. The results presented in this chapter include those associated with the electrical and plasma parameters, however the RF sheath electric field results are reserved for Chapter 6. The chapter is structured as follows: Section 5.1 presents the experimental scenario and characterization of a typical DStarVE discharge utilizing the capacitive and RF compensated Langmuir probes. Section 5.2 presents select time averaged spectral line profiles obtained in the RF sheath and the associated fit preprocessing. Section 5.3 presents the phase resolved measurements utilized to determine the time dependent emission intensity. Section 5.4 presents the methodology associated with the analysis of the time averaged spectral line profiles.

A total of 28 discharges, with varying experimental conditions, were investigate and characterized

in terms of electrical parameters, plasma parameters, and RF sheath electric field. The electrical parameters were measured by use of the DC and I-V probes as described in Section 4.1. The plasma parameters were measured by the use of the capacitive and RF compensated Langmuir probes as described in Section 4.3. The RF sheath electric field was determined through a fit to time averaged π and σ spectral line profiles obtained by the spectroscopic system described in Section 4.2.

To measured the topology of the RF sheath electric field the π and σ profiles where measured as a function of z, the distance from the RF biased electrode surface. Fifteen spatial locations were investigated along the z-axis evenly spaced from 0.8 to 7.9 mm for the parallel field configuration and 0.9 to 8.1 mm for the perpendicular field configuration. Thus acquisition of thirty spectral line profiles were required for each shot. To gain insight into the RF sheath electric field dependence on the operating conditions a total of 28 discharges were investigated, 16 and 12 for the parallel and perpendicular field configurations respectively. For the parallel field configuration two pressures were investigated, for each pressure a high and low density case was investigated. Control of the density was obtained through the microwave power level set point. For each pressure and density regime two RF power levels were investigated. Finally, two working gases were considered: Hydrogen and Helium. For the perpendicular field configuration the same experimental scenario was applied for helium but only one pressure was investigated for hydrogen.

5.1 Discharge Characterization

This section describes the experimental scenario utilized to measure the RF sheath electric field and presents the characterization of the investigated discharges in terms of electrical and plasma parameters. In addition measurements obtained from the capacitive and RF compensated Langmuir probes characterizing typical DStarVE discharges in terms of the spatial distribution of the plasma parameters along the x-axis is presented. The uniformity of the plasma parameters along the x-axis was investigated because of its effect on the electric field along the line of sight of the collection optics. In addition the applicability and accuracy of the probe measurements is explored.

5.1.1 Experimental Scenario

A total of 28 discharges were investigated, each with varying experimental conditions, in which the electric field of the RF sheath was measured. Two field configurations were investigated: the first has a geometry such that the RF sheath electric field was parallel to the externally applied magnetic field. The second had a geometry such that the RF sheath electric field was perpendicular to the externally applied magnetic field. A total of 16 discharges, 8 hydrogen and 8 helium, were studied in the parallel field configuration. A total of 12 discharges, 4 hydrogen and 8 helium, were studied in the perpendicular field configuration.

The experiments were designed such that similar conditions were investigated for both working gases. This was carried out by choosing the pressure and DC bias voltage to be the independent variables. To achieve this the RF power was set such that the desired DC bias voltage would be established. The experimental scenario is as follows for the parallel field configuration: two pressures were investigated 200 and 400 mTorr, for each pressure a high and low density case was investigated. The low density case was obtained by operation of only the RF source while the high density case was obtained by the addition of the ECR source. For each pressure and each density regime two RF power levels were investigated. In the perpendicular field configuration the same experimental scenario was investigated for helium with pressures of 100 and 200 mTorr. For the hydrogen discharges only one pressure was investigate: 100 mTorr. Pressures above 200 and 100 mTorr were not able to be investigated for helium and hydrogen respectively due to arcing on the RF biased electrode surface.

The neutral pressure is desired to be on the order of 1 mTorr in order better simulate the collisionality regime near the ICRF antenna and Faraday screen [107]. However, due to the required spectral and spatial resolution the signal to noise ratio at these pressures was found to be extremely low regardless of the integration time. To find the optimum working pressure the intensity of the spectral line was measured as a function of pressure. It was found for the parallel field configuration that a pressure of $\geq$ 200 mTorr was optimal in terms of signal to noise ratio and integration time. For the perpendicular field configuration it was found that pressures $\geq$ 200 mTorr could not be investigated due to the fact arcing on the RF biased electrode occurred, in addition matching became formidable.

The electrical and plasma parameters were measured for each of the 28 discharges, referred to as shots, and are presented in Appendix C. These parameters were measured to aid in the interpretation of the RF sheath electric field results and to provide the boundary conditions required for the modeling presented in Section 2.2. The plasma parameters were measured with the RF compensated Langmuir probe. The DC and RF components of the RF biased electrode voltage waveform were measured with the DC bias and I-V probes respectively. The RF biased electrode current waveform consists only of an RF component because of the series capacitor in the matching network and is measured with the I-V probe. The RF biased electrode voltage and current waveforms are presented in Figure 5.1 for shots 1 and 19 which correspond to hydrogen in the parallel and perpendicular field configurations respectively. Figure 5.1 shows that a negative DC bias is established on the RF biased electrode such that the waveform only spends a small portion of time above zero. This occurs because the discharge is asymmetric in the sense that more electrode surface is grounded then driven [98]. A comparison of the voltage waveform in the parallel and perpendicular field configurations shows that the DC bias voltage is diminished in the latter configuration. To explore the harmonic content of the waveforms the Fourier transform of these waveforms is taken and presented in Figure 5.2.

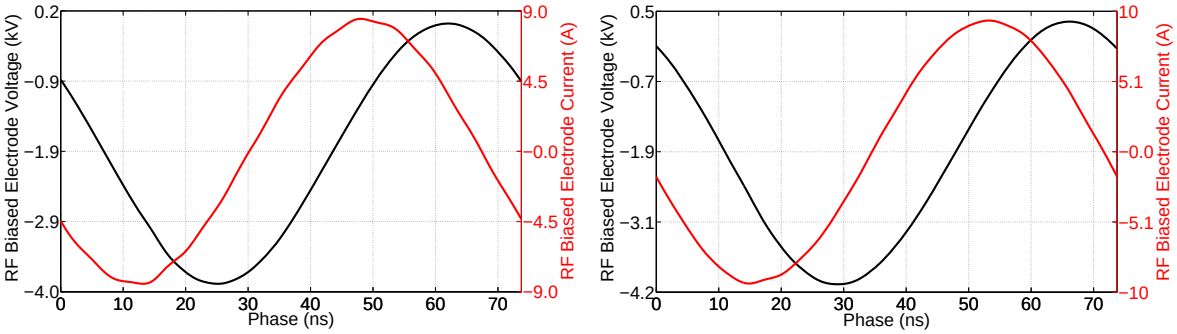

(a) (b)

Figure 5.1: RF biased electrode voltage and current waveforms for shot (a) 1 and (b) 19.

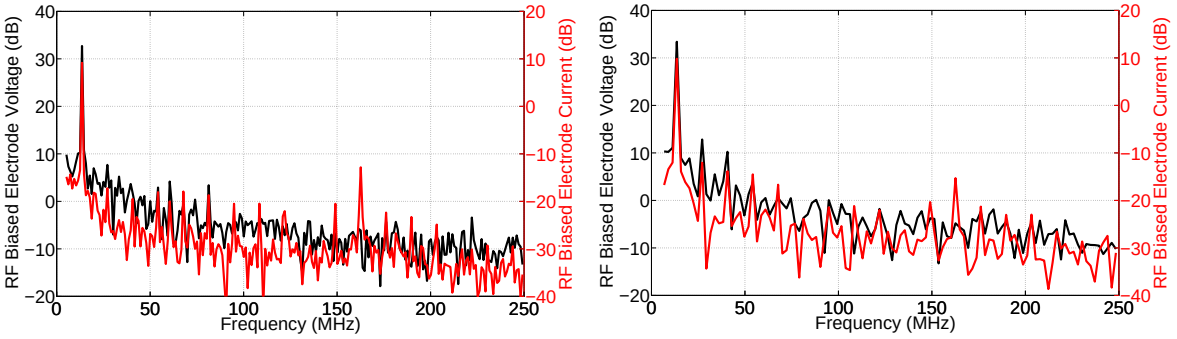

(a) (b)

Figure 5.2: Harmonic spectrum of the RF biased electrode voltage and current waveforms for shot (a) 1 and (b) 19.

The Fourier transform indicates that both the voltage and current waveforms are dominated by the fundamental, this was always found to be the case. In the parallel field configuration both waveforms have a spectrum with harmonics above the noise floor. The current waveform was always found to have a higher intensities of the harmonics. In the perpendicular field configuration essential all of the harmonics are suppressed and has been reported previously in the literature [15].

5.1.2 Capacitive Probe Measurement

The capacitive probe was first utilized to determine if the time dependent component of the plasma potential is negligible in comparison with the voltage waveform at the RF biased electrode surface. The DC and the time dependent components of the RF biased electrode voltage were measured with the DC bias and I-V probes respectively. The capacitive probe measurements were conducted at a spatial location of (0,0,30) mm. The absorbed RF and microwave power was $P_{RF} = 100$ W and $P_{\mu W} = 0$ W respectively. The discharge pressure was $P = 200$ and 100 mTorr for the parallel and

perpendicular field configurations respectively. Figure 5.3 and Figure 5.4 present these voltage waveforms for the parallel and perpendicular field configuration for both hydrogen and helium discharges.

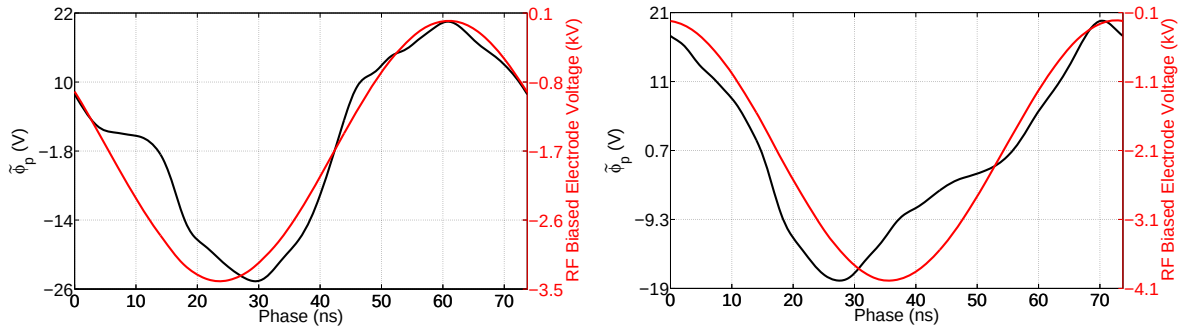

Figure 5.3: Time dependence of plasma potential and RF biased electrode voltage in the parallel field configuration for (a) hydrogen and (b) helium discharges.

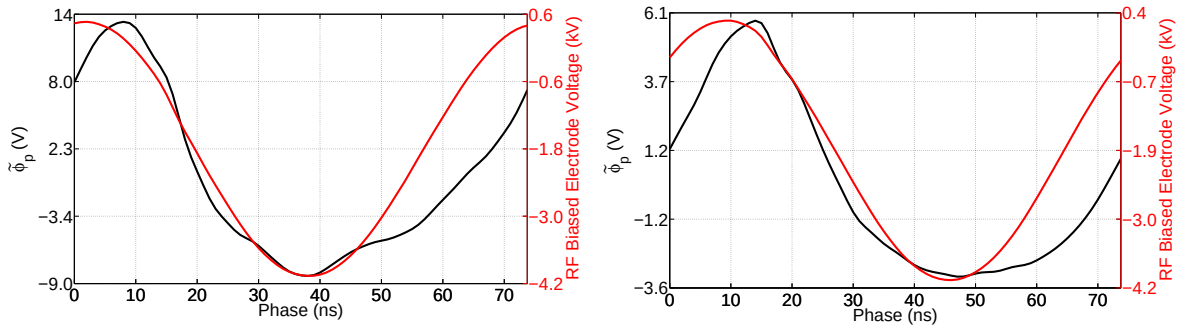

Figure 5.4: Time dependence of plasma potential and RF biased electrode voltage in the perpendicular field configuration for (a) hydrogen and (b) helium discharges.

Comparing the voltage waveforms of Figure 5.3 and Figure 5.4 the time dependent component of the plasma potential is found to be less then the RF biased electrode voltage by more then two orders of magnitude. Due to this large difference the time dependent component of the plasma potential is negligible for both interpretation and modeling of the RF sheath electric field. Therefore the capacitive probe will only be utilized for spatial characterization and to estimate the effectiveness of the RF compensation of the Langmuir probe.

A comparison of the time dependent component of the plasma potential obtained in the parallel field configuration with that in the perpendicular shows that the magnitude is decreased by a factor

of 2 to 3. This arises from the anisotropic mobility of the electron and is expected due to the fact that the capacitative probe is magnetically connected to the RF biased electrode in the parallel field configuration and is not in the perpendicular. The greatly decreased electron mobility in the perpendicular field configuration effectively allows for a larger voltage drop to occur in the RF sheath thus decreasing the time dependent component of the plasma potential.

To check the uniformity of the discharge the capacitive probe was scanned along the x-axis at a distance from the RF biased electrode surface of $z = 30$ mm with y=0 mm for both the parallel and perpendicular field configurations. The experimental conditions were $P = 200$ and 100 mTorr for the parallel and perpendicular field configurations respectively, with an absorbed power of $P_{RF} = 100$ W and $P_{\mu W} = 0$ or 100 W. To present the data the Fourier transform of the waveform was taken and the magnitude of the fundamental was selected. The Fourier transform at a position of $x = 0$ mm with $P_{\mu W} = 0$ is provided by Figure 5.5 for hydrogen and helium discharges in the perpendicular field configuration.

As was evident by the waveforms, the Fourier transform clearly indicates the high level of harmonic content in the spectra. The magnitude of the fundamental was always found to be the strongest component with the first harmonic at least 6 dB down. The trend of the harmonic spectrum is similar for both field configurations.

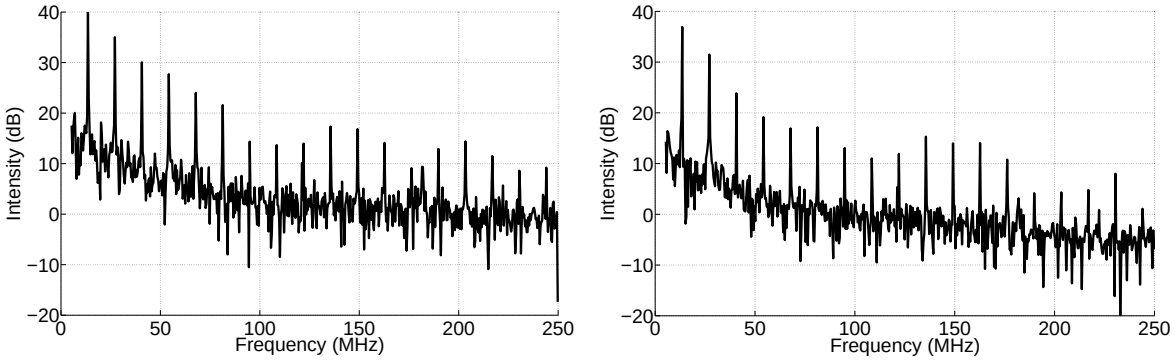

(a) (b)

Figure 5.5: Harmonic spectrum of time dependent component of the plasma potential for (a) hydrogen and (b) helium discharges.

Figure 5.6 presents the magnitude of the fundamental as a function of x-axis position for the parallel field configuration. Measurements were made every 1.6 mm although the 3.5 mm probe tip length dictates the resolution. Therefore it is important to realize the profiles will be significant altered in the sense that features will be averaged over a 3.5 mm window. The $P_{\mu W}$=0 case of Figure 5.6 shows that the time dependence of the plasma potential is peaked and relatively constant over

the RF biased electrode region, $x = -10$ to 10 mm, when considering the 3.5 mm resolution. With the addition of microwave power the time dependence of the plasma potential is decreased and the profile relaxes slightly. The profiles are peaked due to the fact that the probe tip is magnetic connected to the RF biased electrode. Figure 5.7 presents the magnitude of the fundamental as a function of x-axis position for the perpendicular field configuration.

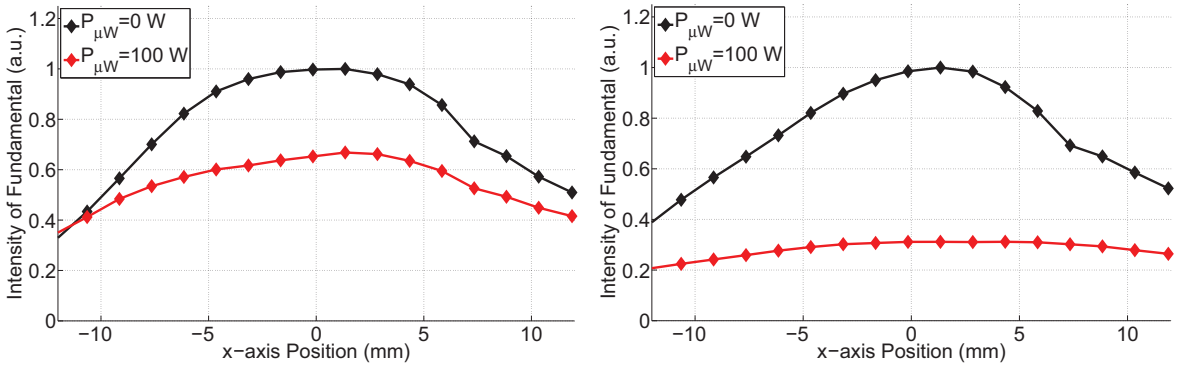

Figure 5.6: Magnitude of the fundamental of the plasma potential as a function of x-axis position in the parallel field configuration for (a) hydrogen and (b) helium discharges.

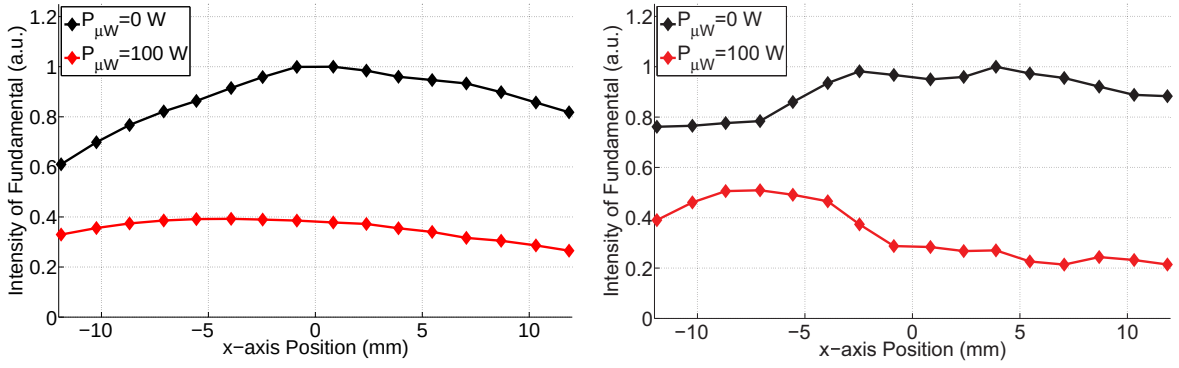

Figure 5.7: Magnitude of the fundamental of the plasma potential as a function of x-axis position in the perpendicular field configuration for (a) hydrogen and (b) helium discharges.

The profiles given by Figure 5.7 show that the magnitude of the fundamental of the plasma potential is relatively constant. As found above, with the addition of microwave power the magnitude decreases. The profiles in the perpendicular geometry are not peaked for two reasons: first the probe

tip is not magnetically connected to the RF biased electrode and second the $\boldsymbol{E} \times \boldsymbol{B}$ force tends to shear the plasma density [123, 15]. The plasma density is difficult to measure without the addition of the ECR source due to the draining of the magnetic flux intersecting the Langmuir probe tip. However carefully conducted measurements show that the absorption of microwave power typically leads to an increase in plasma density, see Appendix C. Therefore Figure 5.6 and Figure 5.7 indicate that the magnitude of the fundamental of the plasma potential is correlated not only to the RF biased electrode voltage but also to electron density.

5.1.3 RF Compensated Langmuir Probe Measurement

The accuracy of the plasma parameters found from Langmuir probe data is highly dependent on LC choke impedance being much greater then that of the sheath. As was discussed in Section 4.3.1 the sheath impedance is a strong function of the electron density. Therefore the electron density will be utilized to determine when the LC choke effectiveness diminishes beyond an acceptable level. The magnitude of the time dependent component of the plasma potential was found not to exceed 30 V and thus will be used as a conservative estimate for the calculation. The acceptable amount of RF voltage dropped in the sheath is taken to be 5 V, as simulated in Section 4.3.1 this gives rise to a 8 % error in kT_e and 4 % error in n_e. The LC choke impedance at 13.56 MHz was found to be 2.3 MΩ thus the sheath impedance must not exceed 90 kΩ assuming $kT_e = 5$ eV. Therefore the electron density must exceed $3 \cdot 10^{16}$ m^{-3} in order to maintain the desired RF compensation. In reality the magnitude of the time dependent component of the plasma potential is significantly less then 30 V, especially for the perpendicular field configuration, resulting in a lower density requirement.

To explorer the effectiveness of the RF compensation, a discharge having a low electron density was investigated. The I-V characteristic was measured in the parallel field configuration at a location of (0,0,30) mm for $P_{RF} = 0$ and 100 W and is presented in Figure 5.8. The working gas was hydrogen at $P = 200$ mTorr with $P_{\mu W} = 100$ W.

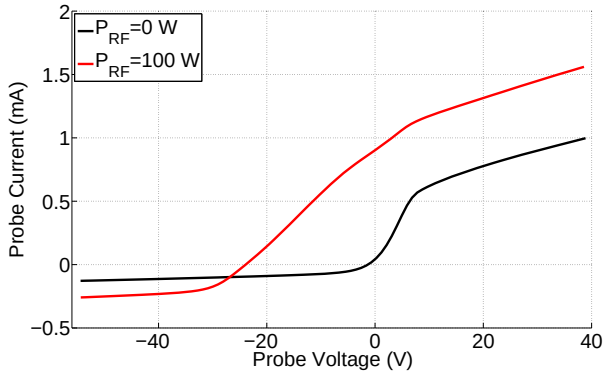

Figure 5.8: I-V characteristic with $P_{RF} = 0$ and 100 W.

The I-V characteristics presented in Figure 5.8 are substantially different. The RF compensation is expected to be significantly incomplete due to the large negative shift in the floating potential and the large decrease in the slope of the transition region. The I-V characteristics were fit and are presented in Figure 5.9. The $P_{RF} = 0$ W discharge was found to have $kT_e = 1.9$ eV while that of the $P_{RF} = 100$ W discharge was found to be 10.5 eV. The addition of RF power is suspected to increase kT_e and alter the electron energy distribution function due to stochastic heating in the RF sheath [97]. However the increase in kT_e from 1.9 eV to 10.5 eV is unrealistic and is partly contributed to incomplete RF compensation. Only the Langmuir probe data for the hydrogen discharges in the parallel field configuration are effected to this level. The remaining Langmuir probe data seems to be adequately RF compensated.

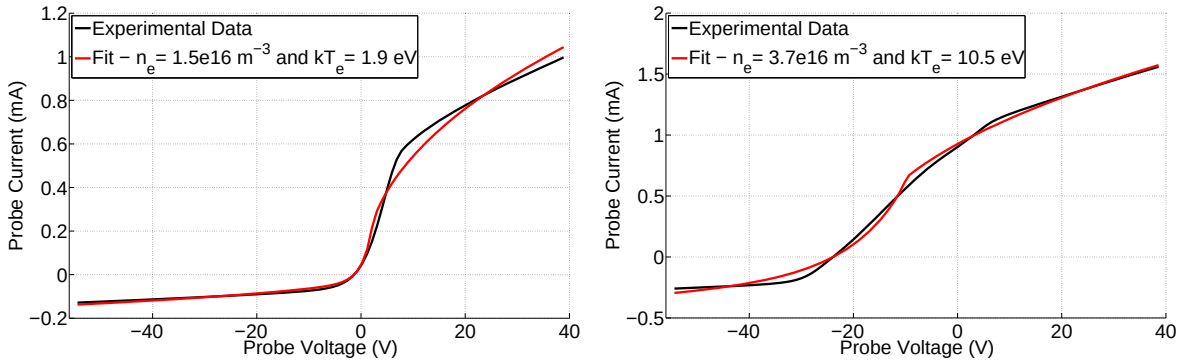

(a) (b)

Figure 5.9: Fitted I-V characteristic with (a) $P_{RF} = 0$ and (b) 100 W.

The electron collection area A_e is typically a fit variable due to the strong dependence of the electron transport coefficient on the magnetic field intensity. However if the electron saturation region of the I-V characteristic cannot be accessed as is the case for high n_e the electron collection area is held fixed at $0.23A_p$, where A_p is the total surface area of the probe tip. This is due to the fact that the ion saturation region has no dependence on A_e and the transition region is only weakly dependent until that of electron saturation is approached.

To show the effect of the magnetic field on the electron transport coefficient an experiment was conducted in which the I-V characteristic was measured as a function of magnetic field intensity. The experiment was conducted in the perpendicular field geometry at a location of (0,0,30) mm with power settings of $P_{RF} = 100$ W and $P_{\mu W} = 0$ W. The working gas was hydrogen at a pressure of $P = 100$ mTorr. Figure 5.10 presents the experimental data for three magnetic field intensities represented by the solid lines, plotted with the associated fit represented by the dashed lines.

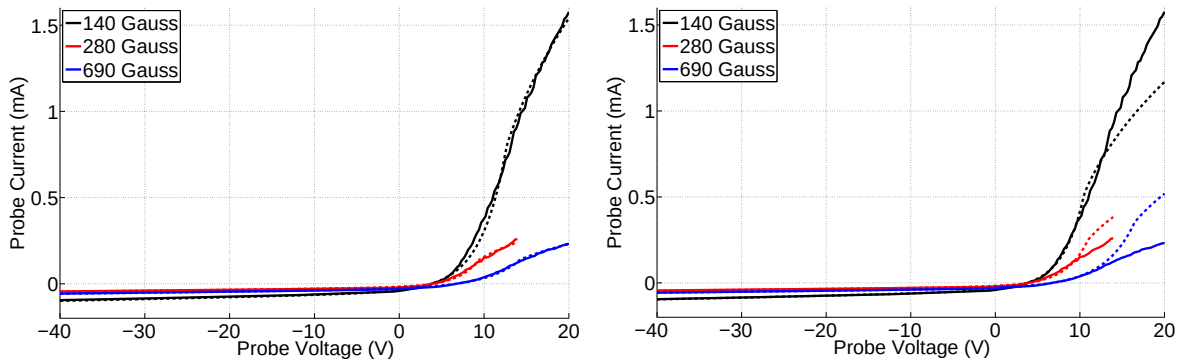

Figure 5.10: Effect of magnetic field on the I-V characteristic fit with (a) A_e as a variable and (b) A_e as a constant.

The fits associated with Figure 5.10a and Figure 5.10b had the electron collection area as a fit variable and a constant set to $0.64A_p$, respectively. For the fits having A_e as a constant the projection area of the probe tip is used. In addition only data below 10 V is utilized. The experimental data given in Figure 5.10 shows that as the magnetic field is increased the electron saturation current significantly decreases. It was found that the I-V characteristic could only be represented by the theory when A_e was allowed to be a fit variable.

The electron collection area normalized to the probe area as a function of magnetic field intensity is presented in Figure 5.11. The black and red curves correspond to the fits having A_e as a variable and constant respectively. Figure 5.11 shows that as the magnetic field intensity increases the normalized electron collection area monotonically approaches 0.23. Therefore when the electron saturation current regime cannot be accessed in the I-V characteristic this value will be utilized.

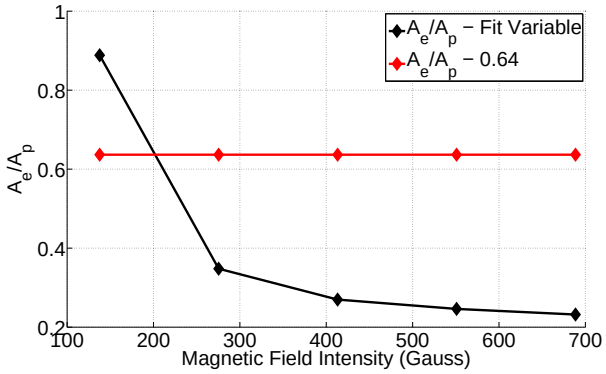

Figure 5.11: Normalized electron collection area as a function of magnetic field intensity.

To determine the sensitivity on A_e the plasma parameters as a function of magnetic field intensity are presented in Figure 5.12. The black and red curves represent the fitting scenarios having A_e as a constant and a variable respectively.

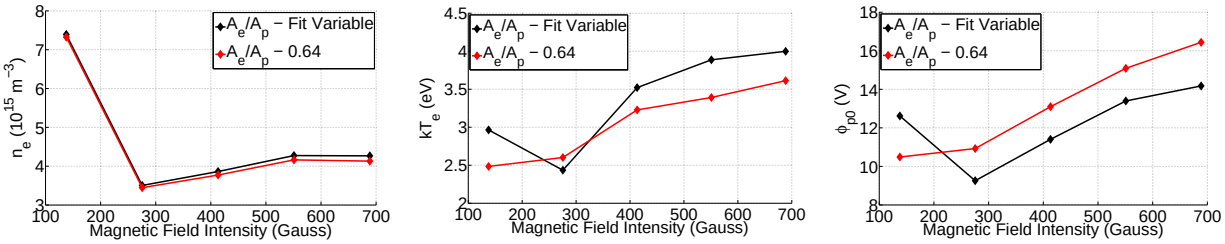

(a) (b) (c)

Figure 5.12: (a) n_e, (b) kT_e, and (c) ϕ_{p0} associated with the variable and constant A_e fit scenarios.

Figure 5.12 shows that the electron density is relatively insensitive to A_e. However the electron temperature and plasma potential were found to be significantly more dependent on A_e, differing nearly 15 % between the two fit scenarios. Therefore combining this error with that associated with incomplete RF compensation, see Section 4.3.1, results in the conservative estimates of ≤ 10 % for n_e, ≤ 25 % for kT_e, and ≤ 20 % for ϕ_{p0}.

To determine the uniformity of the plasma parameters the Langmuir probe was scanned along the x-axis at a distance from the RF biased electrode surface of $z = 30$ mm with $y = 0$ mm. Measurements were made every 1.6 mm and therefore the profile is not expected to be altered significantly by the 1.0 mm probe tip length. The scan was conducted in the parallel and perpendicular field configurations for hydrogen and helium working gases with $P_{RF} = 0$ and 100 W and $P_{\mu W} = 100$ W. The pressure for the parallel and perpendicular field configurations was $P = 200$ and 100 mTorr respectively.

The electron density, electron temperature, and plasma potential as a function of x-axis position are presented in Figure 5.13 for hydrogen in the parallel field configuration.

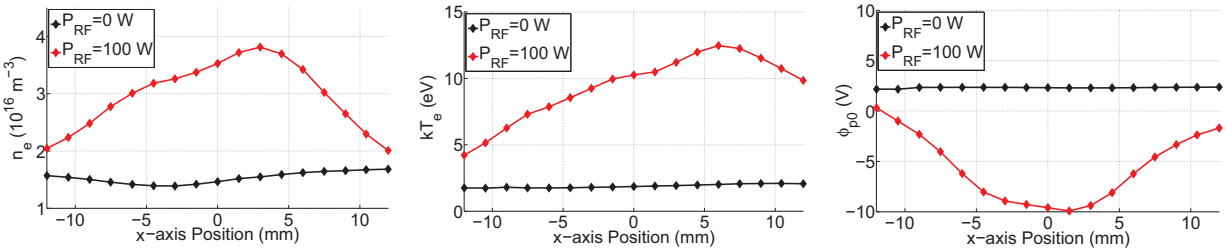

(a) (b) (c)

Figure 5.13: Spatial distribution of (a) n_e, (b) kT_e, and (c) ϕ_{p0} for hydrogen in the parallel field configuration.

The plasma parameters are fairly constant for the $P_{RF} = 0$ W case. However with the addition of RF power the profiles become peaked with a significant variation over the RF biased electrode region, $x = -10$ to 10 mm. The electron density was found to be in the range in which the RF compensation becomes ineffective. Thus the parasitic effects of the time dependent component of the plasma potential are expected to strongly alter the profiles.

The plasma parameters are presented in Figure 5.14 for helium in the parallel field configuration.

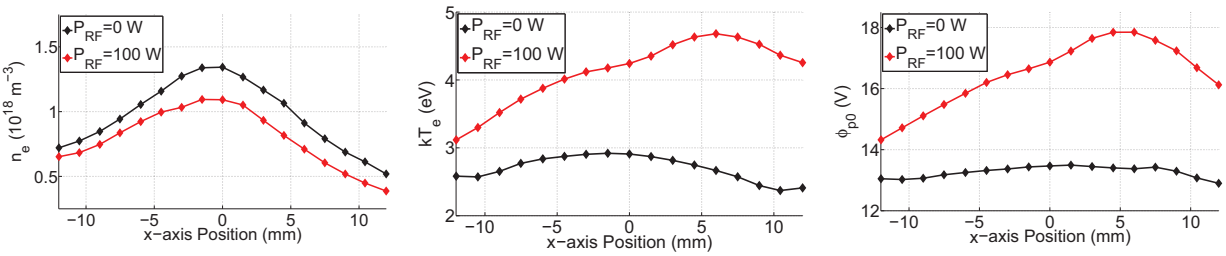

Figure 5.14: Spatial distribution of (a) n_e, (b) kT_e, and (c) ϕ_{p0} for helium in the parallel field configuration.

The plasma parameters are peaked for both the $P_{RF} = 0$ and 100 W cases, with a significant variation over the RF biased electrode region. The electron density was found to be nearly two orders of magnitude greater then that of hydrogen and thus well above the range in which the RF compensation becomes ineffective. The increase in the electron temperature and plasma potential are reasonable and outside of the error range due to RF effects.

The electron collection area is given in Figure 5.15 for both hydrogen and helium discharges in the parallel field configuration.

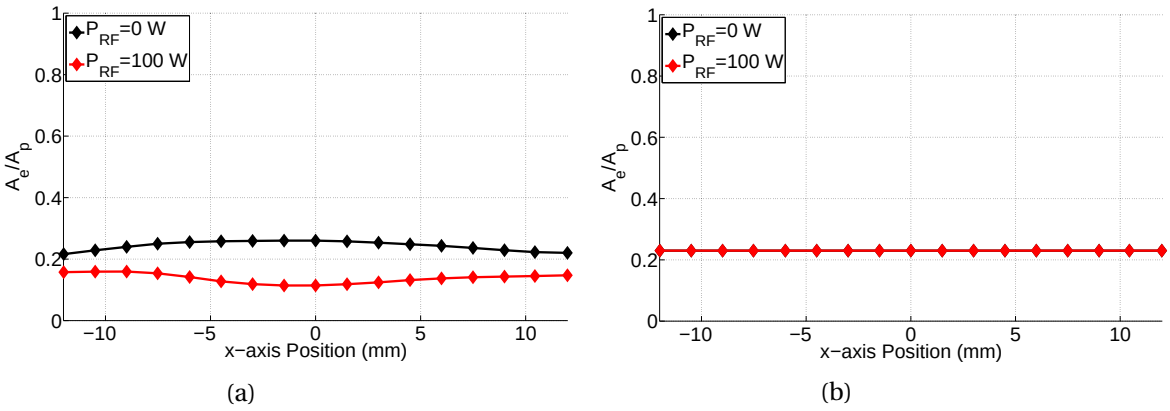

Figure 5.15: Electron collection area for (a) hydrogen and (b) helium discharge.

Figure 5.15 shows that the electron collection area is close to the expected value of $0.23A_p$ for hydrogen. For helium the electron saturation current region could not be accessed and therefor the constant value was used.

The electron density, electron temperature, and plasma potential are presented in Figure 5.16 for hydrogen in the perpendicular field configuration.

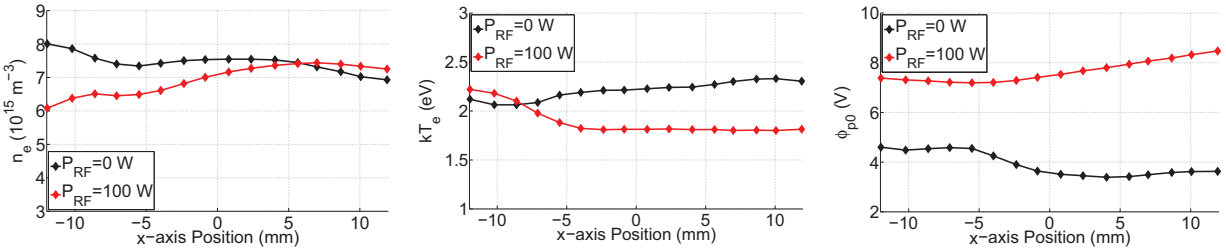

(a) (b) (c)

Figure 5.16: Spatial distribution of (a) n_e, (b) kT_e, and (c) ϕ_{p0} for hydrogen in the perpendicular field configuration.

The plasma parameter profiles presented in Figure 5.16 are significantly different from those of the parallel field configuration. The plasma parameters are relatively constant over the scanned space. In addition the electron density is significantly lower then that of the parallel field configuration. Due to the low electron density the effectiveness of the RF compensation is in question even though the magnitude of the time dependent component of the plasma potential is decrease. However the I-V characteristics do not show strong signs of RF effects and the electron temperature is relatively unaffected between the $P_{RF} = 0$ and 100 W cases.

The plasma parameters are presented in Figure 5.17 for helium in the parallel field configuration.

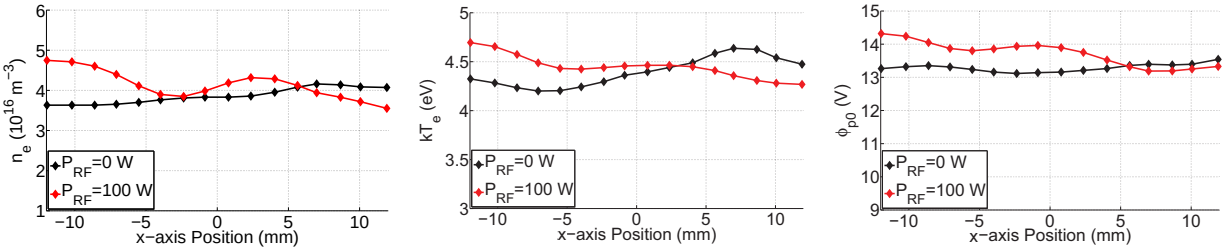

(a) (b) (c)

Figure 5.17: Spatial distribution of (a) n_e, (b) kT_e, and (c) ϕ_{p0} for helium in the perpendicular field configuration.

As was the case for hydrogen, the helium profiles are significantly different then those obtained in the parallel field configuration. The outstanding properties of the helium profiles are similar to those of hydrogen, namely the relatively constant profiles and significantly decreased electron density.

For both the hydrogen and helium discharges the decreased electron density is expected to be caused by the RF electrode assembly impeding the absorption of microwaves. A comparison of Figure 4.1 and Figure 4.2 representing the parallel and perpendicular field configurations respectively shows that the latter has grounded surface near the resonance region. In addition the perpendicular field configuration results in diminished electron transport coefficients along z-axis. This has been shown to lead to a decrease in the electron density and temperature when compared to the parallel field configuration [136]. The relatively flat profiles obtained for both working gases are expected to be caused by the $\boldsymbol{E} \times \boldsymbol{B}$ force tending to shear the plasma [123, 15].

The electron collection area is given in Figure 5.18 for both hydrogen and helium discharges in the perpendicular field configuration. Figure 5.18 shows that the electron collection is close to the expected value of $0.23A_p$ for both hydrogen and helium.

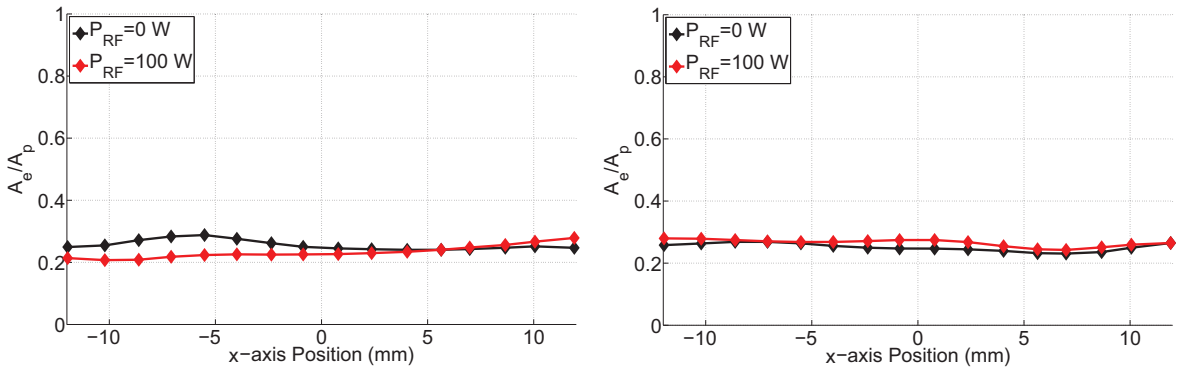

Figure 5.18: Electron collection area for (a) hydrogen and (b) helium discharge.

In summary, the main difference between the parallel and perpendicular field configurations is a significantly decreased electron density and flatter profiles. In addition the electron temperature was significantly decreased for the hydrogen discharges in the perpendicular field configuration. The decreased electron density is attributed to anisotropic transport coefficients in addition to the change in the experimental setup. The flatter profiles are expected to be caused by the $\boldsymbol{E} \times \boldsymbol{B}$ force tending to shear the plasma. The decreased electron temperature is also be attributed to the anisotropic transport coefficients in combination with a more accurate measurement.

5.2 Time Averaged Optical Emission Spectroscopy

This section is focused on the presentation of the time averaged spectral line profiles utilized to determine the RF sheath electric field. To decrease the computational time associated with fitting the spectral line profiles the data is conditioned prior to the fit. The procedure implemented for the prefit conditioning will be presented and discussed.

The spatial distribution of the electric field in the RF sheath was obtained by acquiring two time averaged spectral line profiles at 15 uniformly spaced locations along the z-axis. The location of the measurements ranged from 0.8 mm to 7.9 mm for the parallel field configuration and 0.5 to 7.6 mm for the perpendicular field configuration. A complete set of data required to determine the spatial distribution of the electric field within the RF sheath is referred to as a shot. Therefore a shot consists of the acquisition of 30 time averaged spectral line profiles, 15 for the σ polarization and 15 for the π polarization.

The integration time per spectral line profile ranges from 50 to 300 seconds depending on the discharge parameters and observation location in the RF sheath. The integration time was set such that the signal to noise ratio was ≥ 20. The RF power is typically pulsed for 10 seconds with a duty cycle of 25 %. Pulsed operation is required due to the long integration times and lack of active cooling.

The absorbed RF power, absorbed microwave power, pressure, RF voltage magnitude, DC bias voltage, and the ion saturation current are presented in Figure 5.19 for shot 4.

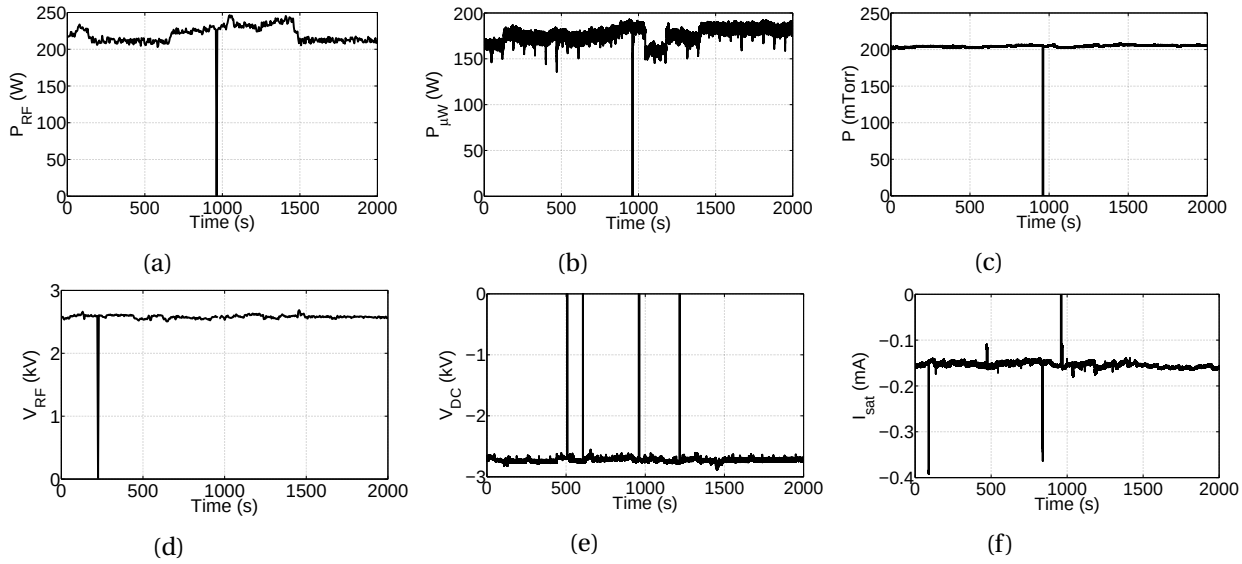

Figure 5.19: Time evolution of (a) absorbed RF power, (b) absorbed microwave power, (c) pressure, (d) RF voltage magnitude, (e) DC bias voltage, and (f) ion saturation current.

To ensure that steady state conditions are maintained the pressure, electrical parameters, and electron density are monitored during the shot. To monitor the electron density the Langmuir probe is biased at -50 V to collect ion saturation current and is located at a position of (0,30,30) mm. The location of the probe was set to ensure the RF sheath electric field would not be perturbed. Figure 5.19 shows that over the duration of the shot, nearly 2000 s, the discharge was maintained at steady state conditions.

5.2.1 Hydrogen Discharge

In Section 3.5.1 it was determined that the H_β ($n = 4 \rightarrow 2$) transition would be utilized through an optimization of electric field sensitivity and emission intensity. For all investigated discharges having hydrogen as the working gas the spectral line profiles displayed similar characteristics within the same field configuration. Thus, to discuss these characteristics and the prefit conditioning shots 1 and 19 will be presented throughout this section. These shots were chosen due to the fact they represent the parallel and perpendicular field configurations respectively and have similar electrical characteristics (see Appendix C). The π and σ raw spectral line profiles are given below in Figure 5.20 and Figure 5.21 for select positions in the RF sheath in the parallel and perpendicular field configurations respectively.

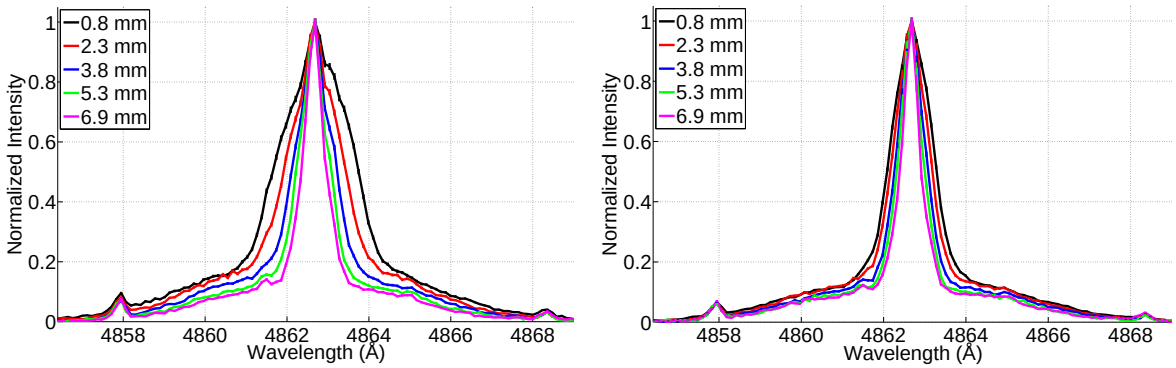

(a) (b)

Figure 5.20: H_β spectral line profile as a function of position in the RF sheath for the (a) π and (b) σ components in the parallel field configuration.

The most outstanding feature of the spectral line profiles given by Figure 5.20 and Figure 5.21 are the 'wings' that extend nearly ±6 Å from the line center. It is determined that these wings cannot be due to an electric field, either macroscopic (Stark effect) or microscopic (Stark broadening). This is because the required intensity for a macroscopic electric field would be on the order of 100 kV/cm. To generate a microscopic electric field of similar magnitude would require an electron density

on the order of 10^{22} m^{-3} [66]. In the most extreme conditions in DStarVE both of these values are orders of magnitude higher then the predictions. The remaining possibility is broadening due to the Doppler effect. In this case the neutral radiators would have, at a minimum, a two temperature distribution consisting of thermal and superthermal groups on the order of 1 and 100 eV respectively.

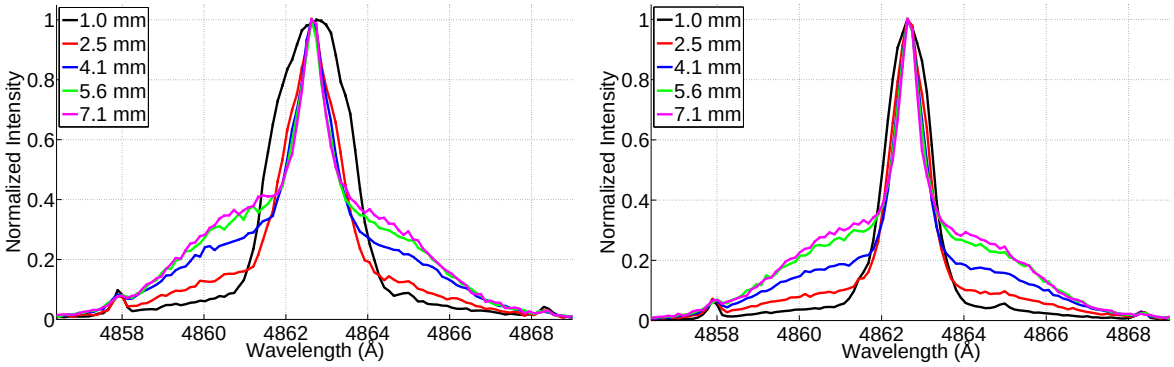

(a) (b)

Figure 5.21: H_β spectral line profile as a function of position in the RF sheath for the (a) π and (b) σ profiles in the perpendicular field configuration

This extensive broadening described above has been significantly reported in the literature and has also been attributed to Doppler broadening [60, 62, 42, 24, 156]. The cause of the neutrals superthermal energy has been proposed to be from charge exchange/heavy particle collisions in the sheath [60, 118] and sputtering of absorbed H atoms on the electrode surface by ion bombardment [62, 118]. The thermal group has a temperature in the range of 0 to 5 eV and is typically composed of many groups [14]. The non-zero temperature is due to the chemical energy associated with the H_2 molecular bond being converted into kinetic energy during dissociation induced by electron impact following the Frank-Condon principal [14].

The superthermal emission is clearly distinguishable from that of the thermal. In addition the broadening is severe enough to smooth out any electric field effects. Therefore removal prior to the fitting process was investigated and is presented below. The spectral line profile at z=7.9 and 7.6 mm in the parallel and perpendicular field configurations respectively is presented in Figure 5.22. It was found that the superthermal emission profile is relatively symmetric and that the molecular transition intensity is weak. In the parallel field configuration the superthermal emission profile is approximately Gaussian. Removal was achieved by subtracting a Gaussian function determined from a fit to select data points from the spectral line profile.

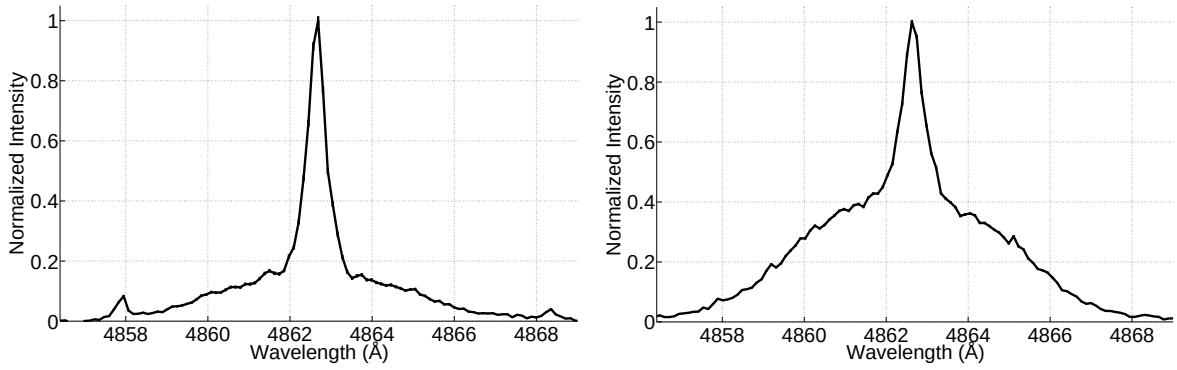

(a) (b)

Figure 5.22: H_β π profile at a position of (a) z=7.9 and (b) 7.6 mm in the parallel and perpendicular field configuration respectively.

Figure 5.23 depicts this superthermal emission fit and removal process for the parallel field configuration. Figure 5.23a presents the Gaussian function fit to the selected data points represented by the blue markers. Figure 5.23b presents the spectral line profile pre and post-removal.

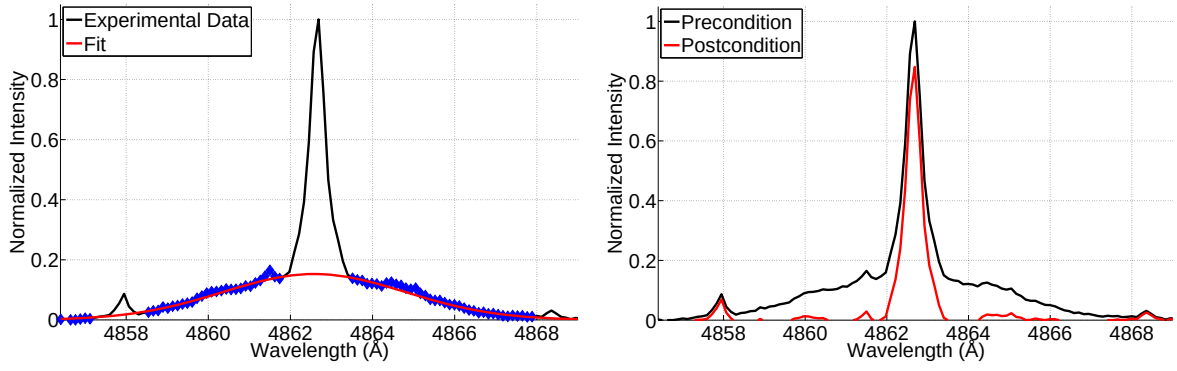

(a) (b)

Figure 5.23: H_β π spectral line profile at a position of $z = 7.9$ mm in the parallel field configuration showing the (a) superthermal emission fit and (b) removal.

Figure 5.23 shows that the superthermal emission is accurately fit and removed from the spectral line profile. Over the wavelength range of interest, 4860.5 to 4864.4 Å, there are 22 possible molecular hydrogen lines [41]. Figure 5.23 indicates the presence of several of these molecular lines, fortunately the intensity of the majority of these transitions is negligible. The molecular line occurring at 4861.5 is of particular interest because it is distinguishable from the H_β line for low electric field intensities and occurs in the wavelength range of interest.

In the perpendicular field configuration the superthermal emission profile was not found to be Gaussian. This was expected if the superthermal was partly due to charge exchange/heavy particle collisions due to the complex ion dynamics in the sheath from the $\boldsymbol{E} \times \boldsymbol{B}$ force [78]. To estimate the superthermal emission profile select data points were fit to a bi-Gaussian function. Figure 5.24 depicts the superthermal emission fit and removal process for the perpendicular field configuration. Figure 5.24 shows that the fitted bi-Gaussian function accurately represents the data points marked in blue. It is assumed that near the edges of the thermal emission profile the bi-Gaussian approximation deviates only slightly from actual superthermal emission profile. The molecular lines discussed above are not distinguishable here and will thus be ignored.

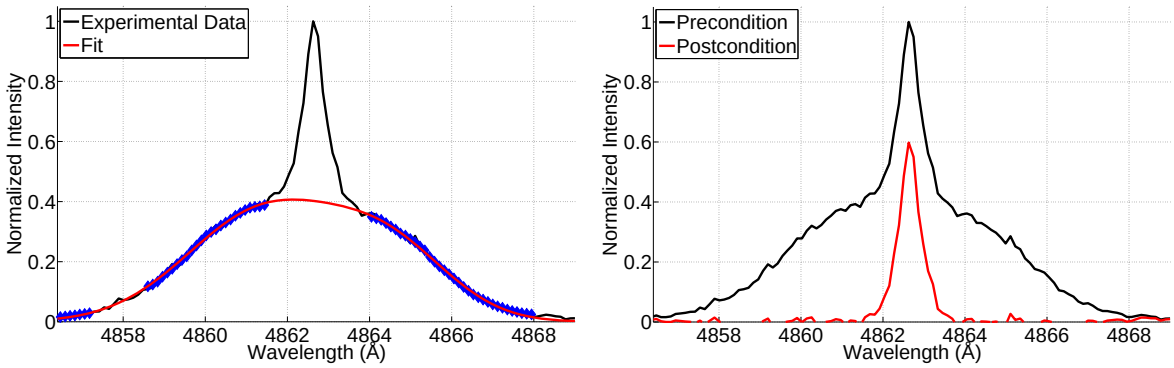

(a) (b)

Figure 5.24: H_β π spectral line profile at a position of $z = 7.6$ mm in the perpendicular field configuration showing the (a) superthermal emission fit and (b) removal.

In the parallel field configuration, although the intensity is weak, the molecular line occurring at 4861.5 Å is removed from the spectral line profile prior to the fit. For low electric field intensities the molecular line is distinguishable from the main line and is removed by subtraction of a fitted Gaussian function determined similarly to the method described above. Figure 5.25 depicts the molecular line fit and removal process. The molecular line intensity was found to be approximately 3 % and thus is not expected to influence the fit significantly. However the removal was carried out regardless of intensity for consistency. At higher electric field intensities the molecular line became encompassed by the main line. To remove the molecular line in this case the parameters associated with all available molecular line fits were averaged to calculate an approximate Gaussian function. It was found that the fit parameters were not strong functions of position in the RF sheath. Additionally, the intensity of select molecular transitions have been measured as a function of position in the RF and have been shown to be relatively constant [61]. Removal of the superthermal emission and the molecular line consist of the conditioning prior to the fit.

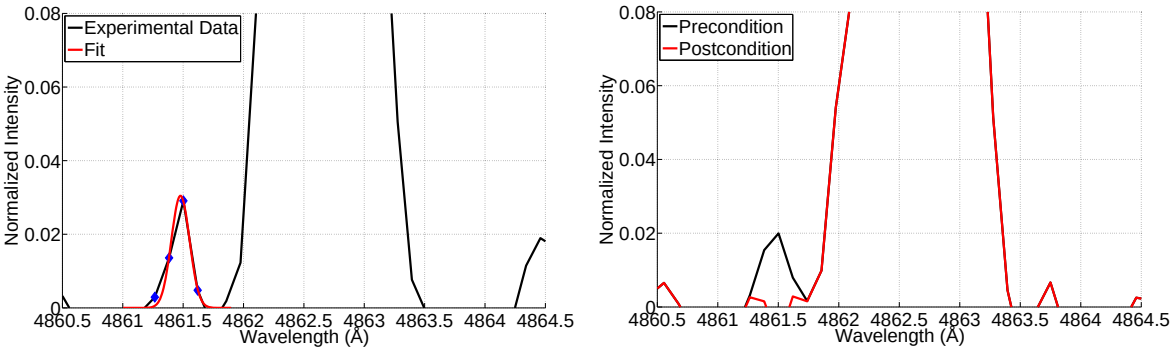

(a) (b)

Figure 5.25: H_β π profile at a position of $z = 7.9$ mm in the parallel field configuration showing the (a) molecular line fit and (b) removal.

The π components of the spectral line profile after data conditioning are presented in Figure 5.26 at spatial locations of $z = 0.8$ and 7.9 mm in the parallel field configuration and $z = 1.0$ and 7.6 mm in the perpendicular field configuration.

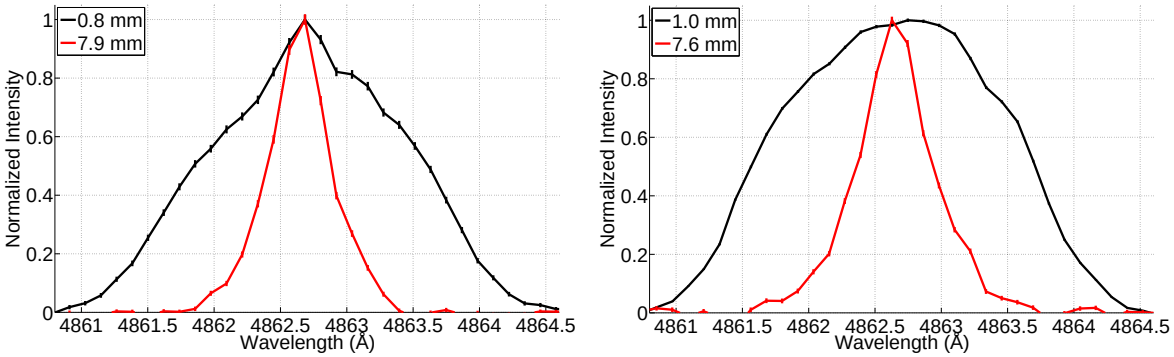

(a) (b)

Figure 5.26: H_β π profiles at a position of (a) $z = 0.8$ and 7.9 mm and (b) $z = 1.0$ and 7.6 mm in the parallel and perpendicular field configurations respectively.

Figure 5.26 presents the typically characteristics of the π profile. In the parallel field configuration the π profile is relatively smooth having a triangular shape in the intermediate electric field range tending towards a Gaussian at low electric field intensities. At the extreme electric field intensities the profile splits into three distinct peaks, one to the left and right of the line center. In the perpendicular field configuration the profile tends to be rounded at the extreme electric field intensities never splitting into a three peak profile. The profile also tends towards a Gaussian as the electric field intensity decreases.

The π and σ profiles of the H_β transition are significantly different as was predicted by the modeling presented in Section 3.5.1. Figure 5.27 presents the π and σ profiles after data conditioning for spatial locations of $z = 0.8$ and 1.0 mm in the parallel and perpendicular field configurations respectively. Figure 5.27 shows that the π profile is effected more strongly by the electric field then the σ profile. The significant difference in the π and σ profiles is exploited during data fitting. The σ profile is relatively smooth and singly peaked for all investigated discharges. The π and σ profiles are slightly asymmetric and skewed towards the red. The cause of which is assumed to be due to non-statistical population density and impurity transitions and will be further explored in Section 5.4

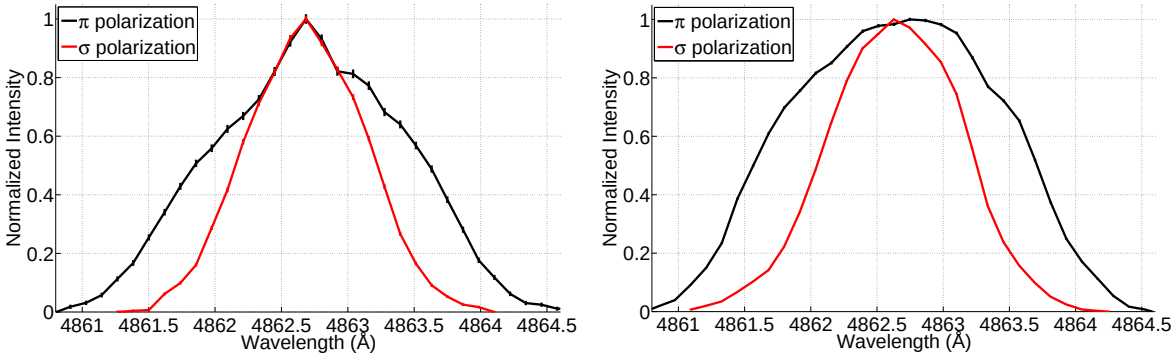

(a) (b)

Figure 5.27: H_β π and σ profiles at a position of (a) $z = 0.8$ and (b) 1.0 mm in the parallel and perpendicular field configurations respectively.

The optical emission in the RF sheath is strongly spatially dependent. Figure 5.28 gives the spatial dependence of the thermal emission intensity calculated by numeric integration for the parallel and perpendicular field configurations. In the parallel field configuration the thermal emission intensity approximately decreases linearly with z. In the perpendicular field configuration the profile is significantly different. Here the profile is highly peaked within 3 mm of the RF biased electrode surface and quickly decays with z. The highly peaked nature is due to the confinement of electrons near the surface of the RF biased electrode by the magnetic field [98] and has been previously measured [15]. A comparison of the intensity near $z = 8$ mm for the parallel and perpendicular field configurations shows the ratio to be nearly an order of magnitude different. Although the electron density is measured at $z = 30$ mm, this observation supports the large difference in electron density between the field configurations.

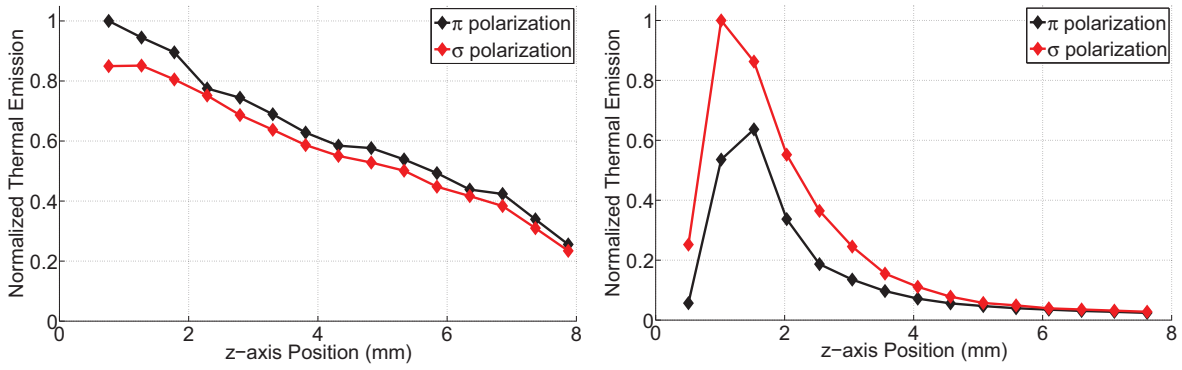

Figure 5.28: H_β π and σ profile integrated area for thermal emission in the (a) parallel and (b) perpendicular field configurations.

Figure 5.29 gives the spatial dependence of the superthermal emission intensity calculated by analytic integration of the fitted functions for the parallel and perpendicular field configurations.

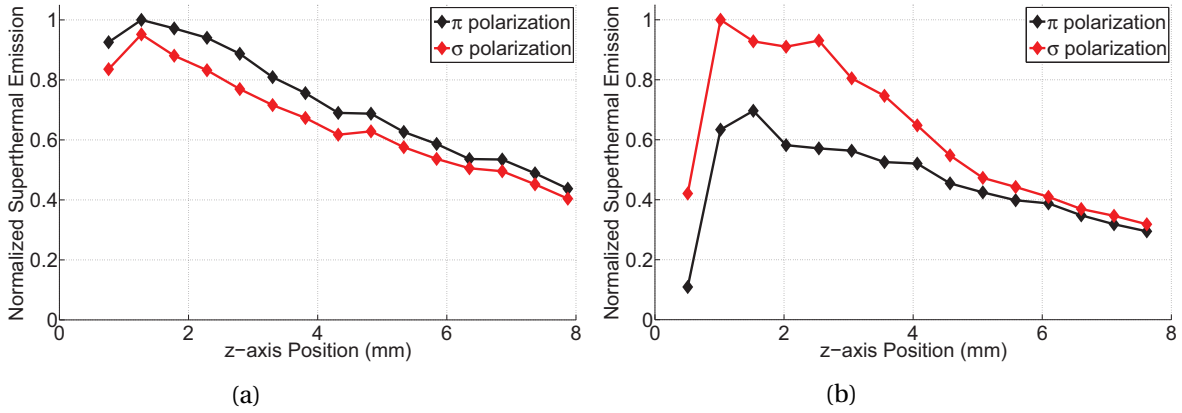

Figure 5.29: H_β π and σ profile integrated area for superthermal emission in the (a) parallel and (b) perpendicular field configurations.

The profiles given in Figure 5.29 are similar to those corresponding to the thermal emission given in Figure 5.28. For the perpendicular field configuration the profile is different in the sense that the peak is significantly broadened. This broadening is explained because the Larmor radius of ions is substantially larger then that of the electrons and thus they are less confined.

In statistical equilibrium the magnetic substates are equally populated through collisions. Here the emission intensity arising from transitions radiating photons having π and σ polarizations are equal. The charge exchange cross sections are highly dependent on the magnetic substate, namely

on the angular momentum quantum number [84]. Therefore if the statistical population cannot be reached the emission intensity of the π and σ profiles will not be equal. Non statistical populations have been measured in active beam spectroscopy diagnostics on tokamak's [45].

It is seen from Figure 5.28 and Figure 5.29 that the intensity of the π and σ profiles are only slightly different in the parallel field configuration. In the perpendicular field configuration this is not the case, the σ profile intensity is significantly larger then that of the π. This result is an indication that for the perpendicular field configuration the magnetic substates are not statistically populated. The above data was taken for $P_{\mu W} = 0$ W, it was found that the injection of microwave power caused the π intensity to dominate the σ intensity for the superthermal emission. This was the only effect of microwave injection on the emission profiles. Due to the complex ion dynamics the calculation of the magnetic substate population would require the coupling of a particle-in-cell code with a corona-radiative model. Thus the assumption will be made that all substates associated with photons having the same polarization will be in statistical equilibrium.

The ratio of the thermal to superthermal emission intensity was taken and is presented in Figure 5.30.

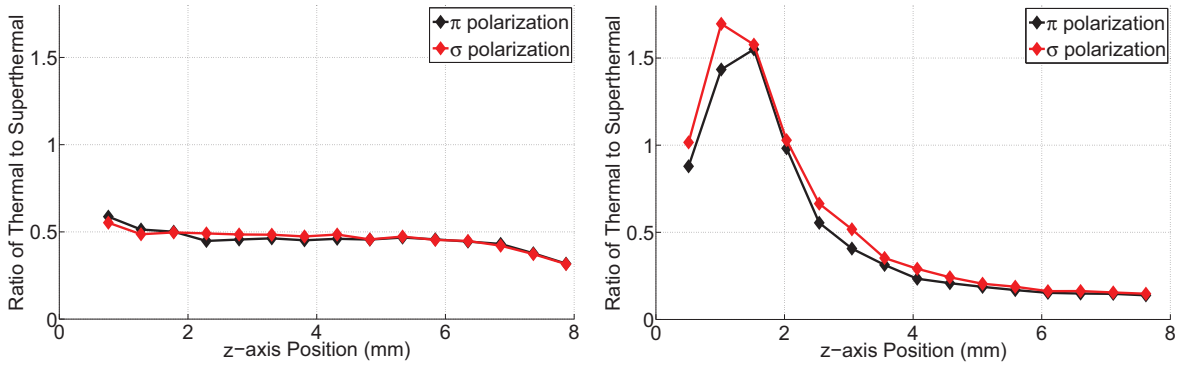

Figure 5.30: Ratio of thermal to superthermal H_β π and σ profile integrated area in the (a) parallel and (b) perpendicular field configurations.

Figure 5.30 shows that the π and σ ratios are nearly equivalent for both field configurations. The ratio in the parallel field configuration is relatively constant with a value of approximately 0.5 indicating equal intensities of thermal and superthermal emission. In the perpendicular field configuration the profile is highly peaked following that of the thermal emission, the ratio decays to a value of approximately 0.15 as the bulk plasma is approached.

To determine where the superthermal emission was originating an experiment was conducted in the parallel field configuration utilizing the H_α transition. The waveguide attached to port 1, see

Figure 4.1, was removed and replaced with a quart window centered about $x = 0$ mm and $y = 0$ mm such that the view was along the z-axis. A collimator with an observation diameter of 1 cm was positioned to view of the RF biased electrode along the z-axis. The experiment was designed to determine if there was a measurable Doppler shift of the superthermal emission with respect to the thermal. Two experiments were conducted. The first measured the Doppler shift as a function of phase and the second measured the Doppler shift as a function of discharge parameters. For the first experiment the phase within an RF period was scanned in 60 evenly spaced increments spanning the entire RF period. The integration time was set to 3 ns. The discharge parameters where $P = 200$ mT and $P_R F = 100$ W. Figure 5.31 presents the H_α spectral line profile at a phase of 0 ns.

As found by similar experiments two superthermal Doppler shifted peaks exist, one to the left and one to the right of the thermal peak [26]. The Doppler shifted peaks represented by the blue markers were each fit to a Gaussian function independently, with the sum given by the red curve. The peaks Doppler shifted to the left and right of the thermal peak are due to hydrogen atoms having a velocity heading away and towards the RF biased electrode respectively. The electric field is primarily pointing towards the RF biased electrode surface, reversing for only a short amount of time with a small magnitude [113, 44]. Therefore there is essentially a continuous ion flux bombarding the surface whose energy is time dependent. It can be concluded that the hydrogen atoms with a velocity heading away from the electrode must be due to atoms being sputtered from the surface induced by ion bombardment or reflection [62, 118].

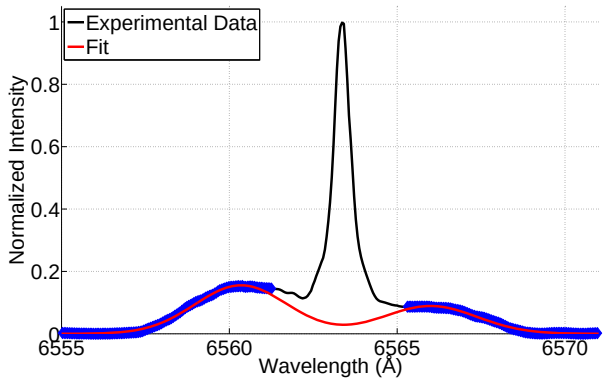

Figure 5.31: Phase resolved H_α spectral line profile obtained viewing the RF biased electrode along the z-axis at a phase of 0 ns

Experiments have shown that bombarding a surface with hydrogen ions produces a fraction of reflected excited neutral atoms with velocities similar to that of the incident [144, 150, 94]. The hydrogen atoms with a velocity heading towards the electrode are due to charge exchange or collision with the accelerating ions [60, 118]. Therefore the left and right Doppler shifted peaks will

be associated with sputtering and charge exchange respectively.

Figure 5.32 gives the Doppler shift in terms of kinetic energy as a function of phase within the RF period for sputtering and charge exchange.

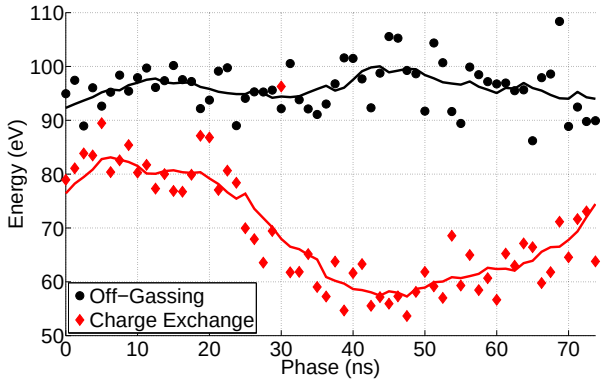

Figure 5.32: Energy as a function of phase for sputtered and charge exchanged hydrogen atoms.

It was found that the kinetic energy of the sputtered hydrogen atoms is relatively constant with respect to phase. Conversely the hydrogen atoms that had undergone charge exchange have a distinct and strong dependence on the phase. The sputtered hydrogen atoms are expected to have a phase dependence but because the atoms are traveling into the bulk of the discharge it is effectively averaged out through the measurement technique. The hydrogen atoms that have undergone charge exchange would be susceptible to the same effect if not for the RF biased electrode surface. Here the atoms that have not undergone radiative decay in the RF sheath will upon interaction with the RF biased electrode surface. The transit time through the RF sheath for the charge exchanged neutrals is on the order of 20 ns, therefore the radiative decay of such neutrals will be inherently phase locked to the RF waveform.

The purpose of the second experiment was to investigate the effect of the superthermal hydrogen atoms as a function of discharge parameter. The same experimental setup was utilized as describe above while observing the time averaged spectral line profile. Figure 5.33 presents the energy of the sputtered and charge exchanged hydrogen atoms as a function of discharge pressure and RF biased electrode voltage. The sputtered hydrogen atoms were found to have a strong dependence on the discharge pressure while the charge exchanged atoms do not. This behave supports the conclusions drawn above on the production of superthermal neutrals. The charge exchange neutrals have only a few mm to travel before colliding with the electrode surface therefore a weaker pressure dependence should be observed due to the fact the mean free path is on the order of a mm. Both the sputtered and charge exchanged atoms have approximately the same dependence on the RF biased electrode voltage. It is expected that the relatively weak dependence on the RF biased electrode voltage is

due to the collisionality. Figure 5.34 presents the energy of the sputtered and charge exchanged hydrogen atoms as a function of discharge pressure.

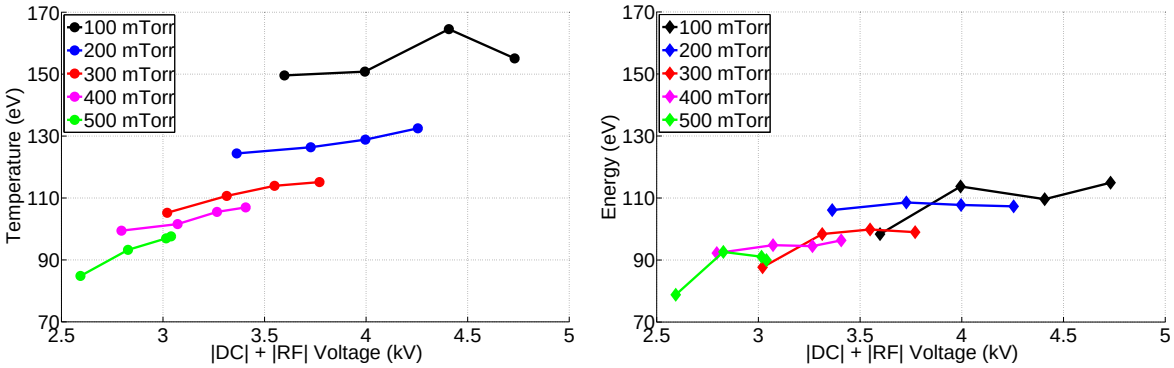

Figure 5.33: Energy as a function of RF biased electrode voltage for (a) sputtered and (b) charge exchanged hydrogen atoms.

Figure 5.34 clearly shows the strong dependence on discharge pressure for the sputtered atoms, a similar trend has been reported in the literature [62]. In summary, the conclusion that is drawn from the experimental measurements presented above is that the origin of the superthermal hydrogen atoms is due to the RF sheath electric field. Two processes contribute to the heating of the neutrals resulting in two distinct distribution functions. Charge exchange and heavy particle collisions result in energetic particles traveling towards the RF biased electrode surface. Sputtering of absorbed hydrogen atoms and reflection of the bombarding ion flux results in energetic neutrals traveling into the bulk discharge.

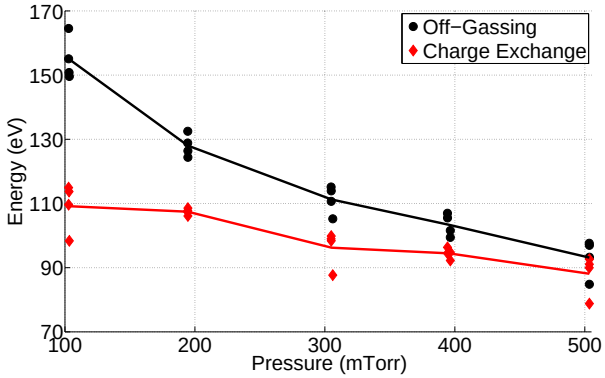

Figure 5.34: Energy as a function of pressure for sputtered and charge exchanged hydrogen atoms.

In conclusion, it is found that the radiator distribution function of the neutrals undergoing the H_β transition is that of a two group having thermal and superthermal energies. The superthermal emission profile is clearly distinguishable from that of the thermal and is removed as part of the data conditioning process prior to fitting. In addition it was found that molecular hydrogen lines where present in the wavelength range of interest, one of which was removable.

5.2.2 Helium Discharge

In Section 3.3.2 it was determined that the $5^3D \rightarrow 2^3P$ He I transition would be utilized through an optimization of electric field sensitivity and emission intensity. For all investigated discharges having helium as the working gas the spectral line profiles displayed similar characteristics within the same field configuration. Thus, to discuss these characteristics and the data conditioning conducted prior to the fit shots 9 and 27 will be presented throughout this section. These shots were chosen because they represent the parallel and perpendicular field configurations respectively and have similar electrical characteristics (see Appendix C). The π and σ raw spectral line profiles are given in Figure 5.35 and Figure 5.36 for select positions in the RF sheath in the parallel and perpendicular field configurations respectively. The raw spectral line profiles clearly depict the strong asymmetry induced by the electric field, most prominent on the blue side of the line. The spectral line profiles have three distinct features about the unperturbed wavelength which will be discussed below.

The radiator distribution function is not obvious as was the case for the H_β transition. A superthermal emission profile is not distinguishable and either is not present or is potentially masked by that of the thermal. To correctly fit the data the existence of superthermal emission must be determined. Therefore an experiment was conducted in the parallel field configuration which consisted of measuring the spectral line profile outside of the RF sheath.

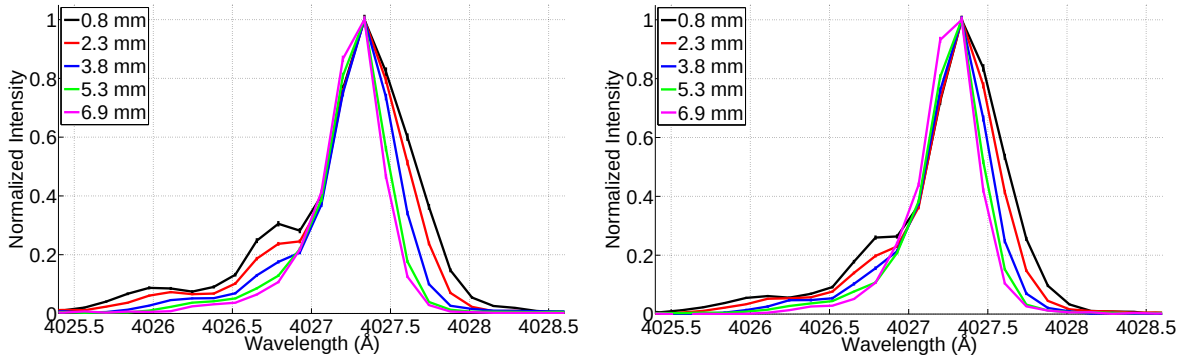

(a) (b)

Figure 5.35: $5^3D \rightarrow 2^3P$ He I spectral line profile as a function of position in the RF sheath for the (a) π and (b) σ components in the parallel field configuration.

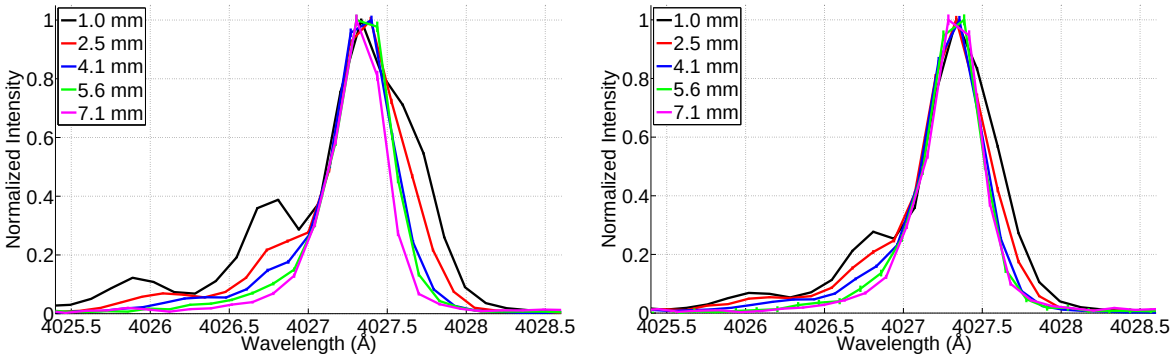

Figure 5.36: $5^3D \rightarrow 2^3P$ He I spectral line profile as a function of position in the RF sheath for the (a) π and (b) σ components in the perpendicular field configuration.

Optical access was granted by use of the 1 3/4" quartz window located on port 2, see Figure 4.1. A collimator was utilized to ensure emission was collected from only the bulk plasma. The discharge parameters were $P = 200$ mTorr, P_{RF}=100 W, and $P_{\mu W}$=100 W. Figure 5.37 gives the experimental data with the associated fit given by the black curve and markers.

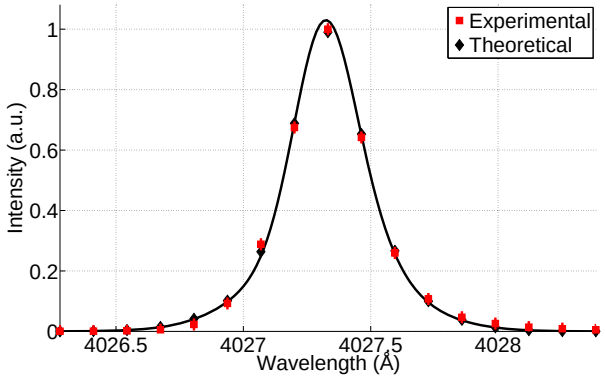

Figure 5.37: $5^3D \rightarrow 2^3P$ He I spectral line profile at a position of $z = 30$ mm.

Utilizing the proper instrument function the spectral line profile was fit to a two group radiator distribution function. The temperature and intensity of the thermal group was set to 0 eV and 100 percent respectively. The thermal group has a temperature of 0 eV because the excitation is caused by electron impact which imparts negligible energy to the helium atom. The temperature and intensity of the superthermal group were the fit variables. The Doppler shift for both groups was set to zero because of the viewing geometry.

It was found that only a two group radiator distribution function would properly fit the data, even

considering an electric field influence. The superthermal group was found to have an temperature of 12.9 eV and an intensity of 54.7 %. The goodness of the fit and the symmetry of the spectral line profile indicate that a superthermal group exists and will thus be considered when fitting the data. The fact that the superthermal emission profile is masked by that of the thermal is due to two reasons. The first comes from the fact that helium has approximately four times the mass of hydrogen. Doppler broadening is proportional to $m^{-1/2}$, therefore the effect will be decreased by a factor of two in comparison. The second arises due to the fact the helium atom has more inertia. The ions will have a dampened response to the RF electric field resulting in lower energy neutrals after charge exchange or sputtering.

To determine if impurity lines exists in the wavelength range of interest the spectral line profile is investigated at the extreme z-axis position. Figure 5.38 presents the π profile at a position of $z = 7.9$ mm and 7.6 mm in the parallel and perpendicular field configuration respectively.

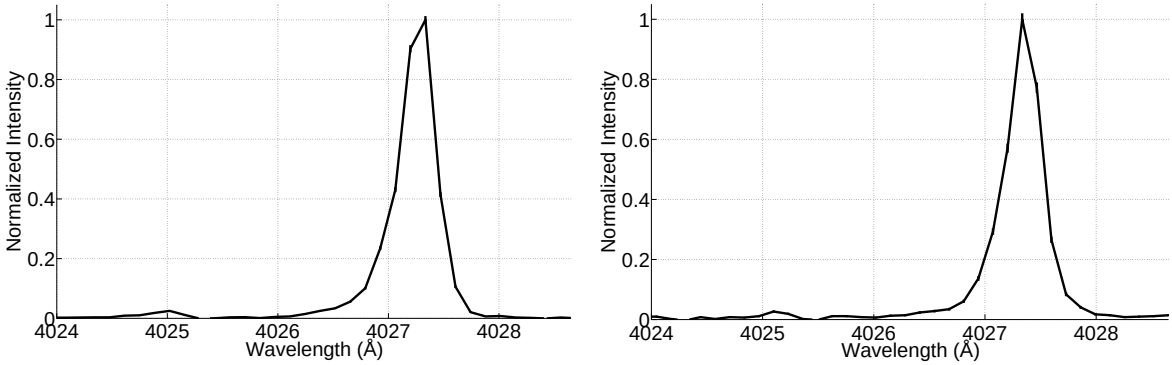

Figure 5.38: $5^3D \rightarrow 2^3P$ He I π profiles at a position of (a) $z = 7.9$ and (b) 7.6 mm in the parallel and perpendicular field configuration respectively.

It was found that an impurity line exists at a wavelength of 4025 Å in the spectra and is attributed to either a W I or Fe I transition [5]. The impurity is present due to ablation of the tungsten probe tip associated with the Langmuir probe or of the stainless steel vacuum chamber walls. For low electric field intensities the impurity line is distinguishable from the main line and is removed by subtraction of a fitted Gaussian function. Figure 5.39 depicts the impurity line fit and removal process.

The intensity of the impurity is approximately 3 % and is not expected to influence the fit significantly. Nevertheless, to be cautious the impurity line was removed. At higher electric field intensities the impurity line became encompassed by the $5^3D \rightarrow 2^3P$ He I line. To remove the impurity line in this case the parameters associated with all available fits were averaged to calculate an approximate Gaussian function to utilize in the subtraction. It was found that the fit parameters

were not strong functions of position in the RF sheath. Removal of the impurity line consists of the conditioning prior to the fit.

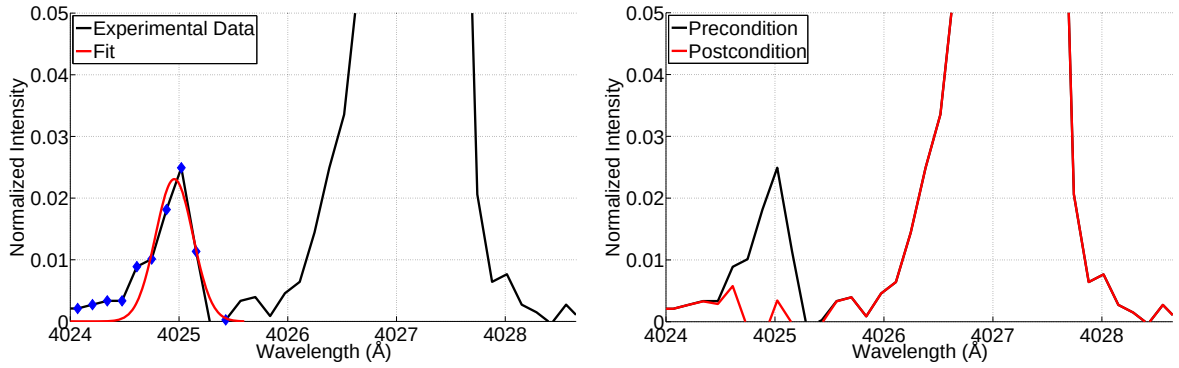

(a) (b)

Figure 5.39: $5^3D \rightarrow 2^3P$ He I profile at a position of $z = 7.9$ mm in the parallel field configuration showing the (a) impurity line fit and (b) removal.

The conditioned $5^3D \rightarrow 2^3P$ He I π profile is presented in Figure 5.40 at spatial locations of $z = 0.8$ mm and 7.9 mm in the parallel field configuration and $z = 1.0$ mm and 7.6 mm in the perpendicular field configuration.

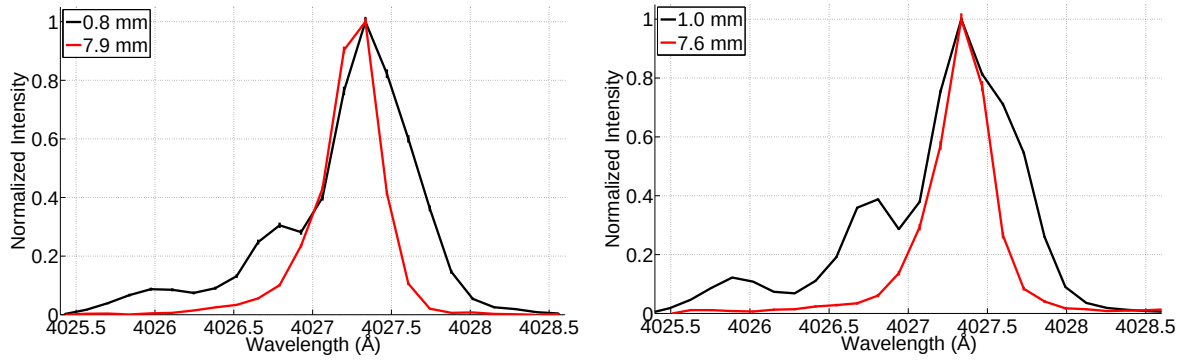

(a) (b)

Figure 5.40: $5^3D \rightarrow 2^3P$ He I π profiles at $z = 0.8$ mm and 7.9 mm and (b) $z = 1.0$ and 7.6 mm in the parallel and perpendicular field configurations respectively.

Three distinct features become present with increasing electric field intensity. Two of these features occur on the blue side of the line and are manifested as peaks. As discussed in Section 3.5.2, the intensity of these peaks are strongly dependent on the electric field intensity. However, at this

spectral resolution only the wavelength of the far blue peak is appreciably dependent on the electric field intensity. The remaining feature is the broadening on the red side of the line. If the electric field is intense enough a split from the main line occurs forming an additional peak.

Unlike the H_β transition the π and σ profiles of the $5^3D \rightarrow 2^3P$ He I transition are similar as was predicted by the modeling presented in Section 3.5.2. Figure 5.41 presents the π and σ profiles after data conditioning for spatial locations of $z = 0.8$ mm and 1.0 mm in the parallel and perpendicular field configurations respectively.

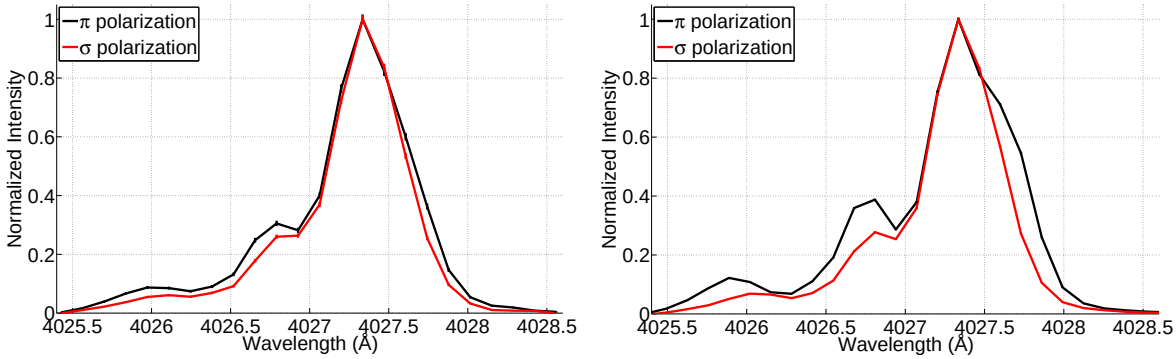

(a) (b)

Figure 5.41: $5^3D \rightarrow 2^3P$ He I π and σ profiles at (a) $z = 0.8$ mm and (b) 1.0 mm in the parallel and perpendicular field configurations respectively.

As expected the π profile is more effected by the electric field then the σ profile. Although the profiles have similar spectral characteristics the differences are expected to aid in the fitting of the data.

The optical emission in the RF sheath is strongly spatially dependent. Figure 5.42 presents the spatial dependence of the total emission intensity calculated by numerically integrating the spectral line profile after data conditioning for the parallel and perpendicular field configurations. It was found that the total emission profiles in both field configurations trend very similar to those of the H_β transition. In the parallel field configuration the total emission intensity approximately decreases linearly with z, leveling out near $z = 6$ mm. In the perpendicular field configuration the profile is significantly different. Here the profile is highly peaked within 3 mm of the RF biased electrode surface and quickly decays with z. A comparison of the intensity near $z = 8$ mm for the parallel and perpendicular field configurations shows the ratio to be nearly an order of magnitude different. Although the electron density is measured at $z = 30$ mm this observation supports the large difference in electron density between the field configurations. The total emission intensity of the π and σ profiles are approximately equal for both field configurations. This suggests that the magnetic substates are equally populated and are thus in statistical equilibrium.

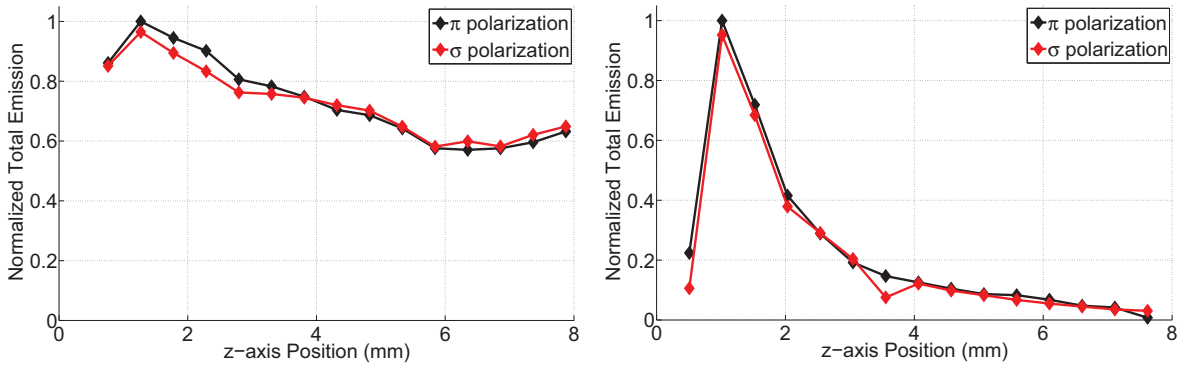

Figure 5.42: $5^3D \rightarrow 2^3P$ He I π and σ profile integrated area for total emission in the (a) parallel and (b) perpendicular field configurations.

In conclusion, it is found that the radiator distribution function of the neutrals undergoing the $5^3D \rightarrow 2^3P$ He I transition is that of a two group having thermal and superthermal energies. The superthermal emission profile is masked by that of the thermal and is not able to be removed prior to fitting. In addition, it was found that either an W I or Fe I impurity line was present in the wavelength range of interest. The impurity line is removed prior to the fitting and consists of the data conditioning process.

5.3 Phase Resolved Optical Emission Spectroscopy

In this section the results associated with the experiments designed to measure the phase resolved integrated area of the spectral line profile will be presented. As discussed in Section 3.2 due to insufficient optical emission the time averaged technique must be implemented. Thus, if the transition emission intensity is time dependent, the phase resolved integrated area must be utilized to fit the time average of the spectral line profile. The phase resolved integrated area is obtained by measurement of the phase resolved spectral line profile and subsequent integration. The measurement is conducted in this manner such that the thermal and superthermal emission can be separated. To achieve an adequate signal to noise ratio the spectrometer diffraction grating was stepped down to 1200 line/mm and the entrance slit width was increased to 100 μm.

To determine if the emission intensity is time dependent the characteristic lifetime of the upper level is examined. The H_β and $5^3D \rightarrow 2^3P$ He I transitions have a lifetime for spontaneous emission of 33 and 105 ns respectively [152]. Comparing these characteristic lifetimes with the 74 ns RF period it is expected that the emission intensity of the H_β will be time dependent while that of the $5^3D \rightarrow 2^3P$ He I will not. To determine if this assumption is correct the emission intensity was measured as a function of phase for both transitions and is presented in Figure 5.43. The

spatial location of the measurement was $z = 1.0$ and the discharge parameters were $P = 200$ mTorr, $P_{RF} = 100$ W, and $P_{\mu W} = 100$ W.

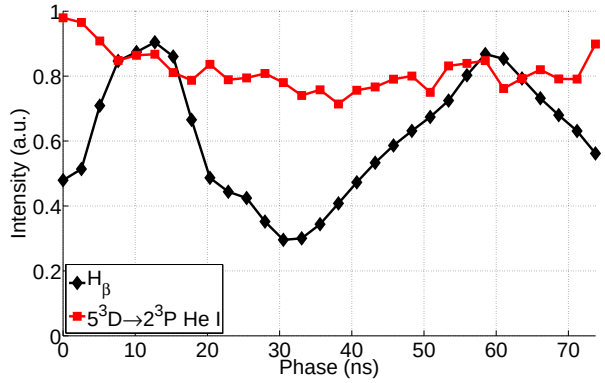

Figure 5.43: H_β and $5^3D \rightarrow 2^3P$ He I π profile integrated area as a function of phase at $z = 1.0mm$ in the parallel field configuration>

It was found that the H_β emission intensity was strongly time dependent while that of $5^3D \rightarrow 2^3P$ He I was not. Thus for the remainder of this dissertation the emission intensity of the $5^3D \rightarrow 2^3P$ He I transition will be assumed constant with respect to time.

The H_α transitions is approximately 3 to 5 times more intense then that of H_β for the investigated discharges. Therefore to further increase the signal to noise ratio the H_α transition will be considered for the phase resolved measurements. Figure 5.44 presents the H_α and H_β π integrated area as a function of phase and space in the parallel field configuration. The discharge parameters were $P = 200$ mTorr, $P_{RF} = 100$ W, and $P_{\mu W} = 100$ W.

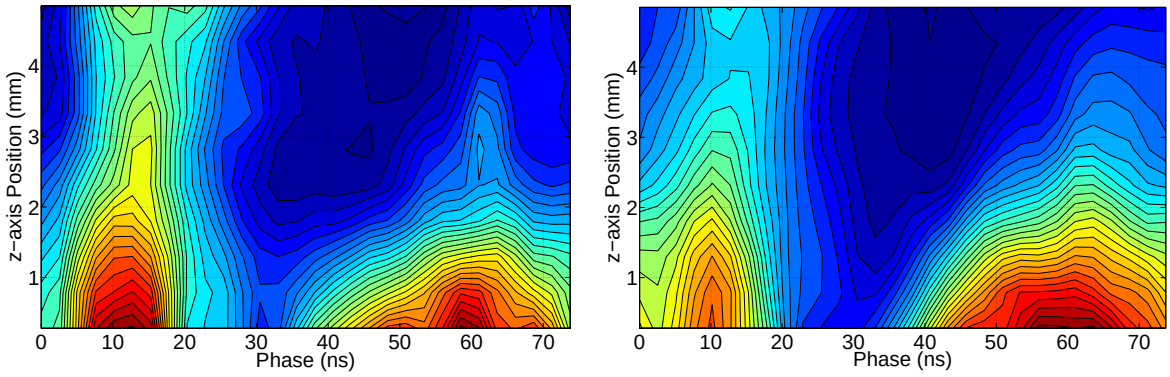

(a) (b)

Figure 5.44: π profile integrated area as a function of phase and space for (a) H_α and (b) H_β in the parallel field configuration.

It was found that the temporal and spatial dependence of the H_α π integrated area was very similar to that of H_β. Additionally the response of the σ integrated area was found to mimic that of the π. Therefore to increase the signal to noise ratio, the π polarization of the H_α transition will be utilized as the universal phase resolved data. Furthermore, to decrease the experimental acquisition time, it is assumed that all investigated discharges regardless of the experimental parameters have a similar temporal response. Variation in the spatial dependence is expected but has no consequence on the fitting of the data. The discharge parameters for the remainder of the experiments presented in this section are identical to those described above unless otherwise stated.

To gain insight into the behavior of the phase resolved emission intensity the RF biased electrode voltage is plotted on the corresponding temporal axis and is presented in Figure 5.45. The discharge pressure was $P = 85$ mTorr and experiment was conducted in the parallel field configuration.

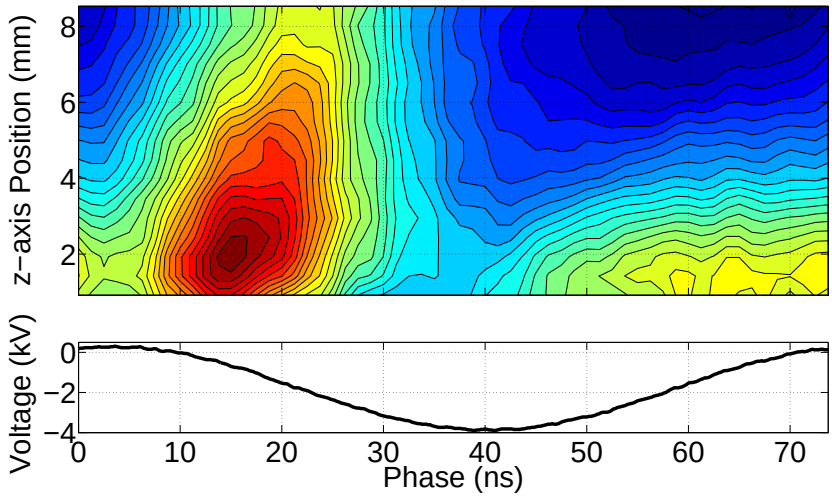

Figure 5.45: H_α π integrated area as a function of phase and space correlated to the RF biased electrode voltage in the parallel field configuration.

Through the use of the correlated RF biased electrode voltage the features of the phase resolved emission intensity can be identified. In the parallel field configuration the phase resolved emission intensity has two distinct peaks. As seen by Figure 5.43 these peaks occur around 10 and 60 ns respectively and are designated as the first and second respectively. The first peak in the emission intensity is very intense and occurs near the maximum of the RF biased electrode voltage waveform. The burst in emission is initiated by the reversal of the electric field occurring close to the electrode surface [63]. Following the field reversal the RF sheath expansion begins. A beam of electrons is formed and directed into the bulk plasma causing intense excitation and ionization. This phenomena has been simulated [135, 146] and observed experimentally [133, 134, 63]. The second peak occurs

after the minimum of the RF biased electrode voltage waveform and is typically of lower intensity then that of the first. As the RF sheath expands the ions are accelerated towards the electrode surface causing de-excitation and sputtering of excited hydrogen atoms upon bombardment [63].

A confirmation of the description given above can be gained by discriminating the thermal from superthermal emission when integrating the line profile. Figure 5.46 presents the phase resolved spectral line profile for a phase of 0 ns obtained at a position of $z = 2.0$ mm in the parallel field configuration.

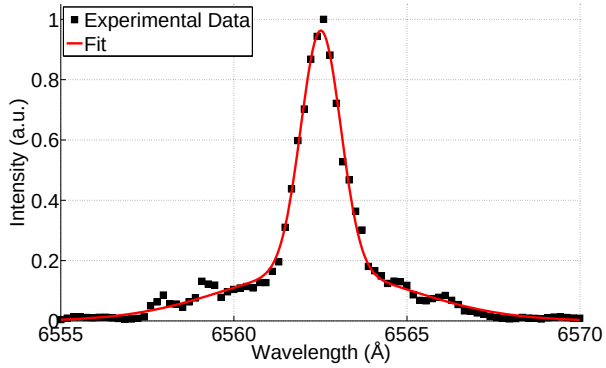

Figure 5.46: H_α π profile measured at a phase of 0 ns and a position of $z = 2.0$ in the parallel field configuration.

The line profile is fit to a bi-Gaussian function, as shown by the red curve of Figure 5.46. The thermal and superthermal emission intensities are determined from the corresponding analytical areas. The areas determined presented in Figure 5.47 as a function of phase in the parallel field configuration.

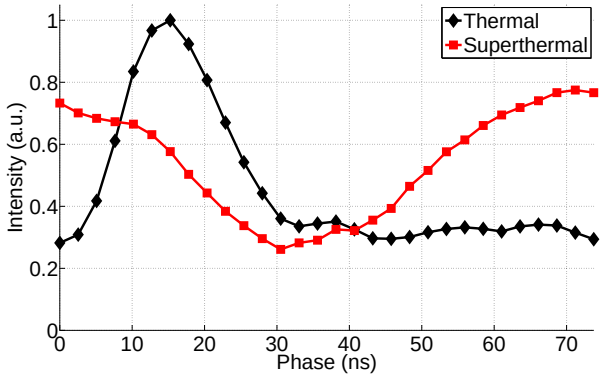

Figure 5.47: Thermal and superthermal emission as a function of phase in the parallel field configuration.

Utilizing Figure 5.47 the contour plot given by Figure 5.45 can be characterized in terms of the temperature associated with the radiator. The temperature associated with the radiator alludes to the process in which the excited state occurs. It is clearly seen that the first peak is associated with the thermal emission which as described above occurs due to electron impact excitation. The second peak is associated with the superthermal emission and is due to fast neutral atoms caused by charge exchange or sputtering of hydrogen atoms from the RF biased electrode surface.

In the parallel field configuration the spatial distribution of the thermal and superthermal emission is clearly discernible. Therefore the spatial structure of the thermal and superthermal emission is reconstructed from the data presented in Figure 5.45. Due to the complex electron and ion dynamics in the perpendicular field configuration, identification of the thermal and superthermal features are formidable. Therefore the first aperture of the collection optics was decreased to 750 μm and a spatial scan was conducted. Figure 5.48 presents the reconstructed and measured superthermal emission as a function of phase and space in the parallel and perpendicular field configurations respectively.

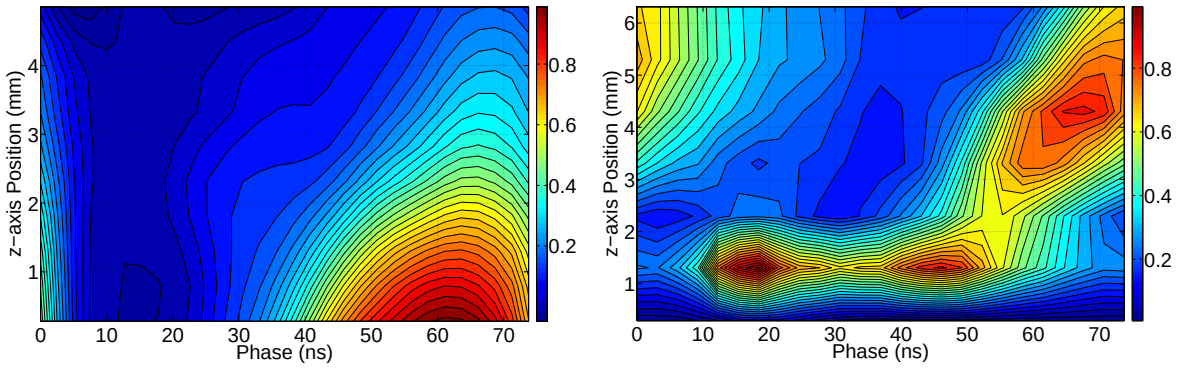

(a) (b)

Figure 5.48: Superthermal emission as a function of phase and space (a) in the parallel and (b) perpendicular field configurations.

In the parallel field configuration the spatial structure is fairly simple. Intense emission occurs near the electrode surface and is attributed to de-excitation of excited neutrals bombarding the RF biased electrode surface originating from charge exchange. The peak seems to be sloped indicating a beam like structure of hydrogen atoms directed into the bulk plasma. The spatial structure in the perpendicular field configuration is complex. Here the emission occurring near the electrode is thought to be also due to bombarding excited neutrals but two peaks occur. Approximately at 50 ns a directed beam of emission is occurring, traveling into the bulk plasma. This is expected to be cause by excited hydrogen atoms being sputtered from the RF biased electrode surface.

The thermal emission is utilized in the fitting of the H_β time averaged spectral line profiles. Figure 5.49 presents the reconstructed and measured thermal emission as a function of phase and space in the parallel and perpendicular field configurations respectively. The thermal emission data is interpolated or extrapolated to the position in which the time averaged measurement is conducted. The thermal emission spatial structure is simple for both the parallel and perpendicular field configurations. In the parallel field configuration thermal emission arises from two phenomena the electric field reversal and the sheath expansion. In the perpendicular field configuration only a peak near the electrode surface is observable. This peak is expected to be caused by the electric field reversal and the RF sheath expansion is not seen.

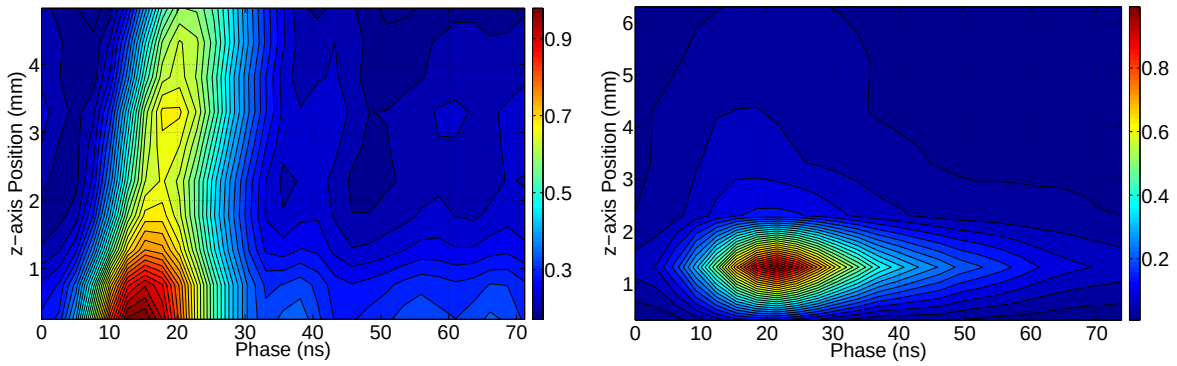

(a) (b)

Figure 5.49: Thermal emission as a function of phase and space (a) in the parallel and (b) perpendicular field configurations.

5.4 Spectral Line Profile Analysis

In this section the methodology associated with the analysis of the time averaged H_β and $5^3D \rightarrow 2^3P$ He I spectral line profiles will be presented. The error associated with select fit variables was simulated utilizing a typical signal to noise ratio. The results of the error analysis will be presented. This section will conclude with a detailed description of the analysis associated with the systematic fitting the spectra.

Utilizing the quasi-static approximation to calculate the theoretical spectral line profile fits were obtained through implementation of the algorithm developed in section 3.4. The model used to fit the H_β and $5^3D \rightarrow 2^3P$ He I spectral line profiles is presented in Table 5.1. The boundaries associated with the fit variables were set to be centered about the previously determined value, with respect to spatial location. The boundaries are given by 0.8 and 1.2 times the previously determined value. Minimum boundary widths were set to ensure adequate sampling of the parameter space. For

the initial fit associated with a shot the boundaries were determined by trail fits. The discretization associated with the fit variables is given by N_D. The number of iterations associated with the fit algorithm was two and was set such that the corresponding error was negligible in comparison with that arising from the spectral noise.

Table 5.1: Model associated with fitting of the spectral line profiles.

Fit Parameter	$\mathbf{H_\beta}$	$\mathbf{N_D}$	$\mathbf{5^3D \rightarrow 2^3P}$ **He I**	$\mathbf{N_D}$
E_0 (kV/cm)	Variable	8	Variable	12
E_1 (kV/cm)	Variable	8	Variable	12
θ_1 (radians)	Variable	8	0	-
I_{R1} (a.u.)	1	-	1	-
λ_{R1} (Å)	0	-	0	-
kT_{R1} (eV)	0.25	-	0	-
I_{R2} (a.u.)	Variable	15	Variable	25
λ_{R2} (Å)	0	-	0	-
kT_{R2} (eV)	Variable	10	Variable	15

Typically the RF sheath electric field has a harmonic spectrum with three to four dominate components. Due to the limited spectral resolution it was found that only the fundamental could be obtained accurately in the fit. Therefore the modeled electric field contains only a single component in the harmonic spectrum. Due to the time averaged nature of the measurement technique discrimination of the sign of the electric field is not possible and therefore the waveform was clamped at zero (see Figure 3.25). This is expected to have a negligible impact on the results due to the fact the electric field reversal is expected to be small [44, 147]. The electric field is thus assumed to always be negative, pointing towards the RF biased electrode surface.

As discussed in Section 5.3 it was found that the H_β transition intensity was strongly time dependent. To accurately correlate the modeled electric field with the time dependence of the transition intensity the phase angle associated with the fundamental, θ_1, was set to a fit variable. The $5^3D \rightarrow 2^3P$ He I transition intensity is time independent and thus the phase angle associated with the fundamental cannot be uniquely determined. As discussed in Section 5.2 the radiator distribution function for both transitions was found to be that of a two group. Due to the viewing geometry the Doppler shift associated with all groups is assumed to be zero. For the H_β spectral line profile it was found that the superthermal group could be accurately removed prior to the fit. Initially the thermal group was modeled having only a single fit variable the radiator temperature, kT_{R1}. As will be discussed below it was found that a single group was inadequate of representing the

thermal distribution function. Through fitting the spectral line profile in a zero electric field location in the RF sheath it was determined that accurate representation could be achieved with two groups. The multi-group thermal distribution is not unexpected as it has been experimental measured in similar RF discharges far from the RF sheath region [14]. As was discussed and found by Baravian *et al.* that the most prominent thermal group has a temperature of 0 to 0.5 eV, therefore the first group radiator temperature, kT_{R1}, was set to 0.25 eV. This fit parameter was set to a constant because both the intensity, I_{R2}, and radiator temperature, kT_{R2}, of the second group must be fit variables. Due to the limited computation resources, the addition of fit variables would be formidable. The first group radiator temperature is expected to be a function of position within the RF sheath but due to its small value it is not expected to effect the fit results significantly.

The $5^3D \rightarrow 2^3P$ He I spectral line profile was found to have a superthermal group that could not be removed prior to the fit. Therefore the radiator distribution function associated with the fit must contain both the thermal and superthermal groups. Due to the excitation mechanism the radiator temperature associated with the thermal group, kT_{R1}, is set to zero and therefore no fit variables are allocated to this group. The superthermal group has two fit variables the intensity, I_{R2}, and radiator temperature, kT_{R2}. In section 5.2 it was shown that the superthermal group associated with H_β was well represented by a Gaussian in the parallel field configuration. In the perpendicular field configuration a bi-Gaussian was required with nonzero Doppler shifts. The assumption is made for the $5^3D \rightarrow 2^3P$ He I spectral line profile that the superthermal group is Gaussian with a negligible Doppler shift in both field configurations.

5.4.1 Calculation of the Fit Error

In this section the methodology and results associated with the error analysis will be presented. The error associated with the fit variables is dominated by the spectral noise due to the fact fit algorithm error is negligible. To estimate this error, noisy spectra were generated and fit. Typical spectral noise was calculated from Eq. 3.11 using the parameters associated with the PyLoN camera given in Table 3.1. The intensity of the transition was set to 1000 counts which resulted in an error of approximately 5 %, roughly a factor of two higher then the actually level. The noise was multiplied by a random number spanning -1 to 1 and added to the simulated spectral line profile. To generate the required statistics twenty spectra where fit per investigated parameter. The error was estimated by taking the 95 % confidence interval associated with the standard deviation of the fitted variable. Due to the size of the parameter space and the large number of fits required per investigated parameter simplified models must be chosen. Therefore only the error associated with select fit variables will be presented.

Three fitting scenarios were investigated: the π and σ profiles were fit together, the π profiles were fit separate, and the σ profiles were fit separate. This was conducted to determine the usefulness of

polarization spectroscopy in aiding the extraction of the electric field parameters. The error analysis associated with the H_β and $5^3D \rightarrow 2^3P$ He I spectral line profiles is presented below.

$\mathbf{H}_\beta$

Due to computing time constraints the exact model given in Table 5.1 could not be used to conduct the error analysis for the H_β spectra. For the error analysis, the following changes were made to the model. The emission intensity was taken to be constant in time, thus the electric field parameter θ_1 was set to zero and the thermal radiator distribution function was approximated with one group. The error associated with the fit variables E_0, E_1, and kT_{R1} is estimated at discrete values. The electric field parameters spanned 0 to 6.0 kV/cm in twelve steps and the radiator temperature spanned 0.5 to 3.0 eV in six steps. The error associated with the radiator temperature in this simplified model will be taken as the error associated with the radiator temperature of the second group, kT_{R2}.

The simulated H_β spectra were fit with variable boundaries centered about the modeled value with widths of 2 kV/cm and 2 eV for the electric field parameters and radiator temperature respectively. The number of discretizations associated with the fit variables was $N_D = 8$ and the number of iterations associated with the fit algorithm was two. The simulated H_β spectra are given in Figure 5.50 for electric field parameters $E_0 = -3.3$ kV/cm and $E_1 = 3.3$ kV/cm. The radiator temperature is $kT_{R1} = 1.0$ and 2.0 eV for Figure 5.50a and Figure 5.50b respectively. The theoretical noise free spectra is given by the solid line. The pixelated spectra superimposed with the noise are given by the markers, all twenty spectra are shown.

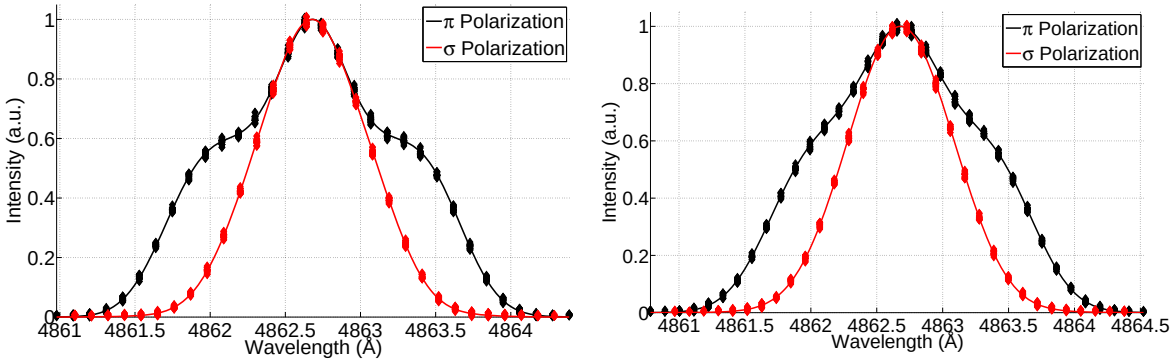

(a) (b)

Figure 5.50: H_β π and σ profiles for $E_0 = E_1 = 3.3$ kV/cm and (a) $kT_{R1} = 1.0$ and (b) 2.0 eV with simulated noise.

Initially the error associated with the fit scenario where the π and σ profiles are fit together as an object will be considered. Figure 5.51a through Figure 5.53a presents the 95 % confidence

interval for E_0, E_1, and kT_{R1} respectively as a function of the electric field parameters E_0 and E_1 for $kT_{R1} = 1.0$ eV. Figure 5.51b through Figure 5.53b presents the equivalent for $kT_{R1} = 2.0$ eV. As shown in Figure 5.51 the error associated with E_0 is a strong function of E_0 and only weakly dependent on E_1, becoming substantial below $E_0 = 2$ kV/cm. For E_1 the dependence is nearly reversed, here the error is dependent on both E_0 and E_1 with a stronger dependence on E_1. The error was found to become substantial below $E_0 = 2.0$ and $E_1 = 2.0$ kV/cm as indicated by Figure 5.52. The error associated with kT_{R1} is dependent on both electric field parameters and becomes substantial above the line $|E_0| = E_1$ as indicated by Figure 5.53. Similar trends were found for the two remaining fit scenarios in which the π and σ profiles were fit independently. Overall it was found the error associate with E_0 and E_1 becomes substantial at lower electric field magnitudes while that of kT_{R1} becomes substantial at higher electric field magnitudes.

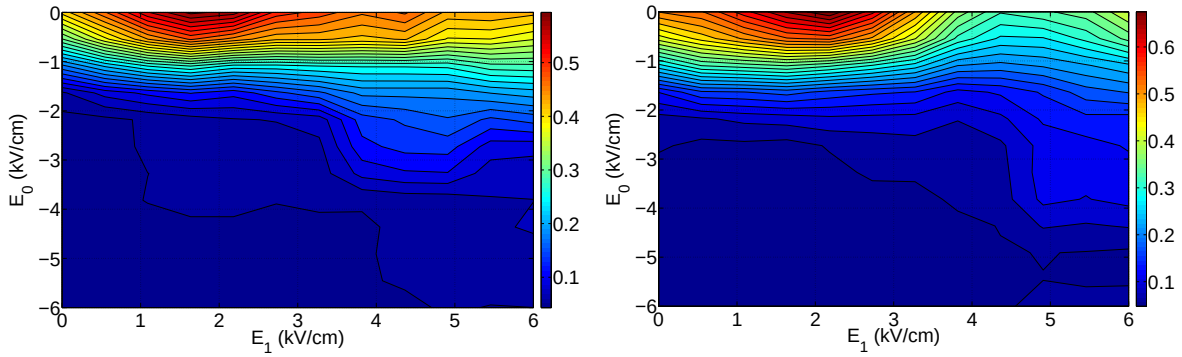

(a) (b)

Figure 5.51: E_0 error as a function of electric field parameters E_0 and E_1 for (a) kT_{R1}=1.0 and (b) 2.0 eV.

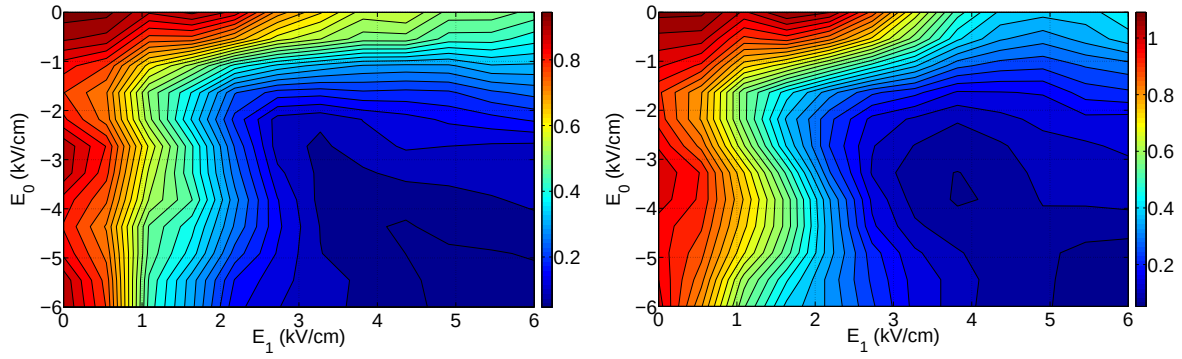

(a) (b)

Figure 5.52: E_1 error as a function of electric field parameters E_0 and E_1 for (a) $kT_{R1} = 1.0$ and (b) 2.0 eV.

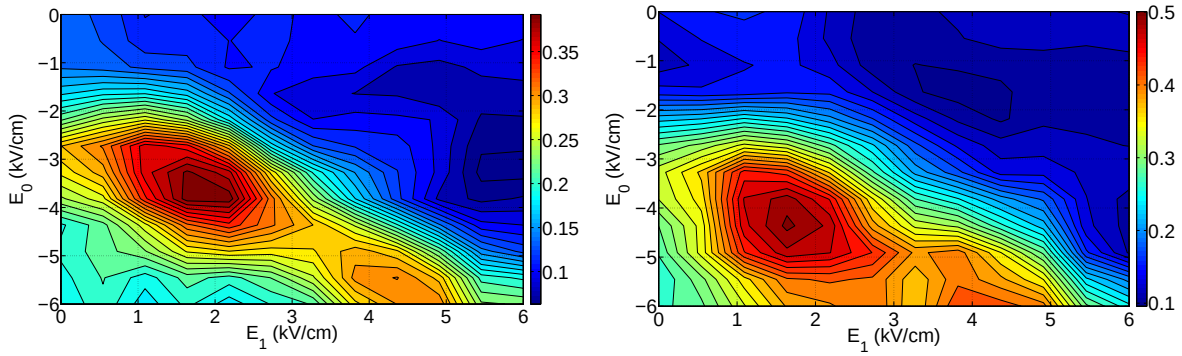

(a) (b)

Figure 5.53: kT_{R1} error as a function of electric field parameters E_0 and E_1 for (a) $kT_{R1} = 1.0$ and (b) 2.0 eV.

The error associated with the investigated fit variables tends to increase with increasing radiator temperature. To demonstrate this, the averaged error is plotted as a function of the radiator temperature and is presented for E_0, E_1, and kT_{R1} in Figure 5.54a through Figure 5.56a respectively. The effectiveness in fitting the π and σ profiles together as an object is investigated by plotting the averaged error ratio of π to π and σ and σ to π and σ fit scenarios. The averaged error ratio is plotted as a function of the radiator temperature and is presented for E_0, E_1, and kT_{R1} in Figure 5.54b through Figure 5.56b respectively.

Overall, it was found that fitting the π and σ profiles together decreased the error when compared to fitting either profile independently. The error associated with fitting the σ profile independently was found to be substantially larger then not only that of the π and σ fit scenario but also the π. This is due to the fact the magnetic substates giving rise to σ polarized photons are significantly less effected by the electric field then those of the π.

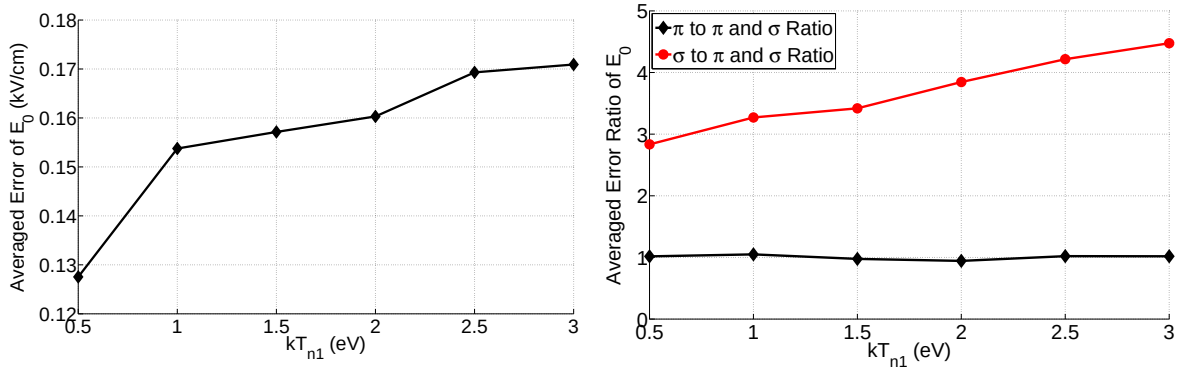

(a) (b)

Figure 5.54: (a) Averaged error from π and σ fit scenario and (b) averaged error ratio as a function of radiator temperature for E_0.

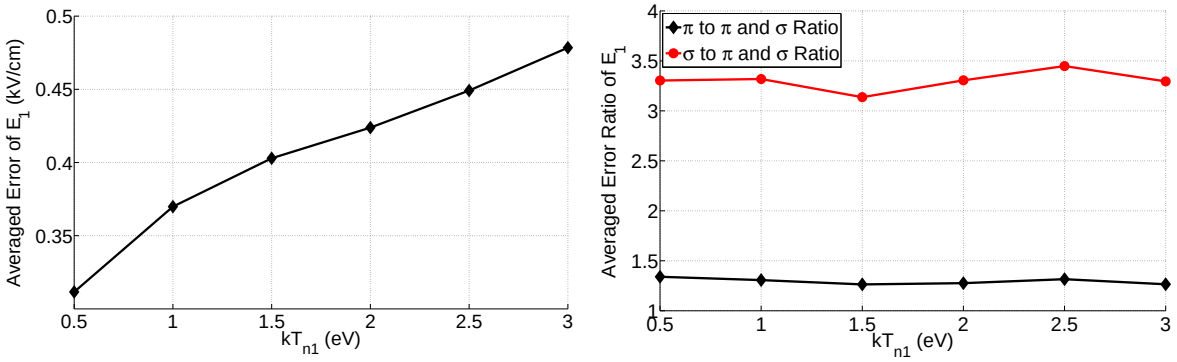

(a) (b)

Figure 5.55: (a) Averaged error from π and σ fit scenario and (b) averaged error ratio as a function of radiator temperature for E_1.

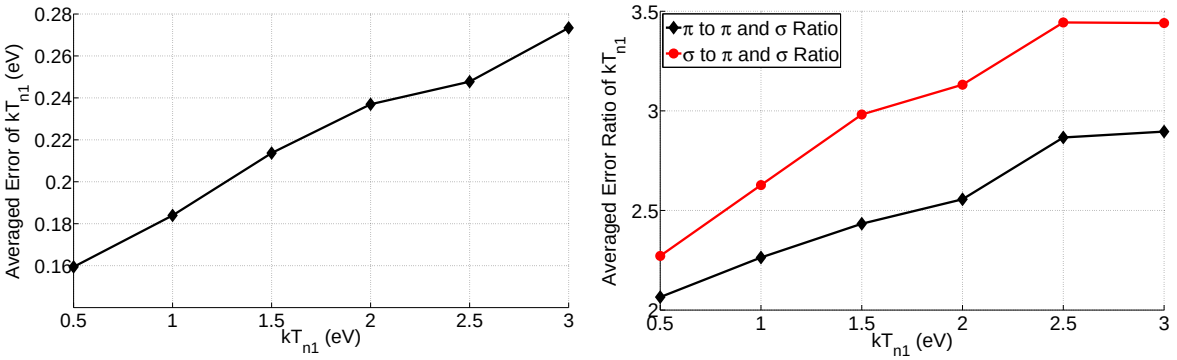

(a) (b)

Figure 5.56: (a) Averaged error from π and σ fit scenario and (b) averaged error ratio as a function of radiator temperature for kT_{R1}.

As shown by Figure 5.54b the averaged π to π and σ error ratio is unity indicating that when determining E_0 both fit scenarios give equivalent results. This is not the case for the E_1 and kT_{R1} variables. When considering the addition of the electric field parameter θ_1 as a fit variable and the extension of the thermal radiator distribution function to two groups it is expected that the averaged error ratios will be increased. Thus it is determined for the H_β spectral line profile that fitting the π and σ profiles together as an object is beneficial.

$5^3D \rightarrow 2^3P$ He I

Due to time constraints the exact model given in Table 5.1 could not be used to conduct the error analysis for the $5^3D \rightarrow 2^3P$ He I spectra. For the error analysis the model was changed such that

only the thermal group of the radiator distribution function was considered. Thus only the error associated with the fit variables E_0 and E_1 is estimated. The error was calculated at discrete values of the fit variables, spanning 0 to 6.0 kV/cm in twelve steps.

The simulated $5^3D \rightarrow 2^3P$ He I spectra were fit with variable boundaries centered about the modeled value with widths of 2 kV/cm. The number of discretizations associated with the fit variables was $N_D = 8$ and the number of iterations associated with the fit algorithm was two. The simulated $5^3D \rightarrow 2^3P$ He I spectra are given in Figure 5.57 for electric field parameters $E_0 = -3.3$ kV/cm and $E_1 = 3.3$ kV/cm. The theoretical noise free spectra is given by the solid line. The pixelated spectra superimposed with the noise are given by the markers, all twenty spectra are shown.

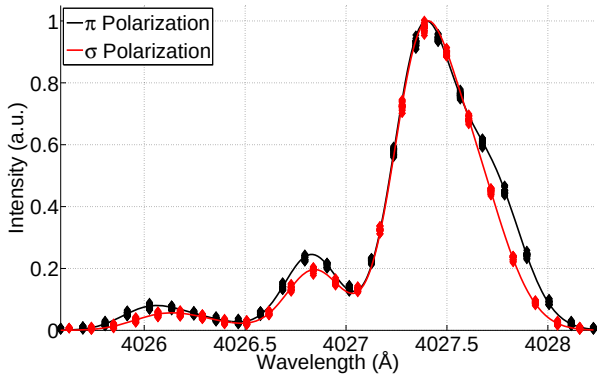

Figure 5.57: $5^3D \rightarrow 2^3P$ He I π and σ profiles for $E_0 = E_1 = 3.3$ kV/cm with simulated noise.

Initially the error associated with the fit scenario where the π and σ profiles are fit together as an object will be considered. Figure 5.58a and Figure 5.58b present the 95 % confidence interval for E_0 and E_1 respectively as a function of the electric field parameters E_0 and E_1. Contrary to the findings associated with H_β, Figure 5.58 shows that the error associated with E_0 and E_1 behave similarly. The error associated with the electric field parameters are found to be strong functions of E_0 and only weakly dependent on E_1, becoming substantial below $E_0 = 2$ kV/cm.

It was found that fitting the π and σ profiles together yielded only a negligible or small decrease in error. When compared to fitting only the π profiles the error was found to be approximately equivalent. When compared to fitting only the σ profiles a slight decrease in error was obtained, the averaged error ratio of σ to π and σ was 1.1 and 1.2 for E_0 and E_1 respectively. Therefore if the superthermal group of radiators could be ignored acquisition and fitting of the σ profile in addition to the π is unwarranted. As was presented above the superthermal emission was found to have an intensity of 54.7 % when compared to the thermal and thus cannot be ignored. Therefore it is expected that the addition of the σ profile will decrease the error associated with the fit and will be implemented.

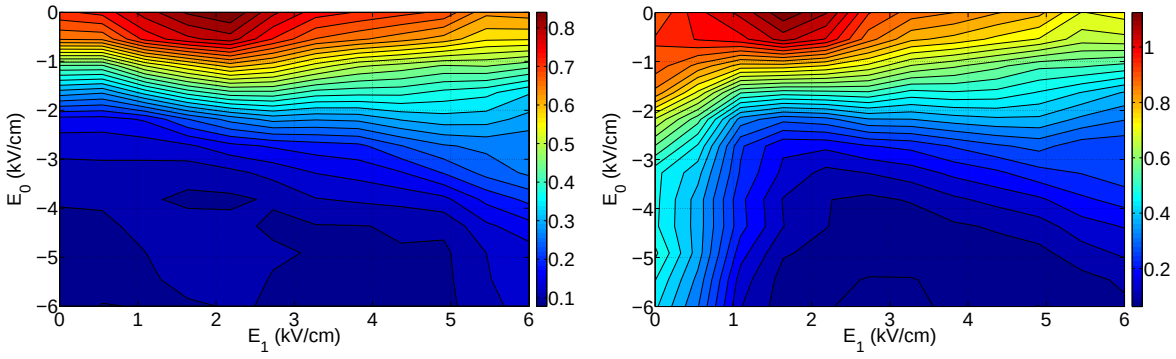

(a) (b)

Figure 5.58: (a) E_0 and (b) E_1 error as a function of electric field parameters E_0 and E_1.

5.4.2 Fitting the Spectral Line Profile

H_β

To discuss the fit to the H_β π and σ profiles shots 3 and 19 where selected for presentation, corresponding to the parallel and perpendicular field configurations respectively. Fitted spectra of additional shots can be found in Appendix D. The discharge parameters of interest for shot 3 are $P = 200$ mTorr, $V_{DC} = -2.7$ kV, $|V_{RF}| = 2.6$ kV/cm, and $n_e = 1.03 \cdot 10^{17}$ m^{-3}. The discharge parameters of interest for shot 19 are $P = 100$ mTorr, $V_{DC} = -1.9$ kV, $|V_{RF}| = 2.2$ kV, and $n_e = 3.49 \cdot 10^{15}$ m^{-3}. The remaining discharge parameters for these shots can be found in Appendix C. The electric field and thermal distribution function parameters associated with the presented fits are given in Table 5.2 and Table 5.3 for shots 3 and 19 respectively.

Table 5.2: Fit parameters associated with the spectra presented for shot 3.

Position (mm)	**E_0 (kV/cm)**	**E_1 (kV/cm)**	**θ_1 (°)**	**I_{R2} (%)**	**kT_{R2} (eV)**
0.8	-4.4 ± 0.1	7.4 ± 0.1	57.1 °	139.8	4.2
7.9	11.9 ± 1.3	12.8 ± 1.5	10.0 °	48.1	3.7

Table 5.3: Fit parameters associated with the spectra presented for shot 19.

Position (mm)	**E_0 (kV/cm)**	**E_1 (kV/cm)**	**θ_1 (°)**	**I_{R2} (%)**	**kT_{R2} (eV)**
1.0	-2.5 ± 0.1	4.8 ± 0.2	3.8	144.5	4.9
7.6	6.7 ± 1.2	10.0 ± 1.2	14.5	44.7	4.3

In general the theoretical spectra fit the experimental data well, with reduced $\chi \approx 1.5$ on average. In the parallel field configuration the quality of the fit increased slightly with electric field intensity, the opposite was found for the perpendicular field configuration. Overall there where no significant trends associated with the reduced χ indicating that the model adequately captures the essential physics. Only a single feature of the H_β spectral line profile could not be adequately represented by the model presented in Table 5.1. This feature is an asymmetry which skews the profile to the right of center and is most prominent in the π profile for high electric field intensities.

To explore the asymmetry, the fitted H_β π profile at positions of $z = 0.8$ and 1.0 mm are presented in Figure 5.59a for shot 3 and Figure 5.59b for shot 19 respectively. Comparing the asymmetries of the π profiles presented in Figure 5.59 a common feature is present, a small but distinct bump at 4863 Å. This feature is present in all of the data with varying degrees of intensity, therefore it is expected to be caused by a molecular or impurity line. For a majority of the data this feature is the main proponent driving the spectral line profile asymmetry, as is the case for that presented in Figure 5.59b.

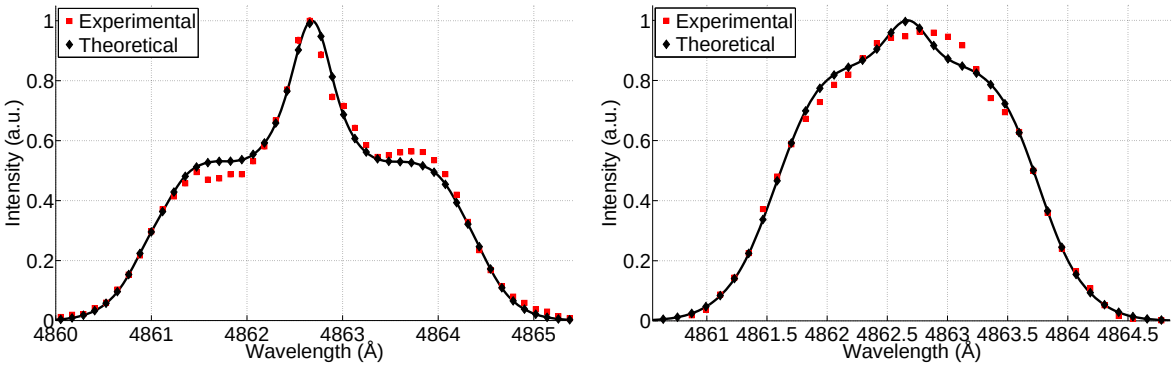

(a) (b)

Figure 5.59: Fit to the H_β π profile at a position of $z = 0.8$ and 1.0 mm for (a) shot 3 and (b) 19 respectively.

At higher electric field intensities an additional asymmetry becomes evident in the π profile. As indicated by a comparison to the theoretical spectrum of Figure 5.59a the peak on the right wing is found to be 6 % more intense then that of the left wing. Naturally the H_β theoretical spectra are slightly asymmetric having asymmetries on the order of only 1 %, for that presented in Figure 5.59a the profile is skewed towards the left by approximately 0.2 %. Therefore the asymmetry is assumed to be caused by the radiator distribution function, molecular lines, or a non-statistical population of magnetic substates; not the electric field.

The superthermal emission is not expected to be the cause of the asymmetry in the parallel

field configuration because the profile is not Doppler shifted and symmetric, see Figure 5.23. In the perpendicular field configuration the superthermal emission profile was asymmetric thus incomplete removal may contribute to asymmetries in the profile. As is shown in Figure 5.59b the asymmetry in the spectrum is less prominent in the perpendicular field configuration then that of the parallel. Therefore it is concluded that the superthermal emission is not the sole contributor.

It was found that the distinguishable molecular lines in the spectrum, such as the 4858 Å line seen in Figure 5.23, have an intensity that is relatively constant with respect to position and polarization. Therefore if the asymmetry is due to molecular lines they would be present in the σ profiles. The H_β σ profile at positions of $z = 0.8$ and 1.0 mm are presented in Figure 5.60a for shot 3 and Figure 5.60b for shot 19 respectively. As indicated by a comparison to the theoretical spectra the σ profiles are very symmetric, where the only distinguishable asymmetry is that at 4863 Å as discussed above.

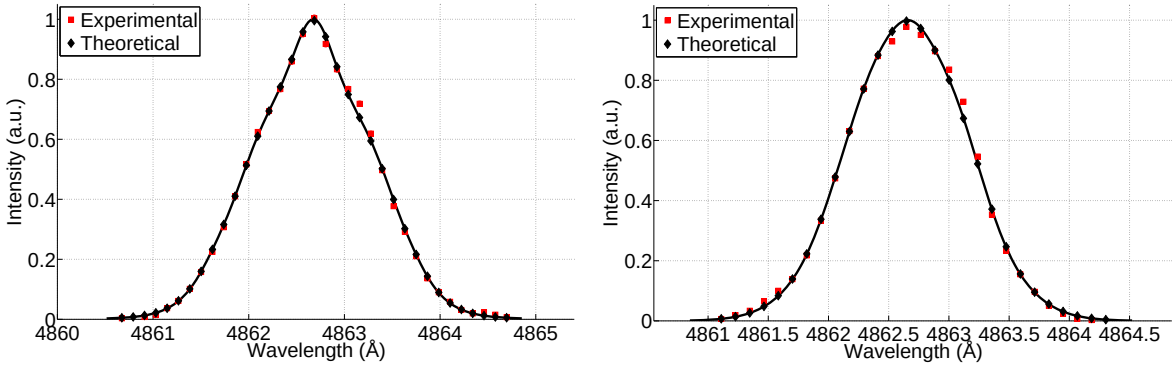

(a) (b)

Figure 5.60: Fit to the H_β σ profile at a position of $z = 0.8$ and 1.0 mm for (a) shot 3 and (b) 19 respectively.

To further investigate the possibility of molecular lines driving the large asymmetry seen only in the π profile the molecular spectrum in the wavelength range of interest is calculated [41]. Figure 5.61a presents the π and σ experimental profiles for shot 3 at a position of $z = 0.8$ mm with the molecular spectrum presented in Figure 5.61b.

As seen by the molecular spectrum the location of the transitions coincide with the observed asymmetry while the intensities do not. Due to the fact the plasma kinetics have a strong role in governing the molecular line intensity Figure 5.61b serves only as a first approximation. It is therefore a possibility that the asymmetry is in fact due to molecular transitions although highly unlikely due to the absence in the σ profile. In addition it is seen that a molecular transition does not occur at 4863 Å and thus this feature is attributed to an impurity. As was found in Section 5.2.2, the impurity line present in the $5^3D \rightarrow 2^3P$ He I spectra was found to be either a W I or Fe I transition. Referencing

the NIST database it is found that the 4863 Å line could be attributed to either a W I or Fe I transition as well [5].

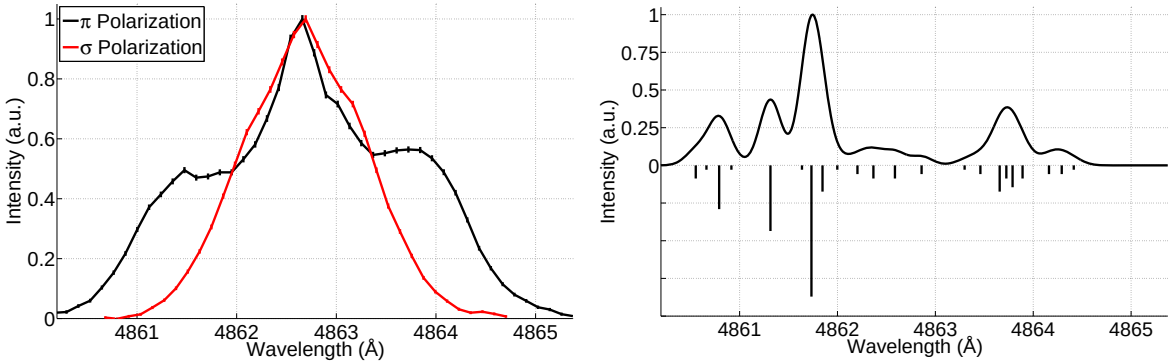

(a) (b)

Figure 5.61: (a) H_β π and σ profiles at a position of $z = 0.8$ mm for shot 3 and (b) simulated molecular hydrogen profile.

The remaining logical possibility driving this asymmetry is a non-statistical population of the magnetic substates. As shown by Figure 5.28 the integrated area of the π and σ profiles differs by nearly 20 % at $z = 0.8$ mm in the parallel field configuration for shot 1 and over 40 % at $z = 1.0$ mm in the perpendicular field configuration for shot 19. Thus revealing that magnetic substates are not in complete equilibrium and therefore supporting this hypothesis. While no definite conclusion can be drawn the non-statistical population of magnetic substates is the most logical explanation for the asymmetry. Due to the fact the asymmetry is most prominent at the extreme electric field intensities and only in the π profiles it is not expected to significantly alter the fitting results.

Comparing the spectral line profiles obtained in the parallel and perpendicular field configurations it is seen that they portray differing characteristic shapes. This is partly due to the fact that the intensity of the electric field is substantially higher in the parallel field configuration as presented in Table 5.2 and Table 5.3. Higher electric field intensity manifests as increased splitting of the spectral line profile, which in the case of the π profile associated with the parallel field configuration is substantial enough to lead to peaked wings about the line center. In addition, a characteristic is present that cannot be attributed to the intensity of the electric field, a broadening about the line center. The spectra associated with the perpendicular field configuration are very broad at the line center displaying a rounded peak, in contrast those associated with the parallel are narrow and highly peaked. Two phenomena are responsible for this characteristic: the time dependent behavior of the electric field and transition intensity. The electric field and transition intensity waveforms associated with the fit to the spectral line profiles at a position of $z = 0.8$ mm for shot 3 and $z = 1.0$

mm for shot 19 is presented in Figure 5.62a and Figure 5.62b respectively. Note that the electric field and transition intensity waveforms are correlated through the phase angle θ_1.

The time dependent behavior of the electric field is seen to be similar for both configurations, although the approximation of the harmonic spectrum having only a single component does not allow for substantial differences. The electric field waveforms are expected to be different. Implications of this approximation on the spectra will be discussed below. The time dependent behavior of the transition intensity is found to be similar except in the value in which the intensity decays too. In the perpendicular field configuration this value is nearly zero while that of the parallel is approximately 0.3. As seen by Figure 5.62 it is during this time period in which the intensity has decayed to its constant value that the electric field intensity is zero. This finding suggests that the spectra associated with the parallel field configuration should be weighted stronger when the electric field intensity is zero, that is at the line center, then those the perpendicular. Thus explaining the differing characteristic of the line center associated with the configurations. Note the peak of the transition intensity coincides at the same phase within the electric field waveform for both configurations.

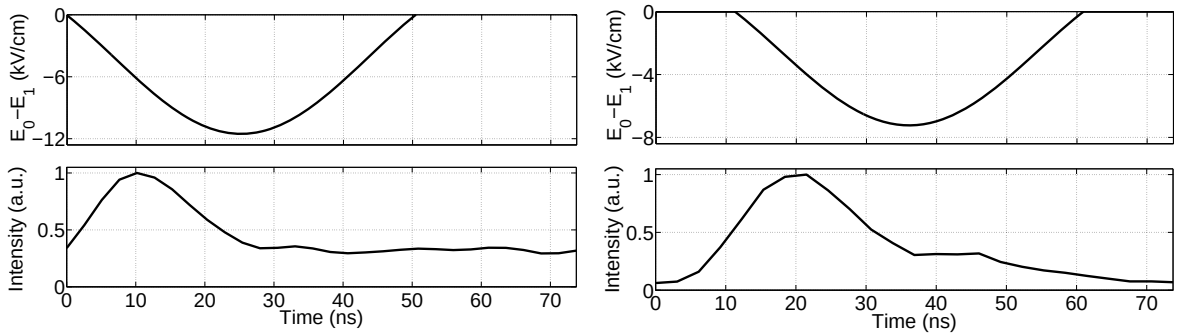

Figure 5.62: Electric field and transition intensity waveforms associated with the fit to the H_β π and σ profiles at a position of (a) $z = 0.8$ mm for shot 3 and (b) $z = 1.0$ mm for 19.

The H_β π and σ experimental profiles at positions of $z = 7.9$ and 7.6 mm are presented in Figure 5.63a for shot 3 and Figure 5.63b for shot 19 respectively. For select shots, such as those presented here, at the extreme z-axis positions the π and σ profiles are nearly identical and non-Gaussian. The electric field effects the π and σ components significantly different (see Figure 3.27), while the radiator distribution function associated with the thermal group is approximately equivalent. Therefore the effect of the electric field can be easily discriminated from that associated with the radiator distribution function because the π and σ profiles are measured independently. As presented in Figure 5.63a the π and σ profiles are equivalent, indicating that the electric field is negligible at $z = 7.9$ mm for shot 3. Those presented in Figure 5.63b are slightly different, thus the electric field is

expected to be nonzero with an intensity ≈ 1 kV/cm.

Initially the thermal radiator distribution function was taken to have only a single group. For high electric field intensities this model was capable of accurately representing the data due to the fact the electric field induced broadening overwhelmed that of the thermal radiator distribution function. As the electric field decreased the single group model revealed its limitations through its inability to fit the data accurately. Using the single group model, the fitted H_β π and σ profiles at a position of $z = 7.9$ mm are presented in Figure 5.64a and Figure 5.64b for shot 3 respectively. The electric field parameters were found to yield a minimum waveform intensity of $E_0 - E_1 = 3.6$ kV/cm, significantly different from the expected value of 0 kV/cm.

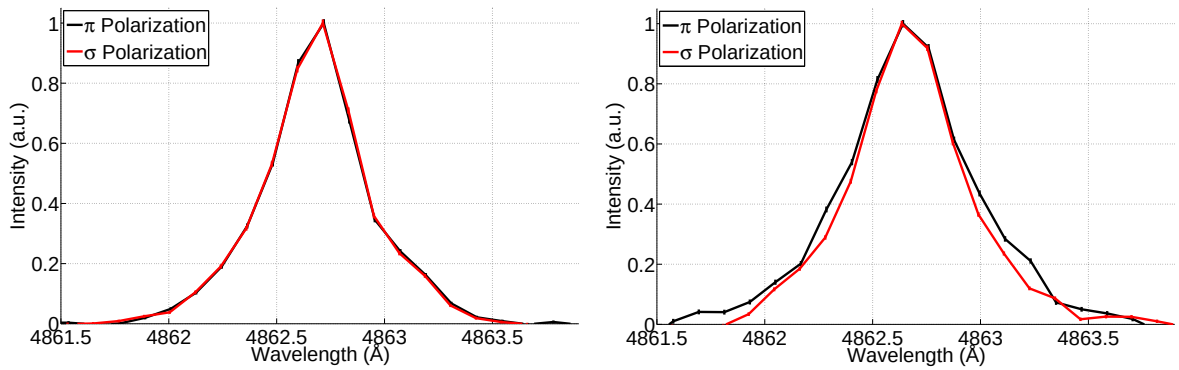

(a) (b)

Figure 5.63: H_β π and σ profiles at a position of $z = 7.9$ and 7.6 mm for (a) shot 3 and (b) 19 respectively.

Fit independently the broadening associated with both the π and σ profiles can be simulated by an non-zero electric field intensity, as indicated by the high fit quality associated with the π profile. It is only when the profiles are fit together as an object can the electric field be ruled out, therefore revealing the usefulness of polarization spectroscopy. As shown by Figure 5.64 the single group model is incapable of representing the broadening observed in both the π and σ profiles obtained at the far end of the RF sheath.

As reported in the literature, multi-group thermal distributions have been observed experimentally in RF discharges for the Balmar series transitions [14]. Therefore the model was extended such that the thermal radiator distribution function was that of a two group. To preform the computations in a reasonable amount of time the temperature associated with the first group was held constant at 0.25 eV. As discussed above this is not expected to significantly effect the results because of the limited range of possible values, 0 to 0.5 eV [14].

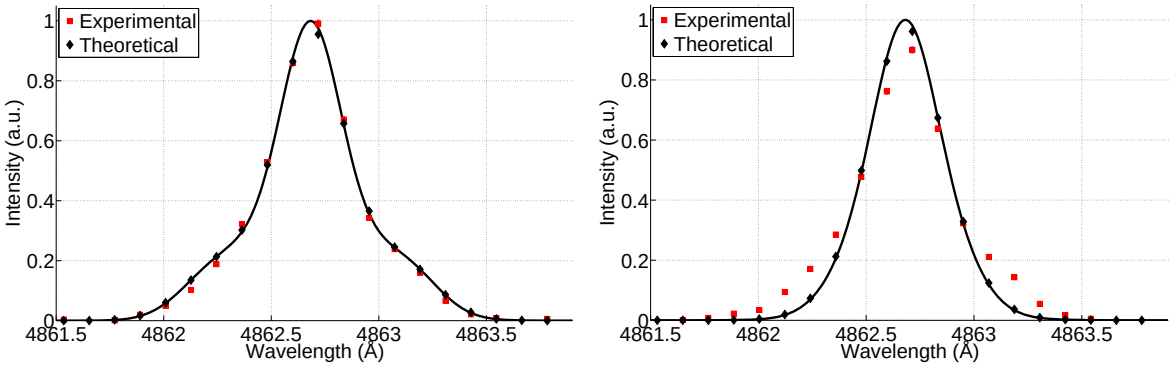

(a) (b)

Figure 5.64: Fit to the H_β (a) π and (b) σ profiles for shot 3 at a position of $z = 7.9$ mm using the one group model.

Using the two group model given in Table 5.1 the fitted H_β π and σ profiles at a position of $z = 7.9$ mm is presented in Figure 5.65a and Figure 5.65b for shot 3 respectively. The electric field parameters were found to yield a minimum waveform intensity of $E_0 - E_1 = 0.9$ kV/cm with the second group having a intensity of $I_{R2} = 48.1$ % and a temperature of $kT_{R2} = 3.7$ eV. As shown by Figure 5.65 both fits are of high quality having electric field parameters nearly equal to zero, as expected. Therefore it is assumed that the two group representation as given in Table 5.1 is adequate in describing the thermal distribution function.

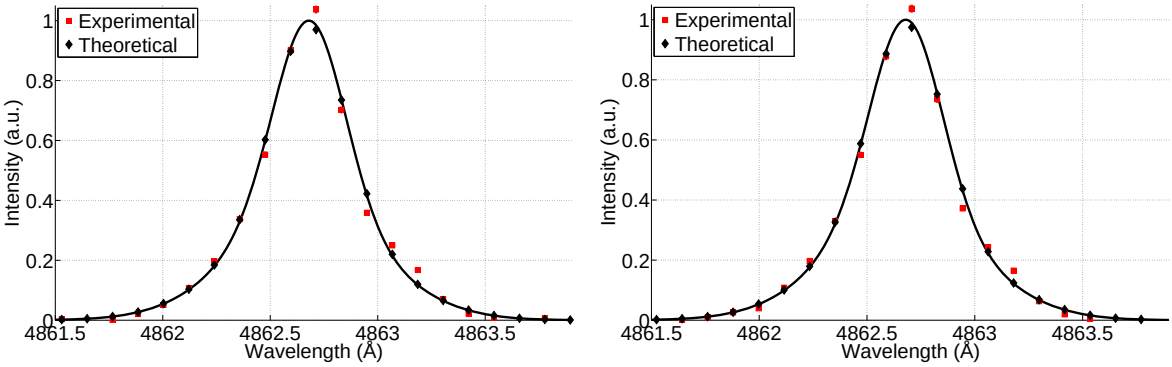

(a) (b)

Figure 5.65: Fit to the H_β (a) π and (b) σ profiles for shot 3 at a position of $z = 7.9$ mm using the two group model.

The reduced χ associated with the fits to the H_β π and σ profiles is presented in Figure 5.66a for shot 3 and Figure 5.66b for shot 19 respectively. In the parallel field configuration the reduced χ

typically has its minimum close to the RF biased electrode surface, where the electric field intensity is high. The reduced χ then increases on average as the electric field intensity decreases, although this trend is rather weak. In the perpendicular field configuration the reduced χ is relatively constant except close to the RF biased electrode where a peak is observed.

Beyond the error associated with the spectral noise and impurity line other possible sources are the beam profile of the collection optics and the finite representation of the harmonic spectrum of the electric field waveform. To determine if the collection optics has a significant effect on the fit results the measured beam profile, presented in Figure 4.18a, was incorporated into the fitting routines. Due to the fact that the spatial profile of the fit variables is required, fitting the data became an iterative process substantially increasing the computational time. It was found that while the reduced χ was slightly decreased the fit results where not significantly altered. The finite width of the beam profile is not expected to contribute significantly and thus was approximated as a delta function.

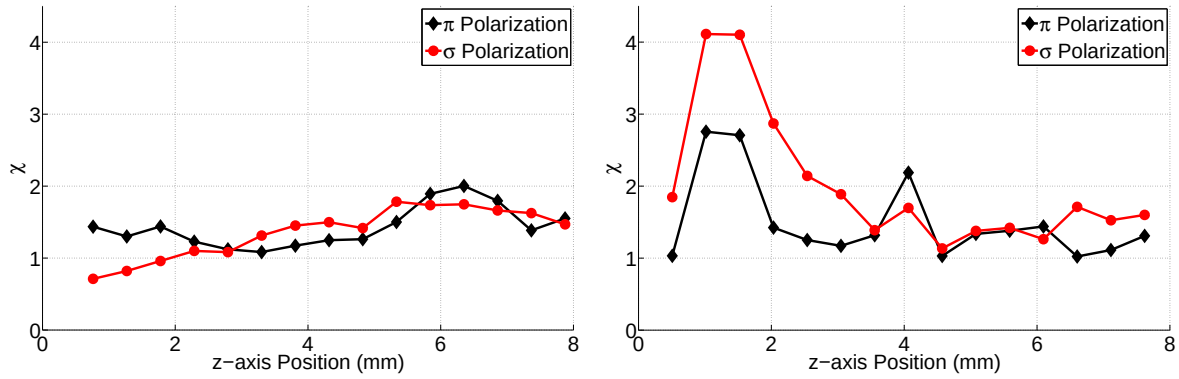

Figure 5.66: Reduced χ fitting parameter associated with the H_β π and σ profiles as a function of position for (a) shot 3 and (b) shot 19.

The majority of the non-quantitative error is expected to be due to the approximation of the electric field harmonic spectrum having only one component. Indicated by the modeling presented in Section 2.3 the spectrum is well represented by a single component near the RF biased electrode where the electric field. As the distance from the RF biased electrode is increase the waveform becomes substantially non-sinusoidal therefore incapable of being represented by a single component. In this region the electric field intensity is relatively weak and therefore the spectral line profile is rather featureless. It is expected that the time averaged electric field is approximated well with the model given here while the time dependence is not, especially at the far end of the RF sheath near the sheath/presheath interface.

5^3D $\rightarrow$ 2^3P He I

To discuss the fit to the $5^3D \rightarrow 2^3P$ He I π and σ profiles shots 11 and 27 where selected for presentation, corresponding to the parallel and perpendicular field configurations respectively. Fitted spectra of additional shots can be found in Appendix D. The discharge parameters of interest for shot 11 are $P = 200$ mTorr, $V_{DC} = -2.7$ kV, $|V_{RF}| = 2.4$ kV, and $n_e = 1.49 \cdot 10^{17}$ m^{-3}. The discharge parameters of interest for shot 27 are $P = 200$ mTorr, $V_{DC} = -1.9$ kV, $|V_{RF}| = 2.0$ kV/cm, and $n_e = 1.01 \cdot 10^{16}$ m^{-3}. The remaining discharge parameters for these shots can be found in Appendix C. The electric field and thermal distribution function parameters associated with the presented fits are given in Table 5.4 and Table 5.5 for shots 11 and 27 respectively.

Table 5.4: Fit parameters associated with the spectra presented for shot 11.

Position (mm)	**E_0 (kV/cm)**	**E_1 (kV/cm)**	**I_{R2} (%)**	**kT_{R2} (eV)**
0.8	-5.1 ± 0.1	4.1 ± 0.1	15.5	30.0
7.9	-1.6 ± 0.4	1.5 ± 0.5	9.4	12.2

Table 5.5: Fit parameters associated with the spectra presented for shot 27.

Position (mm)	**E_0 (kV/cm)**	**E_1 (kV/cm)**	**I_{R2} (%)**	**kT_{R2} (eV)**
1.0	-4.0 ± 0.1	2.9 ± 0.1	4.9	42.4
7.6	-0.4 ± 0.8	2.1 ± 1.0	3.3	105.9

In general the theoretical spectra fit the experimental data well, with reduced $\chi \leq 2$ on average. Typically the fit to the $5^3D \rightarrow 2^3P$ He I profiles were of the same quality as those associated with H_β, in addition the trends where found to be similar. In the parallel field configuration the reduced χ on average increased with z. In the perpendicular field configuration the reduced χ was peaked near a position of $z = 1.5$ mm and on averaged decreased with z. In general the fit quality increased and decreased with increasing electric field strength in the parallel and perpendicular field configurations respectively. Overall the features of the $5^3D \rightarrow 2^3P$ He I spectral line profile were adequately represented by the model presented in Table 5.1 with only a slight disagreement.

To explore a typical fit to the $5^3D \rightarrow 2^3P$ He I spectra, the π profile at a position of $z = 0.8$ and 1.0 mm is presented in Figure 5.67a for shot 11 and Figure 5.67b for shot 27 respectively. For high electric field intensity three prominent features are distinguishable: two peaks left and one peak right of the line center. As shown by the modeled spectra presented in Figure 3.31b this is indicative of a sinusoidal electric field. As the intensity decreases these features begin to merge

together towards the line center. Overall it was found that these three features were adequately captured by the fitted theoretical spectrum, with only a slight disagreement present. Regardless of the electric field intensity the prominent difference between the experiment and the theory is associated with the characteristics of the first peak left of the line center. It was found that the model was incapable of representing the location and broadening of this spectral feature. The location was found to be shifted to the right with respect to the fitted theoretical spectrum and the broadening was found to be more extensive. In addition, at moderate to low electric field intensities this peak was broadened such that it was completely absorbed by the main peak.

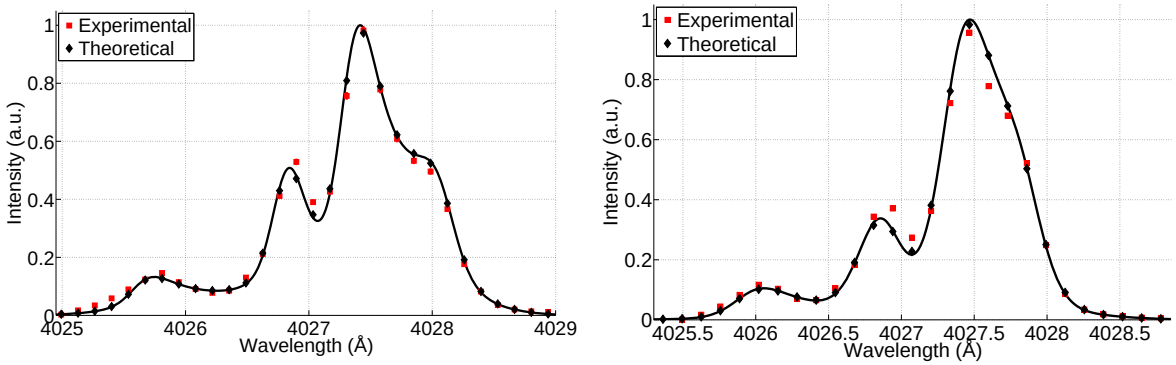

Figure 5.67: Fit to the $5^3D \rightarrow 2^3P$ He I π profile at a position of $z = 0.8$ and 1.0 mm for (a) shot 11 and (b) 27 respectively.

The $5^3D \rightarrow 2^3P$ He I σ profile at a position of $z = 0.8$ mm for shot 11 and $z = 1.0$ mm for shot 27 is presented in Figure 5.68a and Figure 5.68b respectively. At high to moderate electric field intensities it was found that the spectra obtained in the perpendicular field configuration had the largest disagreement with respect to the theory. As seen by Figure 5.67b and Figure 5.68b this disagreement is focused about the spectral feature discussed above.

Comparing the spectra obtained in the parallel and perpendicular field configurations it is seen that they portray differing characteristic shapes, similar to the differences found for the H_β spectra. Here the profiles obtained in the perpendicular field configuration also experience a broadening about the line center that leads to a rounded peak when compared with those of the parallel field configuration. In addition the peak left of the line center is further broadened leading to a greater disagreement with the theory as discussed above. As seen by Table 5.4 and Table 5.5 the electric field intensity associated with the parallel and perpendicular field configurations is substantially different. An increased electric field intensity leads to a greater distinction of spectral features but is not fully capable of explaining the presented differences. Therefore the cause is assumed to be due

to the time dependence of the electric field waveform because the transition intensity is constant in time.

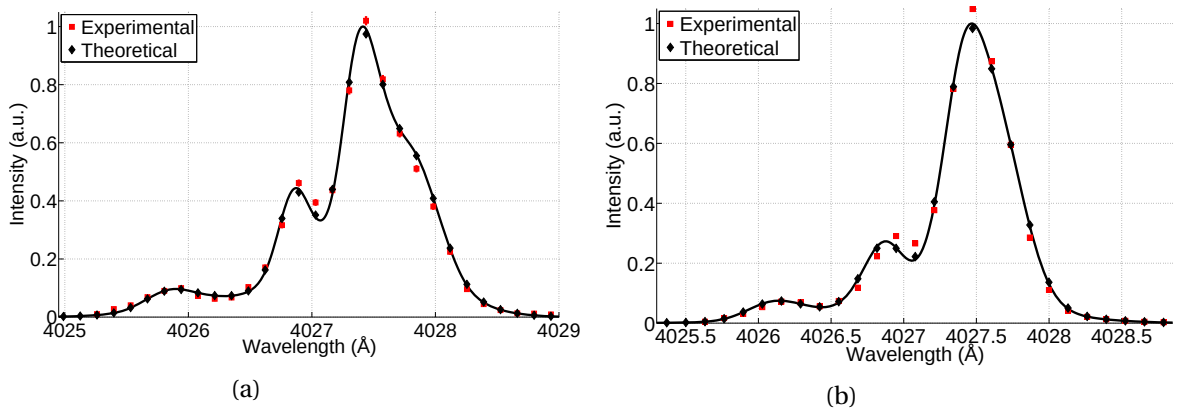

Figure 5.68: Fit to the $5^3D \rightarrow 2^3P$ He I σ profile at a position of $z = 0.8$ and 1.0 mm for (a) shot 11 and (b) 27 respectively.

As seen by Table 5.4 and Table 5.5 the ratio of the E_0 and E_1 electric field parameters is different, 1.2 and 1.4 for the parallel and perpendicular field configurations respectively. Thus the time dependence of the electric field waveform is driving the differences. As described above for the H_β spectral line profile the major source of non-qualitative error is associated with the approximation of the harmonic spectrum of the electric field waveform having only a single component. Indicated by the modeling presented in Section 2.3 near the RF biased electrode this approximation is fairly accurate. As the distance increases the electric field becomes highly non-sinusoidal and thus cannot be accurately represent as such, with a single component. In addition, due to the fact that the thermal group of the radiator distribution function is cold, that is $kT_{R1} = 0.0$ eV, and the superthermal group has a relatively weak intensity the error associated with this approximation will be more evident.

The $5^3D \rightarrow 2^3P$ He I π and σ profiles at a position of $z = 7.9$ mm is presented in Figure 5.69a and Figure 5.69b for shot 11 respectively. At the far end of the RF sheath the electric field is expected to be highly non-sinusoidal. The reduced χ associated with the fits presented in Figure 5.69 is approximately 2 indicating a high fit quality. For low electric field intensities the line profile is rather featureless therefore making unique solutions formidable. It is expected that many fits with equivalent fit qualities can be found all with varying time dependence of the electric field.

The reduced χ associated with the fits to the $5^3D \rightarrow 2^3P$ He I π and σ profiles is presented in Figure 5.70a for shot 11 and Figure 5.70b for shot 27. In the parallel field configuration the reduced χ typically has its minimum close to the RF biased electrode surface, where the electric field intensity is high. The reduced χ then increases on average as the electric field intensity decreases, although

this trend is rather weak. In the perpendicular field configuration the reduced χ is relatively constant except close to the RF biased electrode where a peak is observed.

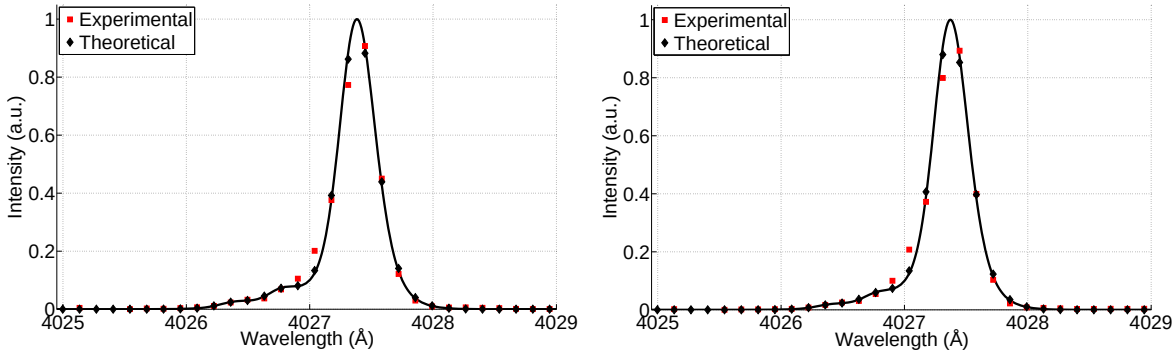

(a) (b)

Figure 5.69: Fit to the $5^3D \rightarrow 2^3P$ He I (a) π and (b) σ profiles for shot 11 at a position of $z = 7.9$ mm.

Beyond the error associated with the spectral noise other possible sources are the beam profile of the collection optics and the finite representation of the harmonic spectrum of the electric field waveform. To determine if the collection optics has a significant effect on the fit results the measured beam profile, presented in Figure 4.18a, was incorporated into the fitting routines. Due to the fact that the spatial profile of the fit variables was required, fitting the data became an iterative process. It was found that while the reduced χ was slightly decreased the fit results were not significantly altered. Thus the finite width of the beam profile is not expected to contribute significantly. Therefore the majority of the non-quantitative error is expected to be due to the approximative electric field waveform having only one component.

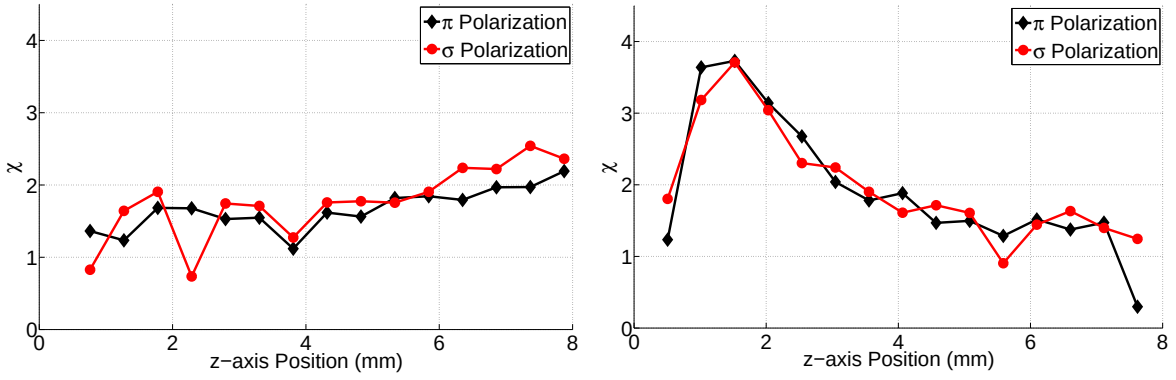

(a) (b)

Figure 5.70: Reduced χ fitting parameter associated with the H_β π and σ profiles as a function of position for (a) shot 3 and (b) shot 19.

Additionally, the trend in the reduced χ is similar to that associated with the intensity. It is believed that the trend is partially due to the fact that the signal to noise ratio has the same trend. In the perpendicular field configuration very intense emission occurs over a small distance in front of the electrode thus the signal to noise ratio is greatly increased.

CHAPTER

6

SPECTROSCOPIC RESULTS

In Chapter 5 the analysis and select results associated with the experiments conducted on DStarVE was presented. In this chapter the experimental scenario was discussed and results associated with the characterization of a typical DStarVE discharge utilizing the capacitive and RF compensated Langmuir probes was given. Select time averaged spectra obtained in the RF sheath were presented along with the methodology associated with the systematic analysis.

In this chapter the electric field and radiator distribution function parameters obtained from fitting the H_β and $5^3D \rightarrow 2^3P$ He I spectral line profiles will be presented as a function of position within the RF sheath. The chapter is structured as follows: Sections 6.1 and 6.2 present the results portraying the underlying trends in the parameters for discharges in the parallel and perpendicular field configurations respectively.

The electric field parameter E_1 represents the magnitude of the fundamental component of the waveform as shown by Eq. 3.5. Due to the fact the series is truncated after the fundamental its polarity is ambiguous. For the purposes of presentation and ease of interpretation E_1 is presented as a positive number for hydrogen and a negative number for helium. The electric field parameters E_0 and E_1 are be referred to as the DC and RF components, respectively. This is because E_0 is the magnitude of the static electric field component and E_1 is the magnitude of the time dependent electric field component at the fundamental frequency.

6.1 Parallel Field Configuration

To discuss the spatial trends associated with the electric field and radiator distribution function parameters shots 3 and 11 where selected for presentation. These shots correspond to hydrogen and helium discharges, respectively, in the parallel field configuration and were chosen because they were utilized in Section 5.4.2 to discuss the spectral line profile fitting. The discharge parameters of interest for shot 3 are $P = 200$ mTorr, $V_{DC} = -2.7$ kV, $|V_{RF}| = 2.6$ kV, and $n_e = 1.03 \cdot 10^{17}$ m^{-3}. The discharge parameters of interest for shot 11 are $P = 200$ mTorr, $V_{DC} = -2.7$ kV, $|V_{RF}| = 2.4$ kV, and $n_e = 1.49 \cdot 10^{17}$ m^{-3}. The remaining discharge parameters can be found in Appendix C.

6.1.1 Electric Field

$\mathbf{H}_\beta$

The electric field parameters E_0 and E_1 and the minimum electric field intensity associated with the waveform are given in Figure 6.1a and Figure 6.1b, respectively, for shot 3.

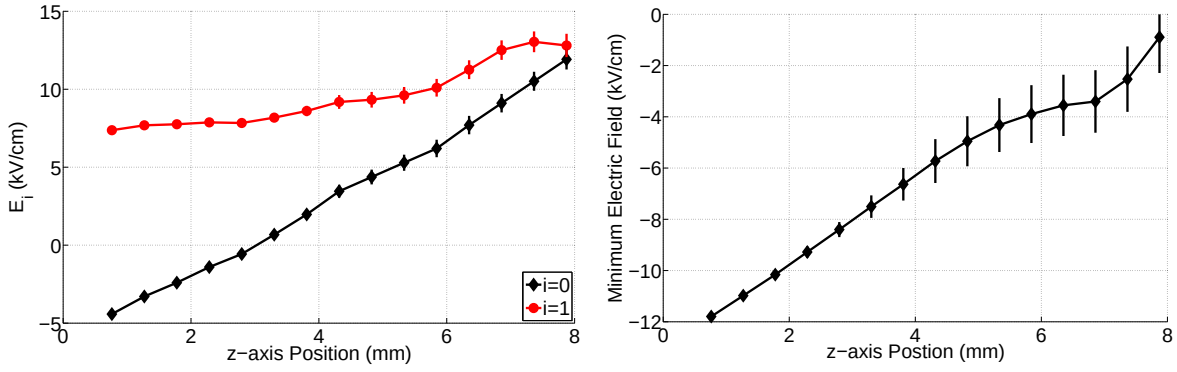

(a) (b)

Figure 6.1: (a) Electric field parameters E_0 and E_1 and (b) minimum electric field waveform intensity as a function of position for shot 3.

The DC electric field component E_0 was found to increase linearly with distance from the RF biased electrode for the hydrogen discharges in the parallel field configuration. Although E_0 continues to increase through zero the minimum intensity associated with the waveform approximately increases monotonically to zero as presented by Figure 6.1b. Note that the electric field is negative and clamped at zero, thus the minimum intensity associated with the waveform is the most extreme value. Due to this constraint E_1 implicitly must be greater then the E_0 for $E_0 > 0$.

While E_0 is negative it was found that E_1 was relatively constant, as indicated by Figure 6.1a for $z \leq 2.8$ mm. E_1 then increases linearly with z up to the far end of the RF sheath, occurring at $z = 6.0$ mm in Figure 6.1a, after which deviation form linearity occurs. This behavior is clearly observed in

the minimum intensity associated with the electric field waveform as presented in Figure 6.1b, here a linear trend is observed for $z \leq 6.0$ mm. As the far end of the RF sheath is approached both E_0 and E_1 increase. This is the response generated by approximating a pseudo-sinusoidal waveform having a narrow width.

As indicated by the modeling presented in Section 2.3 the RF sheath the electric field waveform is expected to have substantial harmonic spectrum at both boundaries of the RF sheath. Therefore it is assumed that for $z \geq 6.0$ mm E_0 and E_1 have a larger error then indicated by Figure 6.1. This error is made explicit in the phase angle θ_1. The phase angle θ_1 and the electric field waveform are given in Figure 6.2a and Figure 6.2b, respectively, for shot 3.

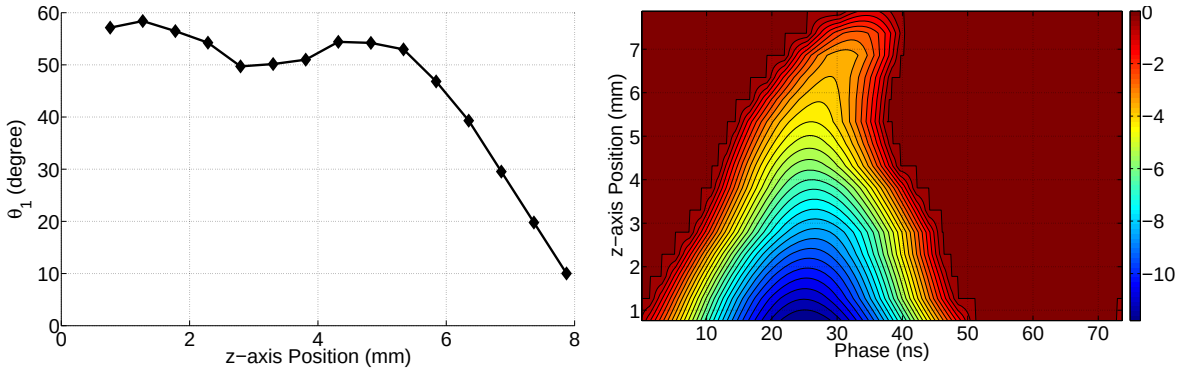

(a) (b)

Figure 6.2: (a) Electric field parameter θ_1 as a function of position and (b) contour plot of electric field as a function of phase and position for shot 3.

It was found that beyond $z = 6.0$ mm θ_1 diverged rapidly for shot 3 and was typically seen when E_1 deviated from its linear trend. This is expected to be due to the fact that representing the harmonic series with a single component is inaccurate. Because θ_1 is determined by correlating the electric field waveform with that of the emission intensity the deviation is equivalent to weighting low field intensities. As predicted by the modeling presented in Section 2.3 at the far end of the RF sheath the electric field waveform deviates from the sinusoidal representation through a decease in the width of the waveform. Therefore the divergence of the phase angle such that lower electric field intensities are weighted stronger correlates with the modeling. As seen by Figure 6.2b the electric field intensity decreases with z in addition the amount of time spent at non-zero field strength decreases with z. The later is caused by the fact that the DC component is allowed to take on positive values.

In order to provide validation the measured electric field described above is compared to the analytical model presented in Section 2.3. The boundary conditions and plasma parameters required for the modeling were taken from the experimentally determined values for shot 3 (Appendix C)

with the exception of the electron temperature. The RF sheath electric field was modeled having a bulk plasma electron temperature of $kT_e = 5$, 10, and 15 eV. To compare the experimental data to the model, the minimum electric field waveform intensity was selected and is plotted as a function of position in Figure 6.3.

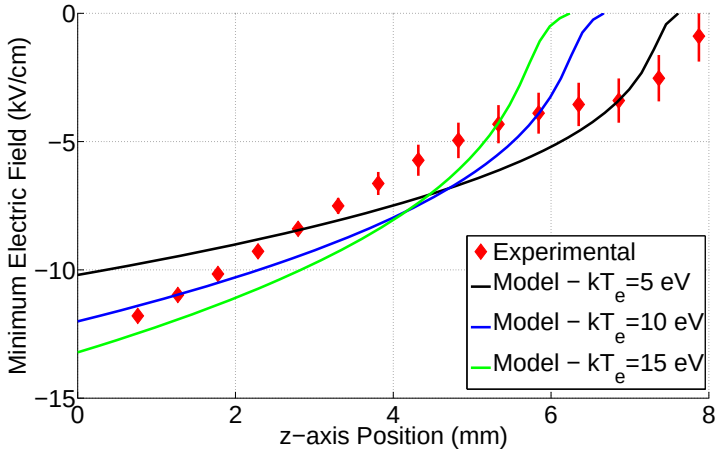

Figure 6.3: Experimental and modeled minimum electric field waveform intensity as a function of position for shot 3.

Considering the approximations, the overall trend in the experimental data was found to be well captured by the model. An electron temperature of 8 eV was found to be most representative, this is nearly a factor of two lower then the measured value of 16.7 eV. As discussed in 4.3.1 the electron temperature measured by the Langmuir probe is expected to be an overestimate and is thus consistent with the modeling results.

$5^3D \rightarrow 2^3P$ He I

The electric field parameters E_0 and E_1 and the minimum electric field intensity associated with the waveform are given in Figure 6.4a and Figure 6.4b respectively for shot 11. As was found for the hydrogen discharges E_0 was found to increase linearly with z for the helium discharges in the parallel field configuration. However E_0 always took on negative values and never crossed zero. Due to this fact E_1 is presented as a negative number for comparison purposes. The trend associated with E_1 was found to closely mimic that of E_0. Additionally, the magnitude of E_1 was found to be less then that of E_0 indicating that the width of the electric field waveform is very broad. For the hydrogen discharges the opposite case was found, representing an electric field waveform with a narrow width. This observation represents the major difference of the RF sheath electric field of the hydrogen and helium discharges. As was found by the modeling conducted in 2.3 this is attributed to helium having more inertial. The minimum electric field intensity as presented by Figure 6.4b is

seen to have the same behavior as E_0 and E_1, nearly linear over the investigated space.

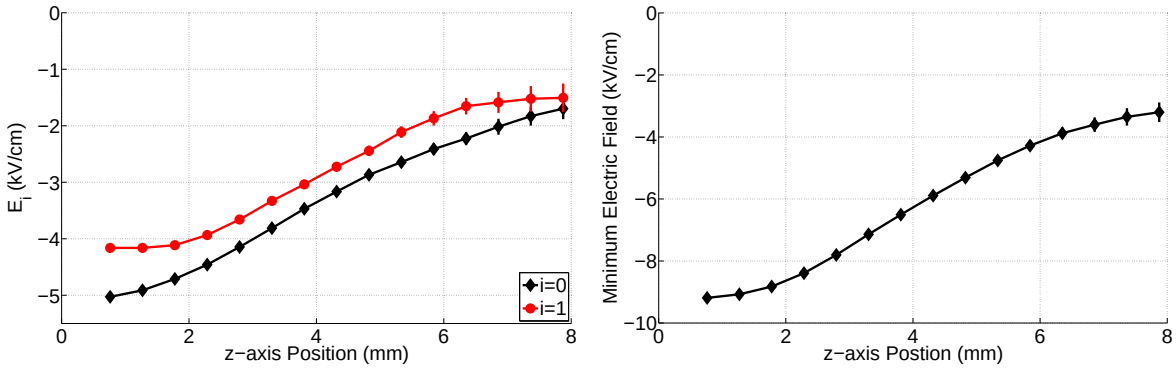

(a) (b)

Figure 6.4: (a) Electric field parameters E_0 and E_1 and (b) minimum electric field waveform intensity as a function of position for shot 11.

In order to provide validation the measured electric field described above is compared to the analytical model presented in Section 2.3. The boundary conditions and plasma parameters required for the modeling were taken from the experimentally determined values for shot 3 (Appendix C) with the exception of the electron temperature. The RF sheath electric field was modeled having a bulk plasma electron temperature of $kT_e = 1$, 2.5, and 5 eV. To compare the experimental data to the model, the minimum electric field waveform intensity was selected and is plotted as a function of position in Figure 6.5.

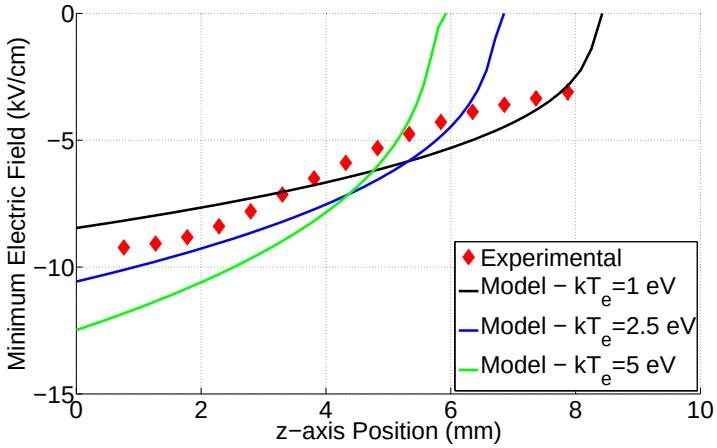

Figure 6.5: Experimental and modeled minimum electric field waveform intensity as a function of position for shot 11.

Considering the approximations, the overall trend in the experimental data was found to be well

captured by the model. An electron temperature of 2 eV was found to be most representative, this is over a factor of four lower then the measured value of 8.7 eV. As discussed in 4.3.1 the electron temperature measured by the Langmuir probe is expected to be an overestimate and is thus consistent with the modeling results.

6.1.2 Radiator Distribution Function

H$_\beta$

The temperature kT_{R2} and intensity I_{R2} associated with the second thermal group of radiators is presented in Figure 6.6a and Figure 6.6b respectively for shot 3.

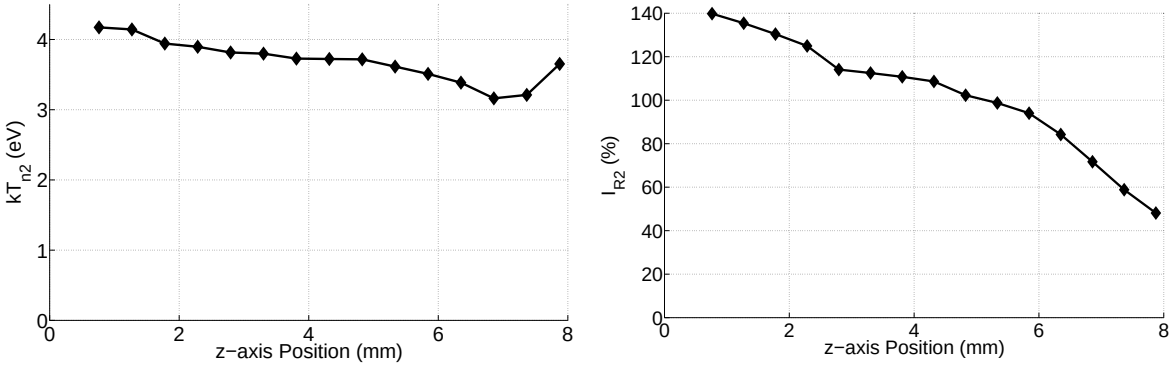

(a) (b)

Figure 6.6: Second thermal group (a) temperature kT_{R2} and (b) intensity I_{R2} as a function position for shot 3.

The temperature kT_{R2} was found to have values between 2.5 and 4.5 eV for all hydrogen discharges in the parallel field configuration. The associated trend was found to decrease slightly with z until the far end of the sheath where an increase is observed. As indicated by Figure 6.6b this trend was found to be weak. It is expected that within the error associated with this measurement kT_{R2} can be considered constant. The intensity I_{R2} however was found to be a strong function of z, specifically for shot 3 I_{R2} decreased monotonically with z. The trend associated with I_{R2} was found to be dependent on the experimental parameters. In general a decreasing trend was observed. The most notable experimental parameter having an influence on I_{R2} was the addition of the ECW source. It was found that I_{R2} decreased with the absorption of microwave power. This reduction had a noticeable effect of both the DC and RF components of the electric field.

$5^3D \rightarrow 2^3P$ He I

The temperature kT_{R2} and intensity I_{R2} associated with the superthermal group of radiators is presented in Figure 6.7a and Figure 6.7b respectively for shot 11.

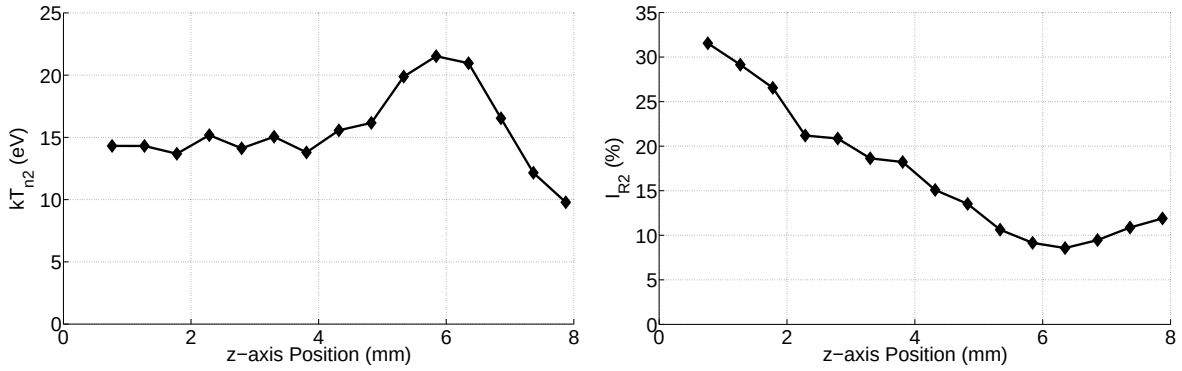

(a) (b)

Figure 6.7: Second thermal group (a) temperature kT_{R2} and (b) intensity I_{R2} as a function position for shot 11.

The temperature kT_{R2} was found to have values ≤ 30 eV for all helium discharges in the parallel field configuration. These values are nearly a factor of three less then those associated with the H_β profile. The associated trend was found to be nearly constant until the far end of the sheath where a slight peak was observed. It is expected that within the error associated with this measurement kT_{R2} can be considered constant. The intensity I_{R2} however was found to be a strong function of z, specifically for shot 11 I_{R2} decreased with z until the far end of the sheath. The trend associated with I_{R2} was found to be consistent over all of the experimental parameters.

6.2 Perpendicular Field Configuration

To discuss the spatial trends associated with the electric field and radiator distribution function parameters shots 19 and 27 where selected for presentation. These shots correspond to hydrogen and helium discharges, respectively, in the perpendicular field configuration and were chosen because they were utilized in Section 5.4.2 to discuss the spectral line profile fitting. The discharge parameters of interest for shot 19 are $P = 100$ mTorr, $V_{DC} = -1.9$ kV, $|V_{RF}| = 2.2$ kV, and $n_e = 3.49 \cdot 10^{15}$ m^{-3}. The discharge parameters of interest for shot 27 are $P = 200$ mTorr, $V_{DC} = -1.9$ kV, $|V_{RF}| = 2.0$ kV, and $n_e = 1.01 \cdot 10^{16}$ m^{-3}. The remaining discharge parameters can be found in Appendix C.

6.2.1 Electric Field

H_β

The electric field parameters E_0 and E_1 and the minimum electric field intensity are given in Figure 6.8a and Figure 6.8b respectively. Although a direct comparison to shot 3, representing the parallel field configuration, cannot be made because the electron density is different by over an order of magnitude the trends in the electric field parameters can be compared. In the perpendicular field configuration it was found that both the DC and RF electric field components behave differently when compared to those obtained in the parallel field configuration. It was found that both E_0 and E_1 are nonlinear functions of z. E_0 increases monotonically with z while E_1 was found to have a minimum approximately when E_0 crosses zero. These trends are representative of all investigated hydrogen discharges in the perpendicular field configuration.

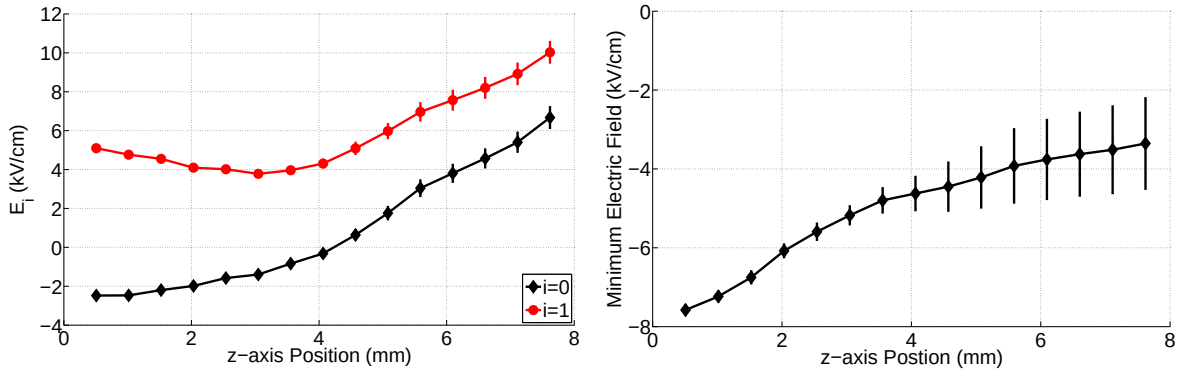

(a) (b)

Figure 6.8: (a) Electric field parameters E_0 and E_1 and (b) minimum electric field waveform intensity as a function of position for shot 19.

The behavior of E_0 can be classified by two regions: before and after the zero crossing occurring at $z = 4.0$ mm. In both regions the functionality with respect to z is approximately linear, the first region is characterized by a slope with a smaller magnitude. At the zero crossing the slope increases and begins to approach that associated with E_0 obtained in the parallel field configuration. In the first region E_1 has a negative slope, at the zero crossing the slope changes signs and approaches a magnitude approximately equal to that of E_0. Comparing this behavior with that associated with the parallel field configuration it is found that the electric field waveform is less peaked with a broader width, more representative of a sinusoidal waveform. The minimum of the electric field waveform is also nonlinear but can be approximated as a linear function within the error bars as seen by Figure 6.8b. Additionally, it is seen that the electric field is still prominent at the maximum measurement position indicating the large width of the RF sheath. This is due to the fact that the

density is very low.

Unlike the parallel field configuration the harmonic spectrum is expected to be dampened in the perpendicular field configuration. This is because of the retarding effect both experienced by the ions and electrons, although the electrons experience this to a much larger extent. In addition this is what is predicted by the modeling for particles having a larger inertia. This is first observed in the fact that the E_1 is substantially larger then E_0 at all locations. In addition this is made more explicit in the phase angle θ_1. The phase angle θ_1 and the electric field waveform are given in Figure 6.9a and Figure 6.9b respectively for shot 19.

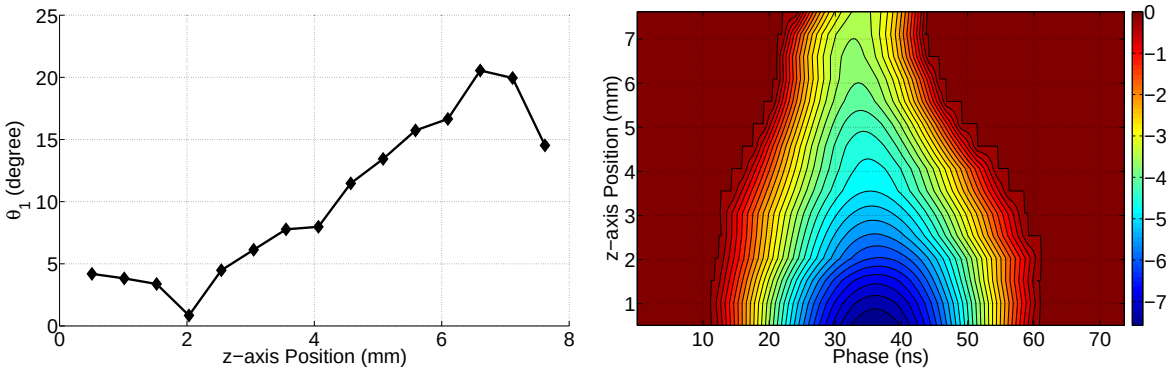

(a) (b)

Figure 6.9: (a) Electric field parameter θ_1 as a function of position and (b) contour plot of electric field as a function of phase and position for shot 19.

It was found that no divergence occurred in θ_1. This is a clear indication that the harmonic spectrum of the electric field waveform can be adequately represented by only a single component. As predicted by the modeling presented in Section 2.3 inhibiting the movement of the ions decreases the harmonic content. As seen by Figure 6.9b the electric field intensity decreases with z in addition the amount of time spent at non-zero field strength decreases with z. The later is caused by the fact that the E_0 is allowed to take on positive values.

$5^3D \rightarrow 2^3P$ He I

The electric field parameters E_0 and E_1 and the minimum electric field intensity associated with the waveform are given in Figure 6.10a and Figure 6.10b respectively for shot 27. Although a direct comparison to shot 11, representing the parallel field configuration, cannot be made because the electron density is different by over an order of magnitude the trends in the electric field parameters can be compared. It was found that both E_0 and E_1 have very similar trends to those associated with the parallel field configuration. The only deviation observed was at the far end of the RF sheath for $z \geq 4.0$ mm, at this point E_1 remained approximately constant. The minimum electric field intensity

as presented by Figure 6.4b is seen to have the same behavior as that obtained in the parallel field configuration.

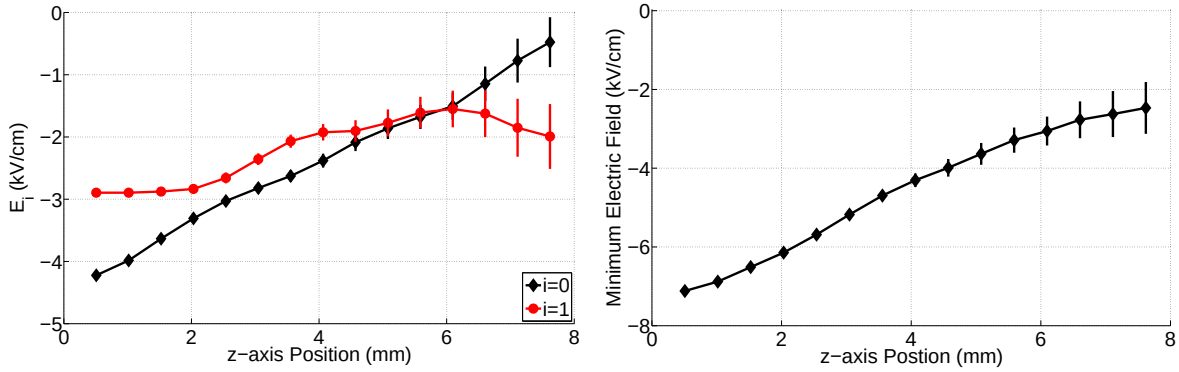

(a) (b)

Figure 6.10: (a) Electric field parameters E_0 and E_1 and (b) minimum electric field waveform intensity as a function of position for shot 27.

6.2.2 Radiator Distribution Function

$\mathbf{H}_\beta$

The temperature kT_{R2} and intensity I_{R2} associated with the second thermal group of radiators is presented in Figure 6.11a and Figure 6.11b respectively for shot 19.

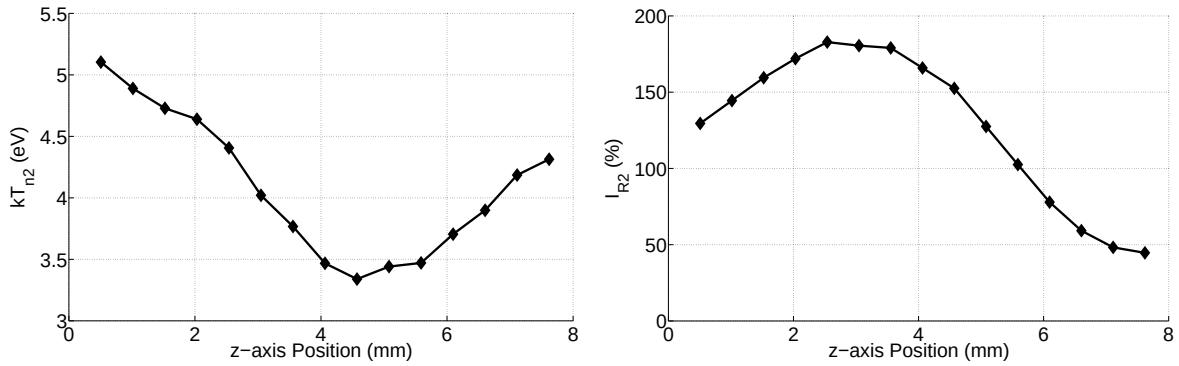

(a) (b)

Figure 6.11: Second thermal group (a) temperature kT_{R2} and (b) intensity I_{R2} as a function position for shot 19.

The temperature kT_{R2} was found to have values between 3 and 6 eV for all hydrogen discharges in the perpendicular field configuration. The associated trend was found to be similar to that obtained in the parallel field configuration. However, in the perpendicular field configuration the trend is

much more pronounced and the minimum occurs at a smaller value of z. As was the case for the parallel field configuration the intensity I_{R2} was found to be a strong function of z. For all hydrogen discharges in the perpendicular field configuration a maximum in the curve occurred close to the RF biased electrode followed by a shape decay. The trend associated with I_{R2} was also found to be dependent on the experimental parameters, although a peaked profile was always observed. The most notable experimental parameter having an influence on I_{R2} was the addition of the ECW source. It was found that the peak associated with the I_{R2} profile was moved closer to the RF biased electrode surface with the absorption of microwave power.

$5^3D \rightarrow 2^3P$ He I

The temperature kT_{R2} and intensity I_{R2} associated with the superthermal group of radiators is presented in Figure 6.12a and Figure 6.12b respectively for shot 27.

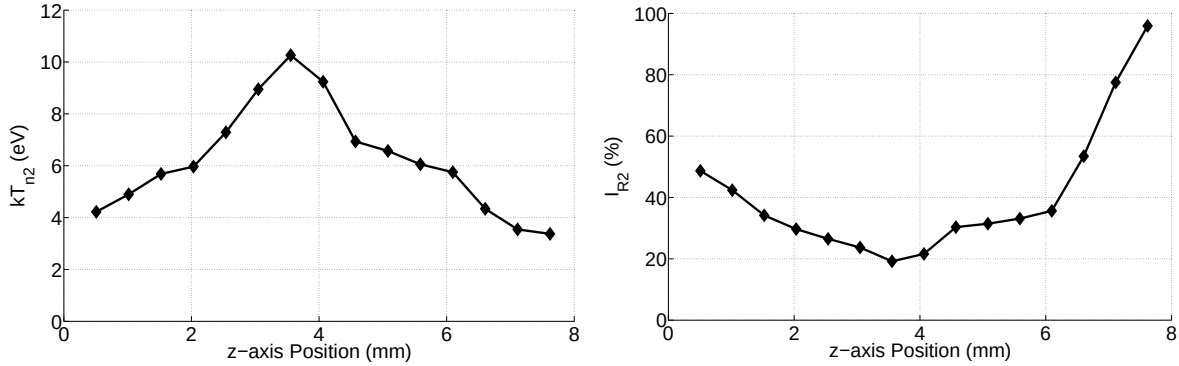

(a) (b)

Figure 6.12: Second thermal group (a) temperature kT_{R2} and (b) intensity I_{R2} as a function position for shot 27.

The temperature kT_{R2} was found to have values ≤ 20 eV for all helium discharges in the perpendicular field configuration. The trend was found to be peaked about the center of the RF sheath. Although, it is expected that within the error associated with this measurement kT_{R2} can be considered constant. The intensity I_{R2} however was found to be a strong function of z, specifically for shot 27 I_{R2} had a minimum about the RF sheath center. The trend associated with I_{R2} was found to be consistent over all of the experimental parameters.

CHAPTER

7

CONCLUSIONS AND FUTURE WORK

Reliable operation of ICRF antennas at reactor-like powers can only be realized and advanced through predictive modeling. Current models do not completely capture the physics associated with the near-field, resulting in a distinct gap between theoretical and actual performance [39, 37]. In order to bridge this gap experimental measurements of the near-field are highly desired. However, due to the large energy flux launched by ICRF antenna only non-local measurements have thus far been obtained [90, 109, 27] resulting in an incomplete understanding of the physics. The main objective of the research presented in this dissertation was to develop and validate a non-perturbative spectroscopic diagnostic capable of measuring time periodic electric fields. As will be described below the successful completion of this objective has been realized, allowing for the first time experimental measurements of the near-field to be made.

The development phase of the diagnostic was carried out in two steps and consisted of atomic physics formulation. The first step involved the calculation of the electronic structure of the one and two-electron atom utilizing the hydrogenic wave function approximation. The second step involved the calculation of the spectral line profile based on the electric dipole connection operator. Chapter 3 presents the systematic mathematical derivation of the formulae required for these calculations.

The validation phase of the diagnostic consisted of applying the atomic physics to measure the electric field topology associated with the capacitively coupled magnetized RF sheath. Passive OES was implemented and the π and σ polarized components were measured independently. The theory associated with this phase is presented in Chapters 2 and 4, while the results are presented

in Chapters 5 and 6.

The capacitively coupled magnetized RF sheath was selected to validate the spectroscopic diagnostic due to its relevance to the near-field of ICRF antenna. In Chapter 2 a simple analytical model of the capacitively coupled magnetized RF sheath in the parallel field configuration was presented and used to provide the validation. In this model the effect of the ion inertia could be simulated by allowing the ions to respond to a dampened sheath potential governed by a variable time constant. It was found that an increase in inertia led to a larger sheath width and a decrease in the harmonic content associated with the electric field waveform.

In Chapter 3 the atomic physics associated with this diagnostic was developed. Additionally, the experimental technique and spectral fitting software used for validation was presented and discussed. The capstone of Chapter 3 is a complete mathematical description of the spectra associated with one and two-electron atoms under the influence of arbitrary static magnetic and time periodic electric field vectors utilizing a generalized observation geometry. It was found that using the Floquet method the spectral line profile calculation was extremely computationally intensive when considering electric field waveforms in the RF range of frequency. In order to speed up the computation the quasi-static approximation was investigated and found to be accurate if either of two limits is satisfied. The first states that the lifetime of the exited state must be much less then the period of the electric field waveform: $\tau^* \ll \tau$. The second states that the broadening parameters must be much greater then the satellite spacing.

Utilizing passive OES techniques to measure spectra under the influence of electric field waveforms in the RF range of frequencies the quasi-static approximation is found to be always valid. This is due to the fact the broadening mechanics dominate the satellite structure. Therefore the quasi-static approximation is used throughout this research. It was found that the H_β and $5^3D \rightarrow 2^3P$ He I transitions were ideal for the validation phase due to there sensitivity to the electric field and the magnitude of the emission intensity.

In Chapter 4 DStarVE was presented, a small scale laboratory experiment designed to serve as a test stand in which the edge environment of the tokamak could be simulated. Two experimental configurations were investigated: electric and magnetic field vectors parallel and perpendicular. The study of these two field configurations is of particular importance. The parallel field configuration has been well studied both experimentally [17] and theoretically [95, 125, 103, 146] and thus was the focus for diagnostic validation. The perpendicular field configuration has received significantly less attention and was studied because it is representative of the ICRF antenna near-field. The basis of the DStarVE experiment consists of an electrode biased at 13.56 MHz immersed in a magnetized plasma generated by excitation of electron cyclotron waves. The RF biased electrode was designed to capacitively couple to the magnetized plasma thus forming the focus of the experimental research efforts, the capacitively coupled magnetized RF sheath. The experiment was designed to generate relatively strong electric fields, ≤ 15 kV/cm in magnitude, extending approximately 1 cm from the

RF biased electrode surface.

In order to validate the atomic physics using passive OES direct access to optical emission originating in the RF sheath region was necessary to eliminate unperturbed emission. This was successfully achieved through the use of a limiter assembly. Utilizing DStarVE the π and σ spectral line profiles where measured in the capacitively coupled magnetized RF sheath as a function of position from the RF biased electrode with a spatial resolution of approximately 300 μm. In order to aid the interpretation of the electric field results obtained from these spectroscopic measurements additional diagnostics were developed in Chapter 4 to characterized the DStarVE discharges in terms of operating, electrical, and plasma parameters.

In Chapter 5 the analysis and select results associated with the experiments conducted on DStarVE was presented. The primary purpose of these experiments was to measure the time dependent electric field topology of the capacitively coupled magnetized RF sheath utilizing the time averaged spectral line profile. In order to supplement these spectroscopic based measurements and to provide the boundary conditions for the analytical model presented in Chapter 2 the electrical and plasma parameters were measured. A total of 28 discharges, with varying experimental conditions, were investigate and characterized. A summary of the electrical and plasma parameters is provided in Appendix C.

The model used to fit the spectral line profiles is as follows. The electric field waveform used for both the H_β and $5^3D \rightarrow 2^3P$ He I spectra consisted of a static and fundamental component, that is the harmonic spectrum had only a single component N_H=1. It was found that higher harmonics could not be accurately obtained due to the spectral resolution associated with passive OES. The H_β transition intensity was found to be strongly time dependent while that of the $5^3D \rightarrow 2^3P$ He I transition was not. Due to this fact only the phase angle associated with the fundamental, θ_1, for H_β was set to a fit variable.

The radiator distribution function associated with the H_β transition was found to consist of both thermal and superthermal emitters. Due to the large temperature difference it was found that the superthermal group emission could be accurately removed form the spectra prior to the fit. Through fitting the H_β spectra obtained in a region of negligible electric field it was found that a one-group distribution function was incapable of representing the thermal group. Utilizing the results of Baravian *et al.* [14] that of a two-group was implemented and found to be accurate. The radiator distribution function associated with the $5^3D \rightarrow 2^3P$ He I transition was also found to consist of both thermal and superthermal emitters. However it was found that the superthermal group was unable to be removed prior to the fit due to a rather low temperature when compared to that of H_β. The thermal group associated with the $5^3D \rightarrow 2^3P$ He I transition was found to be well represented by a one-group distribution function. A summary of select results associated with the spectral fitting is presented in Appendix D.

In Chapter 6 the modeling results presented in Chapter 2 were confirmed experimentally by

comparing the RF sheath electric field associated with the hydrogen and helium discharges. Additionally, it was found that the analytical model represented the experimental data associated with the parallel field configuration well. Thus the validation of the diagnostic was considered successful.

The future work consists of implementation of an active OES technique to locally measure the near-field with high spatial and temporal resolution. It was found that an active technique was required over a passive technique due to the limited spectral and spatial resolution of the later. The suggested active OES technique is based on Doppler-free saturation spectroscopy and yields a measurement having superior spectral resolution. For hydrogen transitions this results in an electric field measurement with an accuracy of 10 to 50 V/cm [7, 43]. Details of the underlying physics and experimental setup can be found in the literature [151, 116], however a brief description is given below. The technique is based on using a tunable wavelength laser beam to excite atoms from the lower to upper levels associated with the transition of interest. In order for the measurement to be Doppler-free the laser beam must differentially excite atoms having a velocity vector in a plane perpendicular to the beam. This is achieved by splitting the original beam into so-called pump and probe beams. These beams are then sent counter-propagating towards each other at a slight angle such that they overlap at a single point in space. The overlap point is the location at which the measurement is obtained, yielding a spatial resolution dictated by the beam width of the laser. The spectrum is measured by recording the intensity of the probe beam while sweeping the wavelength of the laser. The difference in the spectra obtained with the pump beam on and off yields the Doppler-free spectra.

In conclusion a spectroscopic diagnostic capable of measuring time periodic electric fields was successfully developed and validated. The development was carried out by deriving a mathematical description of the spectra associated with one and two-electron atoms under the influence of arbitrary static magnetic and time periodic electric field vectors utilizing a generalized observation geometry. The validation was carried out by implementing passive OES to measure the electric field topology associated with the capacitively coupled magnetized RF sheath. It was found that the analytical model represented the experimental results well. The successful implementation of this diagnostic using active OES can have a rather large significance for magnetic confinement fusion through advancement of ICRF antenna predictive modeling.

REFERENCES

[1] ITER EDA Documentation Series No. 24. Technical report, International Thermonuclear Experimental Reactor, 2002.

[2] Alcator C-MOD homepage. `http://www.psfc.mit.edu/research/alcator`, 2014.

[3] EFDA homepage. `http://www.efda.org`, 2014.

[4] ITER homepage. `http://www.iter.org`, 2014.

[5] National Institute of Standards and Technology. Atomic Spectra Database. `http://www.physics.nist.gov/PhysRefData/ASD`, 2014.

[6] U. Litzen A. Thorne and S. Johansson. *Spectrophysics*. Springer-Verlag Berlin Heidelberg, 1999.

[7] M. Adamov et al. Doppler-free Stark spectroscopy of the second excited level of atomic hydrogen for measurements of electric fields. *Phys. Rev. A*, 75:013409, 2007.

[8] U.S. Energy Information Administration. International energy outlook 2011.

[9] E. Ahedo. Plasma-wall interaction in an oblique magnetic field: Model of the space-charge sheath for large potentials and small Debye lengths. *Phys. Plasmas*, 6:4200, 1999.

[10] R. Akhmedzhanov et al. Observation of the fine structure of hydrogen plasma in a microwave field by intracavity laser spectroscopy. *Sov. Phys. JETP*, 63(1):30, 1986.

[11] S. Autler and C. Townes. Stark effect in rapidly varying fields. *Phys. Rev.*, 100:703, 1955.

[12] S. Baalrud and C. Hegna. Kinetic theory of the presheath and the Bohm criterion. *Plasma Sources Sci. Technol.*, 20:025013, 2011.

[13] M. Baranger and B. Mozer. Light as a plasma probe. *Phys. Rev.*, 123(1):25, 1961.

[14] G. Baravian et al. Doppler broadened Halpha line shapes in RF low pressure H2 discharge. *J. Appl. Phys.*, 61:5249, 1987.

[15] E. Barnat et al. RF discharge under the influence of a transverse magnetic field. *Plasma Sources Sci. Technol.*, 17:045005, 2008.

[16] E. Barnat and G. Hebner. Radiofrequency sheath fields above a metal-dielectric interface. *J. Appl. Phys.*, 96(9):4762, 2004.

[17] E. Barnat and G. Hebner. Radio frequency sheath formation and excitation around a stepped electrode. *J. Appl. Phys.*, 97:063301, 2005.

[18] C. Bender and S. Orszag. *Advanced Mathematical Methods for Scientists and Engineers: Asymptotic Methods and Perturbation Theory*. Springer, 1991.

[19] H. Bethe and E. Salpeter. *Quantum Mechanics of One- and Two-Electron Atoms*. Dover Publications, 2008.

[20] D. Blackwell and F. Chen. Time-resolved measurements of the electron energy distribution function in a helicon plasma. *Plasma Sources Sci. Technol.*, 10:226, 2001.

[21] D. Blochinzew. *Phys. Z. Sov. Union*, 4:501, 1933.

[22] G. Bohm and G. Himmel. Measurement of electric field strengths in a waveguide by means of the dynamic Stark effect in hydrogen and neutral helium spectral lines. *Appl. Phys.*, 21:313, 1980.

[23] J. Booske et al. Experiments on whistler mode electron cyclotron resonance plasma startup and heating in an axisymmetric magnetic mirror. *Phys. Fluids*, 28:3116, 1985.

[24] J. Booth et al. Time-resolved electric field measurements in 30 kHz hydrogen discharges by optical emission Stark spectroscopy. *J. Applied Phys.*, 74:862, 1993.

[25] M. Brambilla. *Kinetic Theory of Plasma Waves: Homogeneous Plasma*. Oxford University Press, 1998.

[26] A. Cappelli et al. Doppler-broadened line shapes of atomic hydrogen in a parallel-plate ratio frequency discharge. *Plasma Chem. Plasma Processs*, 5:317, 1985.

[27] J. Caughman. *The distribution of ion energies incident on an ICRH antenna faraday shield*. PhD thesis, University of Illinois, 1989.

[28] P. Chatterton et al. A self-compensating Langmuir probe for use in RF plasma systems. *Vacuum*, 42:489, 1991.

[29] F. Chen. *Plasma Diagnostic Techniques*. Academic Press, 1965.

[30] F. Chen et al. Measurement of low plasma densities in a magnetic field. *Phys. Fluids*, 11:811, 1968.

[31] R. Chodura. Plasma-wall transition in an oblique magnetic field. *Phys. Fluids*, 25:1628, 1982.

[32] R. Chodura. *Physics of Plasma-Wall Interactions in Controlled Fusion*, chapter Plasma Flow in the Sheath and the Presheath of a Scrape-Off Layer. Springer, 1986.

[33] R. Chodura. Modelling of the plasma at the Faraday screen of an ICRH antenna. *Fusion Eng. Des.*, 12:111, 1990.

[34] P. Chung, L Talbot, and J. Touryan. *Electric Probes in Stationary and Flowing Plasmas: Theory and Application*. Springer-Verlag Inc., 1975.

[35] L. Colas et al. Hot spot phenomena on Tore Supra ICRF antennas investigated by optical diagnostics. *Nucl. Fusion*, 43:1, 2003.

[36] L. Colas et al. RF current distribution and topology of RF sheath potentials in front of ICRF antennae. *Nucl. Fusion*, 45:767, 2005.

[37] L. Colas et al. Key results of long pulse ICRH operation in Tore Supra. *Nucl. Fusion*, 46:S500, 2006.

[38] L. Colas et al. Understanding the spatial structure of RF-induced SOL modifications. *Plasma Phys. Control. Fusion*, 49:B35, 2007.

[39] L. Colas et al. Estimated RF sheath power fluxes on ITER plasma facing components. *J. Nucl. Mater.*, 390:959, 2009.

[40] L. Colas et al. Ion cyclotron resonant heating in Tore Supra. *Fusion Sci. Technol.*, 56:1173, 2009.

[41] H. Crosswhite. *The Hydrogen Molecule Wavelength Tables of Gerhard Heinrich Dieke*. John Wiley and Sons, Inc., 1972.

[42] N. Cvetanovic et al. Influence of cathode material on generation of energetic hydrogen atoms in a glow discharge. *J. Applied Phys.*, 109:013311, 2011.

[43] U. Czarnetzki et al. Space and time resolved electric field measurements in helium and hydrogen RF-discharges. *Plasma Sources Sci. Technol.*, 8:230, 1999.

[44] U. Czarnetzki et al. Investigations on ionic processes and dynamics in the sheath region of the helium and hydrogen discharges by laser spectroscopic electric field measurements. *Appl. Phys. A*, 72:509, 2001.

[45] E. Delabie. *Neutral beam driven hydrogen spectroscopy in fusion plasmas*. PhD thesis, Eindhoven University of Technology, 2011.

[46] C. Deutsch et al. Stark and Zeeman effects on neutral-helium lines. *Phys. Rev. A*, 3:1879, 1971.

[47] D. D'Ippolito et al. Far-field sheaths due to fast waves incident on material boundaries. *Phys. Plasmas*, 15:102501, 2008.

[48] D. D'Ippolito et al. Modeling far-field radio-frequency sheaths in Alcator C-Mod. *Plasma Phys. Control. Fusion*, 55:085001, 2013.

[49] D. D'Ippolito and J. Myra. A radio frequency sheath boundary condition and its effect on slow wave propagation. *Phys. Plasmas*, 13:102508, 2006.

[50] D. D'Ippolito and J. Myra. Analytic model of near-field radio-frequency sheaths. I. Tenuous plasma limit. *Phys. Plasmas*, 16:022506, 2009.

[51] D. D'Ippolito and J. Myra. Analytic model of near-field radio-frequency sheaths. II. Full plasma dielectric. *Phys. Plasmas*, 17:072508, 2010.

[52] A. Edmonds. *Angular Momentum in Quantum Mechanics*. Princeton University Press, 1960.

[53] A. Ekedahl et al. Operational limits during high power long pulses with radiofrequency heating in Tore Supra. *Nucl. Fusion*, 49:095010, 2009.

[54] P. Epstein. On the theory of the Stark effect. *Ann. Phys.*, 50:489, 1916.

[55] P. Epstein. The Stark effect from the point of view of Schrodinger's quantum theory. *Phys. Rev.*, 28:695, 1926.

[56] E. Faudot et al. Parametric study of two-dimensional potential structures induced by radio-frequency sheaths coupled with transverse currents in front of the ion cyclotron resonance heating antenna. *Phys. Plasmas*, 13:0042512, 2006.

[57] U. Flender and K. Wiesemann. Ion distribution functions behind an RF sheath. *J. Phys. D: Appl. Phys.*, 27:509, 1994.

[58] J. Freidberg. *Plasma Physics and Fusion Energy.* Cambridge University Press, 2008.

[59] T. Fujimoto. *Plasma Spectroscopy.* Clarendon Press, 2004.

[60] B. Ganguly and A. Garscadden. Electric field and Doppler emission profile measurements in an obstructed hydrogen discharge. *J. Appl. Phys.*, 70:621, 1991.

[61] T. Gans et al. Time dependence of rotational state populations of excited hydrogen molecules in an RF excited plasma reactor. *Plasma Sources Sci. Technol.*, 10:17, 2001.

[62] T. Gans et al. Observation of fast hydrogen atoms formed by ion bombarding of surfaces. *Contrib. Plasma Phys.*, 42:596, 2002.

[63] T. Gans et al. Prospects of phase resolved optical emission spectroscopy as a powerful diagnostic tool for RF-discharges. *Contrib. Plasma Phys.*, 44:523, 2004.

[64] British Petroleum Global. Statistical review of world energy 2012.

[65] V. Godyak et al. A comparison of RF electrode sheath models. *Tans. Plasma Sci.*, 21:378, 1993.

[66] H. Griem. *Spectral Line Broadening by Plasma.* Academic Press, 1974.

[67] H. Griem. *Principles of Plasma Spectroscopy.* Cambridge University Press, 1997.

[68] G. Guest et al. Whistler wave electron cyclotron heating in uniform and nonuniform magnetic fields. *Phys. Fluids B*, 2:1210, 1990.

[69] N. Hershkowtiz et al. Langmuir probe characteristics in RF glow discharges. *Plasma Chem. Plasma Proc.*, 8(1).

[70] W. Hicks et al. Combined Zeeman and high-frequency Stark effects, with applications to neutral-helium lines useful in plasma diagnostics. *Phys. Rev. A*, 5(2):490, 1971.

[71] J. Hildebrandt. Temporally and spatially resolved plasma satellites in a hollow-cathode source. *J. Phys. B: At. Mol. Phys.*, 16:149, 1983.

[72] J. Hildebrandt. Evanescent wave fields at the plasma frequency in a microwave-generated hollow-cathode plasma. *J. Phys. D: Appl. Phys.*, 39:3625, 2006.

[73] J. Hildebrandt and H. J. Kunze. Measurement of the spectrum of electric-field fluctuations in a plasma by laser-fluorescence spectroscopy. *Phys. Rev. Lett.*, 45(3):183, 1990.

[74] G. Himmel and A. Kamp. Determination of RF electric field strengths in deuterium from satellite structure of Balmer lines. *Appl. Phys. B*, 47:177, 1988.

[75] S. Hirsch and G. Himmel. The high-frequency Stark effect in the Balmer line D-alpha. *Z. Phys. D*, 16:35, 1990.

[76] J. Hollas. *Modern Spectroscopy.* John Wiley and Sons Inc., 2004.

[77] A. Hoskinson and N. Hershkowitz. Effect of finite length on the current-voltage characteristic of a cylindrical Langmuir probe in a multidiople plasma chamber. *Plasma Sources Sci. Technol.*, 15:85, 2006.

[78] L. Hou et al. Two-dimensional radio-frequency sheath dynamics over a nonflat electrode with perpendicular magnetic field. *Phys. Plasmas*, 11(9).

[79] J. Jacquinot. Heating, current drive and confinement regimes with the JET ICRH and LHCD systems. *Plasma Phys. Control. Fusion*, 33:1657, 1991.

[80] E. Jaeger et al. All-orders spectral calculation of radio-frequency heating in two-dimensional toroidal plasmas. *Phys. Plasmas*, 8:1573, 2001.

[81] E. Jaeger et al. Self-consistent full-wave and Fokker-Planck calculations for ion cyclotron heating in non-Maxwellian plasmas. *Phys. Plasmas*, 13:056101, 2006.

[82] E. Jaeger et al. Simulation of high-power electromagnetic wave heating in the ITER burning plasma. *Phys. Plasmas*, 15:072513, 2008.

[83] A. James et al. Imaging of molybdenum erosion and thermography at visible wavelengths in Alcator C-Mod ICRH and LHCD discharges. *Plasma Phys. Control. Fusion*, 55:125010, 2013.

[84] R. Janev et al. *Elementary Processes in Hydrogen-Helium Plasmas.* Springer-Verlag Berlin Heidelberg, 1987.

[85] G. Janssen et al. The influence of static fields on the dynamic Stark spectra of hydrogen Balmer lines. *J. Phys. B: At. Mol. Phys.*, 14:L51, 1981.

[86] R. Kiel. Electrostatic probe theory for free molecular cylinders. *AIAA J.*, 6:708, 1968.

[87] K. Kirov et al. Effects of ICRF induced density modifications on LH wave coupling at JET. *Plasma Phys. Control. Fusion*, 51:044003, 2009.

[88] G. Knoll. *Radiation Detection and Measurement.* John Wiley and Sons, 2000.

[89] H. Kohno. *Numerical Analysis of Radio-Frequency Sheath-Plasma Interactions in the Ion Cyclotron Range of Frequencies.* PhD thesis, Massachusetts Institute of Technology, 2011.

[90] M. Kubic. Measurement of sheath potential in the RF-biased flux tubes using a retarding field analyzer in Tore Supra tokamak. *J. Nucl. Fusion Mater.*, 438:S509, 2013.

[91] M. Kushner. A kinetic study of the plasma etching process. II. probe measurements of the electron properties in an RF plasma-etching reactor. *J. Appl. Phys.*, 53:2939, 1982.

[92] J. Laframboise. *Theory of spherical and cylindrical Langmuir probes in a collisionless, Maxwellian plasma at rest.* PhD thesis, University of Toronto, 1966.

[93] C. Lau et al. Effects of ICRF power on SOL density profiles and LH coupling during simultaneous LH and ICRF operation on Alcator C-Mod. *Plasma Phys. Control. Fusion*, 55:095003, 2013.

[94] S. Leung et al. Optical radiation from low-energy hydrogen atomic and molecular ion-surface collisions. *Phys. Rev. A*, 18:447, 1978.

[95] M. Lieberman. Analytical solution for capacitive RF sheath. *Trans. Plasma Sci.*, 16(6):638, 1988.

[96] M. Lieberman and V. Godyak. Application of the physics of plasma sheaths to the modeling of RF plasma reactors. *Trans. Plasma Sci.*, 26(3):955, 1998.

[97] M. Lieberman and V. Godyak. From Fermi acceleration to collisionless discharge heating. *Trans. Plasma Sci.*, 26(3):955, 1998.

[98] M. Lieberman and A. Lichtenberg. *Principles of Plasma Discharges and Materials Processing, Second Edition.* John Wiley and Sons Inc., 2005.

[99] B. Lipschultz et al. A study of molybdenum influxes and transport in Alcator C-Mod. *Nucl. Fusion*, 41(5):585, 2001.

[100] A. Manenschijn et al. Angular ion and neutral energy distribution in a collisional RF sheath. *J. Appl. Phys.*, 69:2923, 1991.

[101] T. Masayoshi et al. Overdense plasma production using electron cyclotron waves. *J. Phys. Soc. of Japan*, 60(5):1600, 1991.

[102] P. McNeely et al. A Langmuir probe system for high power RF-driven negative ion sources on high potential. *Plasma Sources Sci. Technol.*, 18:014011, 2009.

[103] P. Miller and M. Riley. Dynamics of collisionless RF plasma sheaths. *J. Appl. Phys.*, 82(8):3689, 1997.

[104] J. Myra and D. D'Ippolito. Far field sheaths from waves in the ion cyclotron range of frequencies. *Phys. Plasmas*, 1:2890, 1994.

[105] J. Myra and D. D'Ippolito. Resonance cone interaction with a self-consistent radio-frequency sheath. *Phys. Rev. Lett.*, 101:195004, 2008.

[106] J. Myra and D. D'Ippolito. Slow-wave propagation and sheath interaction in the ion-cyclotron frequency range. *Plasma Phys. Control. Fusion*, 52:015003, 2010.

[107] A. Niemczewski et al. Neutral particle dynamics in the Alacator C-Mod tokamak. *Nucl. Fusion*, 37:151, 1997.

[108] R. Ochoukov. *Investigation of Plasma Potential Enhancement in the Scrape-Off Layer of Ion Cyclotron Range of Frequencies Heated Discharges on Alcator C-Mod.* PhD thesis, Massachusetts Institute of Technology, 2011.

[109] R. Ochoukov et al. ICRF-enhanced plasma potentials in the SOL of Alcator C-Mod. *Plasma Phys. Control. Fusion*, 56:015004, 2014.

[110] D. O'Connell et al. Plasma ionization through wave-particle interaction in a capacitively coupled radio-frequency discharge. *Phys. Plasma*, 14:034505, 2007.

[111] E. Oks. *Plasma Spectroscopy.* Springer-Verlag, 1995.

[112] E. Oks et al. Spectroscopy of atomic hydrogen in dense plasmas in the presence of dynamic fields: Intra-Stark spectroscopy. *Phys. Rev. A*, 44:8338, 1991.

[113] Y. Okuno and H. Fujita. Potential formation near powered electrode in radio-frequency-driven discharge. *J. Appl. Phys.*, 70:642, 1991.

[114] W. Pauli. On the hydrogen spectrum from the point of view of the new quantum mechanics. *Z. Phys.*, 36:336, 1926.

[115] E. Peterson and L. Talbot. Collisonless electrostatic single-probe and double-probe measurements. *AIAA J.*, 8:2215, 1970.

[116] B. Petley et al. A saturated absorption spectroscopy measurement of the Rydberg constant. *J. Phys. B: At. Mol. Phys.*, 13:3099, 1980.

[117] O. Peyrusse. Spectral line-shape calculations for multielectron ions in hot plasmas submitted to a strong oscillating electric field. *Phys. Rev. A*, 79:013411, 2009.

[118] A. Phelps. Energetic ion, atom, and molecule reactions and excitation in low-current H2 discharges: Model. *Phys. Rev. E*, 79:066401, 2009.

[119] W. Press et al. *Numerical Recipes in FORTRAN, Second Edition.* Cambridge University Press, 1986.

[120] B. Quon and R. Dandl. Preferential electron cyclotron heating of hot electrons and formation of overdense plasmas. *Phys. Fluids B*, 1:2010, 1989.

[121] G. Racah. Theory of complex spectra. II. *Phys. Rev.*, 62:438, 1942.

[122] G. Racah. Theory of complex spectra. III. *Phys. Rev.*, 63:367, 1943.

[123] S. Rauf et al. Three-dimensional model of magnetized capacitively coupled plasmas. *J. Appl. Phys.*, 105:103301, 2009.

[124] K. Riemann. Theoretical analysis of the electrode sheath in RF discharges. *J. Appl. Phys.*, 65(3):999, 1989.

[125] M. Riley. Unified model of the RF plasma sheath. Technical report, Sandia National Laboratories, 1995. Report Number: SAND95-0775.

[126] M. Rose. *Elementary Theory of Angular Momentum.* John Wiley and Sons, Inc., 1957.

[127] N. Ryde. About the intensity ratios of the Stark effect components of the hydrogen lines II. Influence of stimulus conditions on the intensity ratios. *ZS. f. Phys.*, 109:108, 1938.

[128] N. Ryde. *Atoms and Molecules in Electric Fields.* Almqvist and Wiksell International, 1976.

[129] P. Sauvan and E. Dalimier. Floquet-Liouville approach for calculating Stark profiles in plasmas in the presence of a strong oscillating field. *Phys. Rev. E*, 79:036405, 2009.

[130] S. Savas and K. Donohoe. Capacitive probes for RF process plasmas. *Rev. Sci. Instrum.*, 60:3391, 1989.

[131] J. Schmidt. High impedance Langmuir probes. *Rev. Sci. Instrum.*, 39:1297, 1968.

[132] E. Schrodinger. An undulatory theory of the mechanics of atoms and molecules. *Phys. Rev.*, 28(6):1049, 1926.

[133] J. Schulze et al. Electron beams in asymmetric capacitively coupled radio frequency discharges at low pressures. *J. Phys. D: Appl. Phys.*, 41:042003, 2008.

[134] J. Schulze et al. Phase resolved optical emission spectroscopy: A non-intrusive diagnostic to study electron dynamics in capacitive radio frequency discharges. *J. Phys. D: Appl. Phys.*, 43:124016, 2010.

[135] J. Schulze et al. Power dynamics in a low pressure capacitively coupled plasma discharge. *Plasma Sources Sci. Technol.*, 19:015014, 2010.

[136] B. Singha et al. Influence of magnetic field on plasma sheath and electron temperature. *Rev. Sci. Instrum.*, 72:2282, 2001.

[137] P. Stangeby. The Chodura sheath for angles of a few degrees between the magnetic field and the surface of divertor targets and limiters. *Nucl. Fusion*, 52:083012, 2012.

[138] R. Stangeby and A. Chankin. The ion velocity (Bohm-Chodura) boundary condition at the entrance to the magnetic presheath in the presence of diamagnetic and ExB drifts in the scrape off layer. *Phys. Plasmas*, 2:707, 1995.

[139] J. Stark. Obervations of the effect of the electric field on the spectral lines I. Transverse effect. *Ann. Phys.*, 43:965, 1914.

[140] T. Stix. *Waves in Plasmas.* Springer, 1992.

[141] I. Sudit and F. Chen. RF compensated probes for high-density discharges. *Plasma Sources Sci. Technol.*, 3:162, 1994.

[142] M. Sugawara. Electron probe current in a magnetized plasma. *Phys. Fluids*, 9:797, 1966.

[143] J. Swift and M. Schwar. *Electrical Probes for Plasma Diagnostics.* Ifille, 1970.

[144] N. Tolk et al. Elliptic polarization of Balmer radiation from low-energy grazing-incidence collisions of hydrogen ions on surfaces. *Phys. Rev. Lett.*, 41:643, 1978.

[145] C. Townes and F. Merritt. Stark effect in high frequency fields. *Phys. Rev.*, 72:1266L, 1947.

[146] D. Vender and R. Boswell. Numerical modeling of low-pressure RF plasmas. *Trans. Plasma Sci.*, 18(4).

[147] D. Vender and R. Boswell. Electron-sheath interaction in capacitive radiofrequency plasmas. *J. Vac. Sci. Technol. A*, 10:1331, 1992.

[148] Q. Wang et al. Spatially resolved diagnostics of an atmospheric pressure direct current helium microplasma. *J. Phys. D: Appl. Phys.*, 38:1690, 2005.

[149] J. Wesson. *Tokamaks*. Oxford University Press, 2011.

[150] C. White and N. Tolk. Optical radiation from low-energy ion-surface collisions. *Phys. Rev. Lett.*, 26:486, 1971.

[151] C. Wieman and T. Hansch. Doppler-free polarization spectroscopy. *Phys. Rev. Lett.*, 17:1170, 1976.

[152] W. Wiese et al. *Atomic transition probabilities: Vol. I hydrogen through neon*. National Bureau of Standards 4, 1966.

[153] J. Wilgen et al. Reflectometer sensing of RF waves in front of the high harmonic fast wave antenna on NSTX. *Rev. Sci. Instrum.*, 77:10E9330, 2006.

[154] J. Wilson et al. Exploration of high harmonic fast wave heating on the National Spherical Torus Experiment. *Phys. Plasma*, 10:1733, 2003.

[155] B. Wood. *Sheath Heating in Low Pressure Capacitive Radio Frequency Discharges*. PhD thesis, University of California, Berkeley, 1991.

[156] T. Wujec et al. Spectroscopic measurements of electric field distributions in dielectric barrier discharges in hydrogen. *J. Phys. D: Appl. Phys.*, 36:868, 2003.

[157] S. Wukitch et al. ICRF specific impurity sources and plasma sheaths in Alcator C-Mod. *J. Nucl. Mater.*, 390:951, 2009.

APPENDICES

APPENDIX

A

UNPERTURBED ENERGY EIGENVALUES

In this appendix the NIST unperturbed energies E_i, where i represents the complete set of quantum numbers in the coupled basis, are given for all magnetic substates of the hydrogen and helium atom having $n \leq 6$ [5]. The magnetic substates are degenerate in the m_j quantum number which has values of

$$m_j \in -j, -j+1 \,..\, j \,. \tag{A.1}$$

A.1 Hydrogen

Table A.1: Hydrogen energy levels in cm^{-1} for n=1 through 3.

$\left\vert \mathbf{n,s,l,j,m_j} \right\rangle$	**n=1**	**n=2**	**n=3**
$\left\vert n,\frac{1}{2},0,\frac{1}{2},m_j \right\rangle$	0	82258.9543992821	97492.221701
$\left\vert n,\frac{1}{2},1,\frac{1}{2},m_j \right\rangle$	-	82258.919113	97492.2112
$\left\vert n,\frac{1}{2},1,\frac{3}{2},m_j \right\rangle$	-	82259.2850014	97492.319611
$\left\vert n,\frac{1}{2},2,\frac{3}{2},m_j \right\rangle$	-	-	97492.319433
$\left\vert n,\frac{1}{2},2,\frac{5}{2},m_j \right\rangle$	-	-	97492.355566

Table A.2: Hydrogen energy levels in cm^{-1} for n=4 through 6.

$\left\|\mathbf{n},\mathbf{s},\mathbf{l},\mathbf{j},\mathbf{m_j}\right\rangle$	**n=4**	**n=5**	**n=6**
$\left\|n,\frac{1}{2},0,\frac{1}{2},m_j\right\rangle$	102823.8530211	105291.63094	106632.1498416
$\left\|n,\frac{1}{2},1,\frac{1}{2},m_j\right\rangle$	102823.8485825	105291.62867	106632.1485242
$\left\|n,\frac{1}{2},1,\frac{3}{2},m_j\right\rangle$	102823.8943175	105291.65209	106632.1620756
$\left\|n,\frac{1}{2},2,\frac{3}{2},m_j\right\rangle$	102823.89425	105291.651993	106632.1620536
$\left\|n,\frac{1}{2},2,\frac{5}{2},m_j\right\rangle$	102823.9094871	105291.659796	106632.1665697
$\left\|n,\frac{1}{2},3,\frac{5}{2},m_j\right\rangle$	102823.90949	105291.65983494	106632.16656761
$\left\|n,\frac{1}{2},3,\frac{7}{2},m_j\right\rangle$	102823.917091	105291.6637	106632.16882614
$\left\|n,\frac{1}{2},4,\frac{7}{2},m_j\right\rangle$	-	105291.66373033	106632.16882188
$\left\|n,\frac{1}{2},4,\frac{9}{2},m_j\right\rangle$	-	105291.666072	106632.17017701
$\left\|n,\frac{1}{2},5,\frac{9}{2},m_j\right\rangle$	-	-	106632.17017434
$\left\|n,\frac{1}{2},5,\frac{11}{2},m_j\right\rangle$	-	-	106632.17107779

A.2 Helium

Table A.3: Para-helium energy levels in cm^{-1} for n=1 through 3.

$\left\|\mathbf{n},\mathbf{s},\mathbf{l},\mathbf{j},\mathbf{m_j}\right\rangle$	**n=1**	**n=2**	**n=3**
$\left\|n,0,0,0,m_j\right\rangle$	0	166277.440141	184864.82932
$\left\|n,0,1,1,m_j\right\rangle$	-	171134.896946	186209.364940
$\left\|n,0,2,2,m_j\right\rangle$	-	-	186104.9666893

Table A.4: Para-helium energy levels in cm^{-1} for n=4 through 6.

$\left\|\mathbf{n},\mathbf{s},\mathbf{l},\mathbf{j},\mathbf{m_j}\right\rangle$	**n=4**	**n=5**	**n=6**
$\left\|n,0,0,0,m_j\right\rangle$	190940.226355	193663.512095	195114.868700
$\left\|n,0,1,1,m_j\right\rangle$	191492.711909	193942.462294	195274.9084660
$\left\|n,0,2,2,m_j\right\rangle$	191446.4557405	193918.28990114	195260.77050808
$\left\|n,0,3,3,m_j\right\rangle$	191451.89746084	193921.13088112	195262.431784358
$\left\|n,0,4,4,m_j\right\rangle$	-	193921.621933101	195262.727124343
$\left\|n,0,5,5,m_j\right\rangle$	-	-	195262.795750108

Table A.5: Ortho-helium energy levels in cm^{-1} for n=1 through 3.

$\left\|\mathbf{n},\mathbf{s},\mathbf{l},\mathbf{j},\mathbf{m_j}\right\rangle$	**n=1**	**n=2**	**n=3**
$\left\|n,1,0,1,m_j\right\rangle$	-	159855.9743297	183236.79170
$\left\|n,1,1,0,m_j\right\rangle$	-	169087.8308131	185564.854540
$\left\|n,1,1,1,m_j\right\rangle$	-	169086.8428979	185564.583895
$\left\|n,1,1,2,m_j\right\rangle$	-	169086.7664725	185564.561920
$\left\|n,1,2,1,m_j\right\rangle$	-	-	186101.5928903
$\left\|n,1,2,2,m_j\right\rangle$	-	-	186101.5486891
$\left\|n,1,2,3,m_j\right\rangle$	-	-	186101.5461767

Table A.6: Ortho-helium energy levels in cm^{-1} for n=4 through 6.

$\left\|\mathbf{n},\mathbf{s},\mathbf{l},\mathbf{j},\mathbf{m_j}\right\rangle$	**n=4**	**n=5**	**n=6**
$\left\|n,1,0,1,m_j\right\rangle$	190298.113260	193346.991344	194936.119697
$\left\|n,1,1,0,m_j\right\rangle$	191217.160290	193800.767563	195192.7772813
$\left\|n,1,1,1,m_j\right\rangle$	191217.049963	193800.712118	195192.7455590
$\left\|n,1,1,2,m_j\right\rangle$	191217.040967	193800.707595	195192.7429742
$\left\|n,1,2,1,m_j\right\rangle$	191444.5006512	193917.16138710	195260.07720298
$\left\|n,1,2,2,m_j\right\rangle$	191444.4821307	193917.15192855	195260.07173649
$\left\|n,1,2,3,m_j\right\rangle$	191444.4809292	193917.15128741	195260.07135803
$\left\|n,1,3,2,m_j\right\rangle$	191451.88970691	193921.12575310	195262.428373005
$\left\|n,1,3,3,m_j\right\rangle$	191451.87394878	193921.11826439	195262.424216836
$\left\|n,1,3,4,m_j\right\rangle$	191451.88108855	193921.12134275	195262.425821479
$\left\|n,1,4,3,m_j\right\rangle$	-	193921.620238142	195262.726141773
$\left\|n,1,4,4,m_j\right\rangle$	-	193921.614948739	195262.723082377
$\left\|n,1,4,5,m_j\right\rangle$	-	193921.617719262	195262.724684231
$\left\|n,1,5,4,m_j\right\rangle$	-	-	195262.795042911
$\left\|n,1,5,5,m_j\right\rangle$	-	-	195262.793050975
$\left\|n,1,5,6,m_j\right\rangle$	-	-	195262.794095149

APPENDIX

B

CALCULATION OF MATRIX ELEMENTS

In this appendix the calculation of the matrix elements E^B_{jm} and $E^{E_n}_{jm}$, associated with Eq. 3.23 and Eq. 3.24 respectively, will be presented. E^B_{jm} is the energy coupled between the quantum states associated with the j^{th} and m^{th} wave functions due to a magnetic field along the z-axis with magnitude B_z. The corresponding Hamiltonian operator is given by

$$H^B = \frac{\mu_\beta}{\hbar} B_z (J_z + S_z) \,. \tag{B.1}$$

$E^{E_n}_{jm}$ is the energy coupled between the quantum states associated with the j^{th} and m^{th} wave functions due to a electric field vector $\bar{E}_n$. The corresponding Hamiltonian operator is given by

$$H^{E_n} = e\,\bar{E}_n \cdot \bar{r} \,. \tag{B.2}$$

As indicated by Eq. 3.5, $\bar{E}_n$ contains the magnitude of the n^{th} harmonic vector components of the waveform $\bar{E}(t)$ and is thus a time independent quantity. Therefore the operator H^{E_n} is equivalent to that of a static electric field.

The only assumption made when calculating the energy and wave function of the quantum states is that states with differing radial quantum numbers n do not mix. The magnetic field operator given by Eq. B.1 is incapable of mixing states with differing n values. Thus this assumption is not limiting in terms of the magnetic field intensity. The electric field operator given by Eq. B.2 can mix

states with differing n values, however the mixing is very weak when the electric field magnitude is ≤ 100 kV/cm [128]. The electric field magnitudes of interest for this research and future work are expected to be ≤ 15 kV/cm and thus the approximation is appropriate.

The calculation is greatly simplified by Racah algebra which takes advantage of the symmetry of the unperturbed atom by working within the spherical basis [121, 122]. Utilizing this representation, the scalar product of two tensors of rank k is given by

$$\boldsymbol{T}^{(k)} \cdot \boldsymbol{U}^{(k)} = \sum_q (-1)^q T_q^{(k)} U_{-q}^{(k)} \,. \tag{B.3}$$

Specifically for the derivations presented here $k = 1$ and thus the tensors $\boldsymbol{T}^{(1)}$ and $\boldsymbol{U}^{(1)}$ are vectors and can be analogously represented as $\bar{T}$ and $\bar{U}$ respectively. Here we will retain the boldface representation for vector operators.

The Hamiltonian associated with the magnetic field given by Eq. B.1 and the electric field given by Eq. B.2 can thus be written as

$$H^B = \frac{\mu_\beta}{\hbar} B_0^{(1)} J_0^{(1)} + \frac{\mu_\beta}{\hbar} B_0^{(1)} S_0^{(1)} \tag{B.4}$$

and

$$H^{E_n} = -\frac{1}{2} e\, E_{1n}^{(1)} r_{-1}^{(1)} + \frac{1}{2} e\, E_{0n}^{(1)} r_0^{(1)} - \frac{1}{2} e\, E_{-1n}^{(1)} r_1^{(1)} \tag{B.5}$$

respectively. Where the following relationship exists between the spherical and Cartesian unit vectors

$$\hat{\epsilon}_1 = \frac{-1}{\sqrt{2}}(\hat{x} + i\hat{y}) \qquad \hat{\epsilon}_0 = \hat{z} \qquad \hat{\epsilon}_{-1} = \frac{1}{\sqrt{2}}(\hat{x} - i\hat{y}) \,.$$

In the deviations given below the Wigner-Eckart theorem will be utilized to reduce the expression of the matrix element and thus will be presented here. The theorem states that the expectation value of the q^{th} component of the spherical tensor operator $T_q^{(k)}$ can be expressed as a product of two factors as given by

$$\langle n', l', s', j', m_j' | T_q^{(k)} | n, l, s, j, m_j \rangle = (-1)^{j'-m_j'} \begin{bmatrix} j' & k & j \\ -m_j' & q & m_j \end{bmatrix} \langle n', l', s', j' || \boldsymbol{T}^{(k)} || n, l, s, j \rangle \,. \tag{B.6}$$

Where the term

$$\begin{bmatrix} j_1 & j_2 & j_3 \\ j_4 & j_5 & j_6 \end{bmatrix} \tag{B.7}$$

is refereed to as the 3j-symbol and can be calculated analytically [52]. The remaining term

$$\langle n', l', s', j' || \boldsymbol{T}^{(k)} || n, l, s, j \rangle \tag{B.8}$$

is referred to as the reduced matrix element and is independent of the project quantum number m_j. Conservation of angular momentum necessitates that the following two criteria to be fulfilled else the 3j-symbol is zero. The first requires that the top row of the 3j-symbol satisfy the equality

$$\left| j^{'} - k \right| \leq j \leq j^{'} + k \tag{B.9}$$

for all possible permutations of j', k, and j. These quantities are said to form a triangle and this relationship is denoted by $\triangle\left(j' k j\right)$ [126]. The second requires that the bottom row of the 3j-symbol sum to zero as given by

$$-m_j^{'} + q + m_j = 0\,. \tag{B.10}$$

The reduced matrix element can be simplified depending on the spherical tensor operator $\boldsymbol{T}^{(k)}$. If $\boldsymbol{T}^{(k)}$ operates on the l quantum number then $s^{'} = s$ and Eq. B.8 can be written as

$$\begin{aligned} &\langle n', l', s', j' || \boldsymbol{T}^{(k)} || n, l, s, j \rangle = \\ &\qquad (-1)^{s+l+j'+k} \left[(2j+1)(2j'+1)\right]^{1/2} \begin{Bmatrix} l' & j' & s \\ j & l & k \end{Bmatrix} \langle n', l', s || \boldsymbol{T}^{(k)} || n, l, s \rangle\,. \end{aligned} \tag{B.11}$$

If $\boldsymbol{T}^{(k)}$ operates on the s quantum number then $l^{'} = l$ and Eq. B.8 can be written as

$$\begin{aligned} &\langle n', l', s', j' || \boldsymbol{T}^{(k)} || n, l, s, j \rangle = \\ &\qquad (-1)^{s'+l+j+k} \left[(2j+1)(2j'+1)\right]^{1/2} \begin{Bmatrix} s' & j' & l \\ j & s & k \end{Bmatrix} \langle n', l, s' || \boldsymbol{T}^{(k)} || n, l, s \rangle\,. \end{aligned} \tag{B.12}$$

Where the term

$$\begin{Bmatrix} j_1 & j_2 & j_3 \\ j_4 & j_5 & j_6 \end{Bmatrix} \tag{B.13}$$

is refereed to as the 6j-symbol and can be calculated analytically [52]. The 6j-symbol can be expressed in terms of the 3j-symbol therefore similar conservation laws apply. The 6j-symbol is zero unless the triangle relations $\triangle\left(j_1 j_2 j_3\right)$ and $\triangle\left(j_4 j_5 j_6\right)$ are satisfied.

B.1 Magnetic Field Matrix Elements

The matrix elements E^B_{jm} are calculated by multiplying Eq. 3.23 by the wave function Φ_m and integrating over all space. Utilizing the orthonormality of the basis set, E^B_{jm} is given by

$$E^B_{jm} = \langle \Phi_m | H^B | \Phi_j \rangle \, . \tag{B.14}$$

The wave functions are given by

$$\Phi_m = |n', l', s', j', m'_j\rangle$$

$$\Phi_j = |n, l, s, j, m_j\rangle \, .$$

Where the subscripts associated with the matrix elements and wave functions should not be confused with the quantum numbers. The Hamiltonian H^B given by Eq. B.1 is substituted into Eq. B.14 resulting in

$$\langle n', l', s', j', m'_j | \frac{\mu_\beta}{\hbar} B^{(1)}_0 J^{(1)}_0 | n, l, s, j, m_j\rangle + \langle n', l', s', j', m'_j | \frac{\mu_\beta}{\hbar} B^{(1)}_0 S^{(1)}_0 | n, l, s, j, m_j\rangle \, . \tag{B.15}$$

The two terms of Eq. B.15 will be treated independently below for the convenience of presentation.

The coupled basis set are eigenfunctions of the operator $J^{(1)}_0$ having eigenvalues $\hbar m_j$. Thus the first term of Eq. B.15 can be simplified as follows

$$\langle n', l', s', j', m'_j | \frac{\mu_\beta}{\hbar} B^{(1)}_0 J^{(1)}_0 | n, l, s, j, m_j\rangle = \mu_\beta B^{(1)}_0 m_j \, . \tag{B.16}$$

Where the selection rules for mixing must be satisfied

$$n' = n \qquad l' = l \qquad s' = s \qquad j' = j \qquad m'_j = m_j \tag{B.17}$$

or else the first term is zero. Utilizing the Wigner-Eckart theorem given by Eq. B.6 the second term of Eq. B.15 can be expressed as

$$\langle n', l', s', j', m'_j | \frac{\mu_\beta}{\hbar} B^{(1)}_0 S^{(1)}_0 | n, l, s, j, m_j\rangle = \frac{\mu_\beta}{\hbar} B^{(1)}_0 (-1)^{j'-m'_j} \begin{bmatrix} j' & 1 & j \\ -m'_j & 0 & m_j \end{bmatrix} \langle n', l', s', j' || \boldsymbol{S}^{(1)} || n, l, s, j\rangle \, . \tag{B.18}$$

Requiring conservation of angular momentum by implementation of Eq. B.9 and Eq. B.10 the following selection rules must be satisfied

$$m_j' = m_j \qquad 1 \in |j'-j| \,..\, |j'+j|$$

or else the 3j-symbol and thus the second term is zero. The operator $\boldsymbol{S}^{(1)}$ operates on the s quantum number thus Eq. B.12 is utilized to express the reduced matrix element as follows

$$\langle n', l', s', j' || \boldsymbol{S}^{(1)} || n, l, s, j \rangle = \\ (-1)^{s'+l+j+1} \left[(2j+1)(2j'+1)\right]^{1/2} \begin{Bmatrix} s' & j' & l \\ j & s & 1 \end{Bmatrix} \langle n', l, s' || \boldsymbol{S}^{(1)} || n, l, s \rangle \,. \tag{B.19}$$

The reduced wave functions $|n, l, s\rangle$ are eigenfunctions of the operator $\boldsymbol{S}^1$ having eigenvalues $\hbar\left[(2s+1)(s+1)s\right]^{1/2}$ thus the following can be written

$$\langle n', l, s' || \boldsymbol{S}^{(1)} || n, l, s \rangle = \hbar\left[(2s+1)(s+1)s\right]^{1/2} \,. \tag{B.20}$$

Where the following selection rules must be satisfied

$$n' = n \qquad s' = s$$

or else this quantity and thus the second term is zero. Substituting Eq. B.20 into Eq. B.19 and the result into Eq. B.18 the final form of the second term is expressed as

$$\langle n', l', s', j', m_j' | \frac{\mu_\beta}{\hbar} B_0^{(1)} S_0^{(1)} | n, l, s, j, m_j \rangle = \mu_\beta B_0^{(1)} (-1)^{s'+l+j+j'-m_j'+1} \\ \cdot \left[(2j+1)(2j'+1)\right]^{1/2} \left[(2s+1)(s+1)s\right]^{1/2} \begin{bmatrix} j' & 1 & j \\ -m_j' & 0 & m_j \end{bmatrix} \begin{Bmatrix} s' & j' & l \\ j & s & 1 \end{Bmatrix} \,. \tag{B.21}$$

Where the corresponding selection rules for mixing are summarized by

$$n' = n \qquad l' = l \qquad s' = s \qquad m_j' = m_j \qquad j' = j \pm 1 \qquad j' = j \neq 0 \,. \tag{B.22}$$

Therefore the matrix element E_{jm}^{B} is given by a summation of Eq. B.16 and Eq. B.21 utilizing the selection rules for mixing given by Eq. B.17 and Eq. B.22 respectively.

B.2 Electric Field Field Matrix Elements

The matrix elements $E_{jm}^{E_n}$ are calculated by multiplying Eq. 3.24 by the wave function Φ_m and integrating over all space. Utilizing the orthonormality of the basis set, $E_{jm}^{E_n}$ is given by

$$E_{jm}^{E_n} = \langle \Phi_m | H^{E_n} | \Phi_j \rangle \, . \tag{B.23}$$

The wave functions are given by

$$\Phi_m = |n', l', s', j', m_j'\rangle$$

$$\Phi_j = |n, l, s, j, m_j\rangle \, .$$

Where the subscripts associated with the matrix elements and wave functions should not be confused with the quantum numbers. The Hamiltonian H^{E_n} given by Eq. B.2 is substituted into Eq. B.23 resulting in

$$\begin{aligned} -\langle n', l', s', j', m_j'| e E_{1n}^{(1)} r_{-1}^{(1)} |n, l, s, j, m_j\rangle \\ + \langle n', l', s', j', m_j'| e E_{0n}^{(1)} r_{0}^{(1)} |n, l, s, j, m_j\rangle \\ - \langle n', l', s', j', m_j'| e E_{-1n}^{(1)} r_{1}^{(1)} |n, l, s, j, m_j\rangle \, . \end{aligned} \tag{B.24}$$

The three terms of Eq. B.24 are associated with the spherical basis vector components of the operator H^{E_n} and thus the expression for the matrix elements associated each term is of the same form. Therefore only the derivation of the first term will be provided below with the final expression of the second and third following.

Utilizing the Wigner-Eckart theorem given by Eq. B.6 the first term of Eq. B.24 can be expressed as

$$\begin{aligned} -\langle n', l', s', j', m_j'| e E_{1n}^{(1)} r_{-1}^{(1)} |n, l, s, j, m_j\rangle = \\ - e E_{1n}^{(1)} (-1)^{j'-m_j'} \begin{bmatrix} j' & 1 & j \\ -m_j' & -1 & m_j \end{bmatrix} \langle n', l', s', j' || \boldsymbol{r}^{(1)} || n, l, s, j\rangle \, . \end{aligned} \tag{B.25}$$

Requiring conservation of angular momentum by implementation of Eq. B.9 and Eq. B.10 the following selection rules must be satisfied

$$m_j' = m_j - 1 \qquad 1 \in |j' - j| \,..\, |j' + j|$$

or else the 3j-symbol and thus the first term is zero. The operator $\boldsymbol{r}^{(1)}$ operates on the l quantum number thus Eq. B.11 is utilized to express the reduced matrix element as follows

$$\langle n', l', s, j' || \boldsymbol{r}^{(1)} || n, l, s, j \rangle =$$
$$(-1)^{s+l+j'+1} \left[(2j+1)(2j'+1) \right]^{1/2} \begin{Bmatrix} l' & j' & s \\ j & l & 1 \end{Bmatrix} \langle n', l', s || \boldsymbol{r}^{(1)} || n, l, s \rangle \,. \tag{B.26}$$

The term $\langle n', l', s || \boldsymbol{r}^{(1)} || n, l, s \rangle$ is referred to as the overlap integral and can be expressed in a simple analytic form when $n' = n$ as given by

$$\langle n, l', s || \boldsymbol{r}^{(1)} || n, l, s \rangle = \frac{6\pi\epsilon_o \hbar^2}{m_e e^2} (-1)^{l+l_>} l_>^{1/2} n (n^2 - l^2)^{1/2} \,, \tag{B.27}$$

where $l_>$ is the larger of l' and l [19, 67]. When considering $n' \neq n$ the overlap integral can be calculated from its general form [19]. The following selection rules must be satisfied

$$l' = l \pm 1$$

or else the overlap integral and thus the first term is zero. There is no criteria on n'. Substituting Eq. B.27 into Eq. B.26 and the result into Eq. B.25 the final form of the first term is expressed as

$$-\langle n, l', s', j', m_j' | e E_{1n}^{(1)} r_{-1}^{(1)} | n, l, s, j, m_j \rangle = -\frac{6\pi\epsilon_o \hbar^2}{m_e e} E_{1n}^{(1)} (-1)^{s+l_>+2l+2j'-m_j'+1}$$
$$\cdot \left[(2j+1)(2j'+1) \right]^{1/2} l_>^{1/2} n (n^2 - l^2)^{1/2} \begin{bmatrix} j' & 1 & j \\ -m_j' & -1 & m_j \end{bmatrix} \begin{Bmatrix} l' & j' & s \\ j & l & 1 \end{Bmatrix} \,. \tag{B.28}$$

Where the corresponding selection rules for mixing are summarized by

$$l' = l \pm 1 \qquad s' = s \qquad m_j' = m_j - 1 \qquad j' = j \pm 1 \qquad j' = j \neq 0 \,. \tag{B.29}$$

Following the above derivation the expression for the second term of Eq. B.24 is

$$\langle n, l', s', j', m_j' | e E_{0n}^{(1)} r_0^{(1)} | n, l, s, j, m_j \rangle = \frac{6\pi\epsilon_o \hbar^2}{m_e e} E_{1n}^{(1)} (-1)^{s+l_>+2l+2j'-m_j'+1}$$
$$\cdot \left[(2j+1)(2j'+1) \right]^{1/2} l_>^{1/2} n (n^2 - l^2)^{1/2} \begin{bmatrix} j' & 1 & j \\ -m_j' & 0 & m_j \end{bmatrix} \begin{Bmatrix} l' & j' & s \\ j & l & 1 \end{Bmatrix} \tag{B.30}$$

with corresponding selection rules for mixing given by

$$l' = l \pm 1 \qquad s' = s \qquad m_j' = m_j \qquad j' = j \pm 1 \qquad j' = j \neq 0 \,. \tag{B.31}$$

Finally, the expression for the third term of Eq. B.24 is

$$-\langle n,l',s',j',m_j'|e\,E_{-1n}^{(1)}r_1^{(1)}|n,l,s,j,m_j\rangle = -\frac{6\pi\epsilon_o\hbar^2}{m_e e}E_{1n}^{(1)}(-1)^{s+l_>+2l+2j'-m_j'+1}$$
$$\cdot\left[(2j+1)(2j'+1)\right]^{1/2}l_>^{1/2}n(n^2-l^2)^{1/2}\begin{bmatrix} j' & 1 & j \\ -m_j' & 1 & m_j\end{bmatrix}\begin{Bmatrix} l' & j' & s \\ j & l & 1\end{Bmatrix} \tag{B.32}$$

with corresponding selection rules for mixing given by

$$l'=l\pm1 \qquad s'=s \qquad m_j'=m_j+1 \qquad j'=j\pm1 \qquad j'=j\neq0\,. \tag{B.33}$$

Therefore the matrix element $E_{jm}^{E_n}$ is given by a summation of Eq. B.28, Eq. B.30, and Eq. B.32 utilizing the selection rules for mixing given by Eq. B.29, Eq. B.31, and Eq. B.33 respectively.

As discussed in Section 3.3.2 the matrix elements $\left\langle\Phi_m\left|\hat{H}\right|\Phi_j\right\rangle$ associated with the electric dipole connection operator are calculated utilizing a similar expression found above for $E_{jm}^{E_n}$. This is due to the fact that the Hamiltonian $\hat{H}=\bar{\epsilon}\cdot\bar{r}$ is of the same form of that given by Eq. B.2. In addition to replacing the quantity $e\,\bar{E}_n$ with the polarization vector $\bar{\epsilon}$ the more general form of the overlap integral must be used due to the fact that $n'\neq n$. The overlap integral given by:

$$\langle n',l',s||\boldsymbol{r}^{(1)}||n,l,s\rangle = \frac{6\pi\epsilon_o\hbar^2}{m_e e^2}(-1)^{l+l_>}l_>^{1/2}$$
$$\cdot\frac{-1^{n_1-l_1}}{4(2l_1-1)!}\left[\frac{(n_2+l_1)!(n_1+l_1-1)!}{(n_2-l_1-1)!(n_1-l_1)!}\right]^{1/2}\frac{(4n_1n_2)^{l_1+1}(n_2-n_1)^{n_1+n_2-2l_1-2}}{(n_1+n_2)^{n_1+n_2}}$$
$$\cdot\left[{}_2F_1\left(-n_{r2},-n_{r1};2l_1;-\frac{4n_1n_2}{(n_1-n_2)^2}\right)-\left(\frac{n_1-n_2}{n_1+n_2}\right)_2^2F_1\left(-n_{r2}-2,-n_{r1};2l_1;-\frac{4n_1n_2}{(n_1-n_2)^2}\right)\right] \tag{B.34}$$

must be replaced by that of Eq. B.27, where ${}_2F_1(\alpha,\beta;\gamma;\nu)$ is the Gaussian hypergeometric function. The selection rules as discussed above are still applicable. The variables n_1, n_2, and l_1 utilized in Eq. B.34 are defined in Table B.1, with

$$n_{r1}=n_1-l_1 \qquad n_{r2}=n_2-l_1-1\,.$$

Table B.1: Overlap integral variable definitions.

Variable	$\mathbf{l'>l}$	$\mathbf{l'<l}$
n_1	n	n'
n_2	n'	n
l_1	l'	l

APPENDIX

C

SHOT DISCHARGE PARAMETERS

In this appendix the various set points, electrical parameters, and plasma parameters are tabulated for each of the 28 discharges, referred to as shots, investigated. The definition of the variables used to characterize the shot are given in Table C.1 for the set points and electrical parameters and Table C.2 for the plasma parameters.

Table C.1: Definitions of set points and the electrical parameters.

Variable	Definition
$\mathbf{P}$	Discharge pressure
$\mathbf{P_{\mu W}}$	Microwave power level
$\mathbf{P_{RF}}$	RF power level
$\mathbf{C_L}$	Load capacitor position
$\mathbf{C_T}$	Tune capacitor position
$\mathbf{P_E}$	Matching network power efficiency
$\mathbf{X_L}$	Plasma reactance
$\mathbf{R_L}$	Plasma resistance
$\mathbf{V_{DC}}$	Electrode DC voltage
$\lvert\mathbf{V_{RF}}\rvert$	Electrode RF voltage magnitude
$\lvert\mathbf{I_{RF}}\rvert$	Electrode RF current magnitude

Table C.2: Definitions of plasma parameter.

Variable	Definition
$\mathbf{n_e}$	Electron density
$\mathbf{kT_e}$	Electron temperature
$\phi_\mathbf{f}$	Floating potential
$\phi_\mathbf{p0}$	Plasma potential
$\mathbf{A_e/A_p}$	Ratio of electron collection area to probe tip area
$\mathbf{A_i/A_p}$	Ratio of ion collection area to probe tip area

The diagnostics and associated theory presented in Section 4.1 were used to measure and determine the electrical parameters. The RF compensated Langmuir probe presented in Section 4.3.1 was used to determine the plasma parameters through a fit to the I-V characteristic.

C.1 Parallel Field Configuration

Table C.3: Power and matching network set points for the hydrogen discharges.

Shot	P (mTorr)	$P_{\mu W}$ (W)	P_{RF} (W)	C_L (V)	C_T (V)
1	200	0	88	1.367	0.550
2	200	194	83	1.368	0.546
3	200	0	210	1.368	0.546
4	200	190	208	1.368	0.546
5	400	0	149	1.367	0.544
6	400	173	140	1.367	0.544
7	400	0	219	1.367	0.544
8	400	171	204	1.367	0.544

Table C.4: Power and matching network set points for the helium discharges.

Shot	P (mTorr)	$P_{\mu W}$ (W)	P_{RF} (W)	C_L (V)	C_T (V)
9	200	0	59	1.459	0.550
10	200	91	74	1.459	0.546
11	200	0	137	1.459	0.550
12	200	107	153	1.459	0.546
13	400	0	65	1.459	0.550
14	400	87	66	1.459	0.550
15	400	0	140	1.459	0.550
16	400	90	133	1.459	0.550

Table C.5: Electrical parameters for the hydrogen discharges.

Shot	$\mathbf{P_E}$ **(%)**	$\mathbf{X_L}$ **(Ω)**	$\mathbf{R_L}$ **(Ω)**	$\mathbf{V_{DC}}$ **(kV)**	$\mathbf{\lvert V_{RF}\rvert}$ **(kV)**	$\mathbf{\lvert I_{RF}\rvert}$ **(A)**
1	67	-605	12	-1.9	1.9	8.2
2	68	-600	12	-1.9	1.8	7.9
3	68	-600	12	-2.7	2.6	11.6
4	68	-600	12	-2.7	2.6	11.4
5	68	-598	12	-1.9	1.9	8.4
6	68	-598	12	-1.9	1.8	8.0
7	68	-598	12	-2.6	2.5	11.2
8	68	-598	12	-2.3	2.1	9.6

Table C.6: Electrical parameters for the helium discharges.

Shot	$\mathbf{P_E}$ **(%)**	$\mathbf{X_L}$ **(Ω)**	$\mathbf{R_L}$ **(Ω)**	$\mathbf{V_{DC}}$ **(kV)**	$\mathbf{\lvert V_{RF}\rvert}$ **(kV)**	$\mathbf{\lvert I_{RF}\rvert}$ **(A)**
9	66	-606	12	-1.9	1.7	7.6
10	67	-601	12	-1.9	1.7	7.4
11	67	-606	12	-2.7	2.4	11.0
12	67	-601	12	-2.7	2.4	10.7
13	66	-606	12	-1.9	1.7	7.6
14	66	-606	12	-1.9	1.7	7.3
15	66	-606	12	-2.7	2.4	10.9
16	66	-606	12	-2.7	2.4	10.6

Table C.7: Plasma parameters for the hydrogen discharges.

Shot	$\mathbf{n_e}$ **(m^{-3})**	$\mathbf{kT_e}$ **(eV)**	$\boldsymbol{\phi_f}$ **(V)**	$\boldsymbol{\phi_{p0}}$ **(V)**	$\mathbf{A_e/A_p}$	$\mathbf{A_i/A_p}$
1	$5.33 \cdot 10^{16}$	17.1	-34.3	-16.9	0.073	1.000
2	$3.93 \cdot 10^{16}$	6.3	-8.5	0.8	0.140	1.000
3	$1.03 \cdot 10^{17}$	16.7	-32.1	-13.5	0.085	1.000
4	$7.42 \cdot 10^{16}$	8.6	-13.8	-1.7	0.128	1.000
5	$7.99 \cdot 10^{16}$	18.5	-33.9	-12.3	0.091	1.000
6	$5.24 \cdot 10^{16}$	4.6	-4.2	3.4	0.175	1.000
7	$8.05 \cdot 10^{16}$	8.8	-14.8	-1.8	0.140	1.000
8	$6.78 \cdot 10^{16}$	8.3	-12.5	0.6	0.159	1.000

Table C.8: Plasma parameters for the helium discharges.

Shot	$\mathbf{n_e}$ **(m^{-3})**	$\mathbf{kT_e}$ **(eV)**	$\phi_\mathbf{f}$ **(V)**	$\phi_\mathbf{p0}$ **(V)**	$\mathbf{A_e/A_p}$	$\mathbf{A_i/A_p}$
9	$8.00 \cdot 10^{16}$	7.3	-18.5	-8.4	0.061	1.000
10	$1.09 \cdot 10^{18}$	4.4	4.2	15.5	0.230	1.000
11	$1.49 \cdot 10^{17}$	8.7	-20.0	-7.2	0.071	1.000
12	$1.41 \cdot 10^{18}$	5.3	3.7	17.3	0.230	1.000
13	$1.27 \cdot 10^{17}$	6.6	-14.9	-4.5	0.081	1.000
14	$9.74 \cdot 10^{17}$	2.6	5.1	11.9	0.230	1.000
15	$2.10 \cdot 10^{17}$	10.4	-12.3	5.3	0.094	1.000
16	$1.01 \cdot 10^{18}$	3.0	5.2	12.9	0.230	1.000

C.2 Perpendicular Field Configuration

Table C.9: Power and matching network set points for the hydrogen discharges.

Shot	**P (mTorr)**	$\mathbf{P_{\mu W}}$ **(W)**	$\mathbf{P_{RF}}$ **(W)**	$\mathbf{C_L}$ **(V)**	$\mathbf{C_T}$ **(V)**
17	100	0	136	1.297	0.543
18	100	131	131	1.297	0.543
19	100	0	193	1.297	0.543
20	100	129	191	1.297	0.543

Table C.10: Power and matching network set points for the helium discharges.

Shot	**P (mTorr)**	$\mathbf{P_{\mu W}}$ **(W)**	$\mathbf{P_{RF}}$ **(W)**	$\mathbf{C_L}$ **(V)**	$\mathbf{C_T}$ **(V)**
21	100	0	77	1.297	0.543
22	100	137	97	1.297	0.543
23	100	0	112	1.297	0.543
24	100	99	121	1.297	0.543
25	200	0	86	1.297	0.543
26	200	88	98	1.297	0.543
27	200	0	129	1.297	0.543
28	200	85	138	1.297	0.543

Table C.11: Electrical parameters for the hydrogen discharges.

Shot	$\mathbf{P_E}$ **(%)**	$\mathbf{X_L}$ **(Ω)**	$\mathbf{R_L}$ **(Ω)**	$\mathbf{V_{DC}}$ **(kV)**	$\mathbf{\lvert V_{RF}\rvert}$ **(kV)**	$\mathbf{\lvert I_{RF}\rvert}$ **(A)**
17	69	-597	12	-1.5	1.8	7.8
18	69	-597	12	-1.5	1.7	7.5
19	69	-597	12	-1.9	2.2	9.6
20	69	-597	12	-1.9	2.1	9.3

Table C.12: Electrical parameters for the helium discharges.

Shot	$\mathbf{P_E}$ **(%)**	$\mathbf{X_L}$ **(Ω)**	$\mathbf{R_L}$ **(Ω)**	$\mathbf{V_{DC}}$ **(kV)**	$\mathbf{\lvert V_{RF}\rvert}$ **(kV)**	$\mathbf{\lvert I_{RF}\rvert}$ **(A)**
21	69	-597	12	-1.5	1.7	7.5
22	69	-597	12	-1.5	1.6	7.0
23	69	-597	12	-1.9	2.1	9.4
24	69	-597	12	-1.9	2.0	8.9
25	69	-597	12	-1.5	1.6	7.1
26	69	-597	12	-1.5	1.6	7.0
27	69	-597	12	-1.9	2.0	8.9
28	69	-597	12	-1.9	2.0	8.7

Table C.13: Plasma parameters for the hydrogen discharges.

Shot	$\mathbf{n_e}$ **(m^{-3})**	$\mathbf{kT_e}$ **(eV)**	$\boldsymbol{\phi_f}$ **(V)**	$\boldsymbol{\phi_{p0}}$ **(V)**	$\mathbf{A_e/A_p}$	$\mathbf{A_i/A_p}$
17	$3.19 \cdot 10^{15}$	12.7	9.8	24.7	0.092	1.000
18	$8.49 \cdot 10^{15}$	1.7	4.4	7.4	0.200	1.000
19	$3.49 \cdot 10^{15}$	13	9.7	25.3	0.095	1.000
20	$8.94 \cdot 10^{15}$	1.9	5.2	8.3	0.182	1.000

Table C.14: Plasma parameters for the helium discharges.

Shot	$\mathbf{n_e}$ **(m^{-3})**	$\mathbf{kT_e}$ **(eV)**	$\boldsymbol{\phi_f}$ **(V)**	$\boldsymbol{\phi_{p0}}$ **(V)**	$\mathbf{A_e/A_p}$	$\mathbf{A_i/A_p}$
21	$5.82 \cdot 10^{15}$	4.4	13.0	19.8	0.078	1.000
22	$6.97 \cdot 10^{16}$	3.3	2.7	11.0	0.256	1.000
23	$1.20 \cdot 10^{16}$	5.0	8.8	16.0	0.095	1.000
24	$6.11 \cdot 10^{16}$	4.7	2.4	13.2	0.199	1.000
25	$8.87 \cdot 10^{15}$	4.1	8.5	15.2	0.086	1.000
26	$4.64 \cdot 10^{16}$	4.0	3.0	11.2	0.150	1.000
27	$1.01 \cdot 10^{16}$	4.2	8.5	15.6	0.091	1.000
28	$3.69 \cdot 10^{16}$	3.3	3.9	11.7	0.208	1.000

APPENDIX

D

SPECTRAL LINE PROFILES

This appendix presents the fitted H_β and $5^3D \rightarrow 2^3P$ He I π and σ spectral line profiles for select shots. The π and σ profiles were fit together as an object utilizing the model presented in Table 5.1, for specific details see Section 5.4.2. The electric field is assumed to always be negative, that is point towards the RF biased electrode surface, therefore the waveform was clamped at zero [44, 147]. A total of 8 shots were selected, 4 having hydrogen and 4 having helium as the working gas in which the H_β and $5^3D \rightarrow 2^3P$ He I transitions were observed respectively. The four shots correspond to discharges in the parallel and perpendicular field configurations having the ECW source on and off. The discharge parameters of interest are presented in Table D.1 for the selected shots, see Appendix C for the complete tables.

Table D.1: Select discharge parameters of the presented shots.

Shot	**Configuration**	**Gas**	**P (mTorr)**	**$P_{\mu W}$ (W)**
3	Parallel	Hydrogen	200	0
4	Parallel	Hydrogen	200	190
11	Parallel	Helium	200	0
12	Parallel	Helium	200	107
19	Perpendicular	Hydrogen	100	0
20	Perpendicular	Hydrogen	100	129
27	Perpendicular	Helium	200	0
28	Perpendicular	Helium	200	85

To portray the quality of the fit as a function of z-axis position the π and σ profiles at three spatial locations are presented. In the parallel field configuration spectra at positions of $z = 0.8$, 3.8, and 7.9 mm are presented. In the perpendicular field configuration spectra at positions of $z = 1.0$, 4.1, and 7.6 mm are presented. Table D.2 through Table D.9 give the fit parameters associated with the selected positions for the shots presented in Table D.1.

Table D.2: Fit parameters associated with the spectra presented for shot 3.

Position (mm)	**E_0 (kV/cm)**	**E_1 (kV/cm)**	**θ_1 (°)**	**I_{R2} (%)**	**kT_{R2} (eV)**
0.8	-4.1 ± 0.1	7.4 ± 0.1	57.1 °	139.8	4.2
3.8	2.0 ± 0.6	8.6 ± 0.7	51.0 °	110.8	3.8
7.9	11.9 ± 1.3	12.8 ± 1.5	10.0 °	48.1	3.7

Table D.3: Fit parameters associated with the spectra presented for shot 4.

Position (mm)	**E_0 (kV/cm)**	**E_1 (kV/cm)**	**θ_1 (°)**	**I_{R2} (%)**	**kT_{R2} (eV)**
0.8	-3.8 ± 0.1	5.8 ± 0.1	48.4 °	139.3	3.8
3.8	0.0 ± 0.4	5.9 ± 0.5	51.6 °	165.5	3.6
7.9	8.4 ± 1.2	11.4 ± 1.3	56.7 °	136.1	3.3

Table D.4: Fit parameters associated with the spectra presented for shot 11.

Position (mm)	**E_0 (kV/cm)**	**E_1 (kV/cm)**	**I_{R2} (%)**	**kT_{R2} (eV)**
0.8	-5.1 ± 0.1	4.1 ± 0.1	15.5	30.0
3.8	-3.5 ± 0.1	3.0 ± 0.1	13.8	18.2
7.9	-1.6 ± 0.4	1.5 ± 0.5	9.4	12.2

Table D.5: Fit parameters associated with the spectra presented for shot 12.

Position (mm)	**E_0 (kV/cm)**	**E_1 (kV/cm)**	**I_{R2} (%)**	**kT_{R2} (eV)**
0.8	-6.7 ± 0.1	6.1 ± 0.1	15.7	35.0
3.8	-2.0 ± 0.3	6.0 ± 0.4	13.1	30.7
7.9	0.0 ± 0.8	1.4 ± 1.1	9.4	11.8

Table D.6: Fit parameters associated with the spectra presented for shot 19.

Position (mm)	**E_0 (kV/cm)**	**E_1 (kV/cm)**	θ_1 (°)	**I_{R2} (%)**	**kT_{R2} (eV)**
1.0	-2.5 ± 0.1	4.8 ± 0.2	3.8	144.5	4.9
4.1	-0.3 ± 0.4	4.3 ± 0.5	8.0	165.9	3.5
7.6	6.7 ± 1.2	10.0 ± 1.2	14.5	44.7	4.3

Table D.7: Fit parameters associated with the spectra presented for shot 20.

Position (mm)	**E_0 (kV/cm)**	**E_1 (kV/cm)**	θ_1 (°)	**I_{R2} (%)**	**kT_{R2} (eV)**
1.0	-2.7 ± 0.1	4.3 ± 0.2	-1.8	185.0	4.1
4.1	-0.5 ± 0.4	4.3 ± 0.5	13.6	127.9	3.1
7.6	5.2 ± 1.1	7.8 ± 1.2	5.7	50.7	4.5

Table D.8: Fit parameters associated with the spectra presented for shot 27.

Position (mm)	**E_0 (kV/cm)**	**E_1 (kV/cm)**	**I_{R2} (%)**	**kT_{R2} (eV)**
1.0	-4.0 ± 0.1	2.9 ± 0.1	4.9	42.4
4.1	-2.4 ± 0.2	1.9 ± 0.3	9.2	21.6
7.6	-0.4 ± 0.8	2.1 ± 1.0	3.3	105.9

Table D.9: Fit parameters associated with the spectra presented for shot 28.

Position (mm)	**E_0 (kV/cm)**	**E_1 (kV/cm)**	**I_{R2} (%)**	**kT_{R2} (eV)**
1.0	-4.3 ± 0.1	3.2 ± 0.1	7.8	43.6
4.1	-2.6 ± 0.2	2.6 ± 0.2	9.6	29.1
7.6	-1.2 ± 0.4	0.6 ± 0.8	9.0	40.1

The π and σ profiles obtained in the parallel field configuration are presented in Figure D.1 through Figure D.6 for the H_β transition and Figure D.7 through Figure D.12 for the $5^3D \rightarrow 2^3P$ He I transition. The π and σ profiles obtained in the perpendicular field configuration are presented in Figure D.13 through Figure D.18 for the H_β transition and Figure D.19 through Figure D.24 for the $5^3D \rightarrow 2^3P$ He I transition. The black curve and markers represent the fitted continuous and pixelated theoretical spectral line profile respectively.

D.1 Parallel Field Configuration - H_β

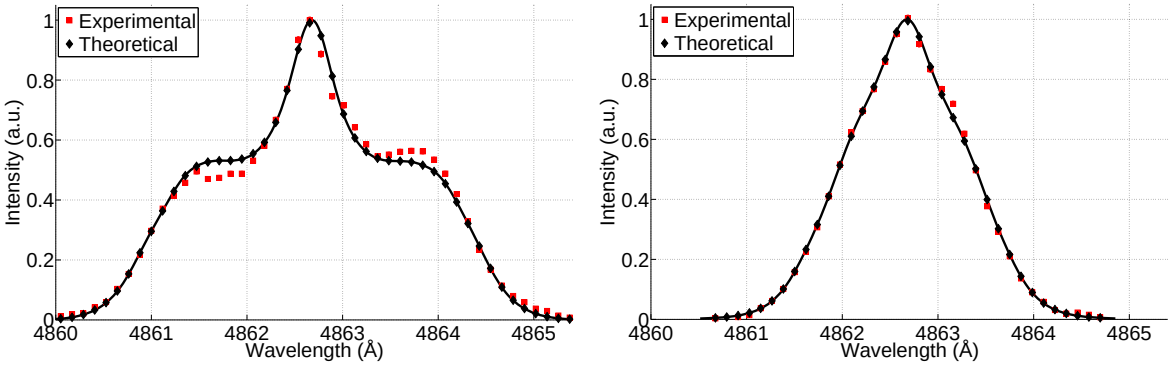

(a) (b)

Figure D.1: Fit to the H_β (a) π and (b) σ profiles for shot 3 at a position of $z = 0.8$ mm.

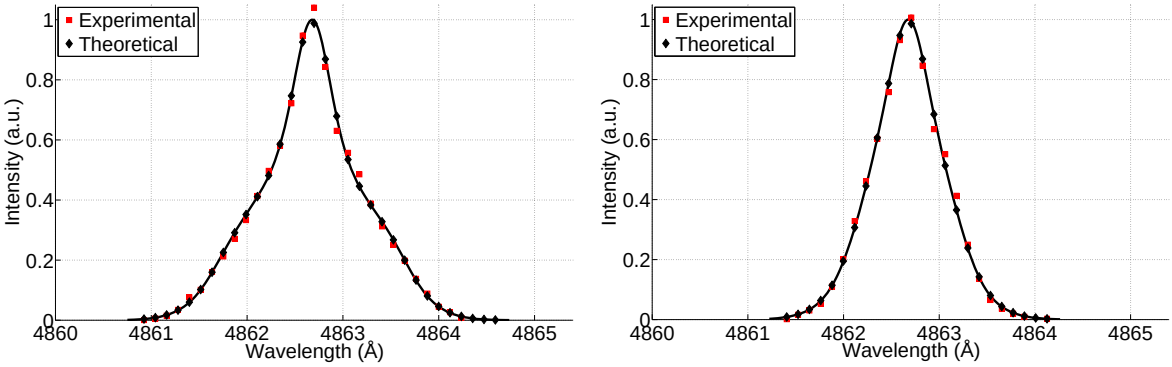

(a) (b)

Figure D.2: Fit to the H_β (a) π and (b) σ profiles for shot 3 at a position of $z = 3.8$ mm.

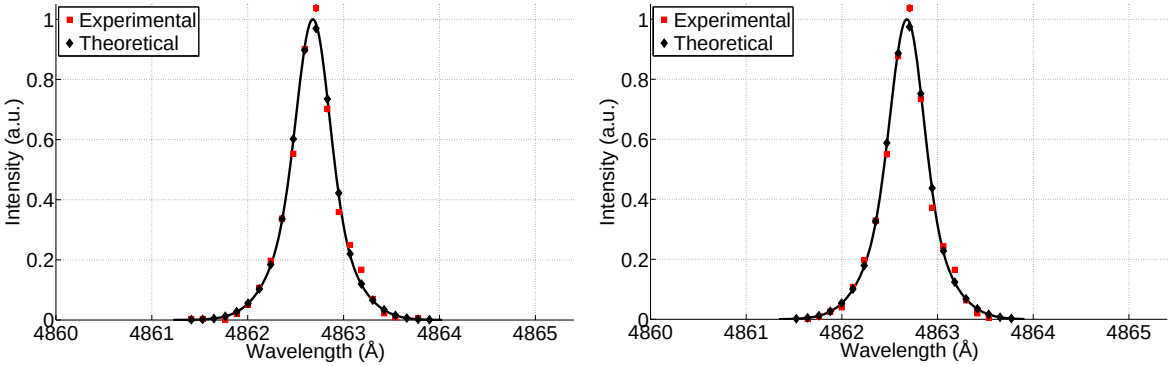

(a) (b)

Figure D.3: Fit to the H_β (a) π and (b) σ profiles for shot 3 at a position of $z = 7.9$ mm.

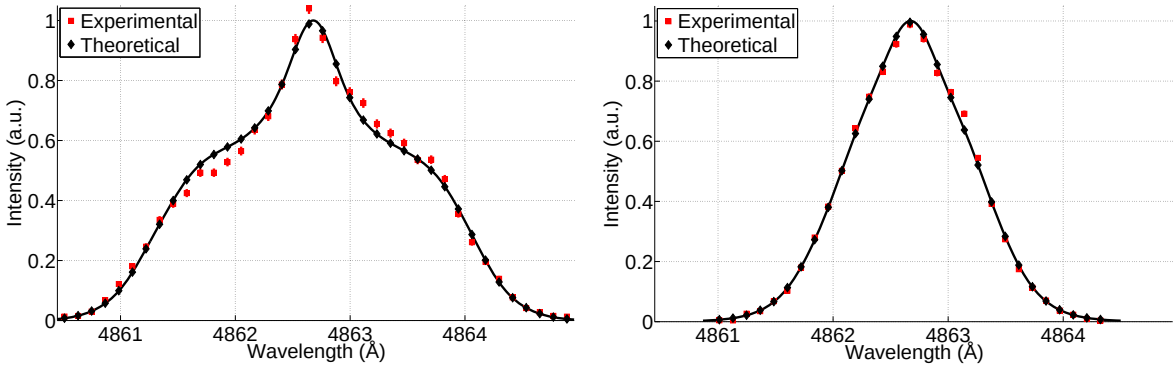

(a) (b)

Figure D.4: Fit to the H_β (a) π and (b) σ profiles for shot 4 at a position of $z = 0.8$ mm.

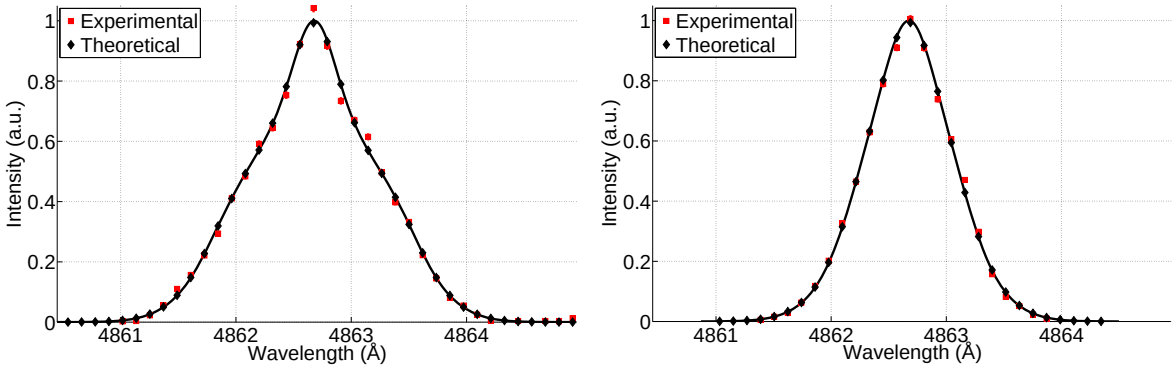

(a) (b)

Figure D.5: Fit to the H_β (a) π and (b) σ profiles for shot 4 at a position of $z = 3.8$ mm.

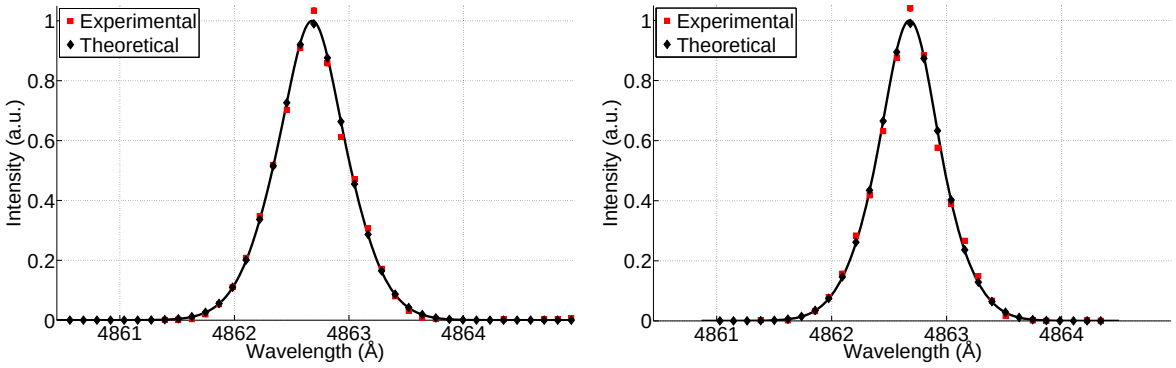

(a) (b)

Figure D.6: Fit to the H_β (a) π and (b) σ profiles for shot 4 at a position of $z = 7.9$ mm.

D.2 Parallel Field Configuration - $5^3D \rightarrow 2^3P$ He I

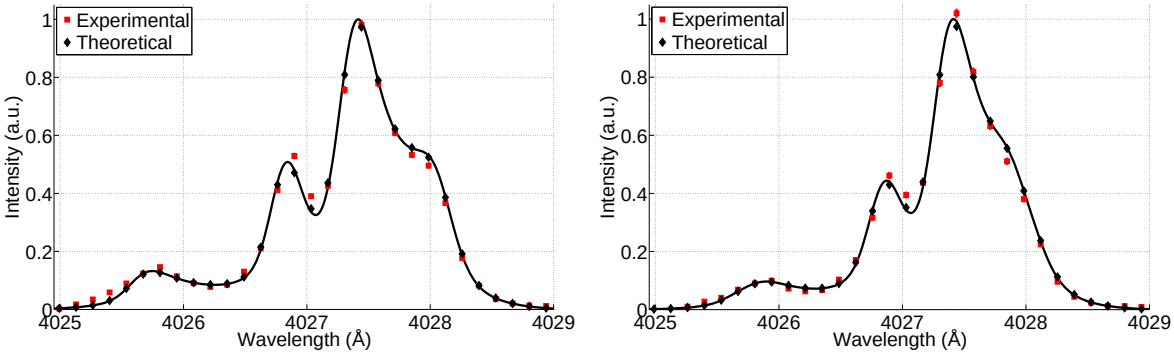

(a) (b)

Figure D.7: Fit to the $5^3D \rightarrow 2^3P$ He I (a) π and (b) σ profiles for shot 11 at a position of $z = 0.8$ mm.

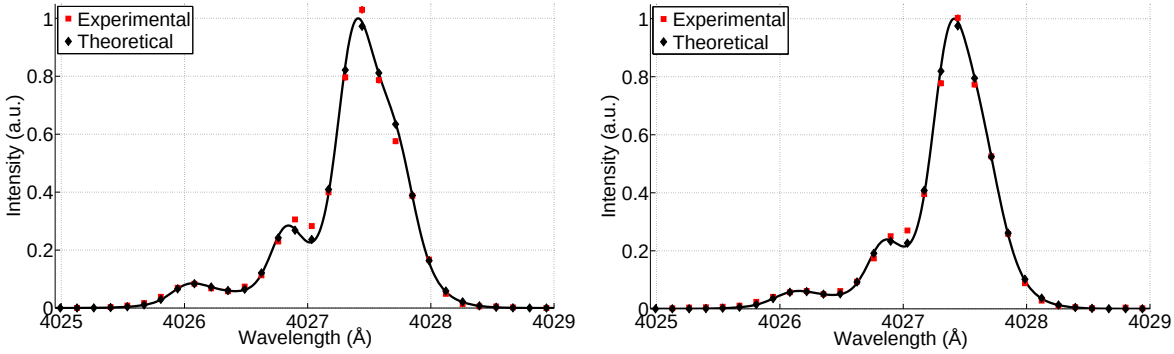

(a) (b)

Figure D.8: Fit to the $5^3D \rightarrow 2^3P$ He I (a) π and (b) σ profiles for shot 11 at a position of $z = 3.8$ mm.

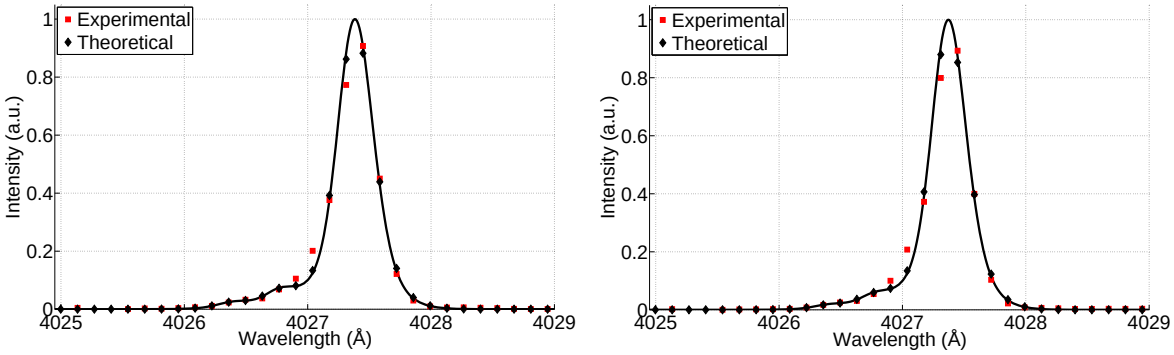

(a) (b)

Figure D.9: Fit to the $5^3D \rightarrow 2^3P$ He I (a) π and (b) σ profiles for shot 11 at a position of $z = 7.9$ mm.

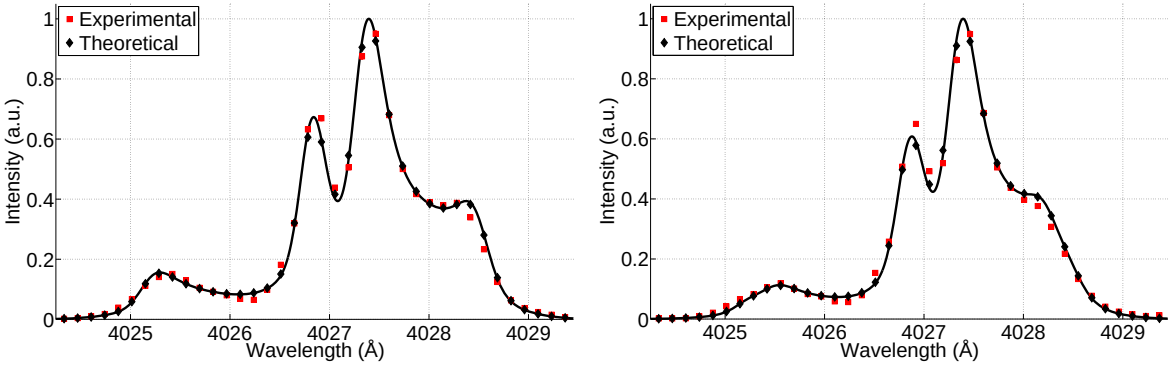

(a) (b)

Figure D.10: Fit to the $5^3D \rightarrow 2^3P$ He I (a) π and (b) σ profiles for shot 12 at a position of $z = 0.8$ mm.

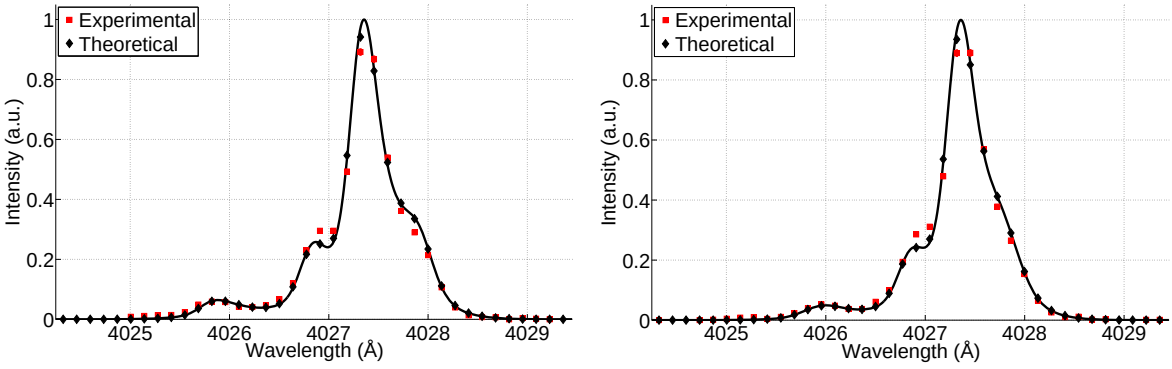

(a) (b)

Figure D.11: Fit to the $5^3D \rightarrow 2^3P$ He I (a) π and (b) σ profiles for shot 12 at a position of $z = 3.8$ mm.

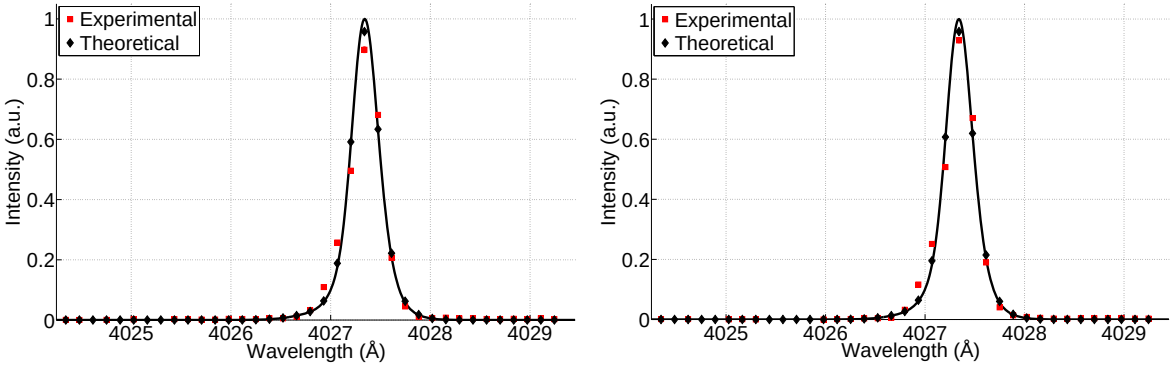

(a) (b)

Figure D.12: Fit to the $5^3D \rightarrow 2^3P$ He I (a) π and (b) σ profiles for shot 12 at a position of $z = 7.9$ mm.

D.3 Perpendicular Field Configuration - H_β

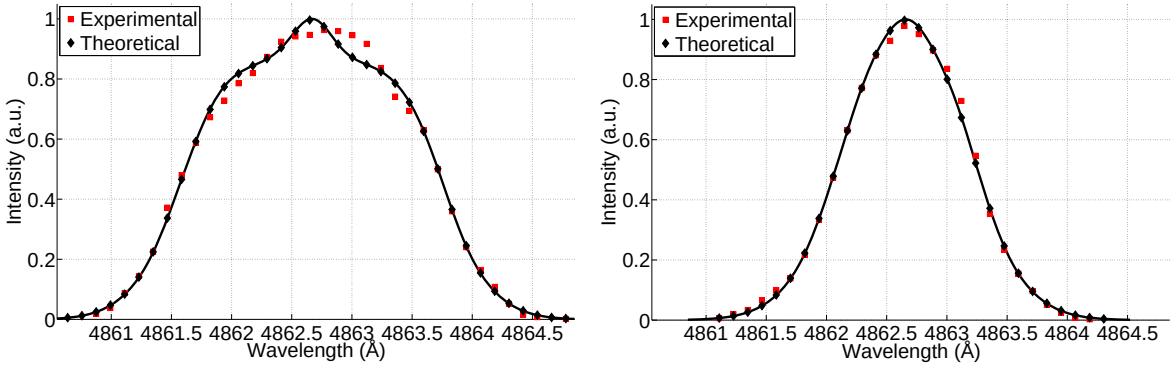

(a) (b)

Figure D.13: Fit to the H_β (a) π and (b) σ profiles for shot 19 at a position of $z = 1.0$ mm.

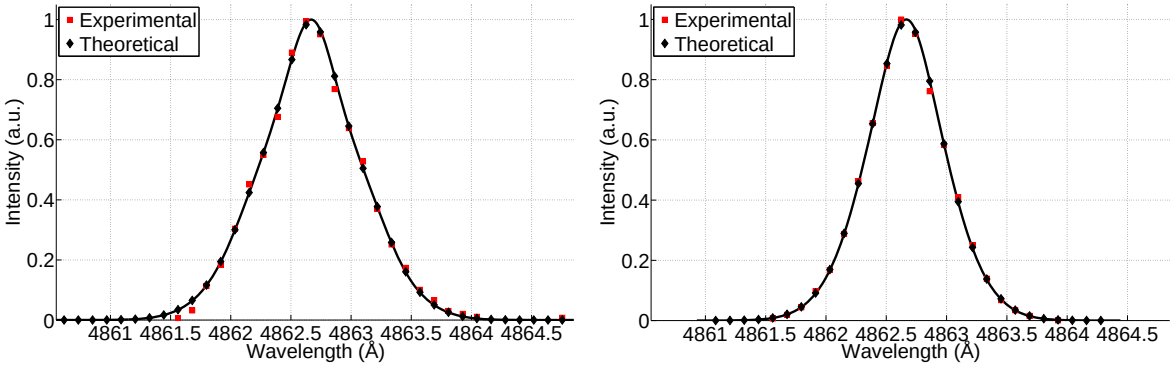

(a) (b)

Figure D.14: Fit to the H_β (a) π and (b) σ profiles for shot 19 at a position of $z = 4.1$ mm.

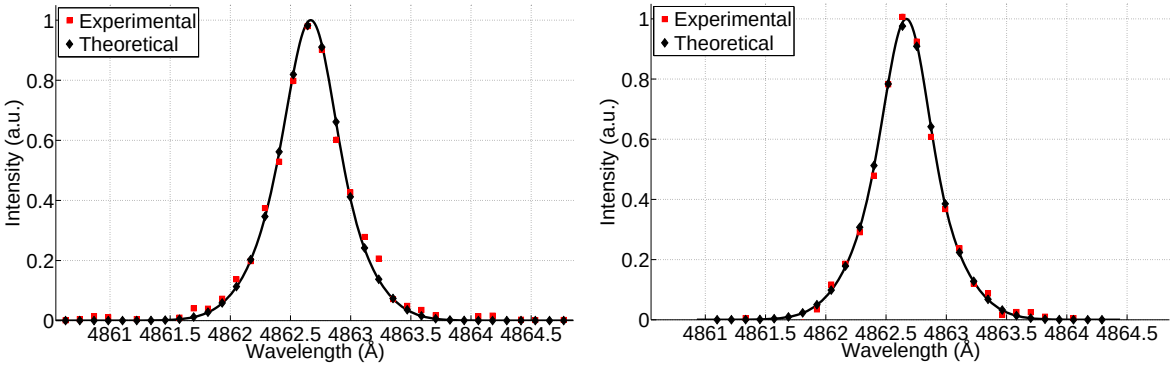

(a) (b)

Figure D.15: Fit to the H_β (a) π and (b) σ profiles for shot 19 at a position of $z = 7.6$ mm.

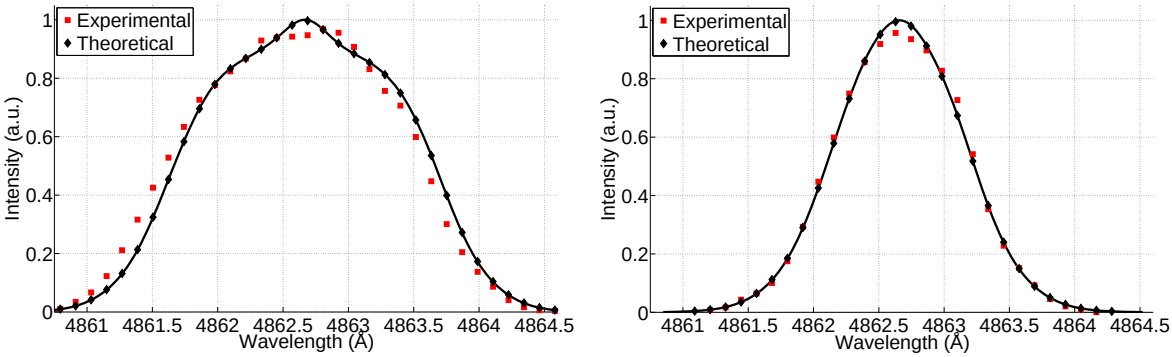

(a) (b)

Figure D.16: Fit to the H_β (a) π and (b) σ profiles for shot 20 at a position of $z = 1.0$ mm.

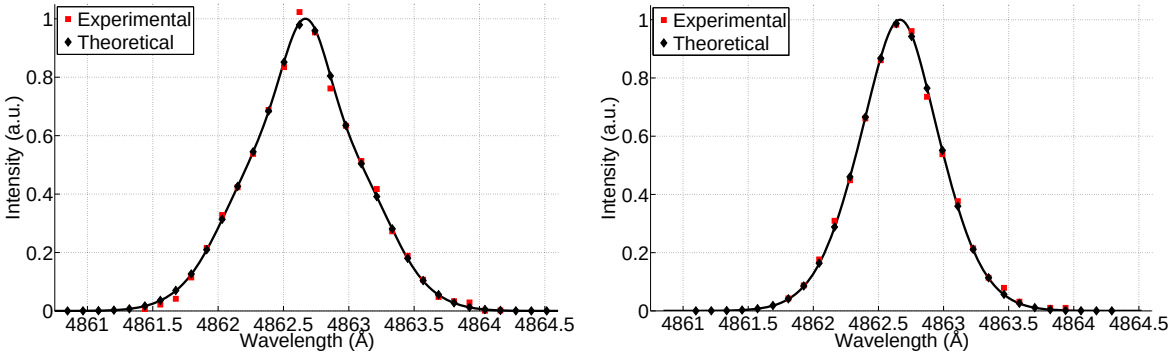

(a) (b)

Figure D.17: Fit to the H_β (a) π and (b) σ profiles for shot 20 at a position of $z = 4.1$ mm.

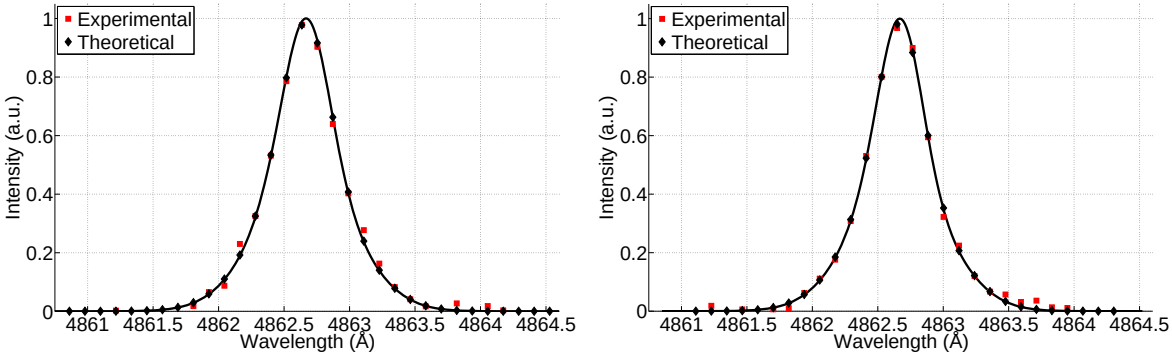

(a) (b)

Figure D.18: Fit to the H_β (a) π and (b) σ profiles for shot 20 at a position of $z = 7.6$ mm.

D.4 Perpendicular Field Configuration - $5^3D \rightarrow 2^3P$ He I

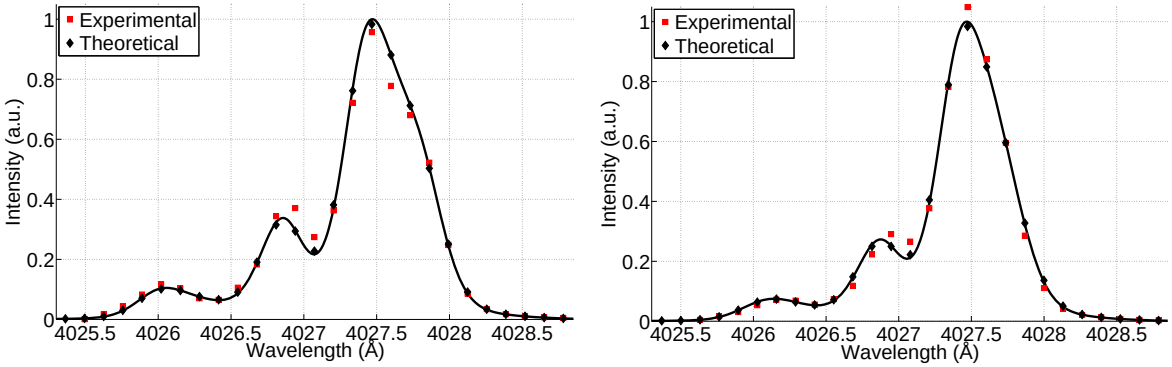

(a) (b)

Figure D.19: Fit to the $5^3D \rightarrow 2^3P$ He I (a) π and (b) σ profiles for shot 27 at a position of $z = 1.0$ mm.

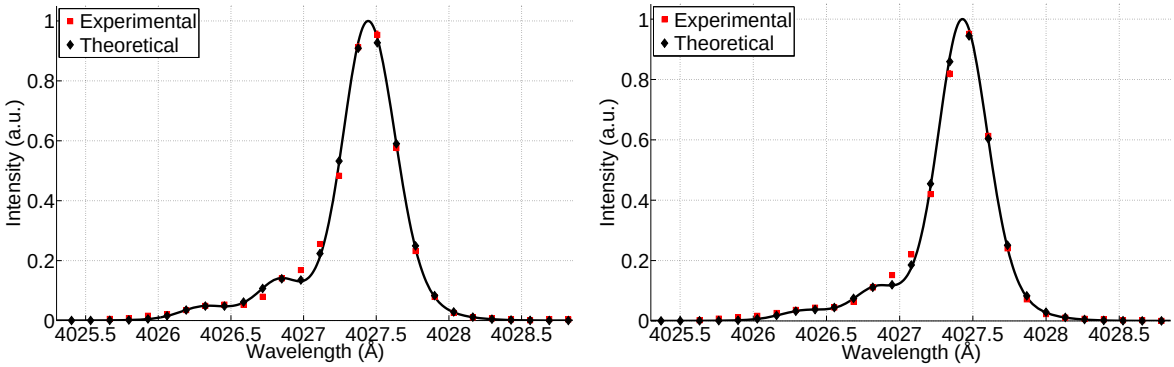

(a) (b)

Figure D.20: Fit to the $5^3D \rightarrow 2^3P$ He I (a) π and (b) σ profiles for shot 27 at a position of $z = 4.1$ mm.

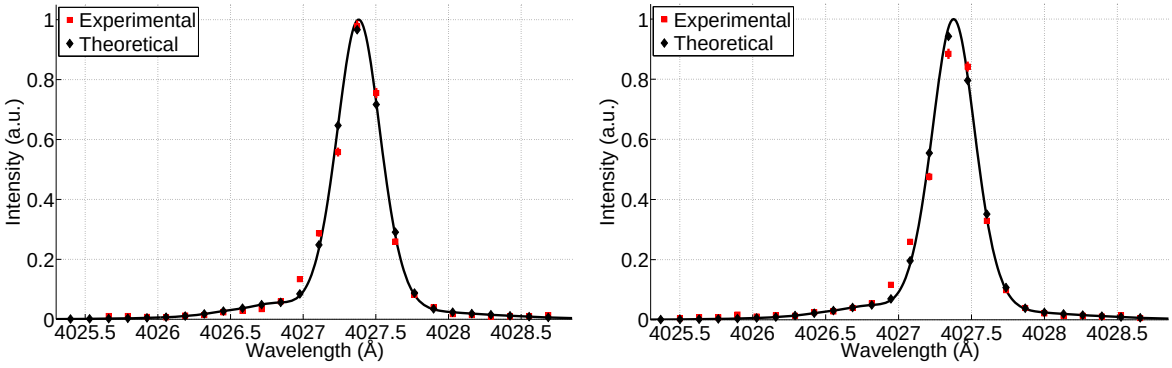

(a) (b)

Figure D.21: Fit to the $5^3D \rightarrow 2^3P$ He I (a) π and (b) σ profiles for shot 27 at a position of $z = 7.6$ mm.

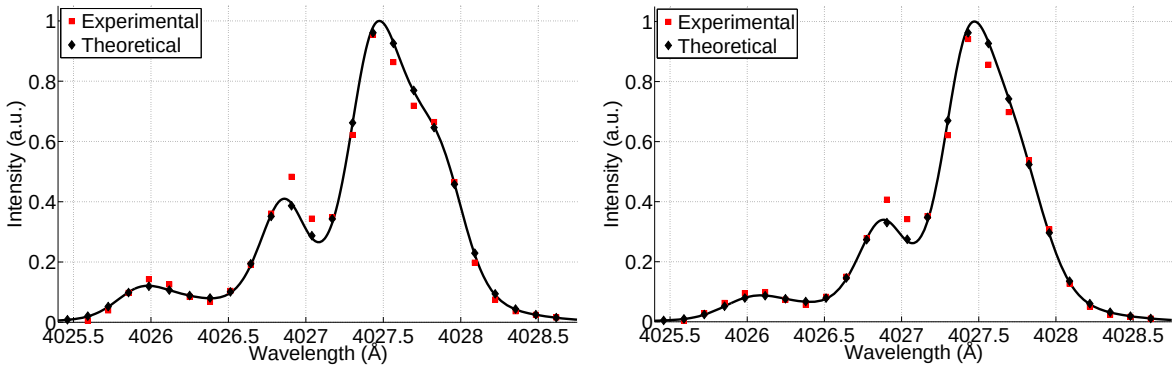

(a) (b)

Figure D.22: Fit to the $5^3D \rightarrow 2^3P$ He I (a) π and (b) σ profiles for shot 28 at a position of $z = 1.0$ mm.

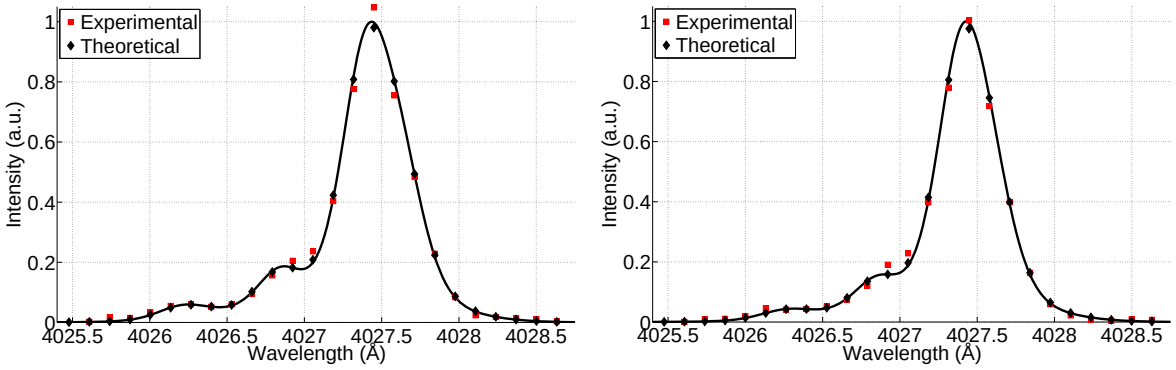

(a) (b)

Figure D.23: Fit to the $5^3D \rightarrow 2^3P$ He I (a) π and (b) σ profiles for shot 28 at a position of $z = 4.1$ mm.

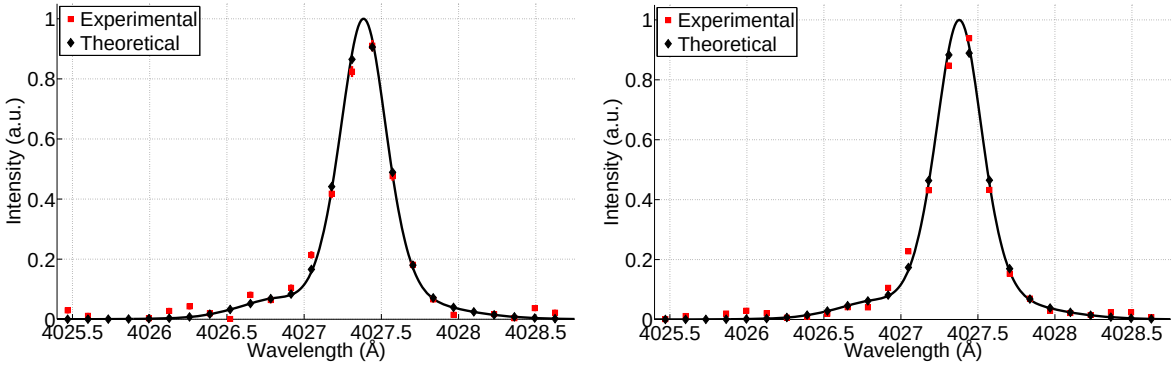

(a) (b)

Figure D.24: Fit to the $5^3D \rightarrow 2^3P$ He I (a) π and (b) σ profiles for shot 28 at a position of $z = 7.6$ mm.